D2.3 – Engineering challenges related to full scale and large deployment implementation of the proposed breakthroughs

DATE: November 2015

PROJECT COORDINATOR:

WavEC Offshore Renewables

GRANT AGREEMENT NR: 646436

PROJECT: WETFEET

The WETFEET – Wave Energy Transition to Future by Evolution of Engineering and Technology project has received funding from the European Union's Horizon 2020 programme under grant agreement No 641334.

Engineering challenges related to full scale and large deployment implementation of the proposed breakthroughs			
Project	WETFEET – Wave Energy Transition to Future by Evolution of Engineering and Technology		
WP No.	2	WP Title	System description
Deliverable No.		2.3	
Nature (R: *Report*, P: *Prototype*, O: *Other*)		R	
Dissemination level (PU, PP, RE, CO)		PU	
Lead beneficiary:		WavEC Offshore Renewables	
Contributing partners		Teamwork, IST, INNOSEA, SSSA, SELMAR, JKUL, Aurora Ventures	
Authors List:		Boris Teillant (WavEC) Kilian Krügel (WavEC) Matthieu Guérinel (WavEC) Miguel Vicente (WavEC) Yannick Debruyne (WavEC) Federico Malerba (WavEC) Marty Gradowski (WavEC) Stefano Roveda (WavEC) Frank Neumann (Teamwork) Hans Von Noorloos (Teamwork) Roelof Schuitema (Teamwork) Rui Gomes (IST) João Henriques (IST) Luis Gato (IST) Adrien Combourieu (INNOSEA) Antoine Neau (INNOSEA) Bruno Borgarino (INNOSEA) Jean-christope Doussal (INNOSEA) Maxime Philippe (INNOSEA) Giacomo Moretti (SSSA) Marco Fontana (SSSA)	
Quality reviewer			
Status (F: final; D: draft; RD: revised draft):		D	
Due Delivery Date:		01/10/2016	
Actual Delivery Date:			

Version no.	Dates and comments
1	28-Jun-2016 Outline proposition
2	04-Aug-2016 Outline revised
3	10-Oct-2016 Full draft
4	21-Oct-2016 All reviews collected
5	31-Oct-2016 Full draft revised – final version edited
6	01-Nov-2016 Final version for submission

Table of Contents

Table of figures

Table of tables

EXECUTIVE SUMMARY

This report presents Deliverable 2.3 of the WETFEET H2020 project – Engineering challenges related to full-scale and large deployment implementation of the proposed breakthroughs. The scope of the document covers all breakthrough conceptually proposed in Deliverable 2.1 and 2.2 [1], [2]. Array breakthroughs are not treated under this Work Package (WP) 2 of the WETFEET project (see the outcome of WP6). This corresponds to 8 ideas, namely:

- The negative spring
- The enhanced added-mass
- Submergence as a survivability strategy
- Dielectric Elastomer Generators as Power-Take-Off (PTO)
- Novel tetra-radial air turbine PTO
- Novel water turbine PTO
- The structural membrane
- The control cocoon as an O&M strategy

Initially, the present document concentrates on the design approaches followed by the two working groups constituted for the analysis of the proposed breakthrough under WP2. Following some discussions within the consortium of the WETFEET project, it was decided to endeavor toward the characterization of reference Wave Energy Converters (WEC) design cases. While this effort goes beyond the objectives of WP2, it aims at setting baseline scenarios against which the proposed breakthrough concepts can be, in turn, benchmarked.

For each breakthrough idea, a preliminary feasibility assessment was carried out. Diverse methods have been deployed to support this preliminary analysis in response of the variety of the concepts. Therefore, this report relies on both numerical techniques and engineering considerations.

At this stage, several challenges toward the full-scale applications of these breakthrough concepts have been highlighted. Whilst few ideas admonish the conceivers to pursue their development with excessive enthusiasm due to identified bottlenecks, others attest of an attractive potential to reduce the cost and/or improve the performance of WECs.

Although these breakthrough ideas were analyzed under specific wave energy case studies, applications to other WEC systems was discussed. In addition to the quantitative and qualitative results of these preliminary feasibility case studies of integrating the breakthrough concepts, projections to future work in relation to the other WPs of the WETFEET project are depicted.

LIST OF ACCRONYMS

AEP	Annual Energy Production
DE	Dielectric Elastomers
DEG	Dielectric Elastomer Generator (to refer to the whole generator)
EAM	Enhanced Added-Mass
CAPEX	Capital Expenditures
IFS	Internal Free Surface
IVV	Immersed Variable Volume
LCOE	Levelized Cost of Electricity
NS	Negative Spring
OPEX	Operational Expenditures
OWC	Oscillating Water Column
PTO	Power Take-Off
SPVD	Submerged Pressure Variable Device
TRL	Technology Readiness Level
TPL	Technology Performance Level
WEC	Wave Energy Converter

1. DESIGN APPROACHES FOR THE BREAKTHROUGHS ANALYIS WITHIN THE TWO WAVE ENERGY CONVERTERS

1.1. Context and motivation

In this report, the key findings from the initial engineering analysis of the breakthrough concepts proposed within the framework of the WETFEET H2020 EU funded project are documented. Building upon the conceptual description of the breakthroughs associated to the OWC spar buoy [1] and the Symphony [2], tailored-made engineering reasoning were developed to examine the feasibility and potential of each breakthrough concept.

Another objective of the work presented herein is the provision of design specifications and recommendations for future experimental testing, in-depth numerical analysis and multi-disciplinary assessment. To facilitate this transition, practical aspects related to the turning of the breakthrough concepts into use at large-scale applications have been examined. Critical requirements for manufacturing, assembly, installation and the associated supporting machinery are highlighted.

Whilst these objectives will help evaluating the feasibility and the challenges of each breakthrough individually, this might not be sufficient to capture the real potential added-value brought by their implementation. For this reason, common effort to resolve this issue was initiated by establishing reference design cases. The goal of having reference design cases is to measure the impact of each breakthrough by comparing a solution considering the breakthrough concept against an alternative option utilizing a design without the breakthrough typically employing more conventional systems or processes.

To pave the way toward the future multidisciplinary benchmarking exercise (which will be undertaken under Work Package 7), the following sections will lay out the foundations of this assessment by providing data for selected WEC designs. In essence, priority is given to the general specifications of the WEC system as well as any relevant performance data with particular emphasis on energy production. Where possible dynamic behavior, structural integrity and reliability information was retrieved from the public domain or generated via in-house numerical tools.

1.2. Design approach for the breakthroughs associated with the OWC spar buoy device

The integration of five breakthrough concepts into the OWC spar buoy is investigated in the remainder of this report. In response to the diversity of the breakthrough ideas and their immaturity, tailor-made numerical engineering analysis has been developed to address the potential and key issues that may come along each of the breakthrough concepts.

Looking at the Technological Readiness Level (TRL) scale as described by the European Marine Energy Centre (EMEC) [3], the current degree of maturity of the breakthrough ideas proposed herein can be

evaluated at TRL2 to TRL4. At this early conceptual stage, it is of paramount importance to realize a feasibility assessment.

Such feasibility assessments are often supported by the deployment of numerical modelling since this technique usually requires less financial investment than experimental testing. Commercially available numerical software packages for the wave energy sector typically cost up to several thousand euros for a lifetime license (e.g WAMIT, OrcaFlex and some others are open-source and free such as WEC-SIM, OPEN-FOAM and DTOcean) while tank testing (or PTO test-rig infrastructure) cost several hundreds up to few thousands per day of usage excluding the construction of the prototype and acquisition of the necessary equipment. Both numerical and experimental modelling require engineering and technical expertise to design and carry out the work.

Furthermore, numerical approaches are generally easily repeatable and tuneable allowing a greater degree of flexibility through parametric and optimisation studies than experiments. In line with the description of WP2 of the WETFEET project, the breakthrough associated with the OWC spar buoy have undergone tailor-made preliminary numerical and engineering analysis. The methodology and most pertinent findings are documented in the remainder of this report.

Acknowledging the need to evaluate the potential of the breakthrough ideas under a coherent framework, the WETFEET consortium decided to make an additional effort in collecting and generating "reference" data. These "reference" data correspond to a "reference" design of the WEC which does not feature the breakthrough ideas. This task will serve as a basis for the benchmarking exercise initiated in this report which will be completed under Work Package 7 of the WETFEET project. The following section describes the path toward the implementation of simulations providing data on several aspects:

- Load assessment of the reference OWC spar buoy design under survival conditions
- Preliminary structural analysis based on the previous loads resulting on recommendations for design improvements
- Load assessment of the two "improved" designs suggested from the preliminary structural analysis
- Compilation of power performance matrix for the reference design
- To complement the system description initiated in Deliverable 2.1 [1] by specifying further sizes, masses and production and installation issues not only from the buoy itself, but also from the anchoring system and grid

1.3. The OWC Spar buoy reference design case – WavEC, INNOSEA, IST

Building on the results reported in WETFEET deliverable 2.1 [1], the analysis for the OWC spar buoy also considers the 100-year storm environmental conditions observed at Leixões (see [1] for details). The preliminary design analysis reported hereafter relies on previous design-work on the OWC spar buoy developed by members of the consortium. The initial geometry follows the optimized shape constructed in Gomes et al. [4].

1.3.1. Load assessment of the OWC spar buoy reference design – first iteration

In this first iteration the original reference OWC spar buoy design, denoted "design #0", is considered. A schematic representation of the OWC spar buoy is shown in Figure 1-1 (and a scantling of the geometry is provided in Appendix A). In order to realize a preliminary structural design analysis of the OWC spar buoy, the main loadings on the column during the 100-year storm event should be estimated. Several assumptions need to be made for a proper assessment of the local loadings on the column. In particular, the following questions have to be answered:

- Which loads have to be considered and which can be neglected? (e.g. gravity, inertia, 1st order diffraction and radiation wave loads, 2nd order wave loads, currents, moorings, etc.)
- Which method / theory should be used? (potential flow/Morison, frequency domain/ time domain)
- What is the worst loading condition? (e.g. maximum inclination, maximum acceleration, maximum shear force, etc.)

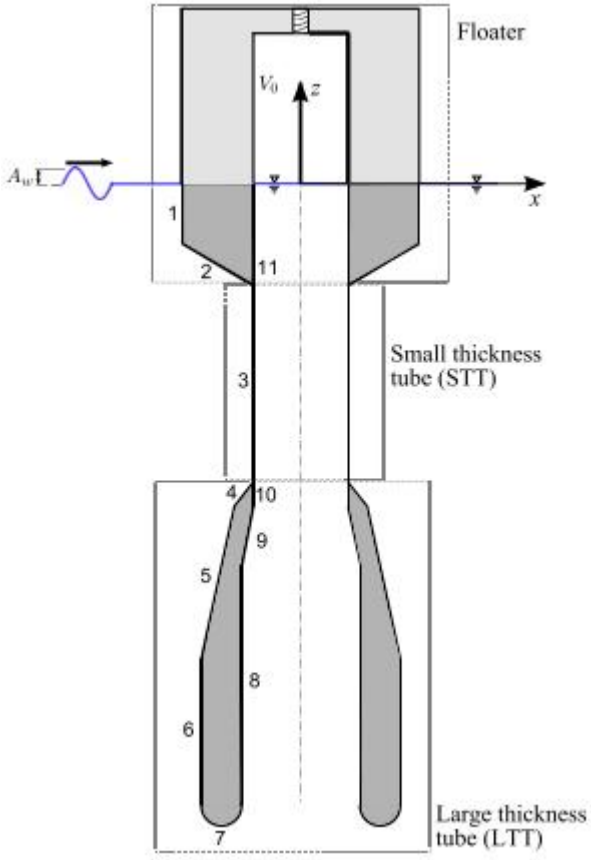

FIGURE 1-1 SCHEMATIC DESCRIPTION OF THE OWC SPAR BUOY

NUMERICAL MODEL SELECTION AND RAOs:

Following an initial series of test cases, 3 different numerical models of the OWC spar buoy structure were built and compared primarily by looking at the Response Amplitude Operators (RAOs). Considering the extreme conditions used for the analysis, the OWC PTO system is assumed to be disconnected since production is not expected to occur in survival mode. As a consequence, there are no external forces on the system that come from the PTO in the present simulations. The different numerical models are the following:

- **Frequency domain linear response with WAMIT ®** [5]**:**

The RAO of the OWC can be obtained directly as an output of WAMIT. This method considers that the OWC is free floating, and only takes into account the body inertia and the first order loads due to the hydrostatic pressure and the excitation and radiation forces. The RAOs were computed for a set of periods ranging from approximately 1.5s to 250s.

- **Time domain response with OrcaFlex** [6] **+ WAMIT**

This model of the OWC is a potential-flow-based time-domain model that considers the 1st order hydrodynamic loadings as well as the mooring forces (Finite Element Method (FEM)). In order to obtain the RAO of the OWC, 10-min simulations in regular wave of unit-amplitude were run for periods going from 3 to 25 s with a delta of 1 s. The simulations included 200 s of build-up and 400 s of sinusoidal wave.

- **Time domain response with OrcaFlex + Morison**

This model of the OWC is a time-domain model that considers non-linear hydrodynamic loadings (Morison's equations) as well as the mooring forces (FEM). In order to obtain the RAO of the OWC, 10-min simulations in regular wave of unit-amplitude were run for periods going from 3 to 25 s with a delta of 1 s. The simulations included 200 s of build-up and 400 s of sinusoidal wave. The post-process included a high-pass filtering of the time-domain response in order to delete transient effects and focus on the wave frequency response.

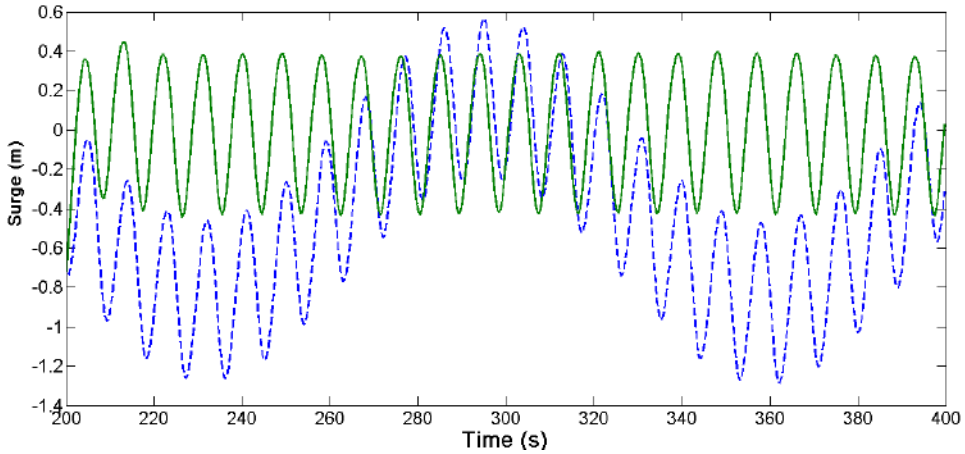

FIGURE 1-2 POST-PROCESSING OF ORCAFLEX-MORISON MODEL RESPONSE. IN GREEN THE ORIGINAL REGULAR WAVE IS REPRESENTED WHILE THE BLUE-DOTTED LINE SHOWS THE FILTERED RESPONSE

- **Comparison of the 3 models**

The convergence of the 3-models was ensured. Main characteristics of the 3 models are summarized in Table 1-1.

TABLE 1-1 PROPERTIES OF THE 3 NUMERICAL MODELS

Model:	WAMIT	Orca + WAMIT	Orca + Morison
Solution	Frequency domain	Time domain	Time domain
Hydrodynamics	Potential flow	Potential flow	Morison
Moorings	N/A	FEM	FEM

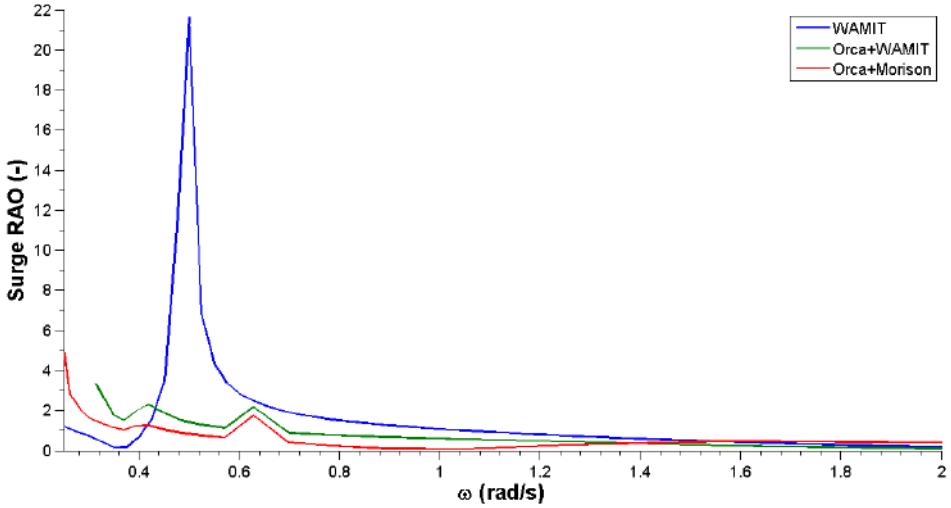

FIGURE 1-3: COMPARISON OF SURGE RAO

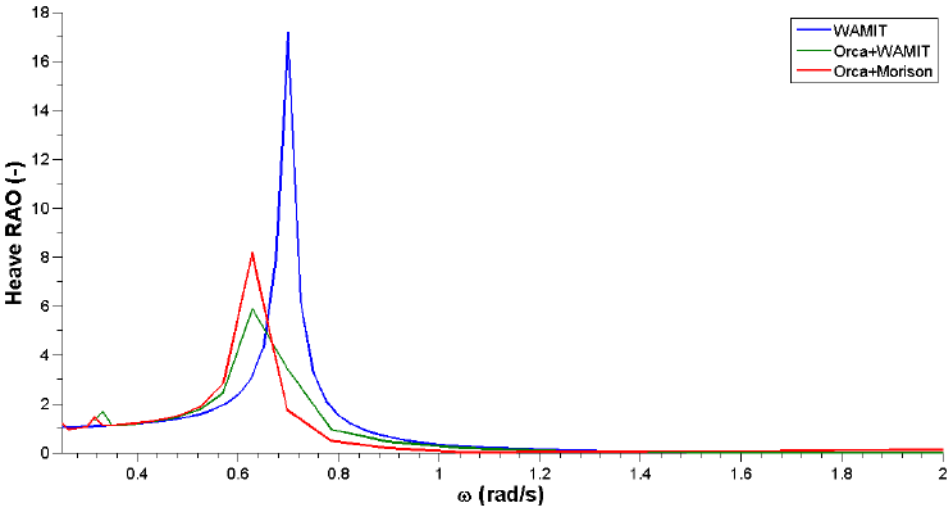

FIGURE 1-4: COMPARISON OF HEAVE RAO

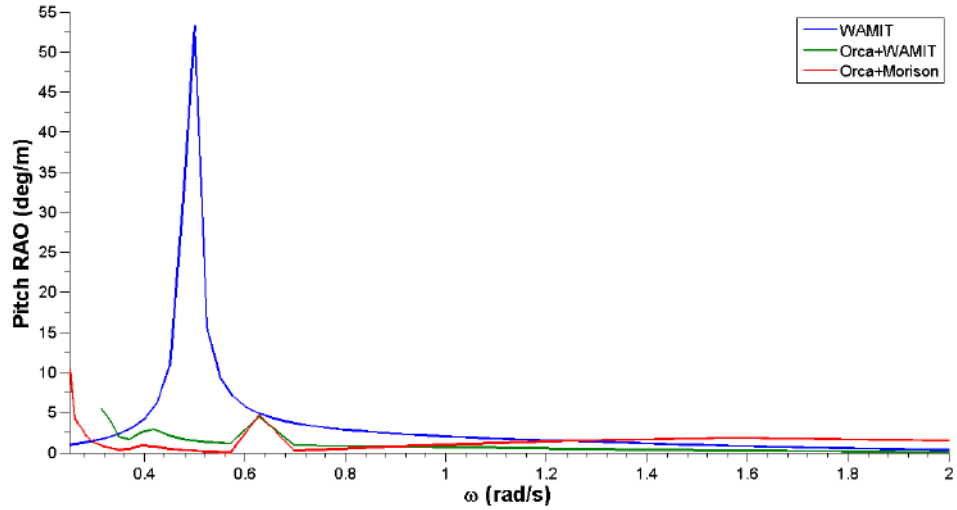

FIGURE 1-5: COMPARISON OF PITCH RAO

The RAO are showed in Figure 1-3 to Figure 1-5. The influence of the mooring is clear:

- The heave resonance period is shifted from 9 to 10 seconds.
- The pitch resonance peak at 12.56 s from the linear model is divided into 2 peaks at 10 s (combination with heave) & 15 s in the non-linear model

In Figure 1-3, the RAO peak observed in surge is believed to be due to the surge / pitch interactions as no external stiffness or damping matrix has been used in the WAMIT simulations. Besides, this can also be verified by looking at Figure 1-5, where the peak in pitch occurs at the same frequency as in surge.

Since the frequency domain does not provide a complete overview of the behaviour of the OWC spar buoy, it is required to take a look at the time-domain models. The RAOs from the two time-domain models have a very similar shape, however the potential flow model anticipates bigger motions of the OWC for periods larger than 6 seconds. Since the structural moment induced by the gravity (resp. inertia) of the OWC increases with the inclination (resp. rotational acceleration) of the OWC, it was decided that the potential flow model is the most conservative approach. Therefore, it was decided to pursue with the 'OrcaFlex + WAMIT' model to estimate the local loading on the column.

GLOBAL LOADS

A time-domain simulation of the behaviour of the OWC in a regular wave of height H_{max} and of period T_{max} has been run to determine the global loadings on the OWC. In this first approach, only the 1st order hydrostatic forces, 1st order excitation forces, 1st order radiation forces, and mooring forces (through Finite Element Method) were included. The simulation reaches a steady and periodic state which was analysed in details.

In figure Figure 1-6, one can see that the response of the OWC is not sinusoidal because of the action of the mooring system. This makes the assessment of the local hydrodynamic efforts on the structure slightly more difficult, as it is explained in the next section.

Since the mooring force is the most 'concentrated' point-load along the OWC (large force applied only at the section which includes the fairlead) the worst moment was chosen to be the moment when the local Lx-connection forces reached a maximum (e.g. at $t = 136.9$ sec in Figure 1-7). It is supposed that this might create the largest moment in the structure. The assessment of the local effort was realized for this particular time-step.

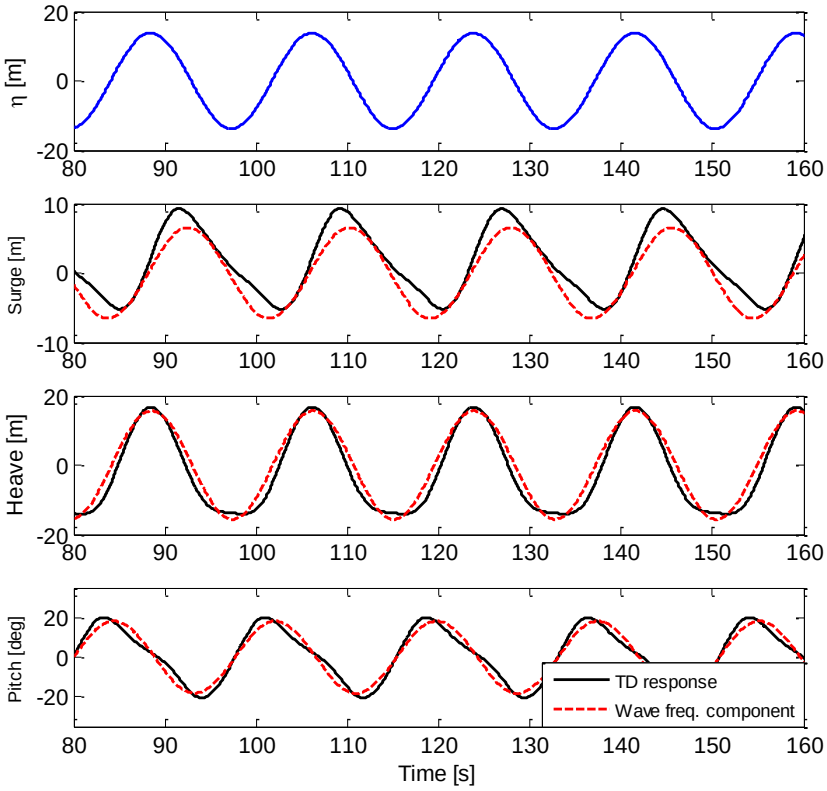

FIGURE 1-6: MOTIONS OF THE OWC IN A REGULAR 100-YR WAVE. THE TOP-FIGURE SHOWS THE SURFACE ELEVATION

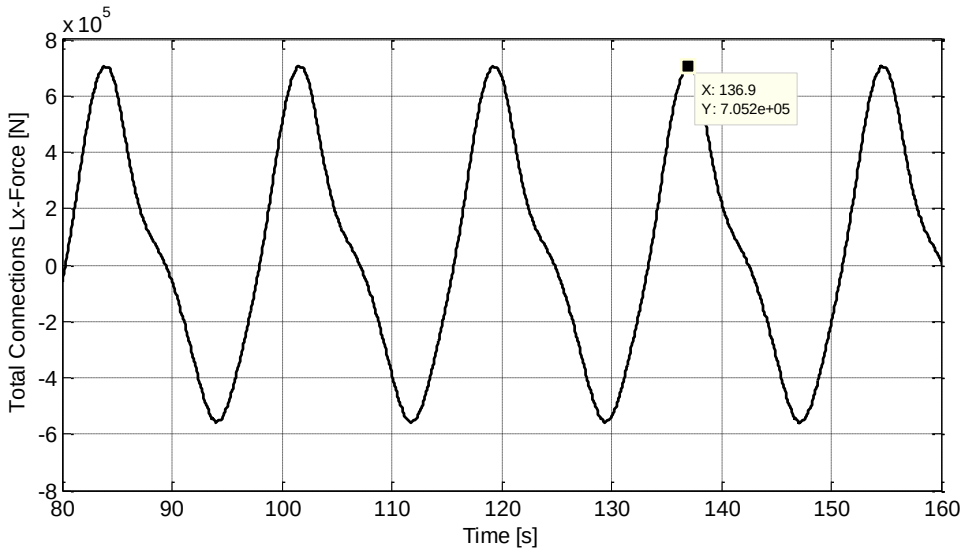

FIGURE 1-7: TOTAL CONNECTIONS FORCES LX UNDER A 100-YR REGULAR WAVE

The consistency of the forces and moments obtained with OrcaFlex has also been checked to ensure the validity of the results. The incoming wave being regular and the OWC spar buoy being axisymmetric the verification is exemplified for the surge, heave and pitch modes only in appendix A. The total excitation is computed using the incoming wave excitation, the radiated efforts from the body, the hydrostatic loads as well as the connections efforts.

ADDITIONAL LOADS

For each loading, the order of magnitude of the forces (locally or globally) should be assessed in order to decide whether to include them or not in the input to the structural model.

- **Current Loads**

An estimation of the local current loads was realized. For each slice, the horizontal current loading F_{Si} is calculated through:

$$F_{Si} = \frac{1}{2}\rho_w C_d A V^2 \,, \qquad \textbf{(1-1)}$$

Where F_{Si} is the horizontal component of the current loading on slice I (in N), ρ_w is the water mass density (kg/m3), Cd (= 1) is the estimated drag coefficient for the OWC (dimensionless), A is the projected area (m^2) in the plane perpendicular to the current stream and V is the current velocity (m/s). After comparison with the diffraction pressure efforts calculated in D2.1 [1], the current loads per slice do not exceed 2% of the diffraction pressure. Therefore, it was decided that the current loadings could be neglected in this structural design for now.

- **2nd order mean drift**

The second-order mean drift force can be assessed with WAMIT based on the momentum conservation principle, without the assumption of energy conservation, as defined by Newman [7]. A comparison between the mean drift force and the surge force is presented in Figure 1-8.

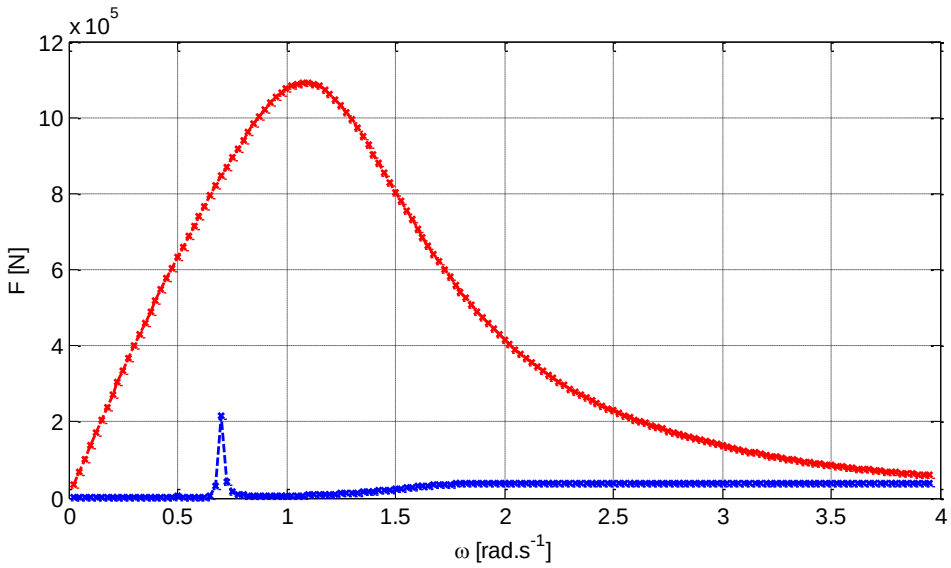

FIGURE 1-8: OWC SURGE MEAN DRIFT FORCE. BLUE CURVE REPRESENTS THE MEAN DRIFT FORCE AND THE RED CURVE THE WAVE SURGE FORCE

There is one small peak located around 0.65 $rad.s^{-1}$. Even though the drift force appears to be only in a narrow band, these effects should be included in order to properly assess their influence should a more extensive study be performed on the OWC in the future. They have been neglected for the structural analysis reported hereafter.

LOCAL LOADS:

Following the work of the previous sections, the 3 components of the loads along the OWC can be calculated, in both the GLOBAL and LOCAL coordinate system. While the methodology to derive the local gravity and inertia loads is presented in section 1.3.2, the following will explain how the hydrostatic and hydrodynamic loads have been locally calculated.

A WAMIT model of the OWCs was built using the so-called high-order method. The OWC geometry is represented by an assembly of panel which size is small enough to ensure that the results converge and that they provide an accurate estimation of the hydrodynamic loads per vertical slices. The maximum panel area is of 0.114 m^2.

At first, it is considered that the OWC is projected against a 1D hollow beam that extends along the vertical z axis (pointing upward). The slices were defined such that their upper and lower limits coincide with the limits of the panels defined by WAMIT (to avoid partial contributions from some panels to some slices which is difficult to quantify).

In order to realize a first structural assessment of the OWCs, the 3D components of the forces induced by the hydrodynamic pressure on vertical slices (of height lower than 0.5 m) along the column when a regular wave passes were computed. The application of this frequency-domain method to estimate the local loads is likely not to be not as straightforward in irregular waves although it has been verified for a couple of cases against a time-domain model in regular wave with a reasonable agreement. The wave considered here being regular, the loads are cyclic and the identification of the worst loads that apply on the structure is rather direct. In the case of irregular waves, this agreement might change as larger nonlinear effects might arise from the mooring lines in the Orcaflex model, which is not the case in the present case.

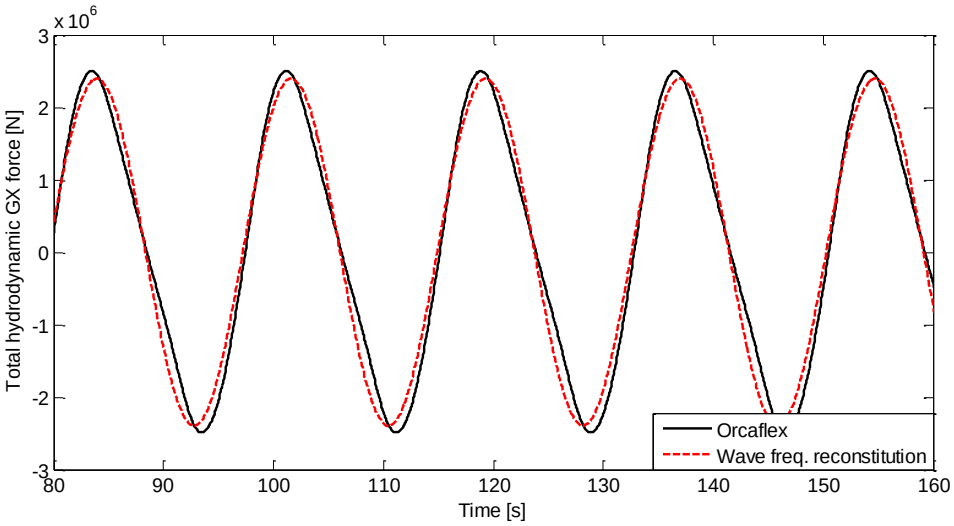

FIGURE 1-9: TOTAL HYDRODYNAMIC FORCES (GX-AXIS) IN 100-YR REGULAR WAVE

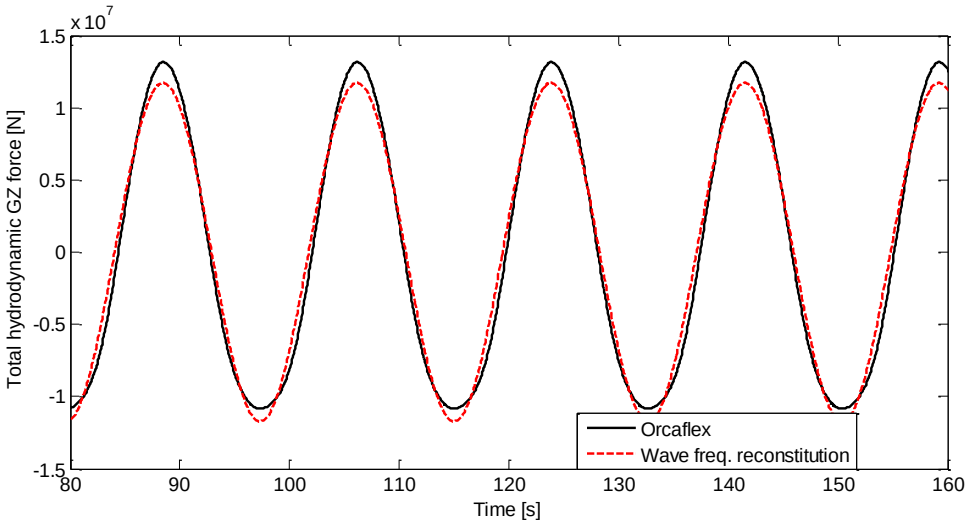

FIGURE 1-10: TOTAL HYDRODYNAMIC FORCES (GZ-AXIS) DURING 100-YR REGULAR WAVE

- **Local mooring loads:**

The overall local mooring loads can be directly read in the time-series output from OrcaFlex (Connection forces L_x, L_y, L_z). The mooring loads are shown in Figure 1-11.

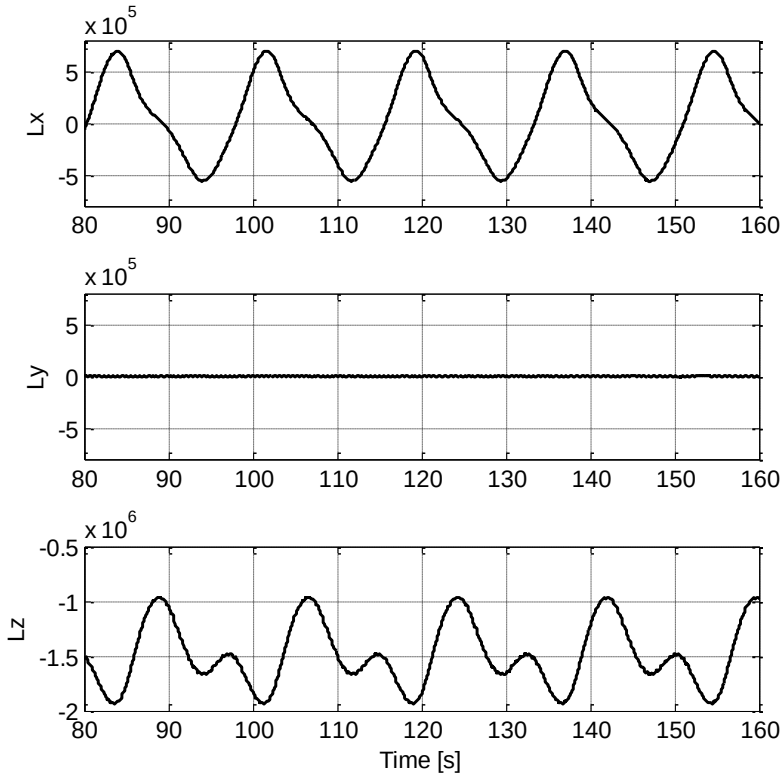

FIGURE 1-11 MOORING CONNECTION FORCES, LX, LY AND LZ CALCULATED IN ORCAFLEX

1.3.2. Preliminary structural analysis of the OWC spar buoy reference design

This section summarizes the preliminary structural assessment of the OWC Spar-Buoy performed by INNOSEA in the context of WETFEET project work package 2. An internal report explains this analysis in more details [8].

The design of the system is at conceptual stage and 3 different diameters (3, 6 and 12m) of the OWC spar buoy were initially considered. Only the configuration with larger dimension is studied in this document.

METHODOLOGY

The OWC Spar-Buoy is a long floating structure made of thin cylindrical panels. Some expected critical structural aspects (non-exhaustive) are listed below:

- Pitch angle is a very important phenomenon for the design of spars. In particular, DNV rules ([9], [10]) insist on the fact that for spars, the so called "P-Δ" effect is critical. This "P-Δ" effect refers to the apparition of internal bending moment in the structure due to a pitch angle θ. This angle induces misalignment of weight and hydrostatic loads which leads to bending. Note that independently from pitch, some load cases may also lead to important bending moment [9], among them is dry lifting and transportation.

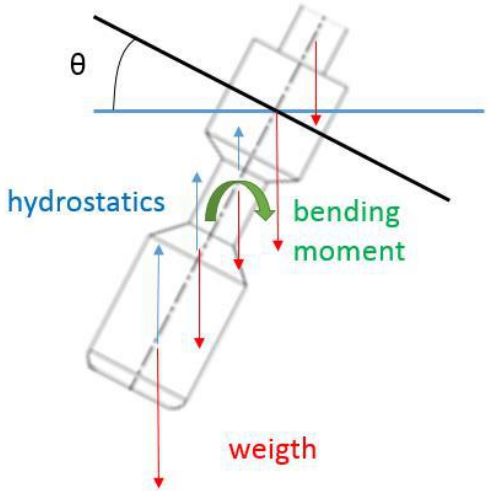

FIGURE 1-12 P-Δ EFFECT DUE TO PITCH ANGLE

- High pressure differences due to the hydrostatic pressure might be critical for the floater and the large thickness tube. In particular, presence of air in the Large Thickness Tube could induce high stresses in the plates, due to the large pressure difference that can be expected (induced by the significant draft of the structure).
- Buckling may be more critical than yield for thin panels, especially for outer shell in large thickness tube. The ultimate strength may be significantly reduced because of buckling.

If substantial thickness increases are required, the following points may be critical:

- Increase of thickness may lead to excessive structure mass that could impact the system hydrodynamic performances and the cost of the produced energy.
- Excessive thicknesses may lead to unfeasible designs from manufacturing and logistic point of views.

For these reasons, it is chosen to adapt the structure general arrangement by adding longitudinal and/or ring stiffeners in order to withstand the design loads.

The methodology developed for this preliminary analysis is based on analytical formulations coming from linear beam theory and shell theory. This methodology includes the following steps:

- Geometry modeling.
- Integration of all the external loads (including loads provided by WAVEC, and other loads calculated by INNOSEA). Forces and moments equilibrium is also checked. If needed, a correction is added in order to guaranty dynamic equilibrium.
- Calculation of internal loads
- Calculation of internal stresses
- Checking of yielding and buckling criteria. Number of bulkheads and stiffeners, and thicknesses are then adapted to minimize structure mass while respecting strength criteria.

DNV Standards are used as design guidelines. The reference standard used is DNVGL-OS-C106 [9] ("Structural Design of Deep Draught Floating Units"). Section 5.A of DNVGL-OS-C106 [9] refers to DNVGL-OS-C101 [11] for the "methods of analysis and capacity checks of structural elements" [9] (LRFD). This analysis uses DNV-RP-C202 [12] as stated by DNVGL-OS-C101 [11] (Section 4.3) for shell structures (OWC Spar Buoy cannot be designed as a tubular member because of the high ratio diameter/wall thickness.).

With this methodology, iteration loops are quick, allowing to get a first realistic scantling estimation. In later stage of the technology development, this estimation will need to be checked and refined using more complex methods, such as finite element methods with shell elements.

Structural elements checked for yield and buckling are inner shell and outer shell (see Figure 1-13). Stiffeners are designed by following rules of DNV-RP-C202 standard, but no specific checks are performed on stiffeners. Bulkheads are not checked.

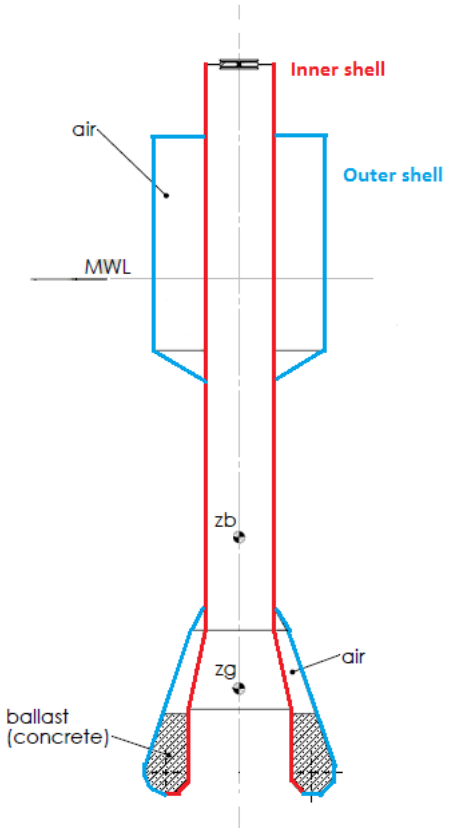

FIGURE 1-13 SYSTEM DESCRIPTION

This methodology is a simplified approach based on assumptions that should be re-assessed at further design stages. Such a methodology is considered suitable in the current project for the following reasons:

- The design is at early conceptual stage, therefore there are significant uncertainties in the data at this stage.
- Different design configurations need to be assessed rapidly.
- The scantling of the design is not known, as the purpose of this analysis is to develop a first realistic estimation of this scantling. Iterations on the scantling have been performed and need to be quick.

For the preliminary structural assessment of the OWC Spar-Buoy, the Design Load Cases (DLC) considered are specified in Table 1-2.

TABLE 1-2 DLC CONSIDERED

DLC	Environmental Conditions	Type of loads considered	Type of loads neglected	Verification
DLC 1 Dry lift	-	• Structural weight	-	• Yield check • Buckling check
DLC 2.1 Operational Conditions	Extreme wave No current No wind	• Structural Weight • Hydrostatic • 1st order wave load • Moorings • Inertial loads	• Distributed current & wind load • Low frequency wave load • Air pressure in chamber	• Yield check • Buckling check
DLC 2.2 Operational Conditions	Extreme wave No current No wind	• Structural Weight • Hydrostatics • 1st order wave load • Moorings • Inertial loads • Air ***over*** pressure in chamber	• Distributed current & wind load • Low frequency wave load	• Yield check • Buckling check
DLC 2.3 Operational Conditions	Extreme wave No current No wind	• Structural Weight • Hydrostatics • 1st order wave load • Moorings • Inertial loads • Air ***under*** pressure in chamber	• Distributed current & wind load • Low frequency wave load	• Yield check • Buckling check

Corrosion and marine growth have not been considered.

INPUT DATA

The input data used for the preliminary structural analysis comes from:

- The conceptual design made by IST (reference [8]).
- The experimental campaign carried out by IST(reference [13]).
- CAD drawings from IST for three diameters of the OWC spar buoy, respectively 3, 6 and 12 meters.
- Meteocean data gathered by WavEC at the site of Leixões (reference [14])
- Hydrodynamic loads, hydrostatic loads, inertia loads and mooring loads from WavEC (see section 1.3.1)

MAIN RESULTS

Main results of this analysis are as follows:

- INNOSEA has proposed that the original design provided by IST (Design 0) is modified to be stiffened at least by the mean of internal bulkheads. This is the result of structural engineering considerations. This leads to the so-called Design 1.
- Structural analysis performed on Design 1 has shown that an improvement of the structure should be performed. Two main approaches have been followed to improve the structure: by the mean of shell thicknesses increase, and by the mean of stiffeners addition. Two Designs are thus proposed.
- A first design, called Design 2 is proposed (see Figure 1-14). This design is obtained by the mean of shell thickness increase.

- A second Design, called Design 3 is proposed (see Figure 1-15). This design is obtained by the mean of stiffeners addition and thickness increase in some location (smaller increase compared to design 2).
- Table 1-3 summarizes the design variations.

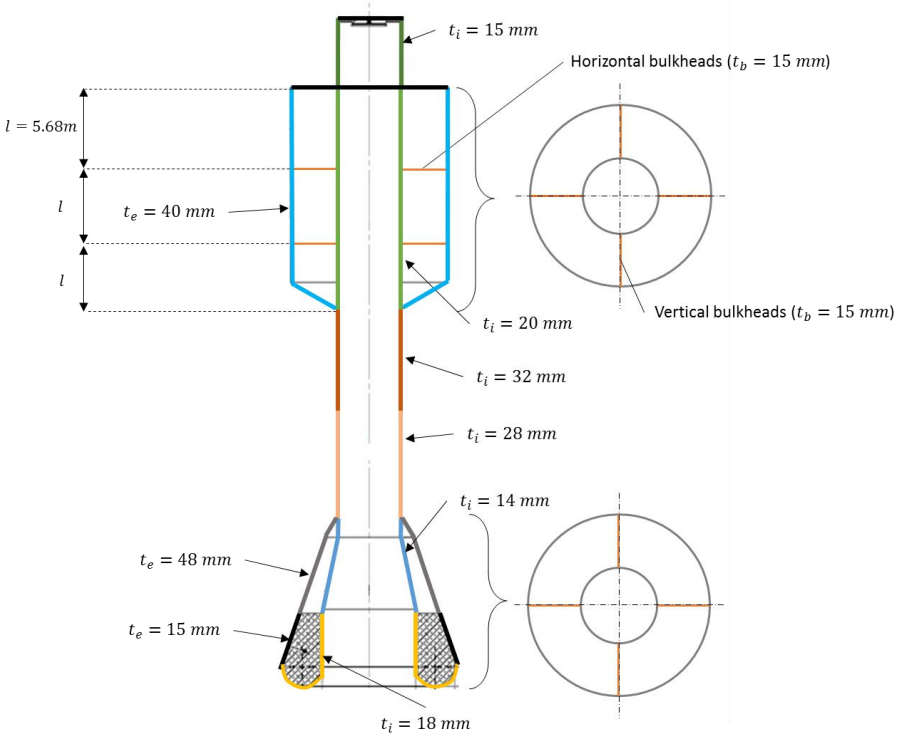

FIGURE 1-14: DESIGN #2

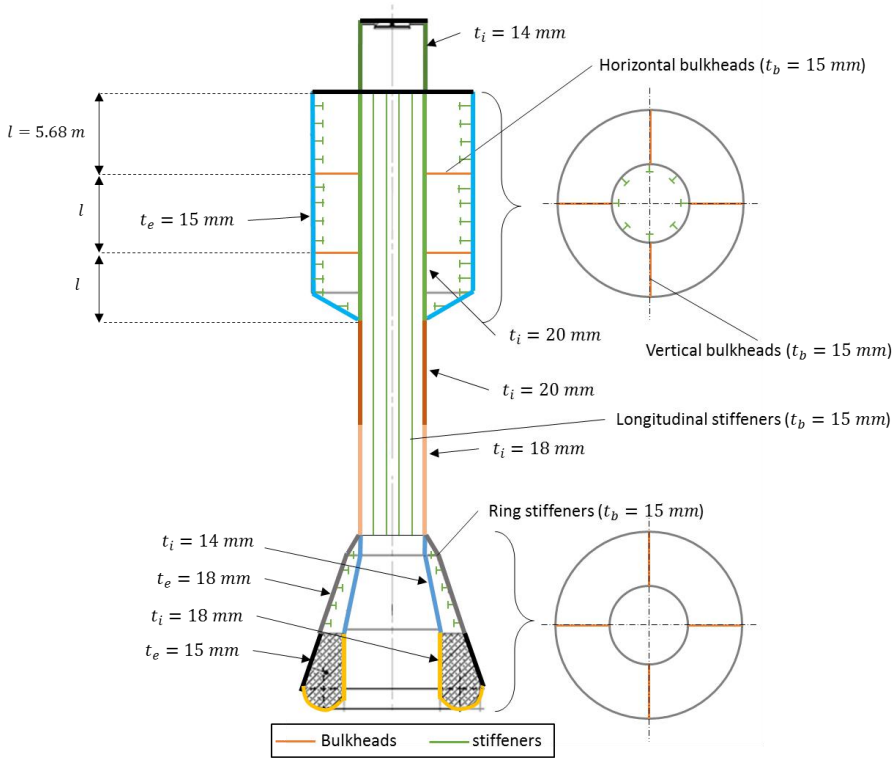

FIGURE 1-15: DESIGN #3

TABLE 1-3 SUMMARY OF THE DESIGNS

design	total weight		CoG position from MSL [m]	draft [m]
	Value [ton]	relative difference with original design		
Design 0: original	1217.4	0%	-28.6	36.0
Design 2: thickened	1514.8	24%	-24.5	39.5
Design 3: stiffened	1456.5	20%	-26.0	38.9

As design is modified, external loads and motion related quantities (e.g. max pitch angle) have changed. A loop of load calculation and structural analysis is needed to analyze the proposed configuration. Modification of the concept design might be proposed by IST if the draft should be kept constant.

It is important to notice that this structural analysis is dependent of input loads. In our case some inconsistency on input loads have been noted, and a correction was needed to be closer to an equilibrium [15]. Regarding hydrostatics, large motions observed during load calculation induce a geometric nonlinearity. The top of buoy goes under water during system motion. This can be critical for PTO in one hand, and it is not clear if this situation was accounted for in the concept definition or if it should be avoided and if motion calculation is impacted by this phenomenon. A consistent evaluation of all loads is needed for further structural analysis

1.3.3. Load assessment of the two-recommended improved reference design of the OWC spar buoy – second iteration

Following the first iteration of load assessment and structural analysis, two alternative designs were proposed. Design #2 was thickened whereas design #3 was stiffened by adding ring stiffeners along the structure. Scantlings of these two alternative designs are presented in Appendix A.

As expected, these two designs affected the OWC hydrodynamic properties, and as such new simulations were needed to assess the impact of such design alterations on the loading assessment. The new mass and design properties for design #2 and #3 are presented in Table 1-. It should be noted that the characteristics of these revised designs have been determine with the objective of keeping the draft identical.

TABLE 1-3: OWC MASS PROPERTIES FOR THE DIFFERENT DESIGNS

Reference	Diameter [m]	Draft [m]	Height [m]	Centre of gravity [m]	Centre of buoyancy [m]	Dry mass [t]	Moment of inertia I_{xx} ($=I_{yy}$) [kg.m²]	Moment of inertia I_{zz} [kg.m²]
Design #0	12	36	51	-28.62	-18.04	1217.4	188.7×10^6	30.3×10^6
Design #2	12	36	51	-22.97	-18.03	1221.1	328.45×10^6	30.8×10^6
Design #3	12	36	51	-25.28	-18.04	1218.3	282.5×10^6	29.4×10^6

The variation of the dry mass is negligible between the different designs. However, there are significant variations for the gravity centre position as well as for the moment of inertia. This is likely to affect the pitch and surge resonance period, and the general behaviour of the system. Plots displaying the motions for the different designs as well as the total local connections forces L_x are presented hereinafter.

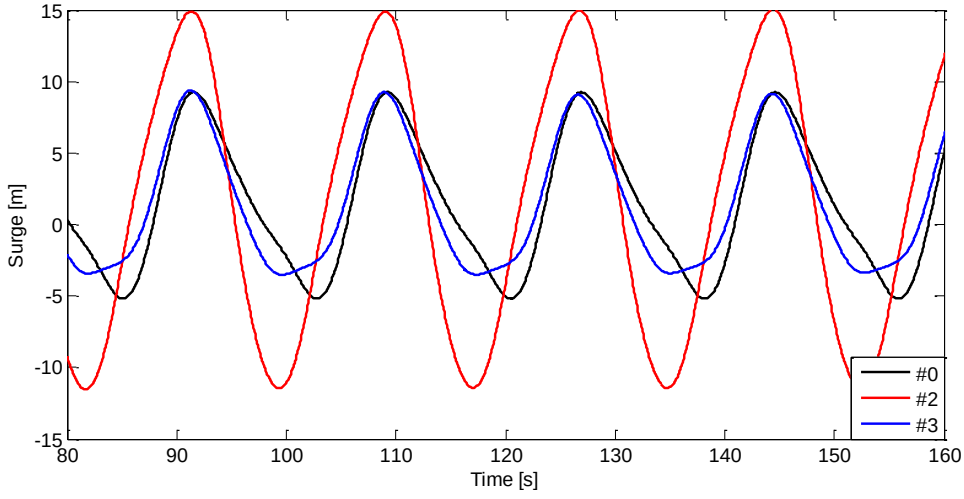

FIGURE 1-16: SURGE DISPLACEMENT COMPARISON

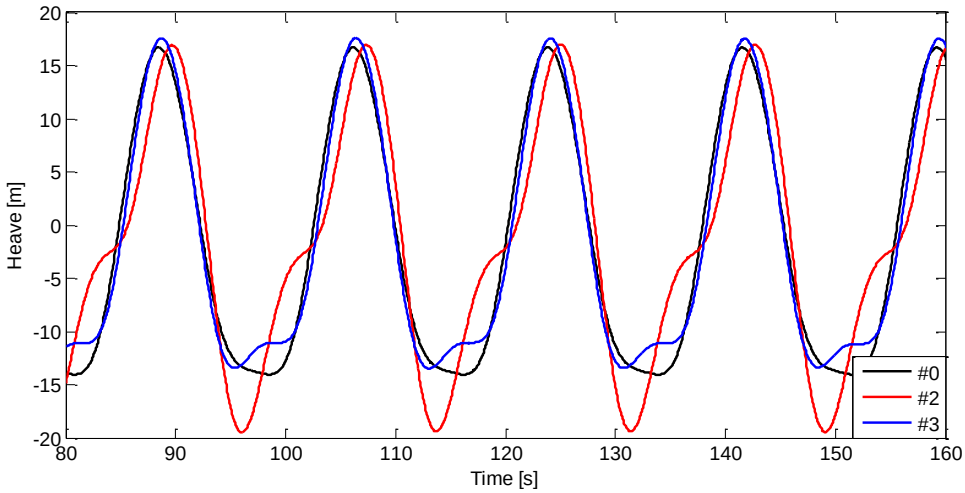

FIGURE 1-17: HEAVE DISPLACEMENT COMPARISON

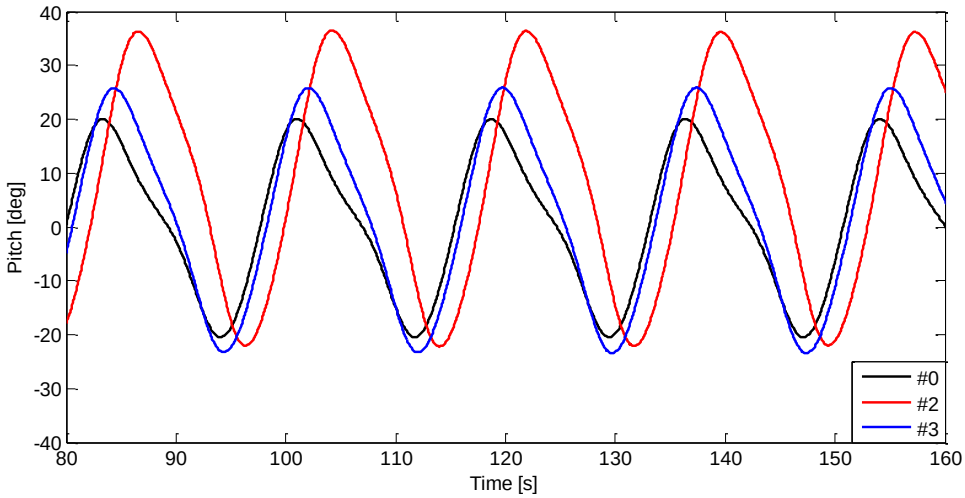

FIGURE 1-18: PITCH ROTATION COMPARISON

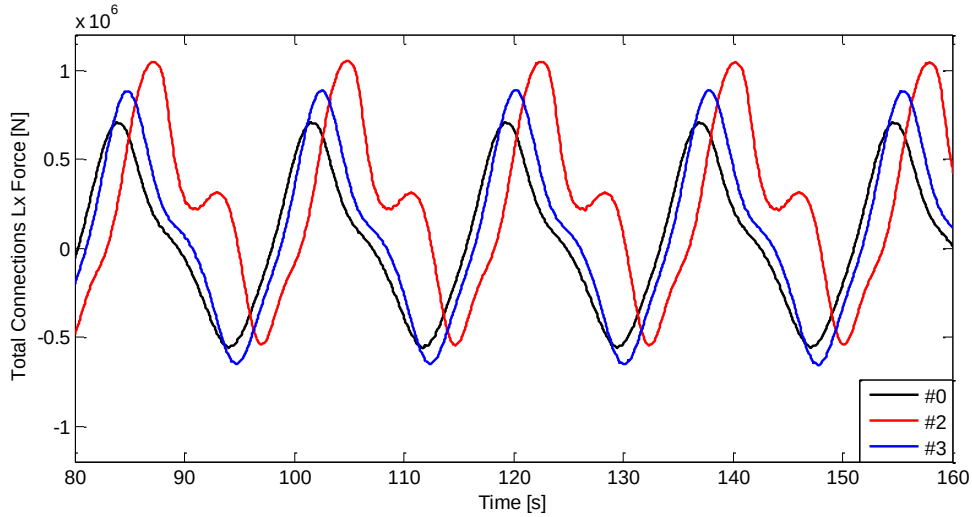

FIGURE 1-19: TOTAL LOCAL CONNECTIONS FORCES COMPARISON

There are clearly significant differences between the different designs, which appears to be mainly due to the increase in the OWC moment of inertia. Indeed, the surge and pitch modes motions are significantly higher for design #2 when compared to the two other cases. As well, the heave displacement is also affected with larger displacements in the troughs.

Design #3 results variations appear to be more moderate than design #2. This is likely due to the fact that the increase of the moment of inertia is not as large as for design #2, but also that its gravity centre is located at a lower position (-25.28m against -22.97m for design #2). It can be noted that while the wave excitation forces and moments remain the same, the radiation and connection efforts can undergo significant changes.

Clearly, the differences observed in terms of loading will induce variations in the structural analysis results. Since the focus of the WETFEET project is to investigate the potential of the breakthroughs rather than achieve a more mature design of the reference OWC spar buoy, it was decided not to iterate the structural analysis with these two new designs.

1.3.4. Power performance data for the reference design of the OWC spar buoy

The performance analysis of the reference full-scale design of the OWC spar buoy, used to obtain the device power matrix, is presented here. The spar-buoy OWC is modelled as a two-body system. The coupling between the two bodies is due to PTO forces and to the forces associated to the diffracted and radiated waves. The numerical model is based on linear wave theory, coupled with a fully non-linear compressibility formulation for the air inside the pneumatic chamber. This, in conjunction with the non-linear flow rate versus pressure drop characteristic of the bi-radial turbine, see Figure 1-20, resulted in a non-linear system, and so a time-domain approach was used. The non-dimensional performance curves of the bi-radial turbine were obtained from model testing [16].

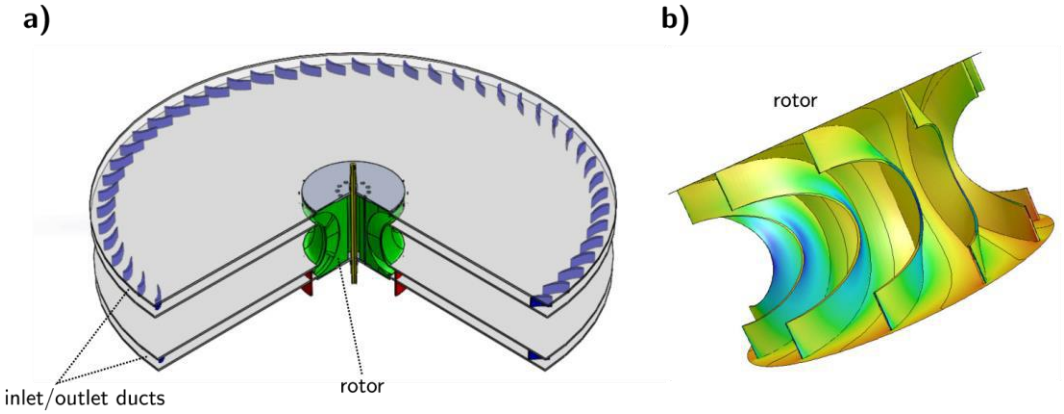

FIGURE 1-20 THE BI-RADIAL TURBINE: (A) THREE-DIMENSIONAL VIEW; (B) DETAIL VIEW OF THE ROTOR

The Spar-buoy (floater and tail tube) is named here as body 1. The air-water interface is modelled as an imaginary weightless rigid piston denoted as body 2. In the present case, the weightless rigid piston should be a good approximation since the OWC diameter is much smaller than the wavelength. Let x_i be the coordinates of the heave mode of the two bodies ($i = 3$ for the heave of body 1 and $i = 9$ for the heave of body 2), with $x_i = 0$ at equilibrium position and the x_i-axes pointing upwards. The equations of motion for the two-body system are

$$(m_1 + A_{33}^{\infty})\,\ddot{x}_1 + \rho_{\mathrm{w}} g S_1\, x_3 + A_{39}^{\infty}\,\ddot{x}_9 - p_{\mathrm{at}}\, S_2\, p^* = F_{\mathrm{d},3} - R_{33} - R_{39}, \tag{1-2}$$

$$(m_2 + A_{99}^{\infty})\,\ddot{x}_9 + \rho_{\mathrm{w}} g S_2\, x_9 + A_{93}^{\infty}\,\ddot{x}_3 + p_{\mathrm{at}}\, S_2\, p^* = F_{\mathrm{d},9} - R_{99} - R_{93}. \tag{1-3}$$

Here, the dots denote time derivatives, g is the acceleration of gravity, ρ_{w} is water density, S_i is the annular cross sectional area of body i, m_i is the mass of body i, A_{ij}^{∞} represents the limiting value at infinite frequency of the added mass of heave mode i as affected by the heave mode j ($i, j = 3{,}9$). The dimensionless relative pressure oscillation inside the chamber is defined as

$$p^* = \frac{p}{p_{\mathrm{at}}} - 1, \tag{1-4}$$

where p_{at} is the atmospheric pressure, and p is the instantaneous pressure inside the air chamber.

Since we assume linear water wave theory, the resulting diffraction force is obtained as a superposition of N regular waves components with a given angular frequency, as described in [17]. The radiation force is defined as $A_{ij}^{\infty}\ddot{x}_j + R_{ij}$, where A_{ij}^{∞} is the impulsive hydrodynamic-added-mass and R_{ij} is a convolution integral representing the load contribution from wave-radiation damping of heave i as affected by heave mode j. The convolution integrals appearing in R_{ij} are approximated by a linear state-space model obtained with a system identification Matlab toolbox for parametric identification, see [18]. The same degree of approximation for all the radiation terms is used.

Hydrodynamic coefficients are computed using the WAMIT software package [19]. This software applies a Boundary Integral Equation Method to determine these coefficients as function of the incident regular-wave frequency, as described in [20].

TABLE 1-4 CHARACTERISTIC WAVE CLIMATE OFF THE WESTERN COAST OF PORTUGAL. EACH SEA STATE, N, OF THE WAVE CLIMATE IS DEFINED BY THE SIGNIFICANT WAVE HEIGHT, H_s, ENERGY PERIOD, T_e, AND PROBABILITY OF OCCURRENCE, P_o [20]

Sea State n	Significant wave height H_s [m]	Energy period, T_e [s]	Probability of occurrence

			P_o [%]
1	1.10	5.49	7.04
2	1.18	6.50	12.35
3	1.23	7.75	8.17
4	1.88	6.33	11.57
5	1.96	7.97	20.66
6	2.07	9.75	8.61
7	2.14	11.58	0.59
8	3.06	8.03	9.41
9	3.18	9.93	10.07
10	3.29	11.80	2.57
11	4.75	9.84	4.72
12	4.91	12.03	2.81
13	6.99	11.69	1.01
14	8.17	13.91	0.39

The pressure in the air chamber is related to the mass flow rate of air through the turbine, $\dot{m}_{\text{turb}}$, (positive for outward flow) which is given by

$$\dot{p}^* = -\kappa(p^* + 1)\frac{\dot{V}_c}{V_c} - \kappa(p^* + 1)^{\beta}\frac{\dot{m}_{\text{turb}}}{\rho_{at} V_c}, \tag{1-5}$$

where ρ is the air density, $V_c = V_0 + S_2(x_3 - x_9)$ is the instantaneous volume of air inside the chamber and V_0 is the volume at still water conditions. Assuming that air behaves as a perfect gas, the compression/expansion of the air in the chamber was modelled as a polytropic process with

$$\beta = \frac{\kappa - 1}{\kappa}, \tag{1-6}$$

where κ is the polytropic index related to the turbine efficiency, as described later.

The performance characteristics of the turbine are usually presented in dimensionless form, where

$$\Psi = \frac{p_{at}\, p^*}{\rho_{in}\, \Omega^2\, d^2}, \tag{1-7}$$

$$\Phi = \frac{\dot{m}_{\text{turb}}}{\rho_{in}\, \Omega\, d^3}, \tag{1-8}$$

$$\Pi = \frac{P_{\text{turb}}}{\rho_{in}\, \Omega^3\, d^5}, \tag{1-9}$$

$$\eta_{\text{turb}} = \frac{\Pi}{\Phi\, \Psi}, \tag{1-10}$$

are the dimensionless pressure head Ψ, the dimensionless flow rate Φ, the dimensionless power coefficient Π and turbine efficiency, see [21]. In Eqs. (1-7), (1-8) and (1-9), Ω is the turbine rotational speed (in radians per unit time) and d is the turbine rotor diameter. The reference density ρ_{in} is defined in stagnation conditions at the turbine entrance. Consequently, reference density is a function of the pressure difference between the air chamber and the atmosphere and was computed as

$$\rho_{\text{in}} = \rho_{\text{at}} \max(\, p^* + 1, 1\,)^{1/\kappa}. \tag{1-11}$$

Neglecting the effects of the variations in Reynolds number (since the Reynolds number is in general large enough for that) and Mach number (see [21]), the dimensionless variables Φ, Π and η_{turb} can be plotted as a function of Ψ, as shown in Figure 1-21Figure 1-21.

In Eq. (1-5), $\dot{m}_{\text{turb}}$ is computed directly from Eq. (1-8) as function of Ψ, Eq. (1-7).

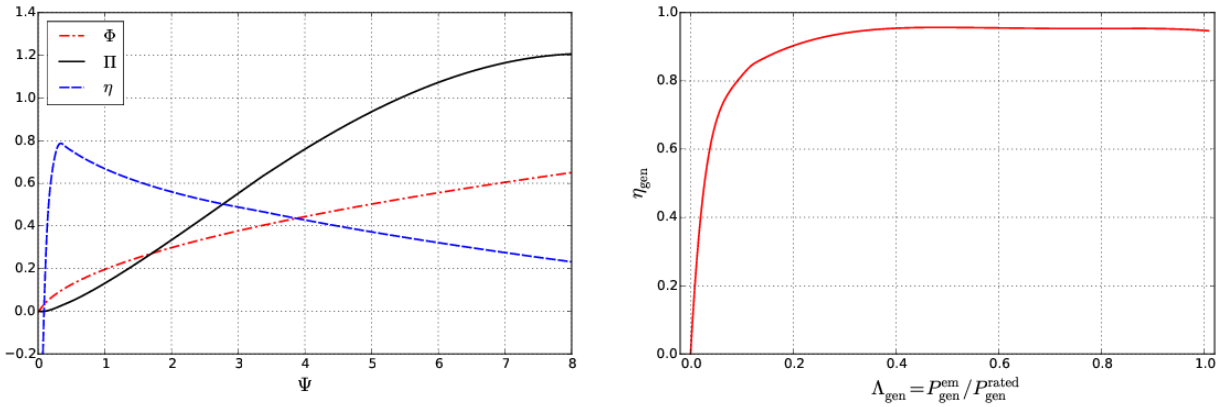

(A) **(B)**

FIGURE 1-21 TURBINE AND GENERATOR CHARACTERISTIC CURVES: (A) DIMENSIONLESS FLOW RATE, Φ, DIMENSIONLESS POWER COEFFICIENT, Π, AND EFFICIENCY, η, AS FUNCTIONS OF THE DIMENSIONLESS PRESSURE HEAD, Ψ, FOR THE BI-RADIAL TURBINE USED IN THE NUMERICAL SIMULATIONS, BASED ON [16]**; (B) GENERATOR EFFICIENCY CURVE TAKEN FROM** [22]

The dynamics of the turbine/generator set is described by

$$I\,\dot{\Omega} = T_{\text{turb}} - T_{\text{gen}}^{\text{em}}, \tag{1-12}$$

where T_{turb} and $T_{\text{gen}}^{\text{em}}$ are the instantaneous turbine aerodynamic torque and the instantaneous generator electromagnetic torque, the latter being imposed by the rotational speed control law. The turbine aerodynamic torque is computed from Eqs. (1-9) and (1-10)

$$T_{\text{turb}} = \rho_{\text{in}}\,\Omega^2 d^5\,\eta_{\text{turb}}\Phi\Psi. \tag{1-13}$$

The polytropic exponent κ is related to the turbine polytropic efficiency (or small-stage efficiency) by (see [21])

$$\kappa = \frac{1}{1 - \dfrac{\gamma - 1}{\gamma}\eta_{\text{turb}}}, \tag{1-14}$$

where $\gamma = 1.4$ is the specific heat ratio for air. For outflow conditions, $p^* > 0$, $\rho_{\text{in}} = \rho$ and the values of η_{turb}, Ψ, and κ are determined iteratively since they form a non-linear system of equations.

The PTO system for the spar-buoy OWC under analysis consists of a bi-radial turbine and a generator. Eq. (1-9) shows that the turbine output power should be proportional to Ω^3 if the time-averaged turbine aerodynamic efficiency is to be maximized. In practice, if the coupling between the turbine aerodynamics and the spar-buoy OWC hydrodynamics is taken into account, we can use a relation of the type

$$P_{\text{gen}}^{\text{opt}} = a\,\Omega^b. \tag{1-15}$$

In a previous study [23], it was found that exponent b should be about 3, for maximum overall (OWC plus turbine) time-averaged efficiency, *i.e.*, if the power output of the turbine is to be maximized.

Furthermore, in the same study, it was found that the optimal time averaged turbine power versus rotational speed for each sea state follows approximately a straight line in a log-log scale.

To avoid overpowering the generator, it was adopted the following control law

$$P_{\text{gen}}^{\text{em}} = \min\left(P_{\text{gen}}^{\text{opt}}, P_{\text{gen}}^{\text{rated}}\right), \tag{1-16}$$

where $P_{\text{gen}}^{\text{rated}}$ is the rated (maximum allowed) power of the generator.

The generator electrical power output was estimated using

$$P_{\text{elect}} = \eta_{\text{gen}}(\Lambda_{\text{gen}})\ P_{\text{gen}}^{\text{em}}, \tag{1-17}$$

where the generator efficiency η_{gen} was taken from [22] (see Figure 1-21) as function of the generator load

$$\Lambda_{\text{gen}} = \frac{P_{\text{gen}}^{\text{em}}}{P_{\text{gen}}^{\text{rated}}}. \tag{1-18}$$

Therefore, the instantaneous generator electromagnetic torque follows the relation

$$T_{\text{gen}}^{\text{em}} = P_{\text{gen}}^{\text{em}}\ \Omega^{-1}. \tag{1-19}$$

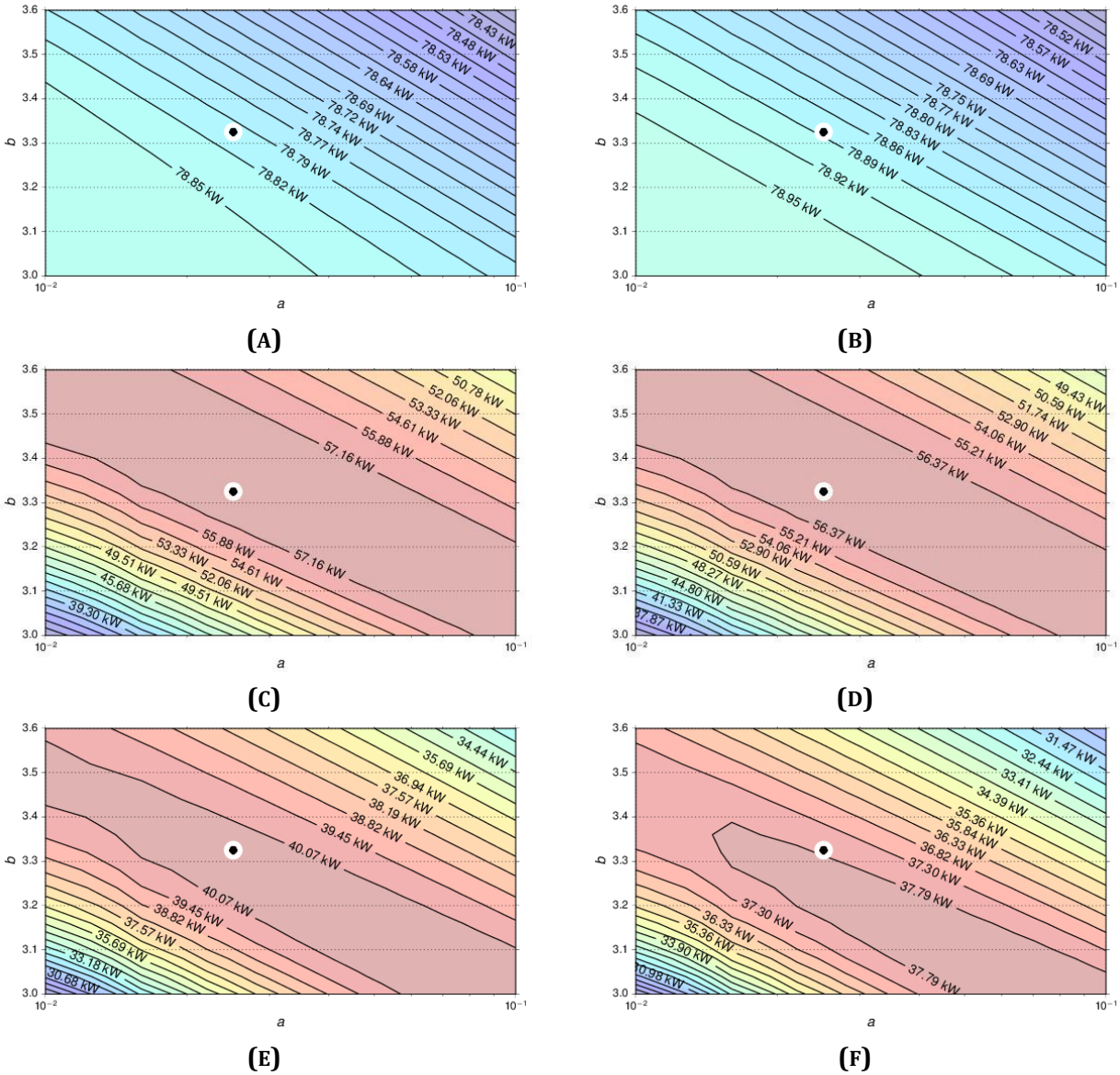

FIGURE 1-22 ANNUAL-AVERAGED POWER OF THE REFERENCE 12 M DIAMETER OWC SPAR BUOY AS FUNCTION OF THE GENERATOR CONTROL LAW CONSTANTS (a, b), EQ. (1-15). RESULTS IN THE LEFT COLUMN CORRESPOND TO A 150 KW ELECTRICAL GENERATOR AND IN THE RIGHT COLUMN TO A 300 KW ELECTRICAL GENERATOR. PLOTS (A) AND (B) REPORT THE PNEUMATIC POWER, (C) AND (D) THE TURBINE POWER OUTPUT, AND (E) AND (F) THE ELECTRICAL POWER OUTPUT. THE COMPUTATIONS WERE PERFORMED CONSIDERING A TURBINE DIAMETER OF 1.4 M AND AN INERTIA OF THE TURBINE/GENERATOR SET OF 600 KG M². THE DOT REPRESENTS THE OPTIMUM VALUES OF a AND b, SEE EQ. (1-15).

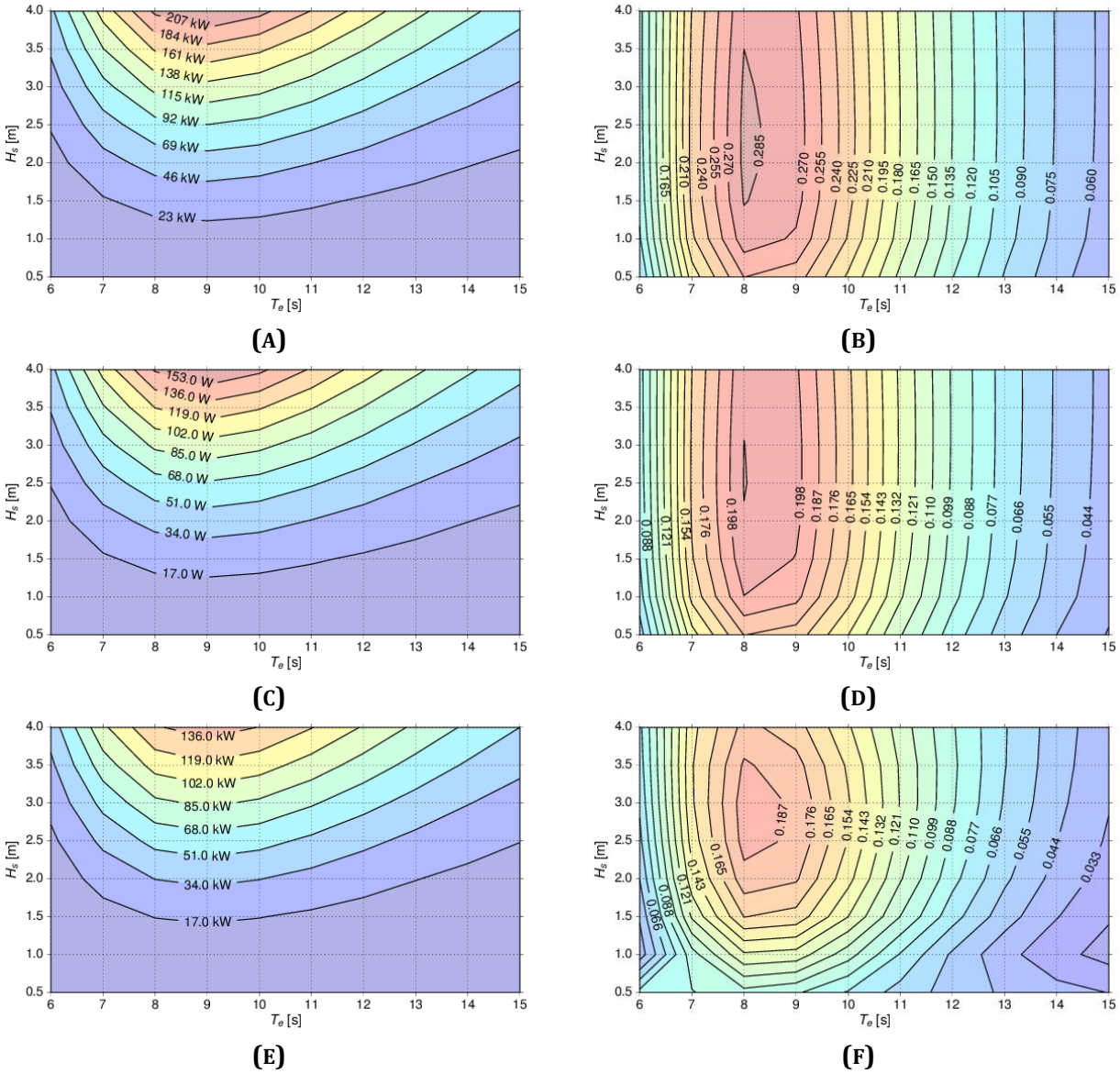

FIGURE 1-23 POWER MATRICES OF THE REFERENCE 12 M DIAMETER OWC SPAR BUOY. LEFT COLUMN DEPICTS RESULTS FOR TIME-AVERAGED POWER OUTPUT, AS FUNCTION OF THE SEA STATE ENERGY PERIOD T_e AND SIGNIFICANT WAVE HEIGHT H_s. RIGHT COLUMN PRESENTS THE CORRESPONDING DIMENSIONLESS CAPTURE WIDTHS. PLOTS SHOW: A) PNEUMATIC POWER OUTPUT, B) DIMENSIONLESS PNEUMATIC CAPTURE WIDTH, C) TURBINE POWER OUTPUT, D) DIMENSIONLESS TURBINE CAPTURE WIDTH, E) ELECTRICAL POWER OUTPUT, AND F) DIMENSIONLESS ELECTRICAL CAPTURE WIDTH. THE COMPUTATIONS WERE PERFORMED FOR A TURBINE DIAMTER OF 1.4 M, A 150 KW ELECTRICAL GENERATOR AND WITH AN INERTIA OF THE TURBINE/GENERATOR SET OF 600 KG M ^{2}.

The parameters *a* and *b* of (1-15) are determined by a exponential least-square fitting of maximum time-averaged turbine power output for a set of sea states as function of the rotational speed, $\Omega_{\mathrm{opt},n}$ (for further detais, see [24]). Here, we considered the set of sea states presented inTable 1-4, which characterizes the wave climate off the western coast of Portugal.

Experimental tests revealed that the bi-radial turbine is characterized by a dimensionless relationship between pressure head and flow rate approximately given by [16]

$$\Psi = K\,\Phi^{5/3}, \tag{1-20}$$

where K is a constant, see Figure 1-21. By using (1-7) and (1-8) we get

$$p^* = \frac{\rho_{\text{in}} K}{p_{\text{at}}}\; Q_{\text{turb}}^{5/3}\; \Omega^{1/3}\; d^{-3}. \tag{1-21}$$

Here $Q_{\text{turb}} = \dot{m}_{\text{turb}}/\rho_{\text{in}}$ is the volumetric flow rate. Since $p^* \propto d^{-3}$, the spar-buoy OWC hydrodynamics and the turbine power output are more sensitive to the turbine diameter, d.

From Eq. (1-21) we found that around the typical turbine operating point of 3000 rpm a change of a few hundred rpm in the rotational speed has a small effect on the buoys' hydrodynamic performance since $p^* \propto \Omega^{1/3}$. Consequently, the bi-radial turbine presents a rather flat power output response, as function of the rotational speed, close to the maximum power output value for each sea state, see Figure 1-22. The low sensitivity of the power outputs to the generator control law is an interesting feature of this PTO system.

Figure 1-22 shows the sensitivity of the pneumatic power, the turbine power output and the electrical power output to the variation of the parameters a and b of the generator control law, Eq. (1-15). The computations were performed considering a turbine diameter of $d = 1.4$ m and an inertia of the turbine/generator set of $I = 600$ kg m ^{2}. The annual-averaged power considers the set of sea sates presented in Table 1-4. The dot shows the optimum values a and b for the generator control law.

As shown in Figure 1-22 (a) Figure 1-22Figure 1-22 (b), the pneumatic power output is almost insensitive to the generator control law. As expected, the electrical power output follows the pattern of the turbine power output.

In Figure 1-22 (c) to Figure 1-22 (f), it can be seen that there is a broad region of values a and b where close to maximum turbine power output can be achieved. The same consideration applies to the electrical power output for the case of a electrical generator with a rated power of 150 kW. Increasing the generator rated power to 300 kW, it can be seen a slightly decreasing of the power output when a decreases and b increases.

The power matrices for the pneumatic power, turbine power output and electrical power output are plotted in Figure 1-23 (a), (c) and (e). Figure 1-23 (b), (d) and (f) presents the corresponding dimensionless pneumatic capture width

$$L_{\text{pneu}}^* = \frac{P_{\text{pneu}}}{\hat{P}_{\text{wave}}\, D}, \tag{1-22}$$

the turbine mechanical dimensionless capture width

$$L_{\text{turb}}^* = \frac{P_{\text{turb}}}{\hat{P}_{\text{wave}}\, D}, \tag{1-23}$$

and the electrical dimensionless capture width

$$L_{\text{elect}}^* = \frac{P_{\text{elect}}}{\hat{P}_{\text{wave}}\, D}, \tag{1-24}$$

where

$$P_{\text{pneu}} = p_{\text{at}}\, p^* Q_{\text{turb}}, \tag{1-25}$$

is the pneumatic power, $Q_{\text{turb}} = \dot{m}_{\text{turb}}/\rho_{\text{in}}$ is the turbine volumetric flow rate, and

$$\hat{P}_{\text{wave}} = \sum_{m=1}^{N} \frac{\rho_{\text{w}}\, g^2 A(\omega_m)^2}{4\,\omega_m}, \tag{1-26}$$

is wave energy flux per unit of wave-crest length of the considered spectrum. These dimensionless capture widths are a measure of the efficiency of each conversion stage in relation to the available power reference, $\hat{P}_{\text{wave}}\, D$.

From Figure 1-23, it is clear that the buoy is tuned for energy periods between 7 to 10 s. Although the pneumatic power, the turbine power and the electrical power increase significantly with the significant wave height, H_s, the dimensionless capture width (a measure of the efficiency) is almost constant for H_s between 1 to 4 m. Comparing the turbine and the generator power outputs it is clear that the generator efficiency has a strong impact on the system performance.

All the depicted results in Figure 1-22 and Figure 1-23 should be considered as qualitative for the larger values of H_s. Under those high-amplitude motion conditions, the model application deviates from the underlying assumptions of the linear wave theory and small motion amplitude.

In the present report, a systematic methodology is proposed for the sizing of the PTO systems for OWC WECs. The optimal sizing and selection of the turbine and the generator is simple and effective, and takes into account the wave climate of the deployment site. Both components of the power take-off system are tightly connected through a simple and effective control law of the generator electromagnetic torque.

The OWC Spar buoy used in the computation is well tunned in the range of energy periods between 7 and 10 s. In the case of a PTO system equipped with a bi-radial turbine, it is shown that the electrical power output has low sensitivity to the generator control law values near the optimum point.

1.4. Design approach for the breakthroughs associated with the Symphony device

The design approach for the Symphony-related breakthroughs differs fundamentally from the one chosen for the OWC Spar buoy, for two simple reasons:

(i) The development of the Symphony-related breakthrough components requires a stage of physical prototype testing - ideally in a real device – in an early stage, since both the turbine and the membrane with its combined functions are disruptive developments. Numerical modelling is a very limited tool for capturing the physical complexity of the processes involved, due to the lack of precedence. To advance the state-of-the-art and avoid a mislead development, their basic functions need to be tested physically, before the focus is laid on optimisation or sophisticated simulation tools.

(ii) Focus of the numerical modelling performed within this work package has been to build an initial time-domain-model (TDM) of the "reactive part", i.e. the breakthrough components integrated in a fully functional Symphony WEC (wave energy converter), as a complete system.

(iii) The development around Symphony is led by a company that has the objective of bringing this technology to the market as a spin-off. This makes the overall concept and the feasibility of the components as part of a functional overall system a priority.

Early prototype testing in manageable dimensions is therefore vital within the context of the breakthrough components developed. The following components are considered as Symphony-relevant breakthrough components, and each of them will be discussed in a separate chapter.

- A novel custom water turbine (chapter **Error! Reference source not found.**);
- Structural membrane (chapter 8);
- Control cocoon: allowing continuous submergence of a WEC (chapter **Error! Reference source not found.**).

The turbine and the structural membrane are both disruptive developments as mentioned above, thus their design, manufacture and testing of a physical model is key for the early stage work. There is no known precedence of such components in wave energy or adjacent technologies, as far as a comprehensive literature research in the beginning of the project has indicated. Proving the basic function of these components is part of the WPs 4 (turbine) and 3 (membrane). Their functional requirements, dimensions and preliminary design exercise based on their representation in the time domain model (see section **Error! Reference source not found.**) are discussed in chapters **Error! Reference source not found.** and **Error! Reference source not found.**, respectively.

The removable control cocoon itself is not vital for the WEC's function (the auxiliary equipment could be simply incorporated inside the device), but rather an innovation making the O&M (Operation & Maintenance) strategy more coherent, and potentially enabling the Symphony concept to achieve better techno-economic performance. Main aspects to be addressed are the ability of including the turbine, the generator and all required auxiliary equipment into the available space, and to ensure that the hydrodynamic behaviour of the WEC without the cocoon (when it is removed for maintenance on land) does not change critically, e.g. yielding unstable situations in storm waves. While the latter is part of the experimental tank testing in WP 3, the preliminary design of the cocoon and its components is discussed in chapter **Error! Reference source not found.** of this document.

In addition to the specific approach to the breakthrough components addressed in the respective chapters, an initial hydrodynamic analysis of the Symphony hull was conducted by the partner INNOSEA [25], using state-of-the-art in-house models. The purpose of this exercise is to provide an initial estimate of the motion characteristics of the Symphony WEC per present state of development, to establish a basis for validation in the model tests in WP 3 of WETFEET, to obtain a first indication of potential surge force eccentricities over the hull and to exclude potential incoherence with the development of the components. This study is attached to this document as Appendix D.

1.4.1. Characterization of 'breakthrough' improvements

Despite a relatively clear physical frontier between the above 3 'breakthrough components', their modelling in the overall system is difficult to describe separately. Especially their contributions to the spring in different, partly decisive situations, is an interaction of the different parts, and an important starting point for the design is the actual combination of effects.

In particular, the structural membrane fulfils several functions when combined with a high-pressure internal water volume and a shaped inner wall, which is the key to overcome the identified difficulties with the 'original' SPDD (Submerged Pressure Differential Device) design with an air volume/gap (see section 1.5). As indicated, in the reference design case, the large size (due to the required air volume) makes the device difficult to handle, and the large air volume acting as spring brings along control challenges; the system can become unstable due to the non-linear characteristics of the spring. A final issue is the complex and bulky/costly design of a braking system that stops the floater in its maximum position. Such a function is vital to guarantee the mechanical integrity of the device, however a technical risk remains with the chosen solution of the reference system. To resolve these issues, it is proposed to alter the coefficient of the gas spring in the WEC. The proposed changes imply altering the shape of the gas spring and using a rubber seal to transfer the force from the gas spring onto the floater. A preliminary qualitative analysis was performed to demonstrate that this is a feasible solution [26]. Altering the coefficient of a gas spring is a new topic in the field of wave energy converters. Consequently, current knowledge on the working principle of this solution is scarce. This is addressed in the following summary of the modelling approach taken for the Symphony development. The aim of this exercise is to investigate the proposed solution for the gas spring, based on the Symphony WEC as an example. This integrates the required functionality in the new environment, and gives a baseline for the design of the components. A full description of this exercise is given in Leitjens [26]

The working principle of altering a gas spring using a flexible seal was not found in literature. The presented model provides a theoretical framework to calculate the effects. No empirical data are available to validate the results at this stage of development. This is a major reason why building the components – and as far as possible a WEC incorporating them -and validating the theoretical results with empirical data from the actual prototype is of highest priority to assess the Symphony-related breakthrough components.

1.4.2. The time domain model (TDM)

A full description of the TDM is presented by Leitjens [26], the relevant chapters of which are attached to this report as Appendix E. The following outlines the TDM approach taken in the Symphony development: "Gas springs are described using physical laws concerning the compression of a perfect gas in an adiabatic process. It is shown that a spring can be altered to meet pre-determined requirements. Furthermore, it is shown that a cylindrical gas spring will result in an unstable system under certain circumstances. Finally, analyses are performed to derive the optimal spring coefficient for energy extraction […]. A coupled set of non-linear differential equations is derived and solved, to obtain the geometry of the Symphony device for given forces. It is shown that the initial pressure and volume can be used to tune the device for variations in the energy period of the waves […]. An energy model of the Symphony is used to simulate the behaviour during operation. A brief description of this model is given followed by the results of simulation […]."

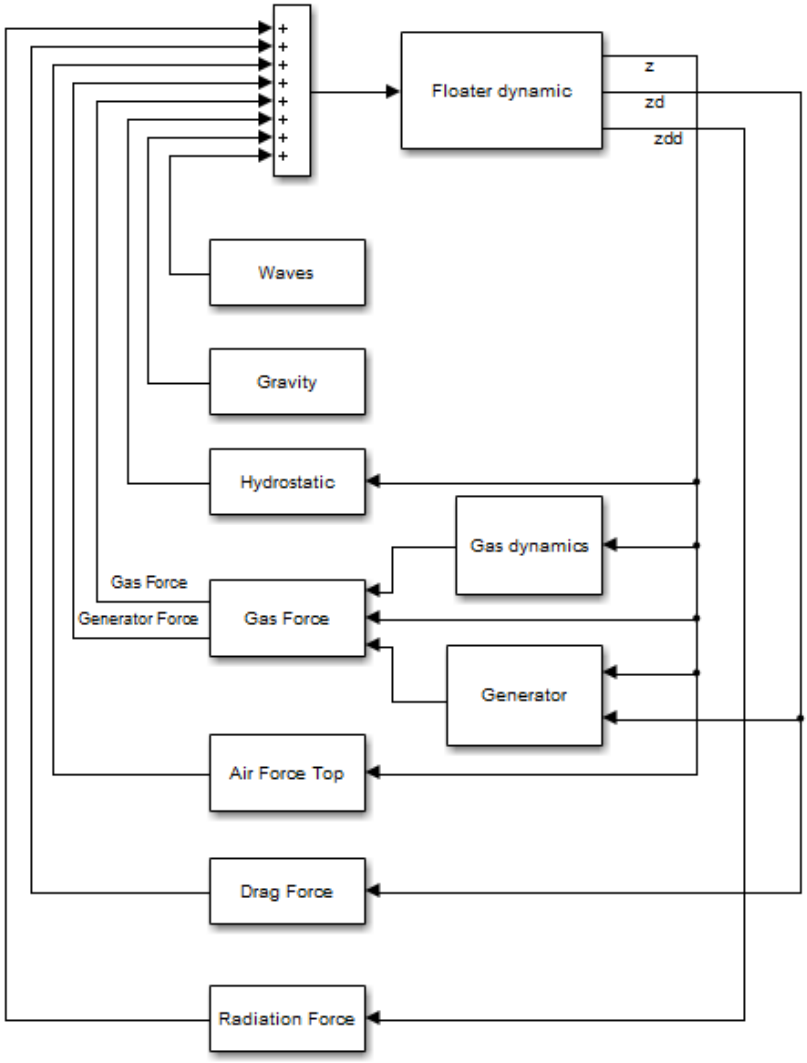

FIGURE 1-24 STRUCTURE OF THE SYMPHONY TDM [2]

THE SPRING

The main issue to be addressed in this exercise is: "How should the gas spring in the Symphony wave power device be designed in order to maximize the efficiency of its energy production as well as functioning as a braking system?"

To answer this question, the subsequent following issues need to be addressed:

1. What is a gas spring?
2. What type of gas spring can convert energy with a maximum efficiency?
3. Which types of gas springs can function as a braking system?
4. How can a spring be adjusted to have pre-determined properties?
5. How should the spring be implemented in Symphony Wave Power to have pre-determined properties?
6. What is the result of spring adjustments in Symphony Wave Power?

The work starts with an analysis of the effect of adjusting the gas spring in the Symphony device by starting to examine the behaviour of a gas spring in general, and conditions for stability of a gas spring. Furthermore, requirements for a gas spring are obtained to ensure its ability to extract power from waves efficiently and to function as a braking system.

Assumptions for ensuring optimal energy production and a functional braking system are derived. Main assumption in this context is that a linear spring is the optimal solution in terms of energy production. Therefore, a linear spring is the design target for this exercise.

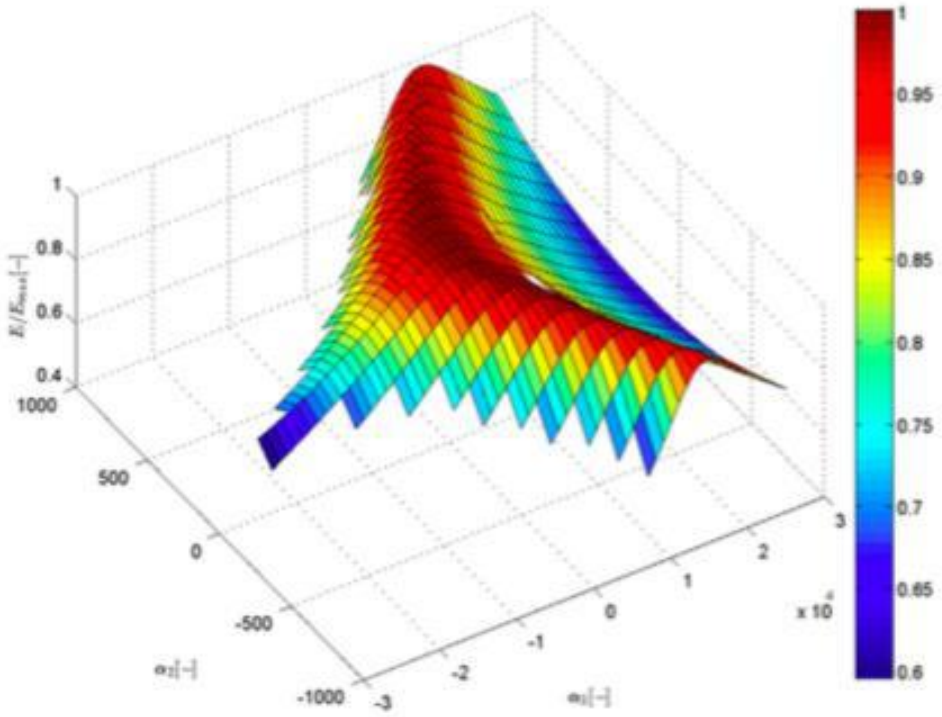

FIGURE 1-25 ENERGY EXTRACTION FOR DIFFERENT CONTRIBUTIONS OF QUADRATIC (α_2) AND CUBIC (α_3) SPRINGS WITH CONSTANT α_1 (LINEAR SPRING). THE Y AXIS REPRESENTS THE RELATIVE ENERGY EXTRACTED BY A SYSTEM WITH NON-LINEAR COMPONENTS, COMPARED TO A LINEAR SPRING.

Figure 1-25**Error! Reference source not found.** displays the stored energy for springs with quadratic and cubic contributions. Non-linear springs turned out to be at risk of becoming unstable and to extract up to 40% less energy. A linear resonant spring extracted the most energy compared to all other considered cases. The hypothesis is only confirmed if all other possible springs are considered; an infinite amount. This was not possible using the method of testing the springs, since it would take infinite time to compute this. Yet, using only second and third order contributions of a similar magnitude as the linear contribution made it likely that a linear resonant spring extracts a maximum amount of energy from a mass-spring-damper system.

It should be taken into consideration that the results discussed above were calculated using a linear damping term to account for mechanical losses. However, the damping function of the Symphony device contains non-linear terms due to drag and consequently radiated waves. Therefore, the application of the above conclusions to the Symphony device needs further work. In some situations, a non-linear spring may extract more energy than the resonant linear spring due to the non-linear damping. But the analysis conducted showed that the amount of extracted energy is not sensitive to non-linear contributions of the spring in case of a linear damping, if the spring does not become unstable and the total stiffness of the system is adjusted. The influence of a non-linear spring, using non-linear damping, is expected to be small as long as the same conditions apply. This is confirmed when comparing the power production of a linear spring and a non-linear spring using the non-linear damping. Taking all the above into account, it was considered the best option to use a resonant linear spring to extract energy in the Symphony device.

THE BRAKING SYSTEM

The braking system in the Symphony-device enables it to extract energy from the floater in given conditions with the objective to guarantee the mechanical integrity of the device. The objective of the braking system is to account for the mechanical integrity of the device in case of a mechanic failure of the PTO system or an out-of-design excitation. The braking system must be designed to withstand an extreme condition in terms of these goals.

Requirements for the braking force are defined in the TDM for normal operation, out-of-design excitation and mechanic failure, leaving freedom of choice for a specific spring force. An exponential function was chosen to model the braking force, assuming that it is a possible approximation of the physical reality that can at the same time conveniently be implemented in the model.

- The PTO as braking system

For keeping the floater within a limited stroke during operation, the PTO system is used. The PTO system is a control system comparing E_{in}, the total amount of energy of the floater, to E_{max}, the potential energy at the maximum position. When the internal energy of the floater exceeds the maximum energy that is permitted, the PTO system damps the surplus of energy:

$$Fcontrol = \begin{Bmatrix} 0 & if E_{in} < E_{max} \\ \frac{(E_{in} - E_{max})}{\Delta T \dot{z}} & if E_{in} > E_{max} \end{Bmatrix} \quad (1\text{-}27)$$

Where:

- $F_{control}$ is the control force damping the movement
- ΔT is the time in which a surplus of energy will be drained (this determines the responsiveness of the system).
- E_{in} is the sum of the potential and kinetic energy in the system.

- The gas spring as indirect braking system

For the case of extreme events as out-of-design excitations or mechanic failure of the PTO system, another braking mechanism is required, as the PTO is either too weak or not able to limit the movement. In these situations, the gas spring is used to detune the device, causing energy losses and subsequent smaller overshoots over the maximum stroke.

All gas springs with continuous and gradually increasing force with increasing amplitude (in this case floater position) are functional braking systems. The larger the force is, the more the device is being detuned. To confirm the working principle, an exponential braking system was chosen. In the TDM simulations, the working principle of using the gas spring as a brake was confirmed. The spring force increases exponentially for amplitudes larger than the operational stroke. Therefore, we may conclude that all of the requirements for a functional braking system are met using the gas spring. A braking study, using a time-domain model to predict the response of the floater in an extreme condition, should be performed to design the definitive shape of the brake. Such analysis is beyond the scope of the present phase of development and will be addressed in the next design steps of the Symphony device. The time-domain model for energy extraction simulation should be used to predict the response of the floater due to extreme conditions. In addition, other than exponential braking forces should be considered in this analysis. Further, future studies should focus on a specific brake force. Multiple braking systems should be proposed and tested in terms of guaranteeing the mechanical integrity of the device, using a time-domain model to predict the response of the floater. This should be weighed against the consequences for the design of the device. This will provide opportunities to find an optimal braking system.

THE LINEAR SPRING

An amount of air is compressed and decompressed within the Symphony device to act as an air spring. The definition of an air spring, the optimum for energy extracting and the functionality as braking system were described in the former sections, where the construction of a resonant linear spring to provide the possibility to extract energy and an exponential spring coefficient for the functionality of a braking system are sketched. The implementation of these fundamental principles in the Symphony device is described in the following. The working principle of a shaped wall within the Symphony device is the key for providing a linear spring: the device is under an initial pressure to ensure compact dimensions. Rubber seals are placed at the lower and upper border of the system to prevent the water in the system to flow into the sea. Consequently, the water in the system is decoupled from the sea. If the floater moves downward, water flows from the upper seals into the gas tank and the air volume decreases. The decreased volume induces an increased pressure in the gas tank, according to the adiabatic compression of air. In turn, the pressure induces an additional upward force from the seals on the floater. This upward force acts as a spring since it is dependent on the position of the floater.

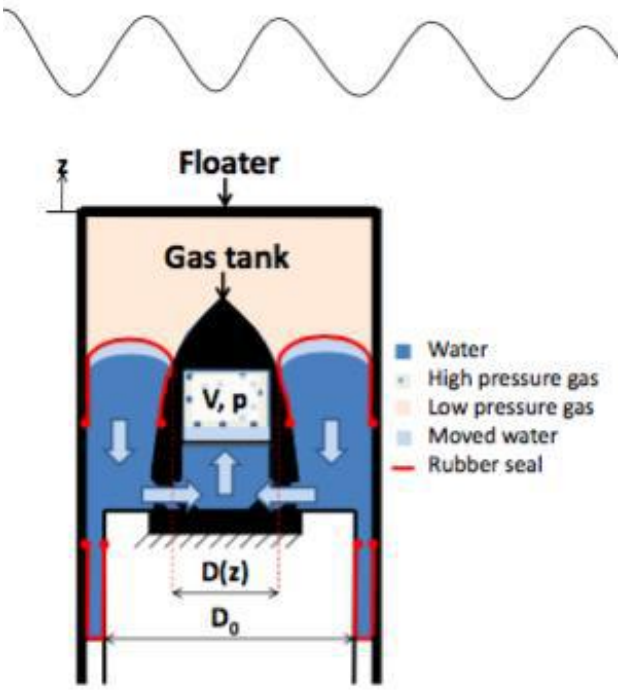

FIGURE 1-26 SCHEMATICS OF THE SYMPHONY DEVICE AND THE SHAPED INNER WALL OF THE UPPER MEMBRANE CONTACT AREA

The change in volume of gas is the amount of water that flows into the gas tank. The seals move half the distance that the floater moves. The amount of water that flows into the tank depends on the inner diameters of the lower and upper seals.

This is one mechanism through which D(z) (see Figure 1-26) influences the spring coefficient. Another mechanism is related to the vertical reaction forces on the floater due to the pressure difference over the seals. In order to explain this mechanism, the vertical force balance over part of the seal is analysed in detail. Prerequisite to D(z) is that the total spring acting on the floater has to be linear and has to correspond to the period of sea waves for a given stroke length. Beyond this stroke length, the spring coefficient has to increase exponentially.

The method to solve for D(z) so that it acts as prescribed spring includes the steps listed below. By this means, the effect of changes in the geometry in design conditions, and the effect of tuning for operational conditions are shown.

- ✓ Step 1: Set of coupled differential equations describing force equilibria in lower seal, upper seal and total seal force;
- ✓ Step 2: Conditions imposed by the problem; including a balance of vertical forces (gravitational force, hydrostatic force, compression of gas in the top of floater, top floater force)
- ✓ Step 3: Boundary conditions, including gas volume at equilibrium position, diameter of the wall at equilibrium position;
- ✓ Step 4: Algorithm for solving D(z) and V(z);
- ✓ Step 5: Applying geometrical constraints to D(z);
- ✓ Step 6: The tuning in operating conditions to approach the design conditions (including the pressure and the gas volume in equilibrium position).

An exemplary visualisation of the effect of changing the geometry in design conditions relative to a constant D by applying the above mentioned method is shown in **Error! Reference source not found.** The results are presented as dimensionless quantities, to demonstrate the relative importance of different effects. The following dimensionless quantities are used:

- $\zeta = 2z/Ds$ (z-coordinate as fraction of the amplitude of the floater's stroke)
- $\widetilde{D}(z) = D(z) / D_{out}$ (diameter relative to the outer diameter)
- The forces are presented relative to the designed resultant force at the amplitude of the floaters stroke length in negative direction, and stiffness is presented relative to the linear stiffness in the design conditions.

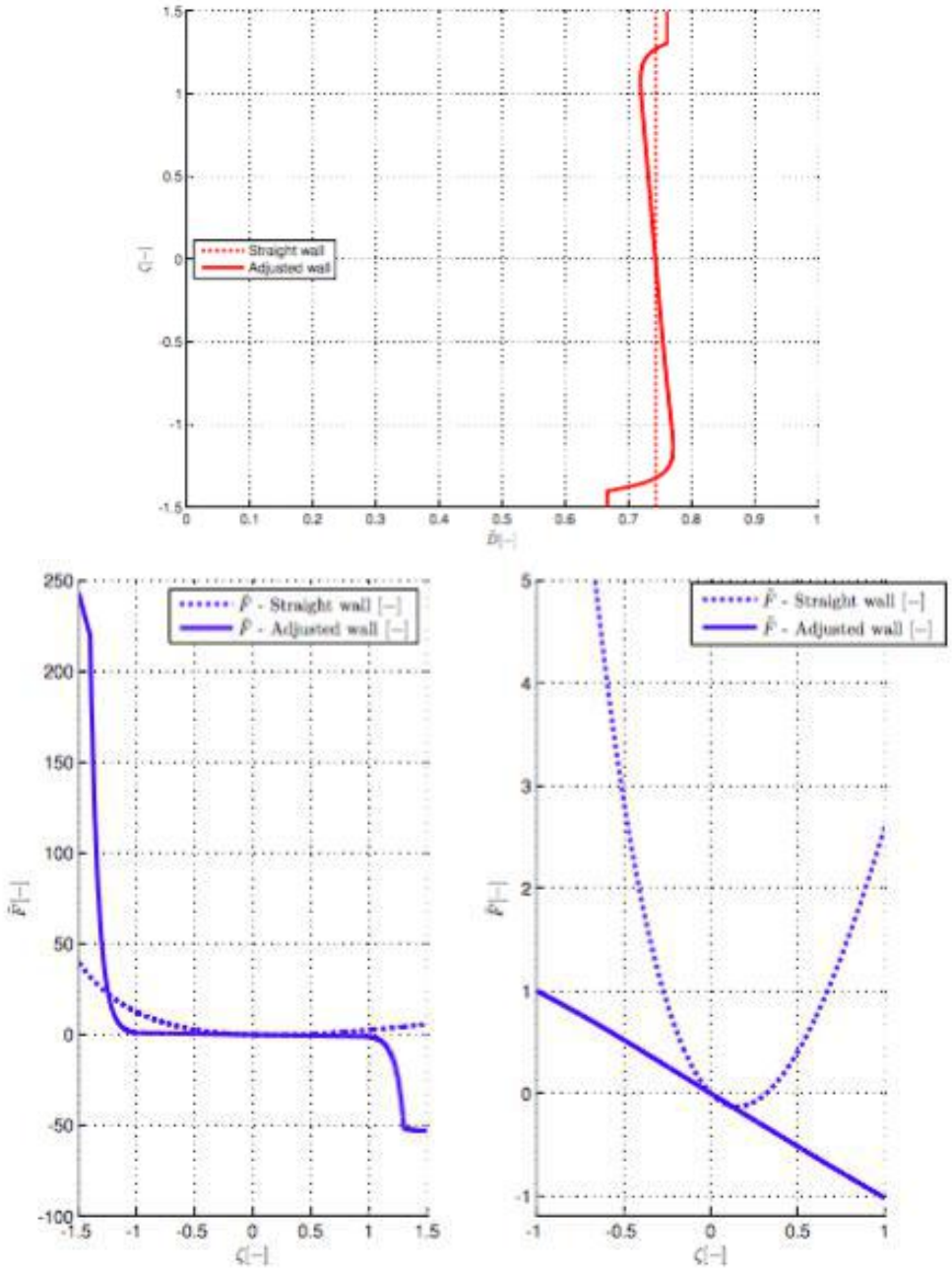

FIGURE 1-27 ABOVE: ADJUSTED GEOMETRY IN ORDER TO ENSURE PRESCRIBED SPRING COEFFICIENT. BELOW: RESULTANT FORCE ON THE FLOATER DUE TO THE GEOMETRICAL CHANGES OF THE WALL, OVERVIEW (LEFT) AND ZOOM (RIGHT).

The forces show the pattern that is predetermined. The force is a positive linear spring for the operational stroke of the device, as can be seen in **Error! Reference source not found.Error! Reference source not found.**Figure 1-27**Error! Reference source not found.** (below, right). The force increases exponentially beyond the operational stroke, as can be seen in Figure 1-27**Error! Reference source not found.** (below, left). The difference between compressing and decompressing is found since the geometrical requirements were met. Therefore, the working principle of adjusting the spring of the Symphony to have a predetermined stiffness is theoretically demonstrated. The spring with straight walls becomes unstable while decompressing. This is shown in Figure 1-27 (below, right) by the positive

contribution of the spring force for positions larger than 25% of the amplitude of the stroke. Therefore, a device with straight walls would not be operable as a functional Symphony WEC.

- The effect of changing the geometry in operating conditions

The device was tuned for the difference between design and operating conditions, whereas the tuning also has an effect on the spring Two changes are considered separately:

- A different energy period of the exciting waves during operation than the design was based on.
- An additional water column due to the presence of the tides. Energy period of the exciting waves.

The spring stiffness of the Symphony changes after tuning for the energy period (the wall is designed on a period of 10 seconds), becoming non-linear. This effect is larger when the device is tuned to smaller frequencies. The device will not become unstable due to tuning for a different frequency than the Eigen frequency of the device.

The spring stiffness change of the Symphony after tuning for tidal changes is larger while compressing the spring (negative ζ). The spring becomes unstable if the device is tuned for the tides, which is why this will not be an applicable solution for compensating the tides. The approach taken in Symphony development has not been decided and is not part of the WETFEET project. However, conceptual work has been initiated and the choice of a dedicated winch system is likely.

THE ENERGY EXTRACTION MODEL

The modifications of the geometry of the gas spring to obtain a linear spring are incorporated in the energy extraction model discussed in the following. A model that predicts the extracted energy should include all forces that affect the motion of the floater. The core of the model is Newton's second law, which provides a relation between the forces acting upon the floater and the motion of the floater. This relation is solved in discrete time steps using a Runge-Kutta discretisation scheme with fixed time steps of 0.005 seconds led to a converged solution.

The forces that act on the floater are:

(i) the hydrodynamic forces due to the coupling between the sea and the Symphony device (based on irrotational flow of an incompressible fluid, no viscous effects; including hydrostatic, radiation and diffraction forces)
(ii) the gravitational forces,
(iii) the forces due to the gas in the dome of the floater,
(iv) the forces due to the compression of gas in the device,
(v) the forces due to the Power Take Off (PTO) system (including linear energy extraction and stroke control), and
(vi) the drag due to movements through water.

The forces can be dependent on the position, velocity or acceleration of the floater. This dependency determines whether forces behaves like a spring, damper or inertia respectively. The forces are discussed in-depth in Leitjens [26].

Further, the resistance of the floater to changes in movement needs to be reproduced. This inertia of the floater is proportional to the equivalent mass of the floater. The inertia of the floater is the resistance of the floater to changes in movement. This inertia of the floater is proportional to the equivalent mass of the floater. The equivalent mass contains three contributions:

(i) The mass of the floater;
(ii) The added mass of the water in the sea moving with the floater;
(iii) The equivalent mass of the water in the SWP system moving with the floater.

The results of the energy extraction model are computed to gain insight in the effects of the adjustments of the air spring, covering the following subjects:

- The energy extraction in normal operation (with tuning).
- The effect of the tuning to the tides, which induces a non-linear spring (discussed separately).
- The effect of the tuning to the energy period, also inducing a non-linear spring. The effect of this non-linear spring is quantified by comparing it to other situations.

The mean extracted power for normal operation for an exemplary situation of a 1.5m Symphony model is outlined below. Normal operation means the following:

- No tides or changes in atmospheric pressure are considered.
- No viscous losses in the interior water flow or in the elastic deformation of the structural membrane are considered.
- The device is tuned to the energy period of the waves, inducing the desired spring coefficient
- The significant wave height differs between 0.5 and 5 meter.
- The energy period differs between 4 and 14 seconds.
- The results are based on a time average over 1800 seconds.

The outcomes for the mean extracted power were as follows (for more details on the mathematical formulations underlying the calculations refer to Appendix E):

P [W]	=<0.5 m	0.5-1 m	1-1.5 m	1.5-2 m	2-2.5 m	2.5-3 m	3-3.5 m	3.5-4 m	4-4.5 m	4.5-5 m	5-6 m	6-7 m	7-8 m	8-9 m	9-10 m	10-12 m	P[Te]
=< 4 s																	0
4 - 5 s		5	130														135
5 - 6 s		174	593	1114	1622												3 503
6 - 7 s		451	960	1557	2158	2732	3373										11 230
7 - 8 s		571	1150	1746	2370	2998	3671	4340	4943								21 791
8 - 9 s		590	1193	1832	2452	3057	3711	4358	0	0							17 193
9 - 10 s			1154	1762	2392	2995	3587	4270	4925	0	0						21 086
10 - 11 s			1105	1690	2293	2861	3447	4048	4684	0	0	0	0				20 129
11 - 12 s			1025	1594	2179	2698	3262	3712	4371	0	0	0	0	0			18 840
12 - 13 s					1981	2493	3012	3492	4076	0	0	0	0	0	0		15 053
13 - 14 s						2264	2723	3237	0	0	0	0	0	0	0	0	8 224
14 - 15 s									0	0	0	0	0	0		0	0

FIGURE 1-28 EXEMPLARY OUTPUT OF THE ENERGY EXTRACTION MODEL INCORPORATED IN THE SYMPHONY TDM; ESTIMATED POWER MATRIX FOR A 1.5M DIAMETER MODEL

CONCLUSIONS

The Symphony device is a wave energy converter, which will be designed to demonstrate improvements from the reference case, a generic SPDD with air volume/gap and linear generator. The Time Domain Model (TDM), developed as fundamental design basis tool, aims to describe the effects of altering the gas spring, the implementation of a modified (linearised) spring in the Symphony device, and the power conversion with a system conditioned according to the requirements.

Gas springs are described using physical laws concerning the compression of an perfect gas in an adiabatic process. It is shown that a spring can be altered to meet pre-determined requirements. Furthermore, it is shown that a cylindrical gas spring with linear characteristics will result in an unstable system at some point. Finally, analyses are performed to derive the optimal spring coefficient for energy extraction.

A coupled set of non-linear differential equations is derived and solved (see Appendix E), to obtain the geometry of the Symphony device for given forces. It is shown that the initial pressure and volume can be used to tune the device for variations in the energy period of the waves. The energy model of the Symphony is used to simulate the behaviour during operation, and to generate power matrix as result.

Further, the following findings should be taken into account regarding the TDM:

- Tidal compensation should not be done by tuning the device, as the system becomes unstable. Exploratory research should be conducted to determine a promising working principle that accounts for the tides.
- The compression of the gas in the gas tank is considered a purely adiabatic process. In reality, some isothermal components (resulting in a polytrophic process) will contribute to the compression of gas. Isothermal effects should be studied to and tentatively quantified for the Symphony device.
- Input parameters from the Symphony device were used to perform the TDM simulations. The Symphony is in a preliminary design phase, which makes accurate input not always available.
- The resultant forces acting on the floater are highly sensitive to the horizontal point in the rubber seals. Analyses using the detailed material properties, the **fabrication and implementations should be used** to obtain sufficiently accurate results.
- Lateral surge forces against which the structural membrane enclosing the high-pressure volume is stabilising are considered, however no eccentricities of these loads. If surge forces are asymmetric over the length of the device, additional bending moments can occur, which have to be assessed in the next development step.
- In determining the equivalent mass, some relatively rough approximations were done. Detailed flow simulations and a detailed design will be necessary to compute the equivalent mass accurately.
- In the TDM, a 100% efficient PTO system is assumed. This will not be the case in reality. The design of the PTO system is one of the main challenges in designing a functioning Symphony device.
- Also losses in the internal water flow, in the material and in the thermodynamics are neglected at this stage. To investigate their significance is among the core objectives of WP4.
- The initial results of the TDM should be computed once again in a more detailed design phase to improve the reliability of the results iteratively, before a physical validation can take place.

The presented model provides a theoretical framework to calculate the dominating effects of Symphony operation. No empirical data are available to validate the results at this stage. It is therefore a high priority to build prototypes of the components for bench testing and validate the theoretical results presented in this report with empirical data from the actual Symphony prototype tests in a subsequent step.

1.5. The Symphony reference design case

1.5.1. Introductory note

The data collection for a (quantified) reference design case for Symphony has been challenging for the Symphony working group. On the one hand, the benefit of measured reference data for new developments is recognized as very useful, and clearly the best and most straight-forward way of measuring the usefulness of an innovative component. On the other hand, there is very little reliable data available from WECs and components in general, and in the case of Symphony-relevant breakthrough components in particular. This is why a quantitative exercise comparing the breakthroughs to 'reference' components directly appears overly ambitious in this context. Apart from the Archimedes Wave Swing (AWS, see e.g. [27], [28]), no other device that has been developed to a minimum stage of development, appears suitable as reference. Following a survey of past and ongoing projects, only the CETO WEC (www.carnegiewave.com), a submerged heaving buoy, has reached sufficient level of development to serve as reference, however it lacks one essential feature of Symphony, namely the variable volume during operation.

The AWS had been developed to the point of construction and full-scale testing of a 2MW pilot plant in 2004, under strong participation of Teamwork, largely involving the present Symphony core working group. However the company and all data related to the ÂWS was sold to the company AWS Ocean Ltd, who follow their own commercial objectives in wave energy development. AWS Ocean Ltd. is not a partner of the WETFEET project. The background data generated during that development can therefore not be used by the WETFEET project, except for items published in the public domain. Most of the specific performance data of the AWS pilot's components is owned by AWS Ocean Ltd and cannot be used in this context by the Symphony working group. Furthermore, data from the pilot was generated under specific conditions, for example using a fixed platform as foundation instead of mooring, and not all components being operational. This is why significant parts of such analyses are normally conducted confidentially and could therefore not be part of a public deliverable. This natural obstacle for a transparent and meaningful comparison of an innovative component based on reference designs roots in the potential commercial interest of the new components when companies are involved.

In order to enable an evaluation of the breakthrough components on an at least partially quantitative basis using the TPL approach (Technology Performance Level, see Weber, Laird [29]), it was therefore decided to reconstruct a hypothetical reference case for a submerged pressure differential device of 6m diameter, using a combination of publicly available data (e.g [27], [28], [30]–[40]), and in-house know-how partly being generic, partly generated in the context of the Symphony development (which by all means is a system with several physical similarities to the reference system). The chosen reference design resembles the 'original' concept of the Archimedes wave swing: an air volume and a gas spring are used as spring, an air gap (internal over-pressure) is used as seal, a hydraulic (water) brake serves as end stop, and a linear generator converts movements into electricity.

1.5.2. Basic submerged pressure differential device concept

The submerged pressure differential devices (SPDD) are a WEC class that has been referenced in more recent attempts to classify devices in categories, as e.g. the EC project AquaRET (www.aquaret.com). The operating principle had first been introduced by the AWS, originally developed by Teamwork Technology BV (Netherlands). The concept resembles an underwater buoy of which the upper part (floater) moves up and down in the wave while the lower part (basement) stays in position. The periodic changing of hydrostatic pressure beneath a wave initiates these cyclic up- and downward motions of the upper part.

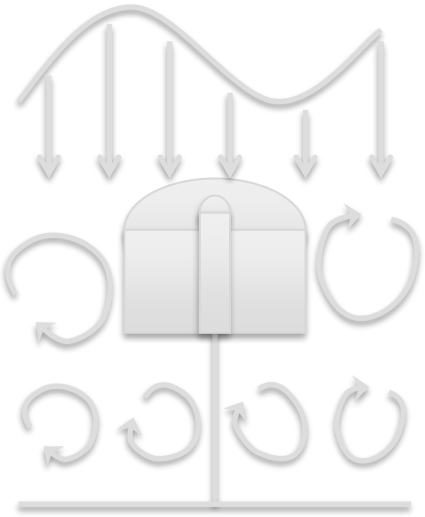

Since1997, significant research has been done to study the effect of a submerged under water buoy, especially for the volume changing buoy (see e.g. [40]).

The concept bases on the physical property of waves, where the diameter of the circular water particle motion for deep water waves is equal to the wave height at the surface and reduces with depth. An underwater body experiences two forces from a passing wave:

- The acceleration force of the circulating water that must move (accelerate) around the body, and,
- the pressure of the water column above the body.

As swell waves have large wave lengths (100 – 500m), WECs of the size of 2-12m can be seen as relative small bodies. Nevertheless, if they start to move and convert energy, they will have an effect on the wave and the forces from the waves to the bodies are reduced (hydrodynamic damping). These aspects are taken into account into the hydrodynamic calculations of the interaction between waves and SPDD, which are well studied and can be relatively easily calculated at present stage (see e.g. [34]).

From a hydrodynamic viewpoint, the reference case (see Figure 1-30) and the Symphony WECs are considered identical, apart from a possibly different length of the lower cylinder required for Symphony, for incorporation of all cocoon elements (see chapter **Error! Reference source not found.**). A simulation of the motion of a generic SPDD (representative of our reference case described here) with stroke limitation of 1m amplitude is exemplified in Figure 1-29. The system is tuned and resonating to the wave frequency.

wave elevation (black); floater position (blue) over time

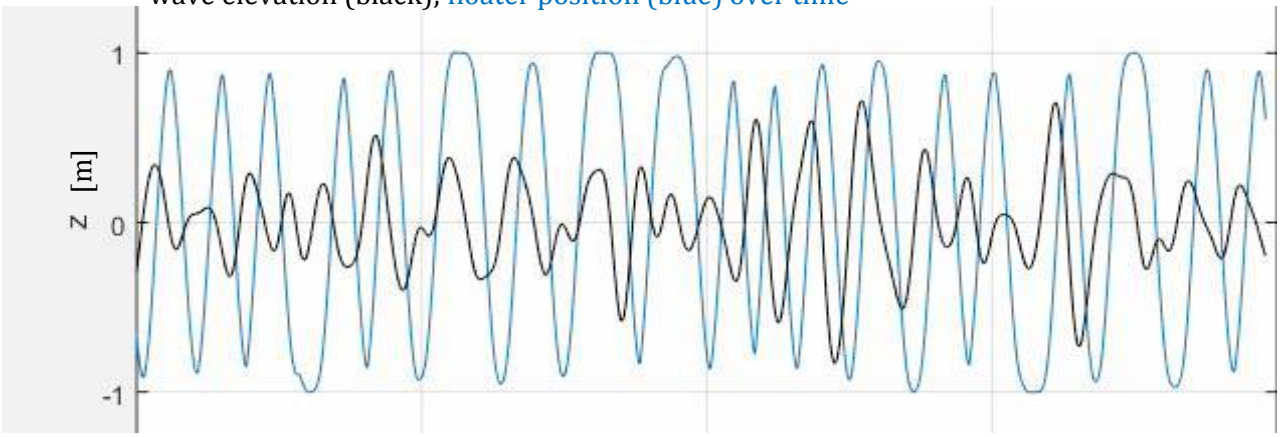

FIGURE 1-29 AN SPDD'S FLOATER POSITION (BLUE) OVER TIME, FOLLOWING AN IRREGULAR SEA STATE (BLACK). THE MOVEMENT OF THE FLOATER IS RESTRICTED TO A MAXIMUM EXCURSION OF 1M.

The mechanically available power equates force times floater velocity, so that an optimal control strategy would require the WEC motion following the wave in a way to maximise the average "force times velocity" during a given sea state. For the Symphony WEC, a time domain simulation was developed that is also representative for indicating such an optimal motion of any generic SPDD. The black line in Figure 1-29 is the wave amplitude and the blue line is the (restricted) motion (restricted due to a structurally imposed stroke limitation). One can see that the motion flattens at the end of the stroke. This is because there is a physical limitation in the construction to obstruct the motion going beyond a certan limit. Such a physical limitation must be included in any heaving WEC, and it is generally referred to as '**end stop'**.

For the energy conversion from linear relative motion into useful (electrical) energy a **PTO (power-take-off)** is used, which requires **bearings** to guide the system and **seals** to keep the water separated from the inside.

Finally, the motion has to react against a reference frame, e.g. a foundation. Similar to the hydrodynamics however, there are no implicit differences between a Symphony WEC with incorporated breakthrough components and a reference design case (see description in section 1.5).

In all the above parts of an SPDD, there are specific engineering challenges, and despite a 2MW pilot plant of this WEC type had already been tested in Northern Portugal, many of the subsystems performed sub-optimal due to them being novel and still under development. Even if some parts can be taken off-the-shelf from existing technology, they still need adaptation and testing in the relevant environment. Significant parts need to be specially designed to allow for optimized performance, which had not been achieved in the only existing case delivering 'hard data' in the context of this exercise. This is why a comparison of a reference design with the components developed within WETFEET has a rather exemplary character, and involves a number of assumptions and generic engineering judgement.

1.5.3. Reference case: a hybrid of documented and re-calculated data

In the following, the findings regarding the above mentioned parts of a reference design for a 6m diameter SPDD are summarized, based on a reconstruction from published references and in-house know-how in the consortium related to the Symphony development.

In the following, a conceptual drawing of the resulting reference design case for a 6m SPDD is presented:

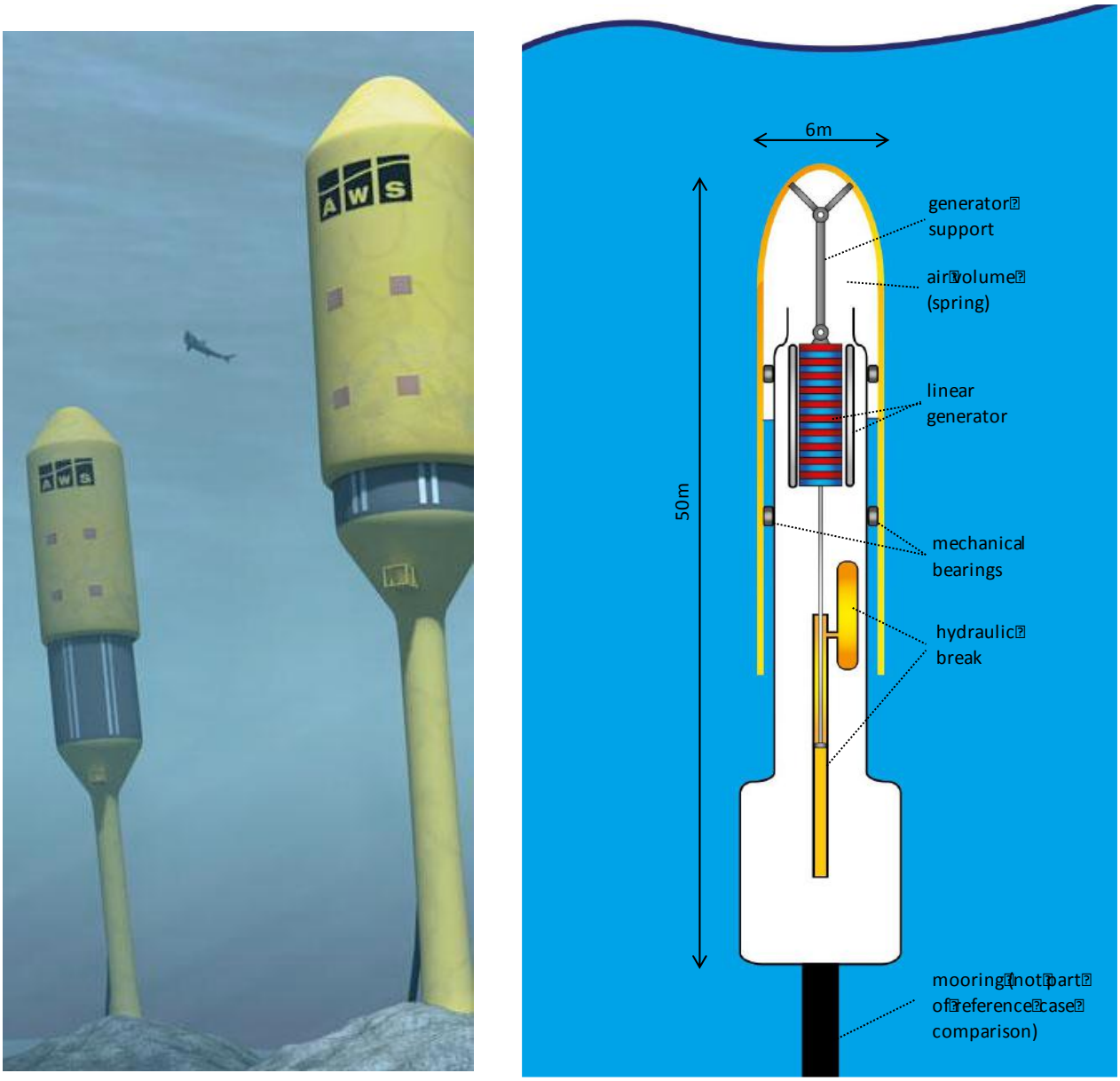

FIGURE 1-30 ESTIMATED REFERENCE DESIGN CASE DIMENSIONS FOR 6M SPDD; UPPER LEFT: ARTIST'S IMPRESSION OF SECOND GENERATION ARCHIMEDES WAVE SWING, REPRESENTING AN EXAMPLE CASE FOR SUCH A WEC DEVELOPED FROM FULL-SCALE PILOT PLANT EXPERIENCE. RIGHT: SPDD REFERENCE CASE LAYOUT

THE GENERATOR

The generator is needed to dampen (break) the motion while converting it into electricity. The magnetic force of the generator counteracts the wave force. The force of a generator is directly related to the amount of magnetic material and therefore the cost. This is why in many WECs a gear is implemented. This can be a gearbox, like in Corpower buoy (see e.g. [41]), or a hydraulic gear. Although there are specialised efficient hydraulics available, they have not yet been applied to power levels required in utility-scale WECs. The velocity of the system is high for a hydraulic seal, which would be required in such systems. Typically, hydraulics are a preferred choice for situations with high force and low velocity (small flow). They have a high grade of maturity in general for industrial applications. Losses are still high in that kind of systems, but much lower for a direct drive, as in the case of a linear generator. Also the number of components needed for a hydraulic PTO is significant, introducing substantial technical risk in the operation.

The same difficulty exists for the otherwise attractive generator system with a mechanical gearbox converting the linear floater motion into rotating motion, enabling the use of a standard rotating generator. Although this would be a cheap and efficient solution, it is difficult to build such a system robust enough and maintenance-free.

Due to the above reasons and the existing real-scale experience, the obvious choice for the reference design of a 6m SPDD is a linear generator. Due to its relatively high force density and efficiency at low speeds, a permanent-magnet (PM) generator is chosen. The magnets are mounted on the translator that moves up and down, so that there is no electrical contact between the moving part (the translator) and the stator, which is important because such an electrical contact can suffer from wear.

The above design choices are reported in Cruz [42] for the 2MW pilot plant of the Archimedes Wave Swing, where additional choices led to a rather large PTO unit.

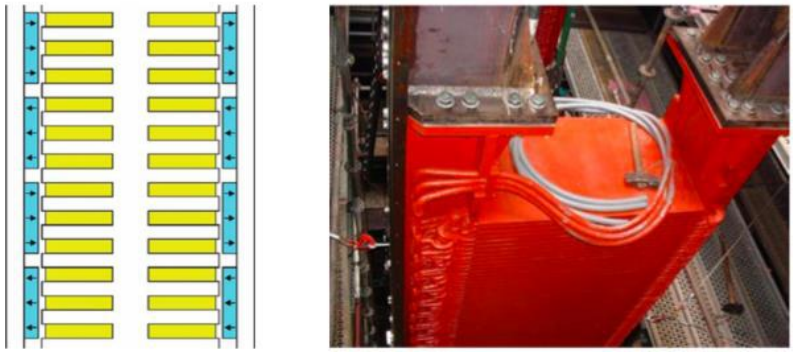

FIGURE 1-31 EXAMPLE OF FULL-SCALE LINEAR PM GENERATOR OF ARCHIMEDES WAVE SWING [4]: LEFT - SECTION OF FOUR POLE PITCHES OF THE LINEAR PM GENERATOR RIGHT – FOTO OF DOUBLE-SIDED 2MW-RATED PM GENERATOR MOUNTED IN AWS PILOT PLANT.

In Figure 1-31, the yellow parts are stator with stator iron and coils in the stator slots in between, blue parts are the translators with the magnets with arrows indicating the magnetisation direction. The rating was obtained by a maximum stroke of 7 m, maximum speed of 2.2 m/s, and a maximum force of 1 MN. Reconstructing this case for a 6m diameter SPDD from this example case, the following rationale is used to define the suggested reference design case:

As there is no gear, all the wave forces have to be counteracted by magnetic force. At a magnetic density of 50kN/m, approx. 10m² of magnetic material are needed. The required generator force to counter the wave force occuring in a maximum operational sea state can be calculated as:

→ wave of 5m heigth induces a wave force at a 6m diameter cylinder of effective area (pi*d^2/4 m^2) x wave amplitude (5/2=2.5m) x specific sea water density (1010 kg/m^3 * 9.8 m/s^2) x depth factor (0.72):

(6^2*3.14/4) 2.5 x 1010*9.8*0.72 =28.26m2 x 17.816N/m2 = **503 kN**

THE END STOP: THE HYDRAULIC BRAKE

It is nearly impossible (i.e. unfeasible from an electro-mechanical engineering point of view) and potentially extremely expensive to make the generator large enough to take all possible forces generated by waves. For this reason, any typical heaving device – including SPDD – has dedicated end stops with the function of damping/braking excessive movements either in extreme conditions, or upon loss of the grid/generator resistance. This component is of high importance for the WEC survivability, and to date has been one of the most difficult technical challenges to solve satisfactorily in heaving devices. The design of the end buffer is different for different systems. One possibility is to use water hydraulics. For the reference design case, it is assumed to have water labyrinths near the end of stroke, which can absorb very high forces by successive damping according to floater position.

This method is implemented by a piston that runs into a cylinder at the end of the stroke. All energy driving the motion and the kinetic energy in this motion, has to be transferred into water pressure and flow. Pushing the water through the small gaps between piston and cylinder creates the pressure. During this process the energy is transferred into heat (turbulence), causing a local increase of water temperature; even water boiling cannot be excluded a priori. The power levels occurring in this situation can reach several MW, which brings along the requirement of a strong structural layout of the part involved. Once the pistons are pushed inside, they need to be retracted when returning to normal operation. Upon retraction, an under-pressure is created, which would hold the piston inside (similar to a suction bucket mooring), which is why a special valve is required in order to allow water flowing into the suction area. Another technical challenge is that for this type of hydraulic brake to function properly, the alignment of the piston and cylinder needs to be accurate, with much lower tolerance than other bearing items. A special design is needed to ensure such accuracy, adding cost and technical risk. Despite the relatively simple and straight-forward principle, a hydraulic (water labyrinth) brake is technically difficult to implement, and no precedence exist for operational experience.

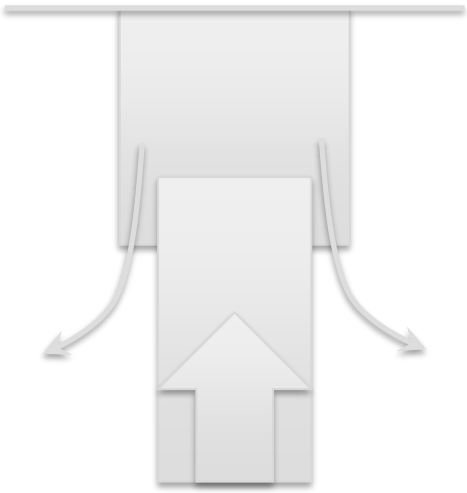

FIGURE 1-32 DESIGN PRINCIPLE OF HYDRAULIC (WATER) BRAKES.

In absence of other convincing end stop systems, such a water brake is suggested for the reference design case of a 6m diameter SPDD. There is no hard data on operational experience, and only rough estimates can be made about material and manufacture costs.

THE BEARING

The outer cylinders moves while the inner cylinder is connected to a fixed or semi-rigid reference, like e.g. a foundation or flexible joint with taut moorings connected to the seabed. Significant sideway forces are induced by waves and potentially by currents, which may be a superposition of ocean, wind and tidal currents. So there is a need of bearings keeping both parts separated from each other, and guiding the up- and down movement within a certain tolerance.

Between the outside cylinder and the inside foundations there are several components, refer to Figure 1-30 (right) for a cross-section, major dimensions and indication of components). 1) the end stops, 2) the hydraulic spring cylinder, 3) the linear generator. All these parts have their own bearings. The end stops are sliding and have a dynamic water bearing. The outer cylinder and the end stop have horizontal

freedom to move, but are vertically interlinked. So the motion of the outer cylinder can be several cm, while the end stops slide within 0.5 mm tolerance. The hydraulic cylinder has a flexible connection, but has internal sliding bearings, so it can move in a horizontal way and is fixed in a vertical way. The linear generator has a high-tolerance bearing that is fully independent from the main bearing. The bearing of the generator is highly (magnetically) loaded and complex. In practise, the generator is divided into sections in which bearings are connected in-between sections.

For the main bearing to ensure the movement of the outer cylinder against the inner cylinder, there are four outside sliding bearings that move against a special material. There can be expected the need of maintenance for this part. In addition to the sliding material, an outer skeleton is needed to house the bearings.

Similar to the hydraulic brakes, the reference design for the (floater) bearings needs to be deducted from the material choice and estimated dimensions of the floater area along its stroke. Although the state of the art of bearings with the required characteristics should allow to address the required functions, there exists no significant operational experience for this component, which introduces a grade of uncertainty of its use as reference design case.

THE SEAL

Since the WEC is permanently submerged, and the internal volume contains electronic and mechanical components, as well as for securing the spring function, there is a vital need to ensure no sea water from the water body around the WEC can enter. Since there are two large bodies moving against each other, there is a need of a large seal, which makes this item a high risk factor, and potentially a high cost. The only straight-forward, reliable and – at the first sight – cost-efficient approach to solve this is to use a siphon, providing an air gap with pressure gradient from inside the WEC to the outside. This is a very reliable seal, however it shows to have some implications turning it difficult to implement as a solution for forthcoming WECs: the air gap is provided by using a large air volume inside the device as (main) spring of the mass-spring system. The pressure level corresponds to the outside pressure of the water body at that depth under water. This results in an upward force acting at the inside of the outer cylinder. To keep the outer cylinder in position, this force must be counteracted with a downwards force. The most obvious would be to add weight to the floater, however this would mean a vast increase of dimensions not required for the structural integrity, making this solution economically unreasonable.

An alternative is to use an additional hydraulic spring, pulling the floater down. This spring has a high pressure inside and needs seals, which increases maintenance demand and technical risk. Although the diameter is relatively small compared to other seals in the system, they still are a difficult challenge and need to be carefully chosen for the purpose-designed unit. In addition to the seals and the spring cylinder, a hydraulic installation and gas vessel (e.g. nitrogen) and controls are required. Although the result is a complex component requiring special installation works, it has shown to be a doable and well-performing unit in practice, which is why it shall be part of the reference design case.

With respect to the role of the seal in the context of evaluating the reference design case, it takes a central role: as a consequence of a (pressurised) air gap fulfilling the vital function of a seal between the two moving bodies, the spring of the device gets pre-tensioned to an extent that it would become dysfunctional, unless an additional component (the hydraulic spring) is introduced. Using an air gap as seal is feasible and straight-forward, but has significant impact on other parts of the system, which become more complex and expensive.

THE DRIVEN, TUNED, DAMPED, MASS SPRING SYSTEM

The SPDD system consists of a driver, a mass, a spring and a damper. The driver is the wave (pressure) pushing the outside hull. The damper is the generator, as discussed above. The mass and the spring need to be tuned so that resonance occurs for energy absorption maximisation purposes. If this is not the

case, the phase between wave and motion will not be ideal and the conversion of power from the wave pressure into the mechanical system is (much) lower.

Without building the total case one can conclude that the motion of a device can be computed from the basic mass-spring-system relations using a simplified frequency domain model, as described in Appendix E [27].

In the chosen reference design case, the seal for the moving bodies is dominant to its total properties, as there is a need for a relative high pressure inside to create the siphon. To maintain the pressure without adding too much mass in the floater, and to straighten the spring curve, an additional gas spring cylinder was added. So there exist three springs in the system (including the implicit negative spring resulting from outside water pressure on the floater). For the resulting (total spring) not only a certain spring coefficient is needed, but also a certain pressure, therefore the spring components are linked into an equilibrium force as well.

For the 6m diameter reference case, the spring components are calculated in a simplified way (see Appendix E) and given in the graphs in Figure 1-33. The numbers should also reflect roughly a scaled version of the original Archimedes Wave Swing device deployed in Portugal in 2004 [27], as throughout this section that experience is the baseline for the considerations presented. However, since no source data from that project was used, the simplified reconstruction resulting in the dimensions presented in the following may imply some inaccuracy.

The most important outcome of this exercise are the (non-linear) total spring and due to this non linearity the variation of the resonance period over the stroke. The effect of this non-linearity can only be calculated through a full time domain model, which is described in detail in Appendix E. Such a model is being under development for the Symphony, but an application to the reference design case is not available in the context of this work. It is known that an accurate tuning of this situation can make a substantial difference in power output.

In addition to the high mass and non-linear spring of the reference design case, a critical disadvantage is the huge volume of the air spring. According to the simplified calculations reconstructing this case, an air volume of 1356 m^3will be required to fulfil the spring functions. With a diameter of 6m and a straight cylindrical shape, this results in a required length of approximately 50m (the order of magnitude of this estimate can be confirmed by referenced data from the 9.5m original device). Although this does not affect the energy transfer negatively, it creates substantial costs as it creates much more buoyancy than needed; also the foundation needs extra force.

With respect to overall device performance, little data exists for this type of WECs As mentioned beforehand, the only existing data in the public domain is what was published about the pilot plant experience of the Archimedes Wave Swing, as well as the follow-up developments. Based on numerical simulations partly validated in tank experiments and in the pilot plant experience, a power diagram was presented for this device, which is reproduced in Figure 1-34.

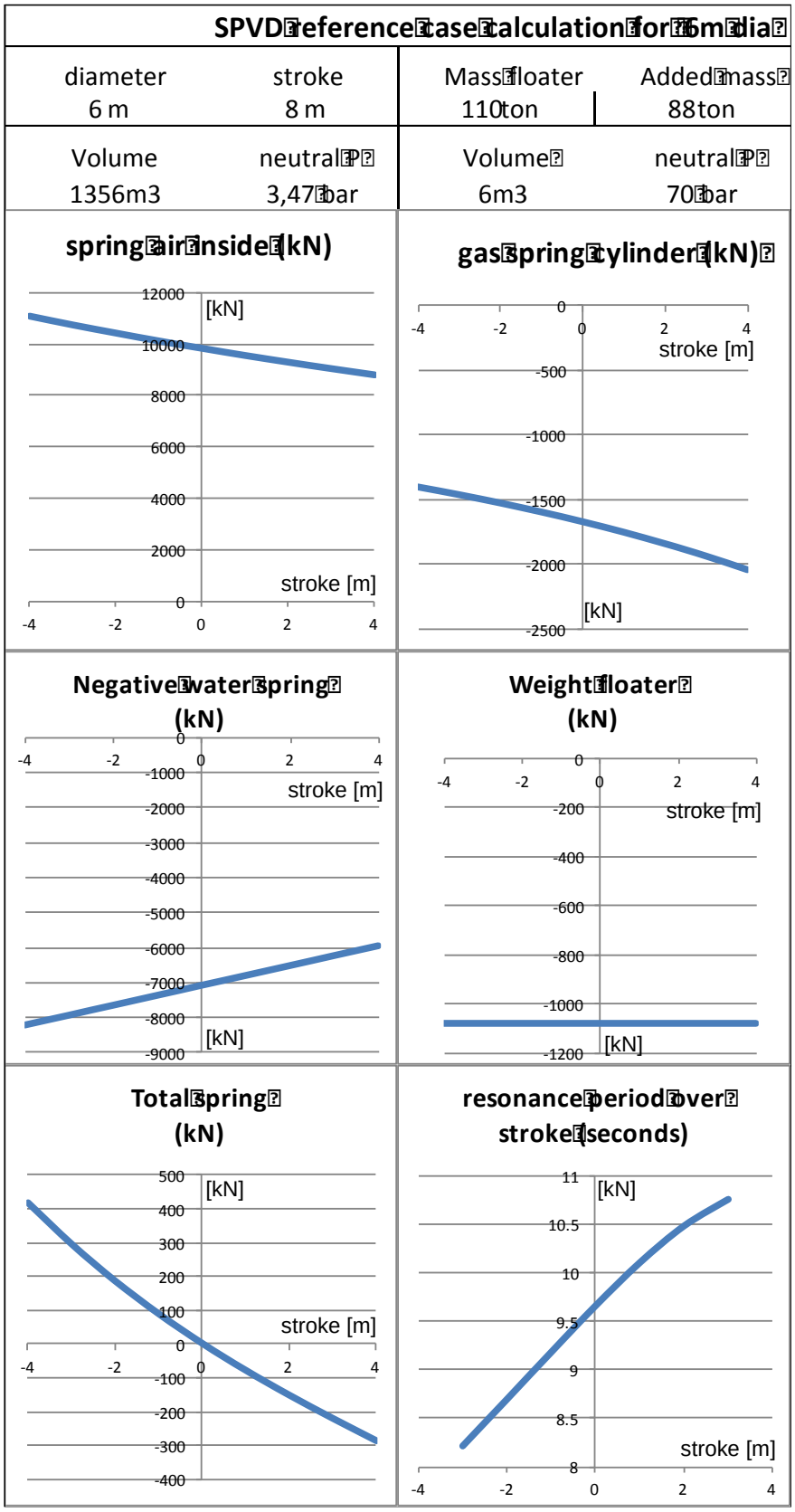

FIGURE 1-33 SIMPLIFIED CALCULATION OF SPRING COMPONENTS OF A 6M SPDD REFERENCE DESIGN

Archimedes Wave Swing – Power Transform Matrix (unrestricted): output in kW

Wave Period – Tpow (s)

Significant Wave Height Hs/g - m	5.0	5.5	6.0	6.5	7.0	7.5	8.0	8.5	9.0	9.5	10.0	10.5	11.0	11.5	12.0	12.5	13.0	13.5	14.0	14.5	15.0	15.5	16.0	16.5	17.0	17.5	18.0
0.5	0	0	0	0	0	0	0	0	0	0	0	0	0	0	0	0	0	0	0	0	0	0	0	0	0	0	0
1.0	2	7	13	19	26	34	41	48	58	68	81	93	105	118	131	144	153	163	183	203	213	223	223	223	223	225	227
1.5	4	15	28	41	56	72	85	99	121	143	173	203	226	248	266	285	309	334	357	380	389	398	398	398	398	403	409
2.0	8	26	49	73	100	127	150	172	210	247	292	337	366	395	418	442	482	523	543	563	579	596	596	596	596	597	598
2.5	15	43	78	113	159	205	234	263	320	376	438	499	531	563	603	643	675	708	741	774	785	797	797	797	797	800	804
3.0	25	61	111	161	227	293	339	386	453	521	600	680	722	765	827	888	897	906	945	984	996	1009	1009	1009	1009	1003	998
3.5	35	92	155	218	305	391	454	517	605	694	772	851	913	975	1036	1096	1119	1141	1163	1185	1198	1211	1211	1211	1211	1208	1206
4.0	35	114	194	273	380	486	572	659	776	894	961	1027	1103	1179	1227	1275	1316	1357	1365	1374	1394	1414	1414	1414	1414	1415	1416
4.5	0	0	235	332	479	626	722	819	957	1096	1168	1240	1320	1401	1449	1497	1547	1598	1590	1583	1610	1637	1637	1637	1637	1616	1595
5.0	0	0	280	400	592	784	899	1014	1144	1274	1380	1487	1569	1651	1691	1731	1785	1838	1807	1777	1806	1836	1836	1836	1836	1806	1777
5.5	0	0	320	432	641	849	1033	1216	1331	1446	1568	1690	1778	1867	1919	1970	1977	1984	1994	2005	2017	2030	2030	2030	2030	1990	1951
6.0	0	0	0	0	680	944	1155	1367	1495	1623	1759	1895	1983	2072	2137	2202	2205	2207	2226	2246	2240	2234	2234	2234	2234	2194	2154
6.5	0	0	0	0	720	1123	1335	1547	1678	1809	1963	2115	2200	2284	2332	2380	2425	2470	2452	2434	2403	2373	2373	2373	2373	2354	2336

FIGURE 1-34 PUBLISHED POWER DIAGRAM FOR AN ARCHIMEDES WAVE SWING ORIGINAL DESIGN (CARBON TRUST, 2005).

The explanations of the suggested reference design case so far are largely based on the 2MW pilot plant experience of the Archimedes Wave Swing, whenever public data is available. Figure 1-34 is assumed to refer to the first commercial-scale vision of the time after the pilot tests. Following the logic so far presented in this section, and using in-house know-how for a simulated down-scaling of the 12m to a 6m diameter, leads to the power matrix for the reference design presented below. Although the source of the scatter diagram in Figure 1-34, Carbon Trust [3], does not explicitly specify these dimensions or other assumptions, the following is deemed to be realistic as basis for this exercise: (i) an idealised PTO is used (no losses and no output limitation); (ii) the dimensions of the AWS are from the prototype: Diameter 12m, Stroke 12m (operational stroke of 10m with 1m safety on each side; in the prototype water breaks would kick in during the last 1m but most likely in the calculation of the power matrix it was considered that all the energy taken from the wave within the stroke was converted into energy); (iii) there is a stroke limitation (judging from the linear variation of the power with Hs for a large Hs); (iv) no drag losses were included (important for larger strokes/diameter ratios). The new values are derived from changing these relevant dimensions in the TDM, as well as the hydrodynamic coefficient estimates, and then running the TDM. The results are shown in Figure 1-35.

Diam: 6 m Stroke 8 m ATRIX FOR 6M DIAMETER SPVD DERIVED FROM PUBLISHED ARCHIMEDES WAVE SWING DATA (Carbon Trust, 2005)

Tpow (s) - Check Carbon Trust Report for definition of Tpow

Hs (m)	5.0	5.5	6.0	6.5	7.0	7.5	8.0	8.5	9.0	9.5	10.0	10.5	11.0	11.5	12.0	12.5	13.0	13.5	14.0	14.5	15.0	15.5	16.0	16.5	17.0	17.5	18.0
0.5	0	0	0	0	0	0	0	0	0	0	0	0	0	0	0	0	0	0	0	0	0	0	0	0	0	0	0
1.0	0	1	2	3	4	6	7	8	10	11	14	16	18	20	22	24	26	27	31	34	36	37	37	37	37	38	38
1.5	1	3	5	7	9	12	14	17	20	24	29	34	38	41	44	48	52	56	60	63	65	66	66	66	66	67	68
2.0	1	4	8	12	17	21	25	29	35	41	49	56	61	66	70	74	80	87	91	94	97	99	99	99	99	100	100
2.5	3	7	13	19	27	34	39	44	53	63	73	83	89	94	101	107	113	118	124	129	131	133	133	133	133	133	134
3.0	4	10	19	27	38	49	57	64	76	87	100	113	120	128	138	148	150	151	158	164	166	168	168	168	168	167	166
3.5	6	15	26	36	51	65	76	86	101	116	129	142	152	163	173	183	187	190	194	198	200	202	202	202	202	201	201
4.0	0	19	32	46	63	81	95	110	129	149	160	171	184	197	205	213	219	226	228	229	232	236	236	236	236	236	236
4.5	0	0	39	55	80	104	120	137	160	183	195	207	220	234	242	250	258	266	265	264	268	273	273	273	273	269	266
5.0	0	0	47	67	99	131	150	169	191	212	230	248	262	275	282	289	298	306	301	296	301	306	306	306	306	301	296
5.5	0	0	53	72	107	142	172	203	222	241	261	282	296	311	320	328	330	331	332	334	336	338	338	338	338	332	325
6.0	0	0	0	0	113	157	193	228	249	271	293	316	331	345	356	367	368	368	371	374	373	372	372	372	372	366	359
6.5	0	0	0	0	120	187	223	258	280	302	327	353	367	381	389	397	404	412	409	406	401	396	396	396	396	392	389

FIGURE 1-35 ESTIMATED POWER MATRIX FOR A 6M SPDD REFERENCE DESIGN.

2. NEGATIVE SPRING CONCEPTS

In this chapter, two methods for the application of a hydrodynamic "Negative Spring (NS)" effect are explored. In the framework of a WEC technology development, the negative spring concept is a strategy to change the dynamics of the device by reducing their usually very high stiffness; this will shift the resonance frequency to lower values and broadening the overall frequency response.

NS are mechanical concepts which aim at improving the performance of resonant WECs by tuning their stifness over a wider range of incoming wave frequencies than just the natural frequency of the structure. By nature, NS are unstable systems when deviated from their equilibrium position. This property is key to reducing the stiffness of heaving point absorber WECs and thus significantly improving the energy density performance (e.g. ratios of annual energy production per unit of mass, per unit area or per unit of PTO force).

Concepts exploiting the NS effects are currently under development by some researchers and technology developers. In particular, the WaveSpring patented technology [43] which is part of the CorPower wave energy device has been the object of several studies over recent years [44], [45]. The WaveSpring provides phase control by a NS mechanical arrangement that inherently widens the response bandwidth of point absorbers without the need for real-time wave information or prediction algorithms.

In the case of the CorPower point absorber device, the NS module acts directly on the linear mechanism of the buoy. This avoids the losses associated with transmitting large reciprocating energy flows through the PTO system, a challenge that has limited the practical use of phase control methods known as reactive control. Experimental wave tank testing of a 1:16 scaled CorPower device [45] featuring pressurized cylinders to simulate the NS arrangement have shown promising results, in particular:

- Three times higher ratio of absorbed energy to significant PTO force.
- Mooring line forces with maximum values less than 2.5 times the mean tension

Another experiment conducted at the wave basin of Aalborg university tested a single rotor of the WEPTOS pitching WEC device with two different NS setups [46]. While no conclusive performance improvement was noticeable from the physical model testing campaign (probably due to frictional losses), a simple numerical model indicates positive benefits in terms of efficiency of the device over a broader wave spectrum compared to the configuration without NS.

Also recently, Zhang and Yang [47] developed a wave-to-wire numerical time domain model capable of simulating the effects of non-linear snap through PTO mechanisms which resemble very much the WaveSpring concept proposed for the CorPower device. Zhang and Yang [47], [48] demonstrated that negative spring effects have the potential to increase the power capture performance of heaving point absorbers in both regular and irregular waves. Further insight regarding the impact of the relative difference between the natural frequency of the body and the incoming wave frequency is given. The effects of the PTO damping coefficient and the significant wave height on the power capture performance of the negative spring concept are similar to those of the linear WEC.

Unlike the mechanical spring arrangement proposed by others, alternative NS concepts will be investigated for the OWC spar buoy. Instead of controlling the PTO mechanism, these alternative methods directly act on the hydrodynamic properties of the device. In the project, two negative spring methods that use hydrostatic effects associated with the shape of the OWC spar structure, will be explored to produce a negative spring effect without requiring any mechanical or electrical component. This is expected to increase the level of reliability of the system as problems associated with the fatigue of mechanical or pneumatic springs are avoided. These two NS methods can be used in other heaving

point absorbers but the extension to other heaving devices other than OWC will not be undertaken in WETFEET.

These two "negative spring" methods were conceived by WavEC Offshore Renewables. The preliminary feasibility analysis reported in the following sections have also been carried out by WavEC Offshore Renewables. The most promising idea is currently going through a patent application and further analysis are also on-going.

2.1. The IVV negative spring method

The Immersed Varying Volume (IVV) is a method to achieve the negative spring effect. In this study the IVV method is implemented in a floating oscillating water column (OWC). Given a specific scatter diagram, a range of the most significant periods is selected. The geometry of the WEC is defined in such a way so it resonates near the minimum value of the period range. The goal of the IVV method is to lead the WEC to resonate at any period of the selected range, depending on the sea state that the device is subject to.

2.1.1. Numerical assessment of the potential of the IVV negative spring method

Firstly, we present the mathematical model for a conventional OWC, without the negative spring concept

CONVENTIONAL OWC WITHOUT THE IVV NEGATIVE SPRING

In this study the linear wave theory is assumed. This allow us to represent any quantity by a time dependent sinusoidal function, which is characterized by its frequency and a complex amplitude, e.g. $x(t) = Xe^{i\omega t}$. Whenever the quantity is real we only take the real part of $Re\left(Xe^{i\omega t}\right)$.

In this report, the WEC has been modeled using the piston mode description of the OWC. In this representation the free surface inside the chamber is assumed completely flat and moving just in one degree of freedom: heave.

With this approximation it is possible to maintain the equations of motion as for two rigid bodies, respectively floater and water column free surface, simplifying the entire model. This approximation is reasonable if the water column diameter is much smaller than the characteristic length of the waves.

The greatest advantage of this method comes during the numerical implementation, when, using panel method-based software such as WAMIT, the free surface can be considered as a unique patch with heaving motion.

The general dynamics of the floater-system can be expressed as follows:

$$m\,\frac{d^2x}{d\,t^2} = -\rho\,g\,S\,x + F_r + F_e - S\,p \qquad (2\text{-}1)$$

Where:

- m is the mass [kg],
- x the vertical displacement of the floater [m]
- t the time [s]
- ρ the water density [kg.m^{-3}]
- g the acceleration of gravity [m.s^{-2}]
- S the cross section area of the floater [m^2]
- F_r the radiation force [N]
- F_e the excitation force [N]
- p the air pressure in the chamber [Pa]

The radiation force is the force we need to impose in the floater to have it undertaking the same motions if there were no incoming waves. The diffraction force is the force we need to impose in the floater to keep it fixed under the action of the incoming wave.

Splitting the radiative force in a component proportional to the WEC velocity (which we call the damping contribution) and another component proportional to its acceleration (the added mass) introduces no loss of generality. With this decomposition, the previous equation becomes:

$$X\,[-\omega^2(m+A)+i\,\omega\,B+\rho\,g\,S]=\,F_e-\,S\,p \qquad (2\text{-}2)$$

Where:

- ω is the frequency of the heaving motion [rad.s^{-1}]
- A is the added mass coefficient [kg]
- B is the damping coefficient [kg.s^{-1}]

The reactance of the system is given by the real term of the equation's left-hand side $-\omega^2\,(m+A)+\rho\,g\,S$.

When the reactance is zero the system is called to be in resonance conditions: as can be shown its heaving speed is in phase with the excitation force and the power output is maximum.

The frequency at which the resonance can be observed is therefore obtained as follows:

$$-\omega^2\,(m+A)+\,\rho\,g\,S=0 \qquad (2\text{-}3)$$

By isolating ω in (2-3**)**

$$\omega=\sqrt{\frac{\rho\,g\,S}{m+A}} \qquad (2\text{-}4)$$

IVV NEGATIVE SPRING

The implementation of the Immersed Varying Volume method here presented consists in adding a structure assembled around the lower part of the OWC cylindrical wall. It is a chamber connected to the sea through an opening below, inside of which there is a mass of air trapped on its top part. The relative motion between the rigid structure and the water inside causes the variation of the immersed volume, changing the WEC dynamics and shifting the resonance frequency to lower values. It is expected that the larger the undisturbed volume of the air chamber, the higher is the decrease in the resonance frequency. Ideally, it would be possible to have more than one chamber, so that the volume of air would be adjustable to tune the resonance frequency to the current sea state.

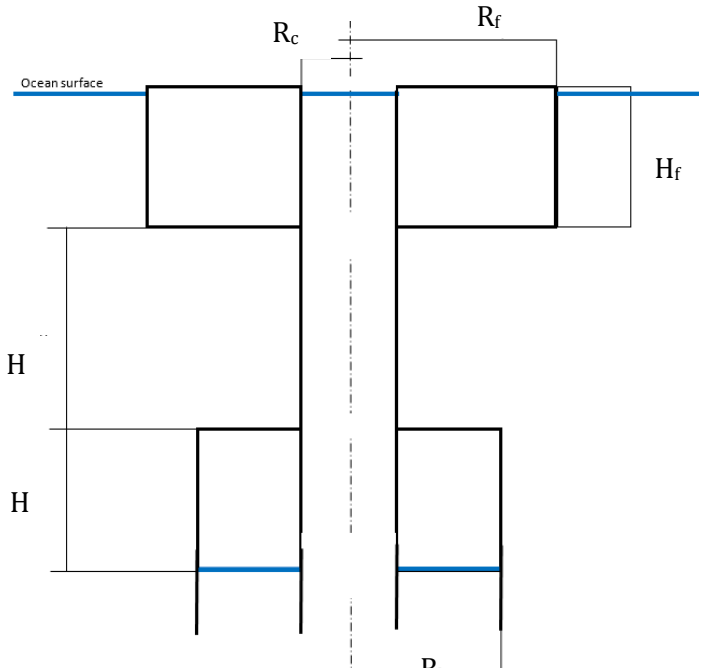

FIGURE 2-1 SCHEMATIC REPRESENTATION OF THE OWC SPAR BUOY AND VARIABLES DEFINITION FOR THE IVV METHOD

As explained in the previous section for the central OWC, the heaving piston mode is also assumed for the motion of the water inside the IVV structure. Note that the top air chamber is closed and connected to the atmosphere through a duct containing a turbine. This is not represented in Figure 2-1.

Hence, the system of equations needs to be modified in order to take into account this new degree of freedom, but also the negative spring effect on the whole structure (top floater and bottom negative spring structure). This system is shown in Eqs. (2-5**)**.

$$
\begin{aligned}
X_1\left[-\omega^2(m + A_{11}) + i\omega B_{11} + \rho\, g\, S_f\right] + X_2\left[-\omega^2 A_{12} + i\omega B_{12}\right] \\
+ X_3\left[-\omega^2 A_{13} + i\omega B_{13}\right] + F_{ns} = A_w\, F_{e1} \\
X_2\left[-\omega^2 A_{22} + i\omega B_{22} + \rho\, g\, S_c\right] + X_1\left[-\omega^2 A_{12} + i\omega B_{12}\right] + X_3\left[-\omega^2 A_{23} + i\omega B_{23}\right] \\
= A_w\, F_{e2} \\
X_3\left[-\omega^2 A_{33} + i\omega B_{33} + \rho\, g\, S_b\right] + X_1\left[-\omega^2 A_{13} + i\omega B_{13}\right] + X_2\left[-\omega^2 A_{23} + i\omega B_{23}\right] \\
= A_w\, F_{e3}
\end{aligned}
\qquad (2\text{-}5)
$$

- X_1 is the vertical displacement of the main body [m]
- X_2 is the vertical displacement of the water column [m]
- X_3 is the vertical displacement of the bottom free surface [m]
- Fe_i is the excitation force acting on each body (structure, central water column and bottom chamber water surface) [N]
- A_{ij} are the added mass coefficients, which contains now cross effects between bodies 1, 2 and 3.
- B_{ij} are the hydrodynamic damping coefficients, which contains now cross effects between bodies 1, 2 and 3.
- S_c is the cross section of the column [m²]
- S_b is the cross section of the spring chamber [m²]
- S_f is the cross section of the floater [m²]

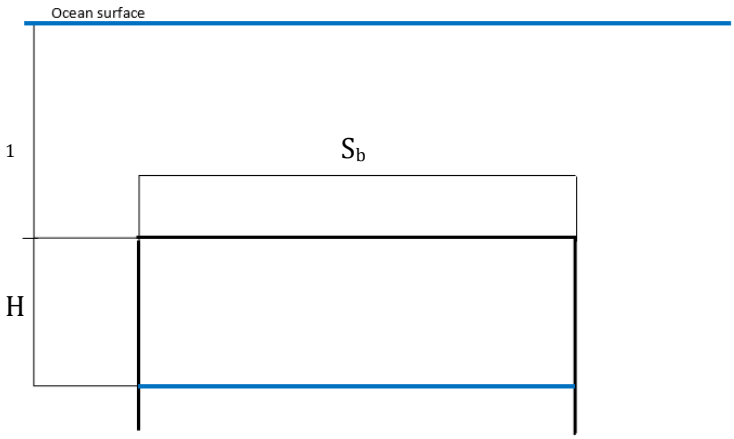

In order to understand the term F_{ns}, let us assume for simplicity a cylinder open in its bottom and closed on the top, with a given mass of air trapped inside.

The cylinder may move up and down around its undisturbed position. The net vertical force on the cylinder is given by

$$F(t) = [p_2(t) - p_1(t)]S_b - W$$

FIGURE 2-2 ILLUSTRATION OF THE NEGATIVE SPRING EFFECT FOR A SIMPLE CYLINDER

Where S_b is the cross section of the cylinder, W its weight and p_1 and p_2 are respectively the pressure in its top and in the entrapped air.

Assuming quasi-static pressure variations, the pressures of the top and inner part of the top surface of the cylinder are given by:

$$p_1(t) = \rho_w h_1(t) g \qquad (2\text{-}6)$$
$$p_2(t) = \rho_w g [h_1(t) + H(t)]$$

Above h_1 is the depth of surface 1 and H is the height of the air volume inside the air chamber. Equation 8 is thus written as:

$$F(t) = \rho_w g H(t) S_b - W \qquad (2\text{-}7)$$

Rewriting $H(t) = H_0 + H'(t)$ where H_0 stands for the non-disturbed value and H' the time dependent component, we obtain:

$$F(t) = (\rho_w g S_b H_0 - W) + \rho_w g S_b H'(t) \qquad (2\text{-}8)$$

The first term on the right-hand side of equation (2-8) is zero if we assume that in undisturbed conditions the box is in equilibrium. So the vertical force due to the change in vertical position is due to the change in buoyancy, as $S_b H'(t)$ is the internal volume change. The net force is therefore:

$$F(t) = \rho_w g S_b H'(t) \qquad (2\text{-}9)$$

The total volume is given by:

$$V(t) = V_0 + v'(t) \qquad (2\text{-}10)$$

where V_0 id the undisturbed volume and as mentioned,

$$v'(t) = S_b\, H'(t) \qquad (2\text{-}11)$$

To compute *v'(t)* we use the isentropic equation for the air pressure change inside the cylinder

$$p_0\, V_0^{\gamma} = p(t) V^{\gamma}(t) \qquad (2\text{-}12)$$

where p_0 is the undisturbed internal air pressure. We can also write

$$\begin{aligned} p(t) &= p_0 + p'(t) \\ V(t) &= V_0 + v'(t) \end{aligned} \qquad (2\text{-}13)$$

from which (2-13**)** can be linearized to give

$$v'(t) = -\frac{V_0}{\gamma\, p_0}\, p'(t) \qquad (2\text{-}14)$$

where *p'(t)* is the pressure fluctuation.

Going back to the WEC problem and using the results above, we take from (2-8**)** that

$$p_2 = \rho_w\, g\, [h_{1_0} + h_1'(t) + H_0 + H'(t)] \qquad (2\text{-}15)$$

From which results that its fluctuation part is given by

$$p_2{}'(t) = \rho_w\, g\, [\, h_1'(t) + H'(t)] \qquad (2\text{-}16)$$

Using (2-12**)** and (2-16**)** we may write

$$H'(t) S_b = -\frac{V_0}{\gamma\, p_0} \rho_w\, g\, [h_1'(t) + H'(t)] \qquad (2\text{-}17)$$

Which leads to

$$H'(t) = -\frac{\frac{V_0\, \rho_w\, g}{\gamma\, p_0 S_b}}{1 + \frac{V_0\, \rho_w\, g}{\gamma\, p_0 S_b}} h_1'(t) \qquad (2\text{-}18)$$

Or

$$H'(t) = -\left(\frac{V_0\, \rho_w\, g}{V_0\, \rho_w\, g + \gamma\, p_0 S_b}\right)\ h_1'(t) \qquad (2\text{-}19)$$

Substituting *H'* in (2-10**)**, F_{ns} becomes

$$F_{ns} = -\rho_w\, g\, S_b \left(\frac{V_0\, \rho_w\, g}{V_0\, \rho_w\, g + \gamma\, p_0 S_b}\right)\ h_1'(t) \qquad (2\text{-}20)$$

Noting that $h_1'(t) = -x_1(t)$, where $x_1(t)$ is vertical upward motion of the floater, represented by X_1 it results from looking at equation (2-2**)** that this term reduces the hydrostatic spring (given by $\rho_w\, g\, S_f$) and so providing the negative spring whose coefficient is

$$\alpha = \frac{S_b\, \rho_w\, g}{1 + \frac{\gamma\, p_0 S_b}{V_0\, \rho_w\, g}} \qquad (2\text{-}21)$$

According to the equation of motion of the structure (2-2**)** the implementation of the IVV method shows that the resonance frequency is now

$$\omega = \sqrt{\frac{\rho\, g\, S_f - \alpha}{m + M}} \qquad (2\text{-}22)$$

ANALYSIS OF THE RESONANCE FREQUENCY

Let us consider the expressions for the resonance frequency in both cases, with and without the implementation of the IVV method. If we want the structure to resonate at ω when without the IVV it resonates at ω_0, using equations (2-1**)** and (2-23**)**, assuming no change in the WEC mass and added mass M, it results in

$$\frac{\omega}{\omega_0} = \sqrt{\frac{\rho_w\, g\, S_f - \alpha}{\rho_w\, g\, S_f}} \qquad (2\text{-}23)$$

And so

$$\alpha = \rho_w\, g\, S_f \left[1 - \left(\frac{\omega}{\omega_0}\right)^2\right] \qquad (2\text{-}24)$$

Using (2-22**)** and after some manipulation it results

$$V_0 = S_b\, \frac{\gamma\, p_0}{\rho_w\, g}\, \frac{1}{\frac{S_b}{S}\frac{1}{1 - \left(\frac{\omega}{\omega_0}\right)^2} - 1} \qquad (2\text{-}25)$$

In order to have a better understanding of the IVV method, we consider a specific case: let us assume that the important range of periods is from 8s to 12s, or a frequency interval of 0.524 rad/s to 0.785 rad/s. This means that the ratio of the new peak frequency (obtained with the IVV method) over the initial peak frequency (without the IVV), w_2/w_1, must vary from 1 to 0.66, in order to cover the selected range of important periods. The dimensions of the WEC are defined so the device resonates at around the 8s (0.785 rad/s), in the case with no active IVV system.

The dimensions corresponding to the reference design case of the OWC spar buoy are: floater radius = 6m, floater draft = 3m, bottom chamber radius = 5m, bottom air chamber draft = 3.5, bottom water chamber draft = 5m, central column radius = 1.75m, total draft = 25.5m.

Taking into account the chosen geometric parameters, and using (2-25**)**, we can obtain the plot in Figure 2-3 representing the air volume necessary for a certain peak frequency shift. For the same set of dimensions, the corresponding hydrodynamic coefficients were computed using the commercial software WAMIT. Then the system of equations of motion was solved, in order to get the response amplitude operator (RAO) of the heaving displacement of the structure. Figure 2-4 depicts the RAOs of the structure for different values of the undisturbed volume of the air chamber.

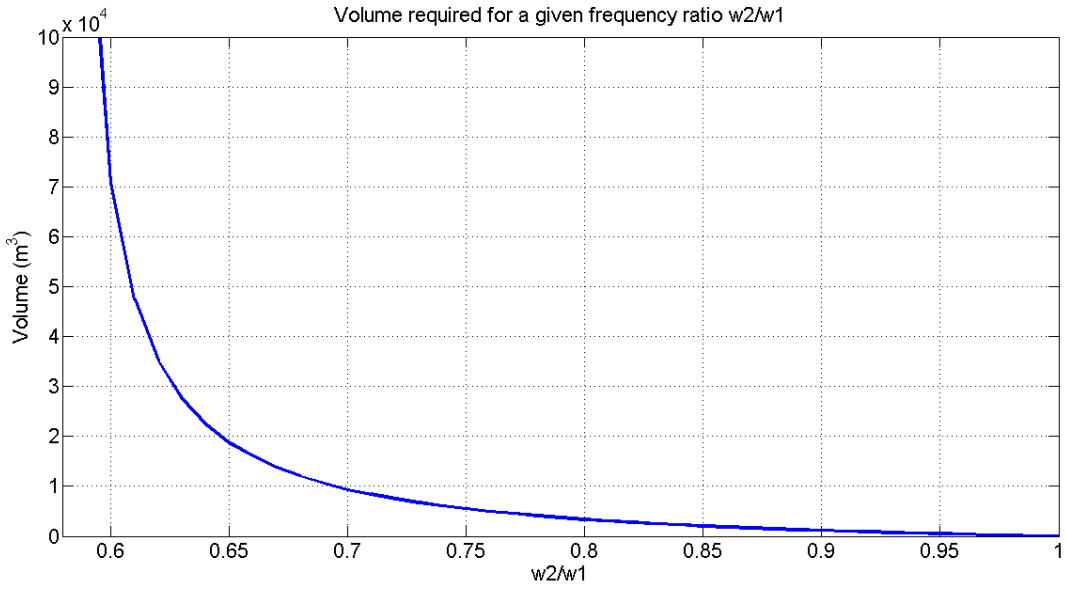

FIGURE 2-3 VOLUME REQUIRED FOR A GIVEN FREQUENCY RATIO

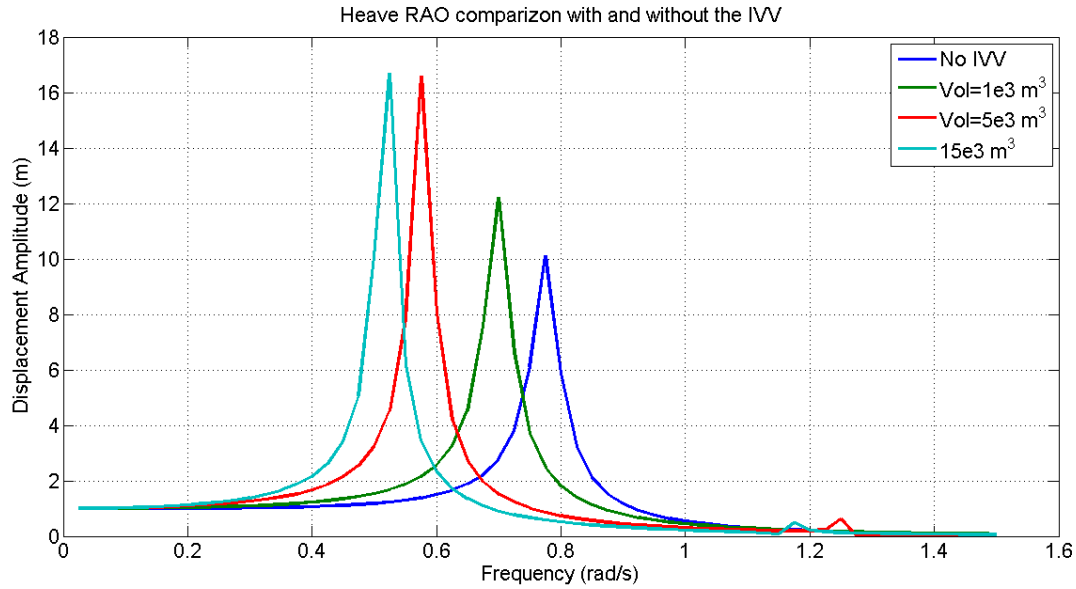

FIGURE 2-4 HEAVE RAOS COMPARISON WITH AND WITHOUT THE IVV METHOD

From Figure 2-4 it can be easily noticed that the air volume required for a resonance frequency shift that covers the total interval of the interesting frequencies, [0.66, 1] rad/s, is quite large, of about 1.6e4 m^3. For the given dimensions, the air volume in the bottom chamber is of about 280 m^3, which leads to a frequency ratio as little as 97%. If we connect the bottom chamber to the top floater, increasing the available volume to approximately 590 m^3 would lead to a ratio of 94%, which is still far from the desired value of 66%.

2.1.2. Engineering constraints and evaluation for large-scale applications

As shown in Figure 2-4, there is in fact a shift in the resonance frequency, but only for a volume of air that is too large in comparison with the bottom chamber volume, or even considering also the top floater volume. The necessary extra-volume must be provided by an extra structure. This increases the complexity of the system and its costs (financial, carbon footprint). Indeed, structural cost will increase due to the material required to accommodate the volume. Complexity will also increase due to the auxiliary equipment to ensure the sealing, and pumping functionality of the IVV method. This is likely to have a negative impact on the reliability of the entire system.

In light of these results the implementation of a negative spring effect using the IVV is not suitable for the device with 6 m radius. As we increase the size of the device the volumes increase with the cube of the scale and so the effect on a bigger WEC will have a greater impact. This aspect has to be explored in forthcoming work. An alternative approach is to look into an array of small WECs interconnected by air tubes to a common air reservoir. Both the exploitation of the IVV for larger devices and in an array will be further studied.

While the use of several chambers appear attractive to

2.2. The HNS negative spring method

Section 2.2 tackles an alternative method for negative spring effect, denoted the Hydrodynamic Negative Spring (HNS)

2.2.1. Numerical assessment of the potential of the HNS negative spring method

The Floating OWC (FOWC) is analogous to a two-body oscillating Wave Energy Converter (WEC), in that the water column acts as a second body with its own resonant frequency. If the WEC's Inner Free Surface (IFS) dimensions are significantly smaller than the wavelength of incoming waves, the second body may be modelled by a massless piston of infinitesimally small thickness placed on top of the water column, with its own set of hydrodynamic coefficients. The IFS of the water column, which is equal to the surface level when the sea is calm. The two IFS and sea surfaces will not be equal when the device is oscillating with the incoming waves.

The HNS method applied to the FOWC involves widening the tube inside the floater and filling this space with seawater on the downward cycle, and transferring the water back to the sea on the upward cycle. In doing so, the buoyancy is reduced on the downward cycle because less seawater is displaced, and increased on the upward cycle because more seawater is displaced. This concept is illustrated in Figure 2-5, where R_1, R_2, and R_{HNS} denote radii of the floater tubeset, the water column, and the expanded air chamber needed for the HNS effect, respectively:

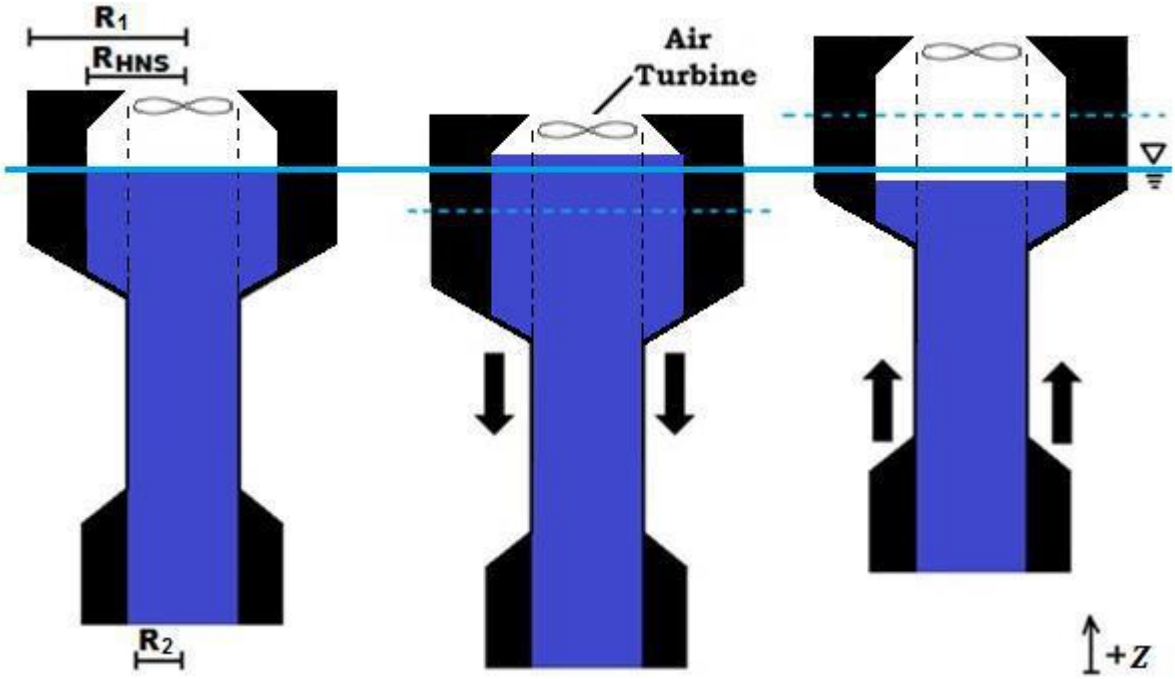

FIGURE 2-5 THE HNS METHOD APPLIED TO THE OWC SPAR BUOY.

In Figure 2-5, it should be noted that the vertical motion of the water column's IFS is much smaller than that of the WEC. This is due to the spar's bottom entrance being deep enough for the surface waves to have minor effect on its hydrodynamics.

The dotted black lines in Figure 2-5 show the dimensions of the original air chamber, proposed in WETFEET Deliverable 2.1 [1]. Due to temporary storage in the air chamber, less seawater is displaced by the WEC on its downward cycle. This reduces the buoyancy force pushing it back up. On the WEC's upward cycle, the stored seawater in its expanded air chamber is returned to the sea, freeing up more seawater volume. This increases the buoyancy force, extending the upward cycle.

When seawater fills the extra space inside the floater, the volume of the displaced water (given by Archimedes' Principle) is altered from that which is shown by Eq (C-1) (in appendix C). Therefore, the hydrostatic restoring force becomes:

$$F_{HS\,j}{}' = -\rho g V_{0j} + \rho g\{V_{0j} - SZ_j + S'(Z_j - Z_k)\} = \rho g S'(Z_j - Z_k) - \rho g S Z_j \qquad (2\text{-}26)$$

where the areas S and S' are given by,

$$S = S_1 - S_2 = \pi({R_1}^2 - {R_2}^2) \qquad (2\text{-}27)$$

$$S' = S_{HNS} - S_2 = \pi({R_{HNS}}^2 - {R_2}^2) \qquad (2\text{-}28)$$

A dimensionless factor α has defined to quantify the amount of wetted floater cross-section remaining after the HNS implementation:

$$\alpha = 1 - {S'}/{S} = \frac{S_1 - S_{HNS}}{S_1 - S_2}, \qquad (2\text{-}29)$$

where α lies on the interval $\alpha \in (0,1]$. The limit where $\alpha = 1$ represents the case with no HNS, while as $\alpha \to 0$, the WEC would come closer and closer to sinking as its calm seas waterline would rise higher and higher (assuming that the WEC's dry mass remains unchanged). There exists another practical limit

to the rising equilibrium waterline: The chamber needs enough difference in height between the water column and the air turbine, so that the turbine is not flooded when the WEC oscillates in the incoming waves.

Before simulating device performance via time-intensive CFD methods, it is desirable to use quicker and coarser Boundary Element Method (BEM) codes (e.g. WAMIT). Such codes typically assume inviscid flow, where drag is neglected. It is also of interest to initially ignore the PTO system, and to investigate the frequency response of the body motions purely due to varying degrees of the HNS effect. In neglecting viscous drag, ignoring PTO reaction, and implementing the HNS method, Eq. (C-5 & C-6) become:

$$\{-\omega^2(m_1 + A_{11}) + i\omega B_{11} + \alpha(C_1 - C_2)\}Z_1 + \{-\omega^2 A_{12} + i\omega B_{12} + (1-\alpha)(C_1 - C_2)\}Z_2 = F_{E,1} \quad (2\text{-}30)$$

$$\{-\omega^2 A_{22} + i\omega B_{22} + C_2\}Z_2 + \{-\omega^2 A_{21} + i\omega B_{21} + (1-\alpha)(C_1 - C_2)\}Z_1 = F_{E,2}\,. \quad (2\text{-}31)$$

From Eq. (2-26**)**, it is shown that the HNS method has the potential to reduce the hydrostatic restoring force on point absorbers. The device designer has the freedom to choose the magnitude of this reduction by strategically choosing the modified air chamber dimensions, as shown in Figure 2-5. The design is, of course, constrained by the need for the WEC to stay afloat: The floater supports the mass of the spar and the ballast, and by flooding an additional portion of its volume, its ability to keep the WEC afloat is reduced. The cross-sectional areas S and S' should be chosen such that the heaving oscillations are prolonged, but not to the point where the device cannot recover and float back upwards.

In addition to the reduction in the hydrostatic restoring force achieved by the HNS method, the hydrodynamic coefficients will also change because they are dependent on the device geometry – geometry that will change as the water column's IFS is expanded inside the air chamber. To investigate trends in the frequency response of the Spar Buoy to an increasing degree of IFS expansion, the WEC geometry considered by WAMIT needed to be modified.

WAMIT's higher order method relies on user-defined surface patches to represent the geometry of a floating body, done via the supplementary Fortran source code *geomxact.f*. Due to the expansion of the IFS, the interior patches representing the air chamber and water column needed to be modified, so as to re-calculate the hydrodynamic coefficients for varying degrees of HNS effect. Inside the floater, both the IFS "massless piston" patch and the cylindrical patch surrounding the water column needed to be expanded.

Once the IFS is expanded, the bottommost section of the conical connecting patch between the tube and the floater (Patch 3, negative spring case of Figure 2-6) will contain water on both of its sides. To take into account the jump in pressure between one side and the other, this section needed to be defined as a "dipole" patch. Alternatively, a finite-thickness wall patch could have been employed. In [4], it is explained that both methods lead to very similar results.

Figure 2-6 shows the configuration of Spar Buoy surface patches, both in the reference case from WETFEET Deliverable 2.1 [1], and in the new configuration that would make the HNS method possible:

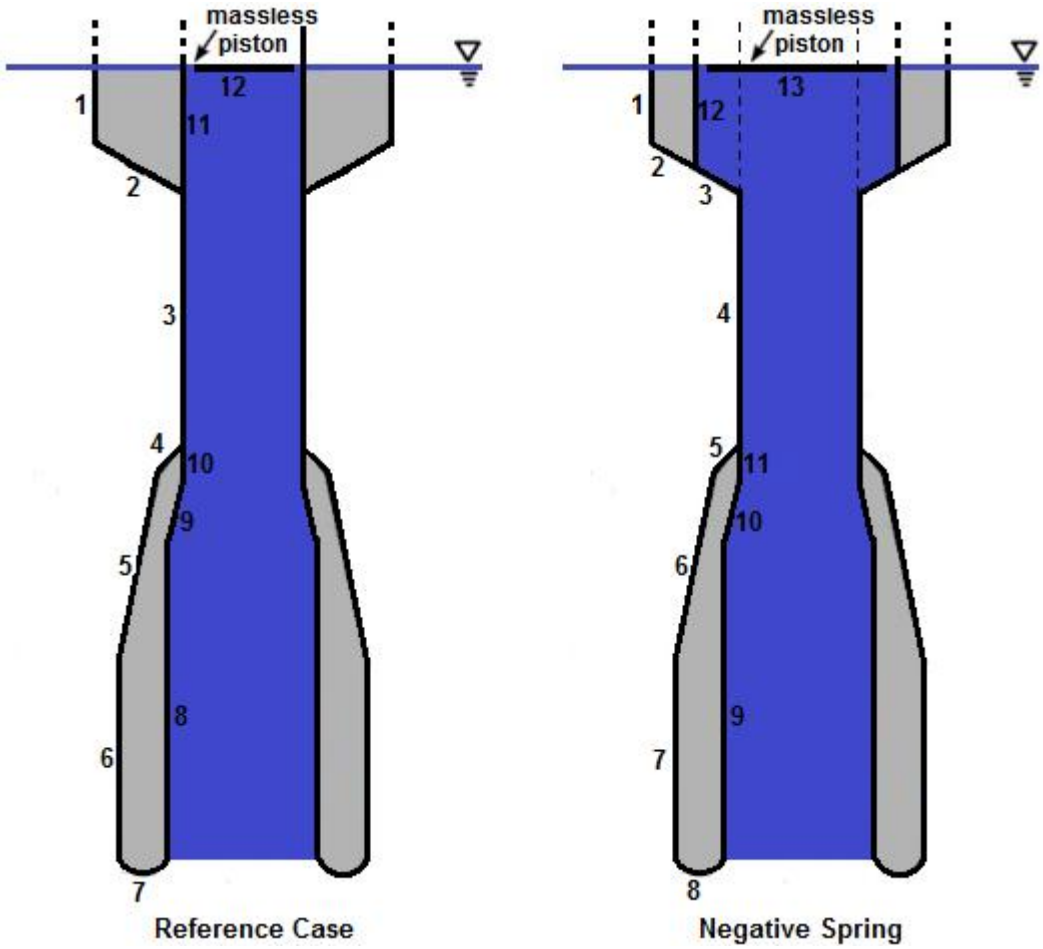

FIGURE 2-6 THE SURFACE PATCHES USED TO DEFINE THE WEC GEOMETRY IN THE HIGHER ORDER METHOD OF WAMIT.

Dipoles are those patches that are in contact with the seawater on both sides. In the negative spring case presented in Figure 2-6Figure 2-6, Patches 3 & 4 are dipoles, in contrast with the reference case, where only Patch 3 is a dipole. Patches 11 & 12 of the reference case needed to be expanded with respect to their original size to model the HNS effect.

The Spar Buoy's bi-radial turbine PTO system is non-linear [2]. As such, a frequency domain analysis on a system with a PTO could not be accurately modelled by a linear spring and damper set. But to qualitatively investigate the effect of the HNS implementation by expansion of the IFS, the frequency response of the IFS motion with respect to the floater tubeset was simulated in WAMIT, without considering the additional damping and reactance of the PTO:

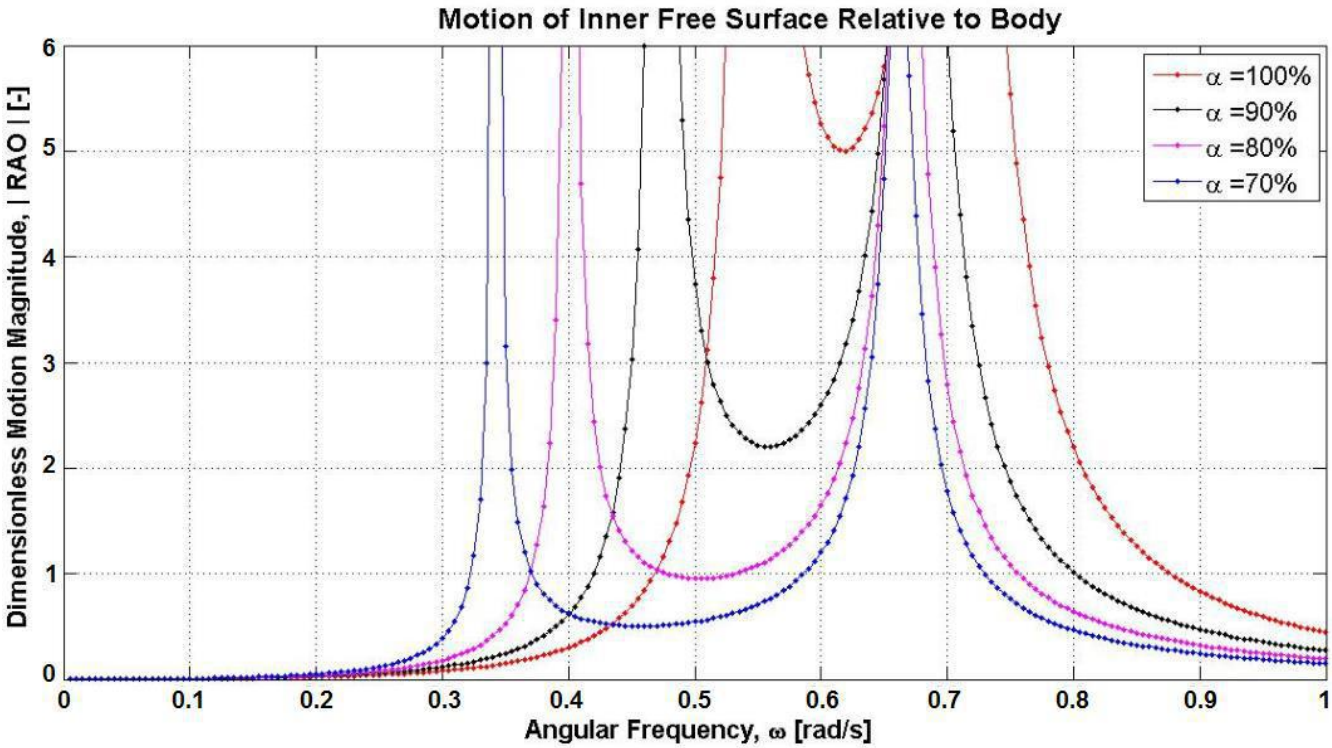

FIGURE 2-7 FREQUENCY RESPONSE OF THE IFS MOTION FOR VARYING DEGREES OF THE HNS EFFECT.

With increasing HNS effect (a decrease in the parameter α), an extension of the bandwidth and a shift in the response to lower frequencies can be observed in Figure 2-7. The height of peaks at the system resonant frequencies has no physical meaning, since viscous and PTO damping were ignored. But the experimentally obtained peaks in the response, from the same system reacting against a purely resistive PTO, would still occur in the same locations. In that case, the height of the peaks would be reduced by the presence of the increased system damping.

From the IFS relative motion shown in Figure 2-7, it is clear that the HNS method has the potential to tune the device response to the lower frequencies wave frequencies that are typically found in the ocean. In the case of Atlantic swells, where typical wave periods are in the range of 9 – 14 s (0.70 – 0.45 rad/s), a response resembling the black curve would likely be the most desirable – an increase in the air chamber radius by less than 60 cm.

Note that the power matrix of the OWC spar buoy when featuring the HNS method has been generated but due to time constraints is not going to be shown in this report. Some final verifications are necessary before releasing this information which will be made available in a future deliverable of WETFEET under WP3. This will help understanding the potential benefit in terms of net Annual Energy Production (AEP) gain and therefore in terms of volume flux through the air turbine.

2.2.2. Engineering constraints and evaluation for large-scale applications

By its nature, implementing the HNS method into a full-scale OWC spar buoy would not induce significant extra engineering challenges other than those inherently foreseen for the reference OWC spar buoy design (see Deliverable 2.1 [1] and section 1.3). Indeed, the HNS method only implies enlarging the IFS of the floater.

The manufacturing and assembly procedure might become slightly more complicated and the structural integrity may also be weakened. To mitigate these risks, further analysis employing non-linear modelling such as Computational Fluid Dynamics (CFD) and experimental testing should be done. In particular, the hydrodynamic behavior precisely where this widening of the internal diameter occurs should be studied. In turn, this would lead to the estimation of the loads experienced at this location and a structural analysis could inform what the revised specifications should be for fabrication of the unit.

Other than that, no specific machinery should be required apart from the appropriate control system instrumentation which should resemble the reference OWC spar buoy design.

As depicted in Section 2.2.1, the HNS method can be readily adapted for any 2-body floating WECs (see appendix C for analytical background). In practice, applying the HNS method appears more suitable for WECs with an IFS which oscillates primarily in heave. Investigating alternative shapes modification of the IFS may disclose other avenues of applications of the HNS to other types of WEC classes.

3. ENHANCED ADDED-MASS

The OWC spar buoy has a geometry that allows the inertia of the vertical motion dynamics to be increased by the geometrical adjustment of the OWC tube lower part (hereinafter also referred as large thickness tube (LTT)). The tuning of the mass and geometry of the LTT is a simple way to adjust the natural frequencies of the buoy and of the OWC to the frequency of the incoming waves, since it affects both the buoy own mass and the hydrodynamic added mass of the buoy and OWC. Hereby, we will refer to this advantageous effect as the enhanced added-mass (EAM). One advantage of the EAM is that the increase of the buoy and OWC masses allows the design of devices with shorter draft but with comparable hydrodynamic performance, avoiding potentially more expensive structures and allowing the deployment in a larger range of water depths. An option to apply the EAM consists of using a non-uniform cross sectional area in the OWC inner tube near the bottom part (or LTT), increasing the mass of water displaced by the device's motion without changing the OWC waterplane area (as well as the hydrostatic restoring coefficient), and without affecting the hydrodynamic performance near the free surface. Additionally, by controlling the volume of the LTT, it is possible to control the mass distribution and the device pitch/roll stability. In general, the LTT should preferably be located deep enough to reduce the interference with the radiation characteristics of the floater, which are essential to maximize power absorption in the case of heaving converters.

Ref. [4] addressed the design of the OWC spar buoy whole geometry, maximizing the annual-averaged power available to the turbine (pneumatic power). Although several optimal geometries were provided, the study considered only two heaving modes (buoy and OWC) and only three parameters for the lower part of the OWC tube. In this work, we consider that the buoy can move in surge, heave and pitch, and the OWC is restricted to heave. Since the pitch motion is considered, the device mass distribution has to be accounted for and stability has to be evaluated. The geometry optimization is specifically focused in the LTT, and therefore in the effect of EAM in the system dynamics and performance. Six design variables are considered and five objective functions are tested, which include combinations of several parameters such as the annual-averaged turbine power output, mass of the steel structure, and levelized cost of electricity.

3.1. Numerical assessment of the potential of the enhanced added-mass

3.1.1. Optimization method

The LTT optimization is focused not only on the geometrical parameters but also on the turbine and mass distribution parameters, since power extraction is very sensitive to those. Previous studies have found that a large computational time is spent in the calculation of the hydrodynamic coefficients when a boundary integral equations method (BIEM) is used [4], [49]–[51]. Since the hydrodynamic coefficients computation are only dependent on geometrical parameters, the optimization problem is

commonly divided in two different sub-problems, which reduces the overall computational time. Here, we decided to divide the optimization problem into the following two problems: (*i*) main optimization; and (*ii*) internal optimization.

Figure 3-1 shows the optimization problem scheme. The internal optimization problem is used exclusively to optimize the turbine and mass distribution parameters for a given converter geometry. This problem is part of the main optimization problem, which is only dedicated to solving the geometrical problem. Therefore, for each device's geometry, the internal optimization guarantees that the optimal turbine and mass distribution parameters are applied.

The two optimization problems and their integration are depicted in Figure 3-1. In both cases, the numerical optimization algorithm Constrained Optimization BY Linear Approximations (COBYLA) is used. This method does not require the evaluation of the objective function gradient to converge. This is an important feature because common spurious oscillations of the objective function, due to numerical approximations generate errors in the function gradient [4], [50]. The optimization algorithm COBYLA is a direct search method that performs linear approximations of the objective function and its constraints [52], [53]. Computations were performed in Python using the COBYLA algorithm from the Scipy optimization library.

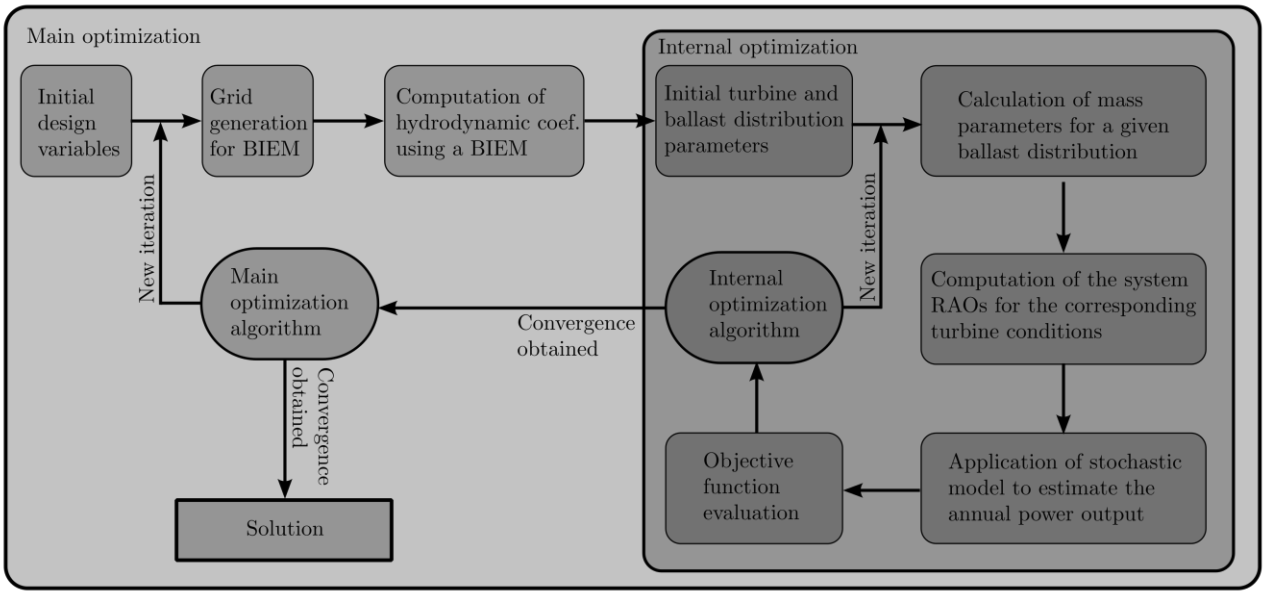

FIGURE 3-1 OPTIMIZATION SCHEME

3.1.2. Modelling the performance under irregular waves

The formulation presented here considers irrotational flow. Linear water wave theory and linear hydrodynamic interactions are considered by assuming that wave amplitude and body motions are small. Due to the OWC spar buoy axisymmetric geometry, the hydrodynamic model of an isolated device considers four oscillation modes, three for the floating structure (surge x_1, heave x_3, pitch x_5) and one for the OWC internal free surface (heave x_9). A description of the model oscillation modes can be found in Figure 3-2. The equations of motion for this system considers the wave excitation force, the wave radiation force, the hydrostatic force, the force due to the air interaction with the inner free surface and drag forces due to the viscous flow effects acting on the device hull. The wave excitation force and radiation force coefficients (added inertia and radiation damping) were computed using the boundary integral equation method (BIEM) WAMIT [54]. The BIEM requires the discretization or parametrization of the device wetted surface.

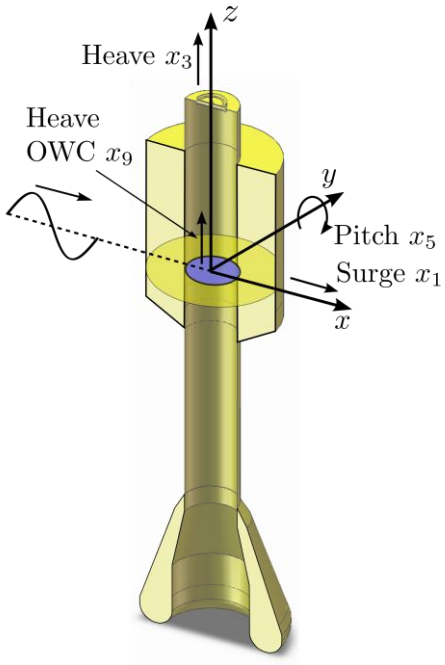

FIGURE 3-2 DESCRIPTION OF THE OWC SPAR BUOY MODEL AND OSCILLATION MODES

The dynamics of the air inside the OWC air chamber considers air as an ideal gas and the air compression/expansion inside the chamber as an isentropic processes, as proposed in [55], the mass flow rate of air through the turbine can be approximated as proportional to the relative velocity between the buoy and OWC heave ($x_3 - x_9$) and to the time-derivative of the pressure difference between the air chamber and the atmosphere (assuming that the air chamber volume variations are much smaller than the still water volume)(for details see [4]). For the linearization of the isentropic relationship, the speed of sound in air and air density can be assumed constant and equal to their values under atmospheric conditions. With the exception of very rough sea conditions, the isentropic linearized relationship provides a good approximation for the air chamber dynamics [56].

Moreover, we consider a turbine with a linear characteristic curve, i.e., with a proportional relation between the flow rate passing through the turbine and the pressure drop. As showed in [57] for an OWC spar buoy device, multi-stage Wells turbine can provide better overall performance than the single stage version. A detailed description of multi-stage Wells turbines with guide-vanes between rotors can be found in [58]. Since no data from model testing are available, it was assumed that dimensionless performance curves for a multi-stage turbine can be obtained from the curves for the corresponding single-stage turbine, as described in [57].

Considering that the model interacts with two-dimensional regular waves with amplitude A_w and angular frequency ω, travelling with the x-axis direction, and since all the forces are linear, the equations of motion can be solved in the frequency domain.

The energy extraction from the floating device under irregular wave conditions is modelled using a stochastic method, as presented in [59]. This approach applies linear response amplitude operators (RAOs) obtained from a frequency-domain model for the computation of the power extraction and analysis of statistic representative values under random wave conditions. It was assumed that a given sea state is represented by the superposition of regular wave components, each with its own amplitude, frequency and random phase angle. This assumption implies that the wave elevation can be described as a stationary, ergodic and Gaussian process. This theory, developed in [60], [61], has been applied in

a wide range of ocean engineering applications [62], [63]. For simplicity, all irregular wave sea states are defined by the semi-empirical Pierson-Moskowitz energy density spectrum S_ω, see [63].

To account for the drag forces acting on the system, we adopted the method suggested in [64] , which linearizes the drag forces using the standard deviation (root-mean-square) of the oscillatory flow velocity [62]. This approach considers that a given oscillatory velocity u follows a Gaussian probability distribution with mean zero and standard deviation σ_u. The minimization of the difference between the quadratic force (proportional to $|u|u$ and the linear approximation shows that $|u|u \approx \sqrt{8/\pi}\sigma_u u$. We consider two sources of viscous drag forces: (*i*) one force proportional to the relative velocity between the buoy and the water flow at the same vertical level as the drag-inducing surface (here we consider two drag-inducing surfaces, as in [65]); (*ii*) the other force proportional to the relative velocity between the buoy and the OWC.

The standard deviation of the device motion (surge, heave, pitch) and pressure difference can be determined through the numerical integration of the corresponding RAOs with the sea state energy density spectrum S_ω. Since the turbine has a linear characteristic curve, the power extraction can be determined from the pressure difference standard deviation (root-mean-square value). For detailed formulation, see [59]. The annual-averaged power output was determined from the representative sea states from a wave climate off the western coast of Portugal.

The levelized cost of electricity (LCOE) was estimated using a simple model based on the annual-averaged power output, the mass of steel and mass of concrete (ballast) required for the device fabrication. The LCOE model is based on the work reported in [66], [67]. The capital expenditure (CAPEX) is determined from the sum of the costs from device fabrication (steel structure, ballast and turbine), mooring system, installation, grid connection and project development. The operational costs (OPEX) are assumed to be proportional to the CAPEX yet affected by the interest rate over the project time life. The annual energy production (AEP) is determined from the values of the irregular wave model. Table 3-1 presents the parameters considered for the LCOE calculation.

TABLE 3-1 PARAMETERS CONSIDERED IN THE ESTIMATION OF THE LCOE

Parameter	Value
Project time life [years]	20
Interest rate [-]	0.15
Capacity factor [-]	0.35
Availability factor [-]	0.90
OPEX-to-CAPEX ratio [-]	0.05
Cost of steel structure per unit mass [€/kg]	3.250
Cost of concrete ballast per unit mass [€/kg]	0.04098

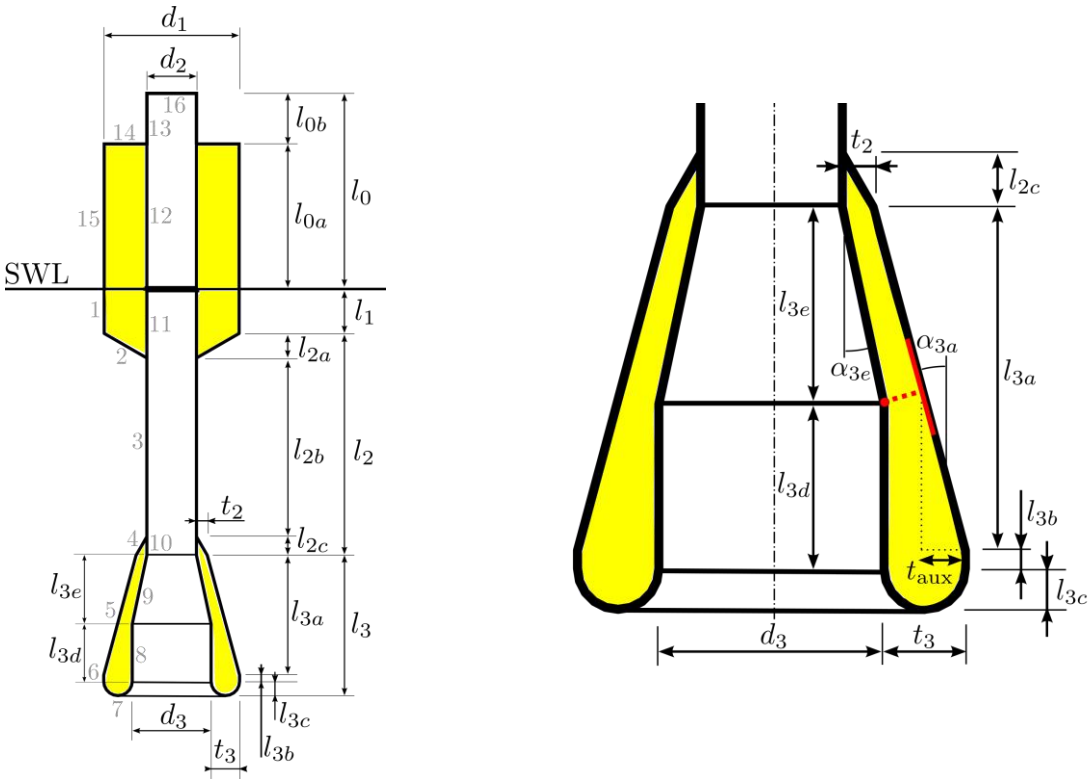

(A) (B)

FIGURE 3-3 CUT SECTION VIEW OF THE OWC SPAR BUOY GEOMETRY WITH RELEVANT DIMENSIONS: (A) COMPLETE GEOMETRY; (B) DETAILED VIEW OF THE LTT

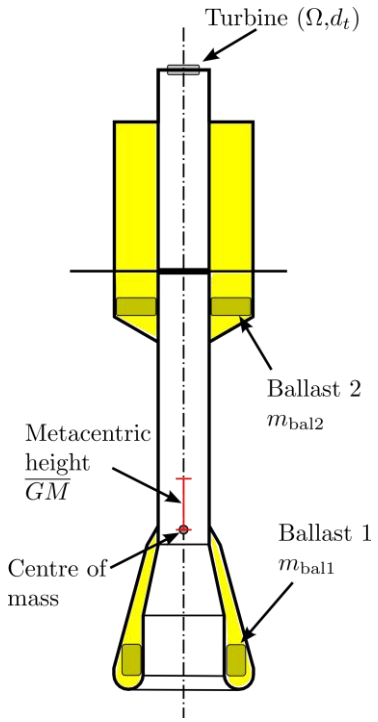

FIGURE 3-4 PARAMETERS USED IN THE TURBINE AND MASS DISTRIBUTION OPTIMIZATION (INTERNAL OPTIMIZATION PROBLEM)

3.1.3. Mass distribution and stability considerations

The OWC spar buoy mass distribution is determined by considering the geometry presented in Figure 3-3(A). The buoy geometry consists in a set of 16 surfaces with simple shapes (cylindrical, conical, annular, toroidal). We assumed that those surfaces represent steel plates with constant thickness. Each surface was parameterized and the surface area, mass, centre of mass and moment of inertia were determined. The total steel structure mass m_{stl}, z-coordinate of the centre of mass and moment of inertia were determined using the parallel axis theorem. The device total mass m_1 is computed from the displaced water volume. Therefore, the mass of ballast is given by

$$m_{\mathrm{bal}} = m_1 - m_{\mathrm{stl}} \,. \tag{3-1}$$

We consider that the ballast can be located in two vertical positions (z_{bal1} and z_{bal2}) in the buoy to allow the control of metacentric height, as presented in Figure 3-4, therefore $m_{\mathrm{bal}} = m_{\mathrm{bal1}} + m_{\mathrm{bal2}}$. The lower possible vertical position of the centre of mass occurs when the ballast is entirely at the lower position (ballast 1), which corresponds to the maximum metacentric height ($\overline{GM}_{\mathrm{max}}$). The higher possible vertical position of the centre of gravity occurs when the minimum value of the metacentric height is reached. The minimum value of the metacentric height ($\overline{GM}_{\mathrm{min}}$) is predefined to guarantee stability. Note that, if the metacentric height is lower than its minimum value, the geometry is not feasible since it does not have the minimum stability characteristics. Thus, a smaller steel thickness should be considered.

For optimization purposes, we define the dimensionless parameter c_m, which is used to control the metacentric height $\overline{GM}$

$$c_m = \frac{\overline{GM} - \overline{GM}_{\mathrm{min}}}{\overline{GM}_{\mathrm{max}} - \overline{GM}_{\mathrm{min}}} \tag{3-2}$$

where c_m can take values between 0 and 1, which guarantees that $\overline{GM}$ is always within acceptable values ($\overline{GM}_{\mathrm{min}} < \overline{GM} < \overline{GM}_{\mathrm{max}}$).

By knowing c_m, it is possible to determine the device centre of mass z-coordinate, the fraction of ballast in the bottom part of the device and the moment of inertia at the device.

The stability of the device can be evaluated by its metacentric height $\overline{GM}$. In this model we impose that the metacentric height is above a minimum value. However, spar-type structures are typically prone to parametric resonance problems (dynamic instability) [10], which results in large undesirable pitch/roll motions [68]. The problem can be mitigated by introducing pitch/roll damping equipment on the buoy [69] or by avoiding being near to the following condition [70],

$$T_{n5} = 2T_{n39} \,, \tag{3-3}$$

where T_{n5} is the buoy's pitch natural period and T_{n39} is the buoy-OWC combined heave natural period. In this case, the buoy-OWC combined heave natural period was used instead of the buoy's heave natural period since the most critical situation occurs when the air chamber is closed (for turbine protection) and the buoy and the OWC move together as a single body, with a resonance period around T_{n39}.

Ideally, the effect of parametric resonance on the device dynamics should be accounted for by a model that measures the instantaneous variations of the buoyancy and wave forces on the device's hull (see e.g. [70]). However, since the model adopted here does not allow such detail, we decided to design the device by simply avoiding the condition shown in Eq (3-3). In the case of typical OWC spar buoy geometries, increasing T_{n5} excessively to guarantee that it stays above $2T_{n39}$, results in very small $\overline{GM}$. Therefore a balance between $T_{n5}$and $2T_{n39}$ must be found. Here, we decided to avoid parametric resonance by designed the device according to the following condition

$$T_{n5} = 2.2T_{n39} \,. \tag{3-4}$$

3.1.4. Geometry optimization results

The results presented in this section were obtained using the methodology described previously. In all optimizations, the initial geometry is the 12 m diameter and 36 m draft buoy reported in [71]. Table 3-2 shows the parameters used in the modelling of the device dynamics.

TABLE 3-2 PARAMETERS USED IN THE MODELLING OF THE OWC SPAR BUOY DYNAMICS

Parameter	Value
Water depth [m]	80
Water density [kg/m³]	1025
Air density [kg/m³]	1.2041
Steel density[kg/m³]	7800
Steel thickness [m]	0.015
Turbine coefficient [-]	0.68
Number of turbine stages	3
Turbine maximum tip speed, $V_{\text{tip,max}}$ [m/s]	180
Surge natural period [s]	100
Minimum metacentric height $\overline{GM}_{\text{min}}$ [m]	1.5

The main optimization problem considered six variables (design parameters), all being dimensions of the LTT ($l_3, d_3, t_2, t_3, l_{3a}, l_{3e}$). Table 3-3 shows the six geometrical design parameters and their lower and upper bounds. In order to avoid undesirable or unrealistic geometries, the five inequality constraints presented in Table 3-4 were considered. The three first inequalities refer to the angles of the conical surface (see Figure 3-3(B)), which were limited to a maximum angle of 15 deg to avoid flow separation effects under decelerating flow conditions. Those angles can be determined from the dimensions of the LTT. The fourth inequality avoids the interception of the inner and outer surface, as described in Figure 3-3(B), where t_{aux} is determine from the dimensions of the LTT. The fifth inequality guarantees a minimum value for the length of the small thickness tube.

TABLE 3-3 DESIGN PARAMETERS CONSIDERED FOR THE GEOMETRY OPTIMIZATION OF THE OWC SPAR BUOY LTT (MAIN OPTIMIZATION PROBLEM)

Design parameter	Initial guess	Lower bound	Upper bound
$\frac{l_3}{l_2 + l_3}$	0.36925	0.20	0.80
$\frac{d_3}{d_2}$	1.48699	1.00	2.00
$\frac{t_{23}}{d_2}$	0.19926	0.10	0.50
$\frac{t_3}{d_2}$	0.62830	0.10	0.50
$\frac{l_{3a}}{l_{3a} + l_{3b}}$	0.95000	0.05	0.95

$\frac{l_{3e}}{l_{3d}+l_{3e}}$	0.55562	0.05	0.95

TABLE 3-4 DESIGN PARAMETERS OF THE GEOMETRY OPTIMIZATION OF THE OWC SPAR BUOY LTT (MAIN OPTIMIZATION PROBLEM)

	Constraint	Units
1	$\alpha_{3a} > 0$	deg
2	$\alpha_{3a} < 15$	deg
3	$\alpha_{3e} < 15$	deg
4	$t_{aux} < t_3$	-
5	$l_{2b} > d_2/4$	-

The internal optimization problem is dedicated to solving the optimal mass distribution and turbine parameters. Table 3-5 displays the parameters used in the internal optimization, namely the turbine rotational speed Ω, turbine diameter d_t and metacentric height coefficient c_m. The lower and upper bounds are presented as well as the initial guess used to start the optimization process. In this case, two constraints were considered, as shown in Table 3-6. The first constraint (inequality) represents a limitation in the maximum turbine tip speed to avoid undesirable flow compressibility effects on the blades. The second constraint (equality) refers to the empirical condition derived to avoid parametric resonance, as indicated in Eq. (3-4).

TABLE 3-5 DESIGN PARAMETERS OF THE TURBINE AND MASS DISTRIBUTION OPTIMIZATION (INTERNAL OPTIMIZATION PROBLEM)

Parameter	Initial guess	Lower bound	Upper bound
Ω [rad/s]	130.0	40.0	300.0
d_t [m]	2.00	0.75	3.50
c_m [-]	0.10	0.00	1.00

TABLE 3-6 CONSTRAINTS OF THE TURBINE AND MASS DISTRIBUTION OPTIMIZATION (INTERNAL OPTIMIZATION PROBLEM)

	Constraint	Units
1	$\Omega\frac{d_t}{2} < V_{\text{tip,max}}$	-
2	$T_{n5} = 2.2T_{n39}$	-

TABLE 3-7 OBJECTIVE FUNCTIONS OF THE FIVE OPTIMIZATION RUNS (WITHOUT PENALTY FUNCTIONS)

	Description	Objective function

1	Annual-averaged turbine power maximization	$-\frac{\bar{P}_{t,\mathrm{ann}}}{\bar{P}_{\mathrm{ref}}}$
2	Annual-averaged available power maximization	$-\frac{\bar{P}_{\mathrm{avai,ann}}}{\bar{P}_{\mathrm{ref}}}$
3	Annual-averaged turbine power per steel mass maximization	$-\frac{\bar{P}_{t,\mathrm{ann}}}{m_{\mathrm{stl}}}\frac{m_{\mathrm{ref}}}{\bar{P}_{\mathrm{ref}}}$
4	Annual-averaged turbine power per total mass maximization	$-\frac{\bar{P}_{t,\mathrm{ann}}}{m_{1}}\frac{m_{\mathrm{ref}}}{\bar{P}_{\mathrm{ref}}}$
5	Levelized cost of electricity minimization	$\frac{C_{\mathrm{LCOE}}}{C_{\mathrm{LCOE,ref}}}$

Here, we consider five different optimization runs. In each optimization, a different objective is considered. The same design parameters and constrains are kept unchanged for all optimizations. Table 3-7 shows a description of the optimization objective and of the objective function. Note that the optimization is always solved though the minimization of the objective function, therefore the objective function f has to be formulated adequately.

The objective function f is affected by two penalty functions used to mitigate large surge and pitch motions (undesirable motions), which are not represented in the objective function in Table 3-7. Those functions evaluate the annual-averaged standard deviation value of surge and of pitch and penalize the objective function accordingly. A tuning factor can be adjusted to balance the weight of each penalty function.

The optimization results are presented in Table 3-8, Table 3-9, and in Figure 3-5.

Table 3-8 presents the design parameters of each optimization run. The values of the original geometry (12 m diameter and 36 m draft buoy reported in [71] are also presented for comparison (optimization 0). These values were used as the initial guess for each optimization run. The comparison between the initial and optimized geometry can be found in Figure 3-5. As observed, each optimizations shows very different results.

TABLE 3-8 OPTIMUM DESIGN PARAMETERS FOR THE FIVE OPTIMIZATION RUNS AND INITIAL GEOMETRY DIMENSIONS

Optim.	l_3 [m]	d_3 [m]	t_2 [m]	t_3 [m]	l_{3a} [m]	l_{3e} [m]	Ω [rad/s]	d_t [m]	c_m [-]
0	11.447	7.164	0.960	3.027	9.437	5.519	135.9	2.135	0.0841
1	10.492	7.625	1.306	2.258	8.789	6.414	160.5	1.916	0.1129
2	11.323	7.713	1.117	2.264	9.681	6.638	151.0	1.948	0.1159
3	6.200	7.382	2.317	2.317	4.789	4.789	196.6	1.682	0.1060
4	13.782	8.680	0.482	1.174	12.535	7.206	150.5	1.950	0.2507
5	7.236	7.551	1.976	2.174	5.841	5.099	192.1	1.705	0.1151

Table 3-9 shows results for the each optimization and results for the initial geometry (optimization 0). The value of the objective function f is compared with the initial value for each optimization (value in parenthesis). The difference found between the annual-averaged power available reported in [71] and the one presented in Table 3-9 is related with the used of drag forces in the model presented here, which

were chosen to provide a relative importance to the drag forces in the system dynamics. The relative difference in the annual-averaged power output is about 15%.

The maximization of the turbine power output (optimization 1) exhibits an improvement of 3.2%, when compared with the original geometry. The geometry displays some differences which are reflected in the decrease of the total buoy mass. The natural heave period decreases approximately 6%.

The maximization of the annual-averaged power available (or pneumatic power, optimization 2) presents an improvement of 2.4%, when compared with the original geometry. The geometry parameters show the smaller differences in all optimizations when compared with the original geometry. This was somehow expected since the original geometry was optimized with the same objective. It is also worth to notice that optimizations 1 and 2 display similar results.

The maximization of the annual-averaged turbine power per unit steel mass of the floating structure was carried out in optimization 3. The results show an improvement in annual-averaged turbine power output but with values smaller than optimization 1 and 2, as expected. The LTT length shows a reduction when compared with the original geometry, reducing the overall device surface area and therefore steel mass, without compromising excessively the power extraction.

The maximization of the annual-averaged turbine power per unit device total mass (optimization 4) exhibits a decrease of the annual-averaged turbine power output. From Figure 3-5, we observe that the optimization converged to a very thin geometry to minimize the device total mass. The device total mass decreased 37%, and as a consequence, the natural heave period decreasing about 14%. The inner and outer surface of the LTT are almost in contact, i.e., in the limit of constraint 4 from Table 3-4.

The minimization of the LCOE (optimization 5) shows values similar to the maximization of the annual-averaged turbine power per unit steel mass (optimization 3).

TABLE 3-9 SUMMARY OF THE FIVE OPTIMIZATION RESULTS

Optim.	Eval.	m_1 [t]	m_{stl} [t]	T_{n3} [s]	$\bar{P}_{t,\text{ann}}$[kW]	$\bar{P}_{\text{avai,ann}}$ [kW]	f [-]
0	-	1217.3	252.2	9.08	86.2	50.7	-
1	83	1084.7	246.3	8.52	88.3	52.3	-0.5101 (-0.4948)
2	108	1080.8	248.9	8.56	88.3	52.1	-0.8613 (-0.8412)
3	127	1057.0	234.1	8.29	88.2	52.5	-0.5421 (-0.4866)
4	109	762.3	251.5	7.81	84.1	50.0	-0.7715 (-0.4928)
5	144	1035.2	236.0	8.25	87.9	52.3	1.743 (1.896)

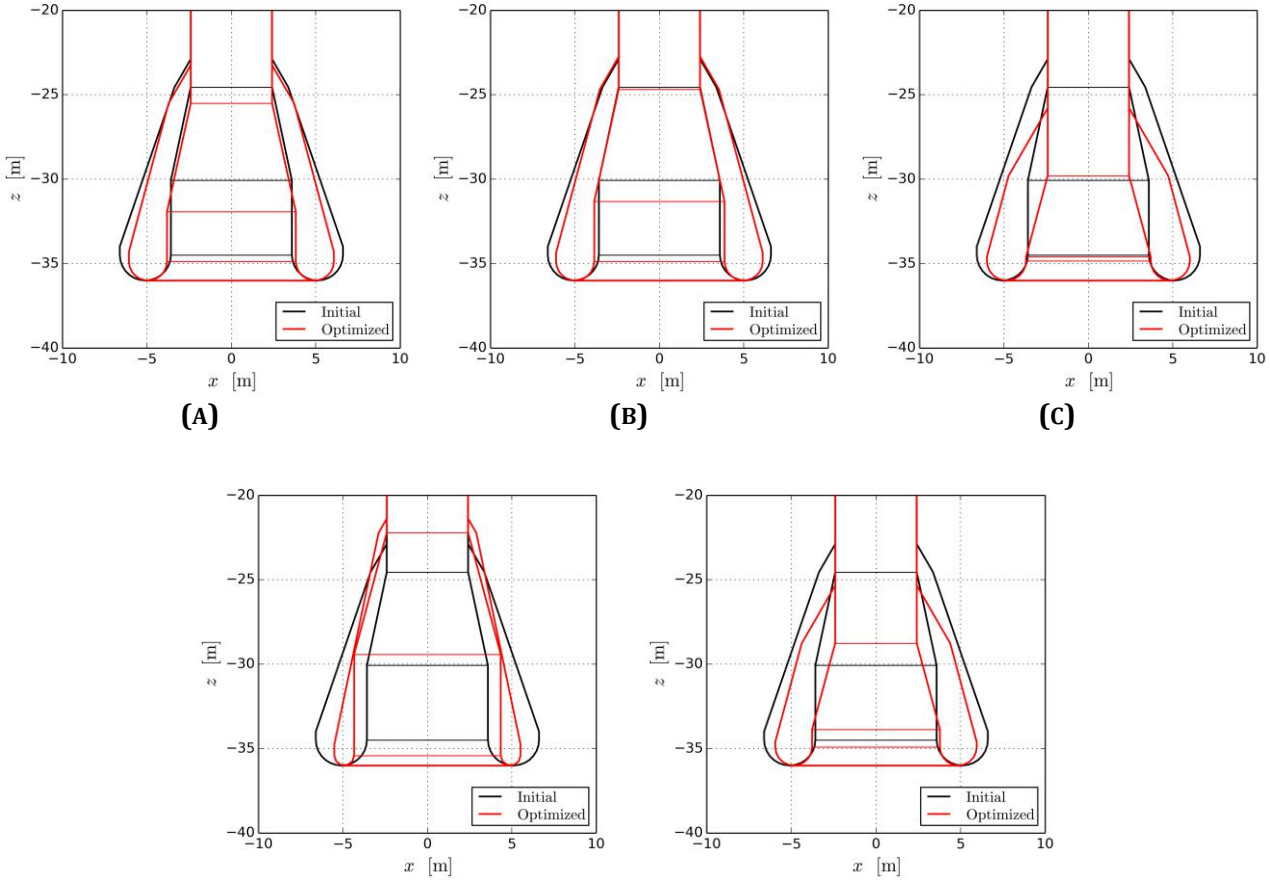

FIGURE 3-5 OPTIMIZATION RESULTS WITH COMPARISON BETWEEN THE INITIAL GUESS AND THE OPTIMIZED LTT GEOMETRY, FOR ALL OPTIMIZATION RUNS: (A) OPTIMIZATION 1; (B) OPTIMIZATION 2; (C) OPTIMIZATION 3; (D) OPTIMIZATION 4; (E) OPTIMIZATION 5

3.1.5. Concluding remarks

We developed an optimization method to design the shape of the OWC spar buoy lower tube, the large thickness tube. This part of the device is responsible for the enhanced added mass effect characteristic. Several optimizations runs, with the same design parameters and initial conditions but with different objectives, were computed. The converter performance under irregular sea states with several degrees of freedom is modelled in the framework of linear wave theory. The turbine parameters and the ballast distribution on the device are also optimized. Six geometrical parameters are considered for the large thickness tube optimization.

Five optimal geometries, corresponding to five different optimization objectives are presented. All calculations consider the geometry from a previous work as the starting point for the optimization process. The maximization of the annual-averaged turbine power output and the maximization of the annual-averaged available power provide similar results. The power improvements, when compared with the original geometry, are 3.2% and 2.4%, respectively. Similar results are also found when the maximization of the annual-averaged turbine power per unit steel mass and the minimization of the levelized cost of electricity. This suggests that the minimization of the steel structure mass, while maintaining a reasonable performance, may be a simple design criterion. When compared with the original geometry, the maximization of the annual-averaged turbine power per unit steel mass exhibits a decrease in steel mass of 7% and an increase of 3.2% in power output. Results also show that

maximization of the power output per unit total device mass may not be an adequate design criterion, since it places much relevance in the mass of the ballast, which have a much lower cost than steel.

3.2. Engineering constraints and evaluation for large-scale applications

3.2.1. Engineering considerations for full-scale deployment

The results presented in Section 3.1, shows that the performance between the optimized original geometry reported in [4] and the geometry obtained with the new and more detailed optimization method improved marginally. This may suggest that the performance is not very sensitive to the LTT geometry and therefore less costly or more practical designs (e.g., concerning the manufacturing process) can be considered for a full scale deployment.

As previously described, the LTT geometry influences several aspects of the device dynamics, affecting the device performance in different ways. On one side, the LTT geometry affects the device dynamics in heave, providing the so called EAM effect. The geometrical characteristics and size for the LTT provide advantageous inertia characteristics that result in a power extraction enhancement when compared with similar devices with the same draft. On the other side, the LTT geometry also affects the device own mass distribution, more specifically the range of possible mass distributions that the device can tolerate. Mass distribution is particularly important for the roll/pitch dynamics, as it influences the device stability and the natural roll/pitch periods. In general, roll/pitch motion should be minimized to avoid negative impact on power extraction and an over-designed structure. In spar-type devices, as the one considered here, parametric resonance is also a common problem that can be minimized with a correct mass distribution. Since the LTT geometry affects several factors in the device dynamics it is very important to address this problem with an integrated design approach.

Another point that should be highlighted and could be considered for the full scale device is the possibility of including appendages to reduce large roll/pitch motions. The structural design of spar-type converters is especially sensitive to the maximum heel angle, and therefore reducing its value can provide a reduction in the steel structure mass even if this includes adding other components. The undesirable large roll/pitch motions that can be triggered by parametric resonance (see [68], [70]), have the potential to be reduced by including vertical fins on the exterior surface of the converter. An initial study showed that the application of the fins on an OWC spar buoy reduces the device motions [69]. However, the effectiveness of this equipment still needs to be tested under a larger range of wave conditions, including extreme ones. An example of these fins is presented in Figure 3-6. By placing the fins vertically, they yield small influence on the heave motion.

One of the underlying assumptions considered for the LTT optimization was that the power take-off system (turbine-generator set) is operating in a passive way, i.e., working as if it was a damper and not affecting the resonance frequency of the system (although the air compressibility effect can slightly shift it). This does not mean that the turbine is not being controlled to keep the system under optimum damping level, just that the system is not able to change its dynamic characteristics (as in reactive control). This way, the device only responds efficiently to a limited range of wave frequencies and the LTT geometry was optimized based on this condition. Therefore, the applications of control strategies that are able to change the dynamic characteristics of the device (e.g. reactive control, latching control) are not likely to improve the performance of this particular optimized device for the same wave conditions. Novel or adaptive control strategies should be re-designed or developed.

As discussed above, the LTT shape presents several engineering issues that affect the device normal operation. However, the LTT shape may also present implications on engineering issues related with manufacturing, installation and operation & maintenance. Manufacturing can be simplified and the associated costs reduced if cylindrical surfaces are preferred to conical surfaces. If appendages (e.g. fins) are applied on the LTT, the manufacturing complexity may increase. As previously identified, the LTT shape affects the device mass distribution. In this line of thought, the LTT may have an impact on the

transport and installation operations, since these are directly affected by the mass distribution. In general, if the device is transported horizontally with the ballast installed, a decrease of the LTT volume would represent an increase of buoyancy modules used for those activities. The mass distribution may also have a significant impact on operation and maintenance activities, especially if a low metacentric height design is considered. The necessity of taking additional equipment into the converter deck may reduce the metacentric height into unreasonably low values, and the device stability can become compromised.

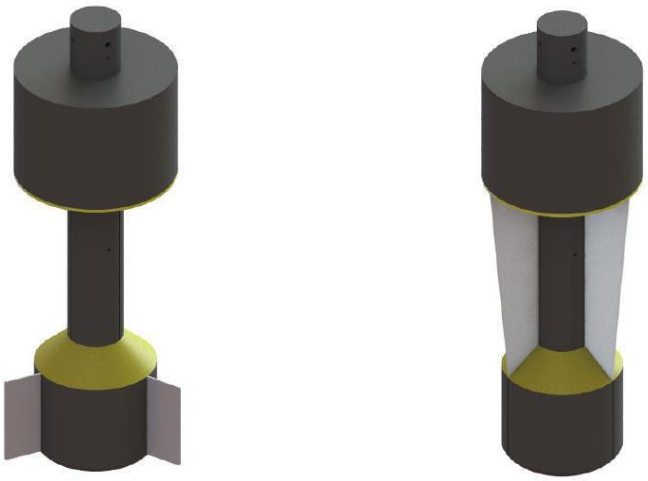

(A) (B)

FIGURE 3-6 EXAMPLE OF TWO POSSIBLE FINS CONFIGURATIONS FOR THE REDUCTION OF PITCH/ROLL MOTIONS

3.2.2. Recommendations for future work

In this work, we used the initial 12 m diameter OWC spar buoy and optimized the LTT geometry in more detail and considered also the effect of the mass distribution in the device dynamics. The improvements were marginal. However, it is worth noticing the limitations of the optimization algorithm. COBYLA searches for the optimum point taking the initial guess as the starting point. Depending on the objective function, the algorithm can tend to the closest local minimum/maximum near the initial guess. Therefore, expanding the search domain can provide us a better solution. Two options to circumvent this problem consist in either testing different initial guesses (LTT geometries) with the same algorithm or by using an algorithm that is not prone to converge into local minima/maxima, e.g. a genetic algorithm. Both solutions require a considerably larger computational effort.

In Section 3.1, we assumed that the thickness distribution was constant for all steel plates. However, this is not likely to be the final configuration determined from a detailed structural analysis. Future optimizations of the LTT should include an updated thickness distribution. The impact of this modification in the model presented in Section 3.1 should be relevant in the mass distribution (pitch motions) but not in the power performance since the ballast should be adjusted accordingly to mass of the new steel structure, so that the total mass of the device is kept unchanged.

In the geometry optimization method presented in Section 3.1, some factors may have been disregarded, namely factors that were not directly related with the mass of the device or its annual averaged power extraction. Some examples may be constraints in the geometry to ease installation and maintenance operations, or the manufacturing process (e.g. limit the number of conical surfaces).

Future work should also focus on more precise method to determine the optimum mass distribution. This may be a complex problem to solve since there is no ideal solution. On one side, a large metacentric height corresponds to an undesirable low natural roll/pitch period and the device is prone to parametric

resonance (dynamic instability). On the other side, a small metacentric height may compromise the device stability. Therefore it is important to develop methods to detect and evaluate the occurrence of these dynamic instabilities. Such method has to be capable of computing the instantaneous hydrostatic force and incident wave forces on the device wetted surface (see e.g. [70]). The same numerical model could also be used to evaluate efficiency of fins [69] and the device performance under extreme wave conditions.

The hydrodynamic analysis was based on the potential flow solvers, therefore neglecting the influence of viscous flow drag effects. Although empirical formulas were applied in the equation of motion to simulate approximately those effects (especially on the inner and outer surfaces of the LTT), more precise methods could provide better results. Experimental tests or computational fluid dynamic (CFD) calculations could provide a better insight on the phenomena.

4. SUBMERGENCE AS A SURVIVABILITY STRATEGY

In this section, the analysis of the submergence as a survivability strategy for the OWC spar buoy is presented. At first, the switch from operational (floating) to survival (submerged) configuration is not part of this preliminary study, only the submerged configurations are investigated. However, section 4.1.3 engages with the engineering analysis of the submergence process. Discussions related to the potential challenges associated with this submergence procedure are also included in the next section.

4.1. Numerical assessment of the potential of the submergence as a survivability strategy

After some initial discussions within the consortium of the WETFEET project, it was decided to consider the OWC spar buoy in a fully horizontal position when being submerged. Given the relative high draft of the OWC spar buoy in relation to the water depth considered for the reference design case (80 meters water depth), it seems more appropriate to bring the OWC spar buoy in a horizontal position while being submerged. This would allow higher submergence depth to be reached while mitigating the risk of collision with the seabed. It is also believed that such a position will prevent the buoy from having large movements in survival conditions, and that there will be little pressure variations along the structure.

Four different submergence depths have been taken into consideration: 1/3, 1/2, 2/3 and 3/4 of the water depth. At a later stage, an inclination of the buoy from its purely horizontal configuration may be introduced for both static and dynamic stability reasons.

4.1.1. Frequency-domain analysis

As previously mentioned, the depths at which the OWC spar buoy was located for this submergence study were respectively 26.67, 40, 53.33 and 60m below the Still Water Line (SWL). Figure 4-1 presents the horizontal configuration of the OWC spar buoy as simulated in WAMIT.

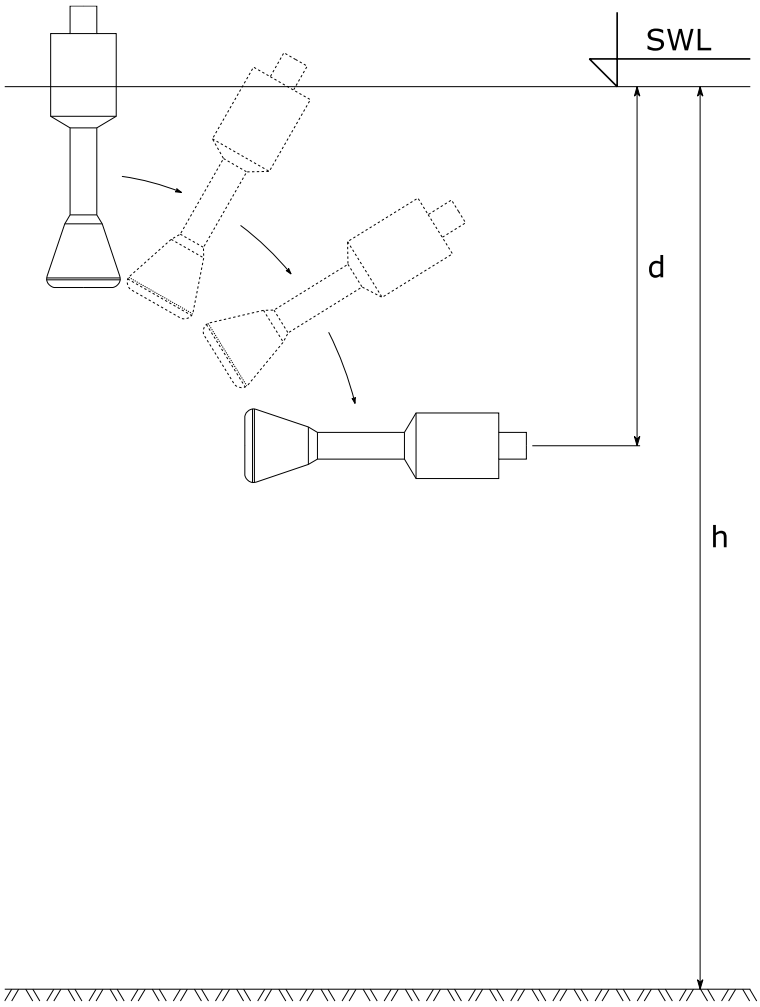

FIGURE 4-1 REPRESENTATION OF THE SUBMERGED HORIZONTAL OWC SPAR BUOY. THE MEAN WAVE-DIRECTION COMES FROM THE LEFT TO THE RIGHT OF THE FIGURE

EXCITATION FORCES AND MOMENTS

In the frame of these simulations, the buoyant part of the buoy is assumed to be filled with sea water. Though the analysis in WAMIT does not give many insights on the dynamic behaviour of the study, it gives the possibility to assess the evolution of the excitation forces depending on the depth at which the WEC is located.

Excitation forces and moments for the surge, heave and pitch modes are shown in Figure 4-2 and Figure 4-3, respectively.

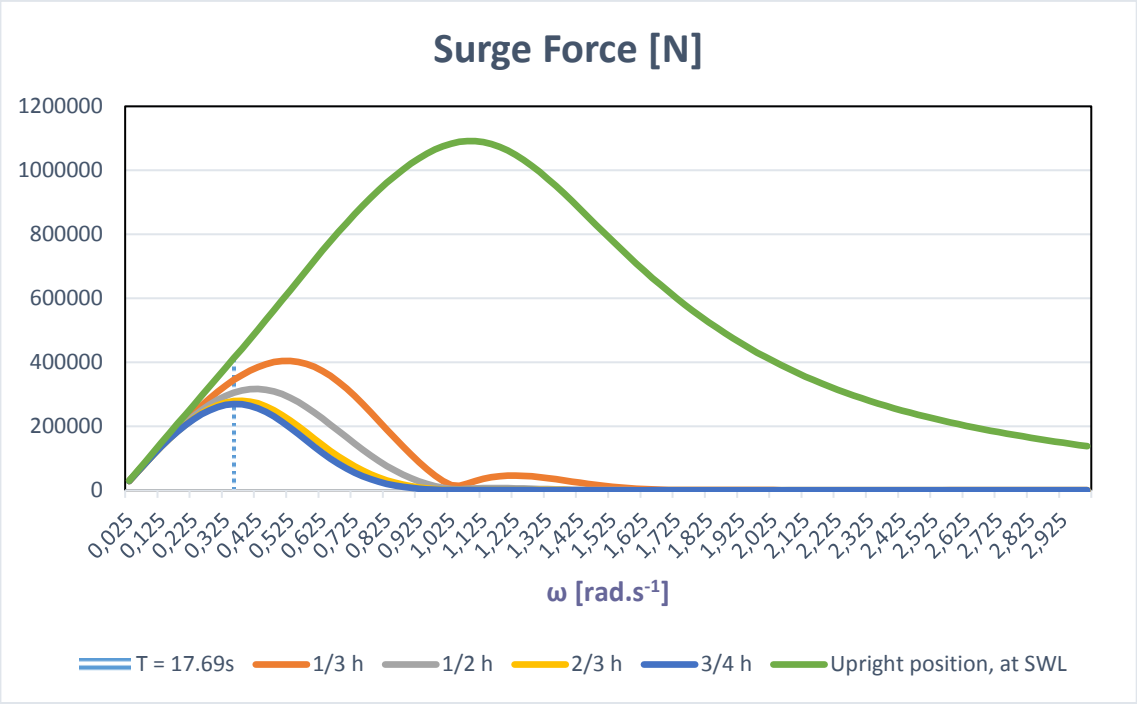

FIGURE 4-2: SURGE EXCITATION FORCE EVOLUTION WITH DEPTH, COMPARED TO THE UPRIGHT POSITION

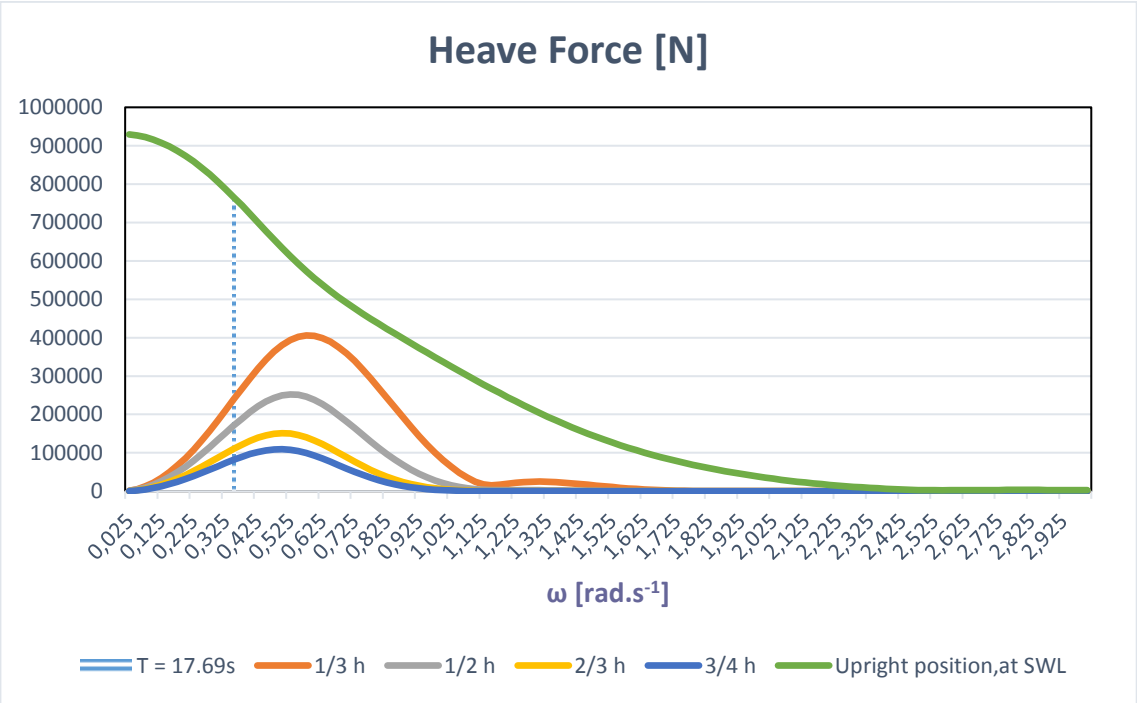

FIGURE 4-3: HEAVE EXCITATION FORCE EVOLUTION WITH DEPTH, COMPARED TO THE UPRIGHT POSITION

The submergence tests show a general reduction in the excitation forces and moments as the OWC spar buoy goes deeper under the SWL. This is expected as the hydrodynamic pressure decreases exponentially with the depth. However, if such a configuration is selected, a balance should be found

between the excitation forces reduction and the increase of static pressure, as the latter might impact the OWC structural design.

Looking at the whole frequency range simulated in WAMIT, there is a significant difference in the surge excitation force between the OWC spar buoy upright position and the submerged ones. Indeed, he maximum occurs around 1.125 rad.s-1 (approx. 5.6s), whereas it lowers to a frequency of 0.55 rad.s-1 (approx. 11.4s) for the first submergence test and goes down to 0.375 rad.s-1 (approx. 16.8s) for the deepest configuration. The corresponding maxima also decrease, passing from 1.09MN to 404kN at d = 1/3h and 269kN at d = 3/4h for a unit amplitude wave. This is also due to the fact that there is less surface exposed to the surge force as the OWC was rotated by 90º. When checking the period studied for the extreme hydrodynamic loads, the difference in excitation force between the upright position and the subsequent submerged configurations varies from 15% for d = 1/3h to 35% for d = 3/4h.

In the case of the heave excitation force, a net decrease can also be observed, which is even more significant as the submergence depth increases. The curves shape of the submerged configurations differs from the upright position as the OWC does not pierce the free-surface anymore. As in the surge case, the force maxima frequencies decrease with the depth, and their values also lower, starting at 400kN for d = 1/3h to reach a value of 108kN. This is interesting as such reductions are likely to have a beneficial impact on the OWC motions in survival mode. At the period used for the extreme hydrodynamic loads computation, these submerged configurations could represent advantages as the excitation force reduces from approx. 744kN for the upright position to 239kN for d = 1/3h, and to 89kN for d = 3/4h.

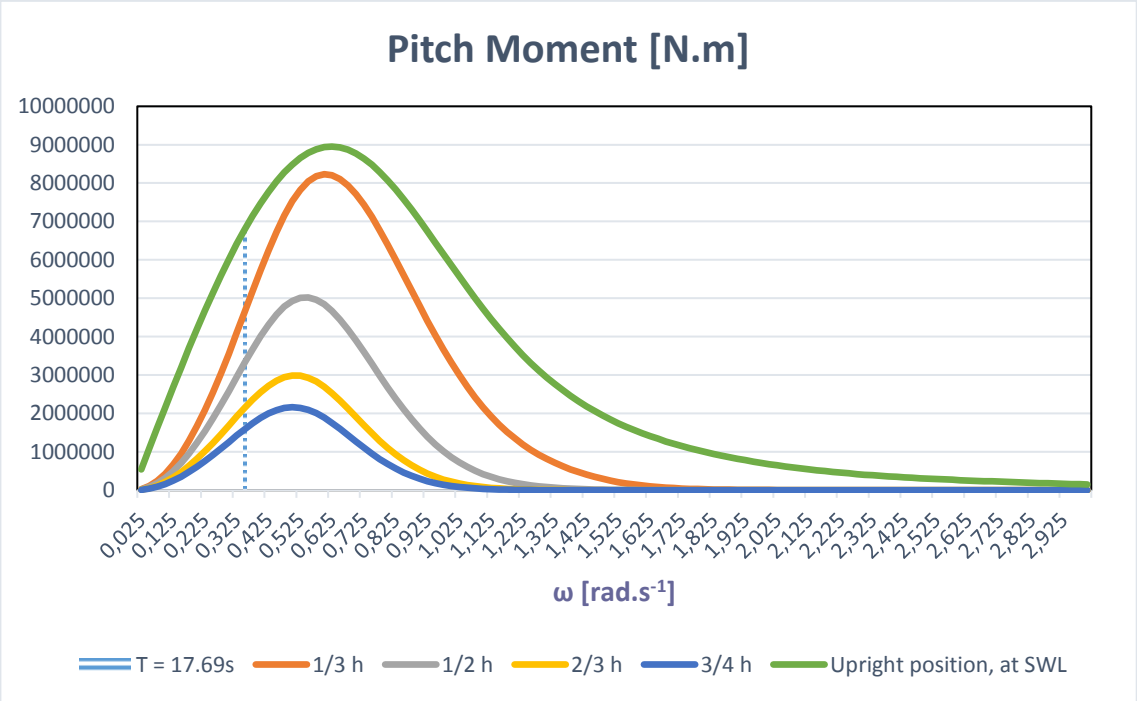

FIGURE 4-4: PITCH EXCITATION MOMENT EVOLUTION WITH SUBMERGENCE DEPTH, COMPARED TO THE UPRIGHT POSITION

Contrary to the translational modes, at first the pitch moment of the submerged depth appears to be closer to the upright position one. This is especially true for d = 1/3h, where the curve evolution is somehow similar to what is observed in the upright position, though with lower values. The reduction becomes significant for d = 1/2h. Here again, the frequency corresponding to the maxima lowers with the submergence depth, and the ratio between these maxima and the upright position one starts at

approx. 8% for d = 1/3h to reach 75% for d = 3/4h. These differences are important, and show that a deeper submergence is more suitable in terms of structure integrity in survival conditions. The excitation forces and moments are just one part of the problem, and an agreement should be found between excitation forces, static pressure, stability and cables disposition.

Besides, it is important to note that the linear potential theory has some limitations when it comes to survivability. Indeed, it only considers first order effects, whereas harsh environments normally involves steep waves known to be highly nonlinear (with higher orders effects not taken into account in the linear theory). Should a more in depth numerical study be needed, investigations with numerical tools such as Computational Fluid Dynamics analysis might be necessary

STATIC PRESSURE

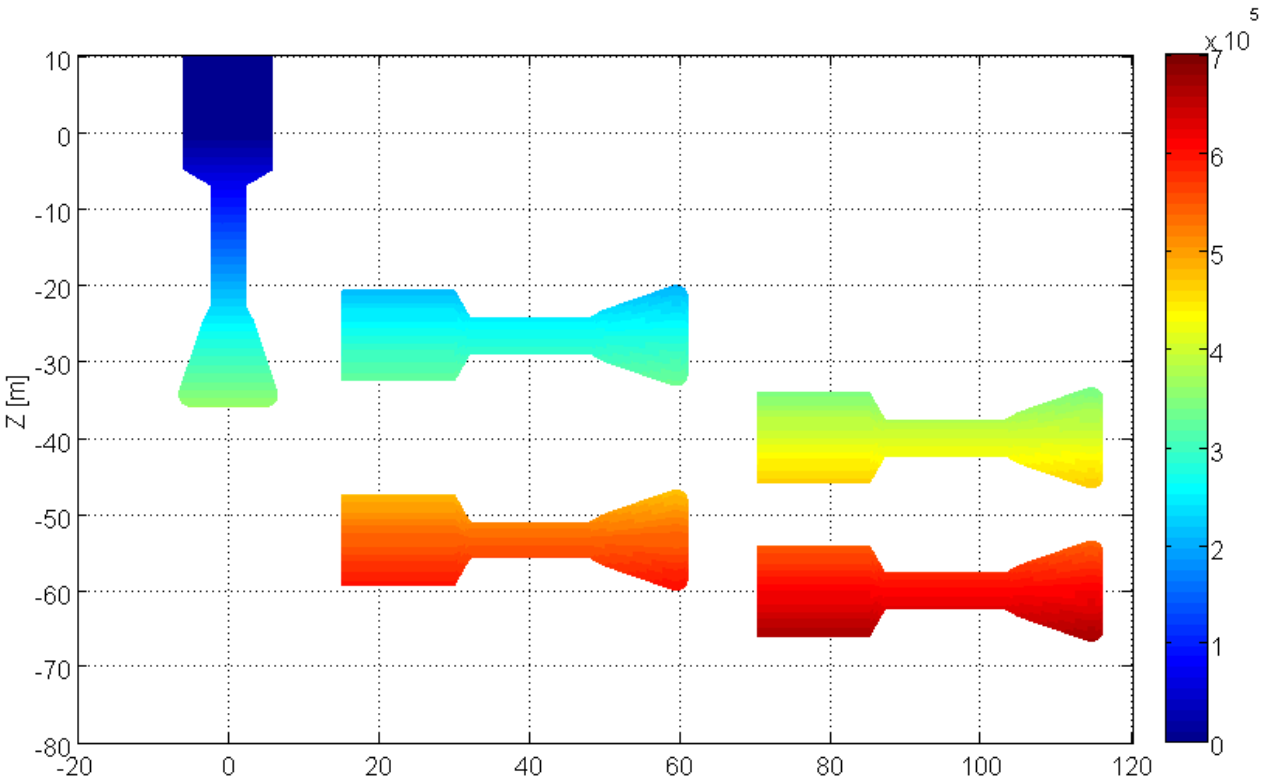

The evolution of the static pressure in function of the submergence depths is presented in figure **Error! Reference source not found.**. At d = 1/3h, the pressure at the OWC local z-axis is 315kPa, and increases to 473kPa, 630.2kPa and 709kPa for d = 1/2h, 2/3h and 3/4h, respectively.

As the pressure is more than doubled between 1/3h and 3/4h, it would be interesting to know whether the OWC spar buoy structure can withstand this pressure, which is believed to be predominant at such depths.

These horizontal positions being somehow "ideal", stability analysis is performed with attention as the OWC presents some stability issues in this position. Part of the work initiated is presented hereinafter.

4.1.2. Time-domain analysis

The objective of the initial hydrodynamic test was to determine at which water depth the submerged device has no motion (or almost no motion) excitation in the event of an extreme storm wave (based on

the same environmental conditions assuming the 100-year storm wave off the coast of Leixões). To this extent, the WEC has been modelled in OrcaFlex as a vessel based on the assumption that the OWC spar buoy is filled with water (and somehow) with an equal mass distribution. The coefficients for the vessel were obtained from WAMIT where the different submerged depths were modelled.

The moorings used for the normal operation conditions were attached to the vessel structure considering the normal attachment points and the 120º distribution.

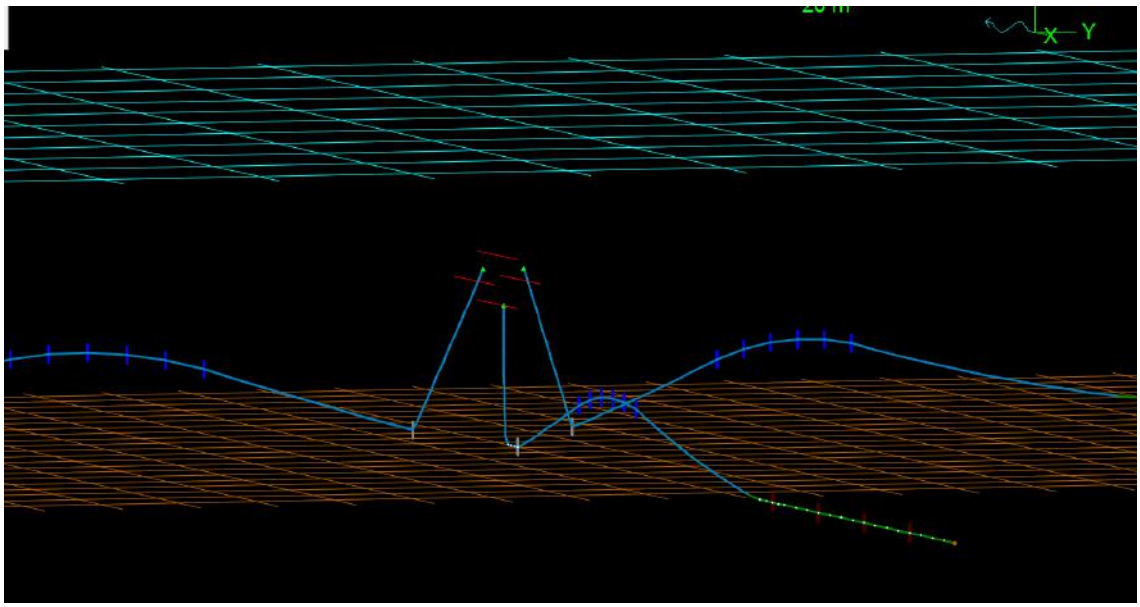

FIGURE 4-5: 3D VIEW OF THE ORCAFLEX SUBMERGED OWC MODEL

Since the vessel was modelled to be in equilibrium (without moorings) when submerged, when the moorings are placed the additional vertical mooring force applied to the device needs to be counterbalanced by an additional buoyance force. This is performed by adding an extra floater attached to the device and at a given point where the equilibrium in terms of force and momentum is maintained.

The volume / mass of the floater needs to be calculated for each of the submergence depths considering the respective position of the mooring fairlead points.

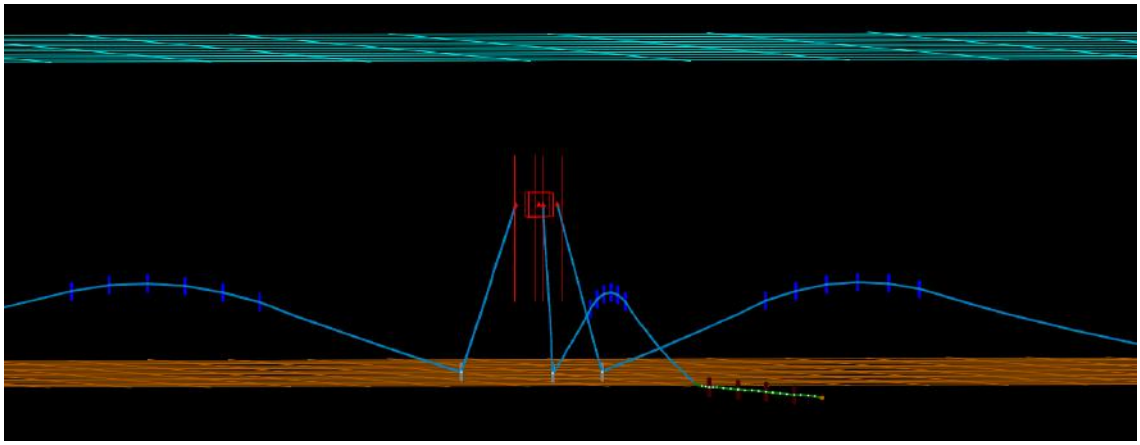

FIGURE 4-6: SNAPSHOT OF THE OWC ROTATION DUE TO STABILITY PROBLEMS

However, some problems in convergence in OrcaFlex in terms of static equilibrium or dynamic stability are occurring in the simulations, as the OWC tends to rotate and does not properly converge to a static position. As a consequence, new simulations for a device slightly tilted are to be performed where the centres of gravity and buoyancy (together with the position and mooring cable lengths) are used as inputs to achieve stability. These simulations will be carried out once a more stable initial configuration of the submerged case will be found.

4.1.3. 2-Dimensional analysis

Further to the preliminary frequency and time-domain analysis carried out to have an initial understanding of the effect of the submergence depth on the hydrostatic and hydrodynamic behaviour of the OWC spar buoy, the switch from operational (floating) to survival (submerged) configuration should be studied. As an initial step of the analysis, simplified submerged study has been performed. That comprises the determination of a statically stable device configuration in submergence as well as the computation of the mooring line tension.

For this study a 2D model has been built, consisting of a submerged cylinder attached to the seabed by two mooring lines. This cylinder has a positive resulting force of buoyancy and gravity, thus making it going upward if not constrained by the mooring lines.

The approach is iterative, where the pitch angle of the spar buoy at rest is changed for each iterative loop to find the static solution. The parameters of the study are the distance between the seabed and the bottom of the buoy, d (in m), and the distance between the mooring lines attachments with the seabed, L (in m).

After setting these two parameters, the model is able to determine the static equilibrium and thus the pitch angle of the device at rest.

This 2D model has been implemented in Matlab Simulink and then the results verified by OrcaFlex simulations.

Four different submergence depths have been taken into consideration: d = 50 m, d = 30 m, d = 20 m and d = 15m (respectively 50 m , 70 m, 80 m and 85 m from the still water line, SWL). Then for every depth value, four different distances between the mooring lines attachments: L = 400 m, L = 600 m, L = 800 m, L = 1000 m.

The OWC has been tested in various pitch angle configurations of the spar buoy at various depths. The water depth is 100 m. Figure **Error! Reference source not found.** presents simulated OWC spar buoy model.

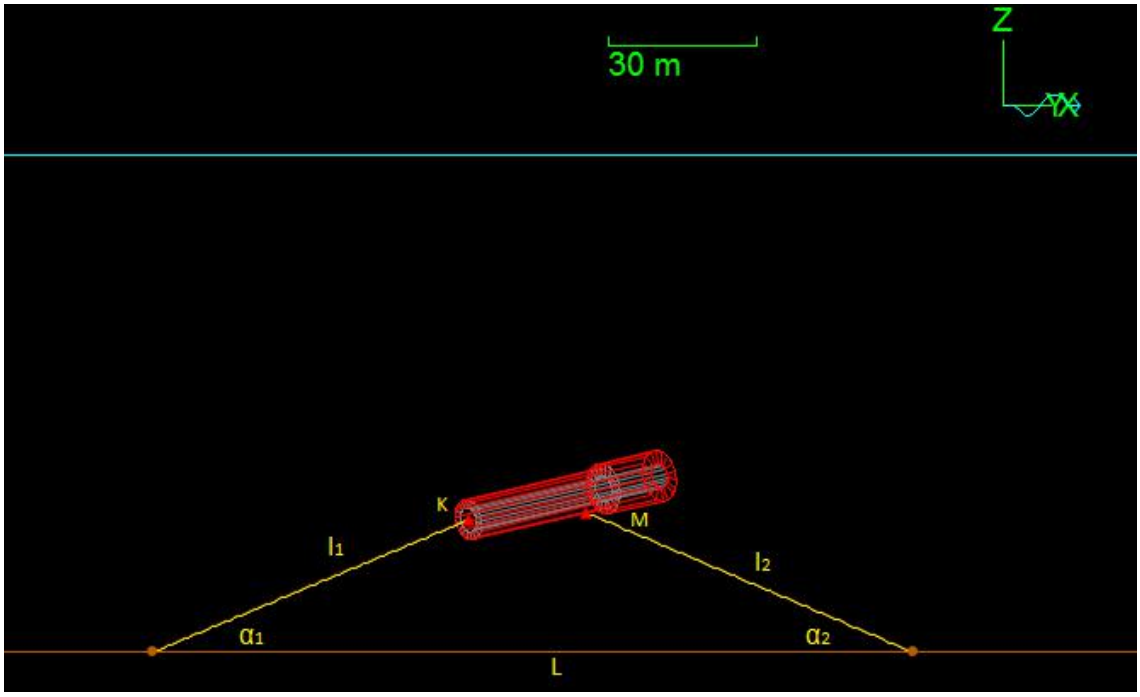

FIGURE 4-7 VIEW OF THE ORCAFLEX SUBMERGED OWC SPAR BUOY MODEL

The static equations of forces and moment equilibrium of the OWC Spar buoy are the followings (using the parameters notations exhibited in Figure 4-7 where angles are in degrees and forces in Newton):

$$\begin{aligned}\sum F_x &= (F_b - F_g)sin\theta - R_1 cos(\alpha_1 - \theta) + R_2 \cos(\alpha_2 + \theta) = 0 \\ \sum F_z &= (F_b - F_g)cos\theta - R_1 sin(\alpha_1 - \theta) - R_2 \sin(\alpha_2 + \theta) = 0 \\ \sum M_G &= (OG - OB)F_b cos\theta + (H - OG)R_1 sin(\alpha_1 - \theta) - (OG \\ &\quad - OM)R_2 \sin(\alpha_2 + \theta) + \frac{D}{2} R_2 \cos(\alpha_2 + \theta) = 0\end{aligned} \tag{4-1}$$

F_b and F_g are the buoyancy force and the gravity force acting on the device, respectively (in N). R_1 and R_2 the reactive force played by the two mooring lines (in N). The pitch angle is between the horizontal and the vertical axis of the Spar buoy. While θ denotes the pitch angle of the device, α_1 and α_2 are the angles between the mooring lines and the seabed. Finally, OG, OB and OM are the distances between the top of the buoy, O, the centre of gravity, G, the centre of buoyancy, B, and the attachment with the second mooring line, M, which is by design 5 m above the still water level when the buoy is floating in operational conditions. The pivot of the moment equation is the centre of gravity.

The geometrical correlations of the model reads:

$$\begin{aligned} d &= l_1 sin\alpha_1 \\ l_2 sin\alpha_2 &= l_1 sin\alpha_1 + KM sin\theta \\ KM cos\theta + l_1 cos\alpha_1 + l_2 cos\alpha_2 &= L \end{aligned} \tag{4-2}$$

where l_1 and l_2 are the length of the mooring lines, while KM the distance between the attachments of theirs on the buoy.

The approach of the model is iterative, with F_G, F_B, d, L, l_1 and l_2 being constant parameters. Starting with an initial θ_0, α_1 and α_2 are computed, which yield the outputs R_1, R_2. This process is implemented in a loop with increasing θ (ramp input). It stops, when all three equations of equilibrium written in (4-1) are satisfied.

The first part of the calculation involves the geometrical parameters. Then, as α_1 and α_2 are known, R_1 and R_2 are calculated using equations (4-3):

$$R_1 = \frac{(F_b - F_g)sin\theta + R_2 \cos(\alpha_2 + \theta)}{\cos(\alpha_1 - \theta)}$$
$$R_2 = \frac{(F_b - F_g)(cos\theta - \tan(\alpha_1 - \theta)sin\theta)}{\sin(\alpha_2 + \theta) + \tan(\alpha_1 - \theta)\cos(\alpha_2 + \theta)} \quad (4\text{-}3)$$

Finally if the result of the momentum equilibrium $\sum M_G = 0$ equation rearranged to calculate θ as a function of α_1, α_2, R_1 and R_2 (see equation (4-4)), shows the same value supposed as attempt, the calculation ends, otherwise it is the new input and the calculation goes on until convergence. The static solution is given by that value of θ, R_1 and R_2.

$$\theta = \tan^{-1} \frac{\left(OG - \frac{H}{2}\right)F_g + \frac{H}{2}R_1 sin\alpha_1 - (\frac{H}{2} - OM)R_2 sin\alpha_2 + \frac{D}{2}R_2 cos\alpha_2}{\frac{H}{2}R_1 cos\alpha_1 + \frac{D}{2}R_2 sin\alpha_2 + (\frac{H}{2} - OM)R_2 cos\alpha_2} \quad (4\text{-}4)$$

Figure 2 shows the comparison between the Matlab Simulink model and a validation model using Orcaflex. The difference between the results is small and decreasing with the depth d.

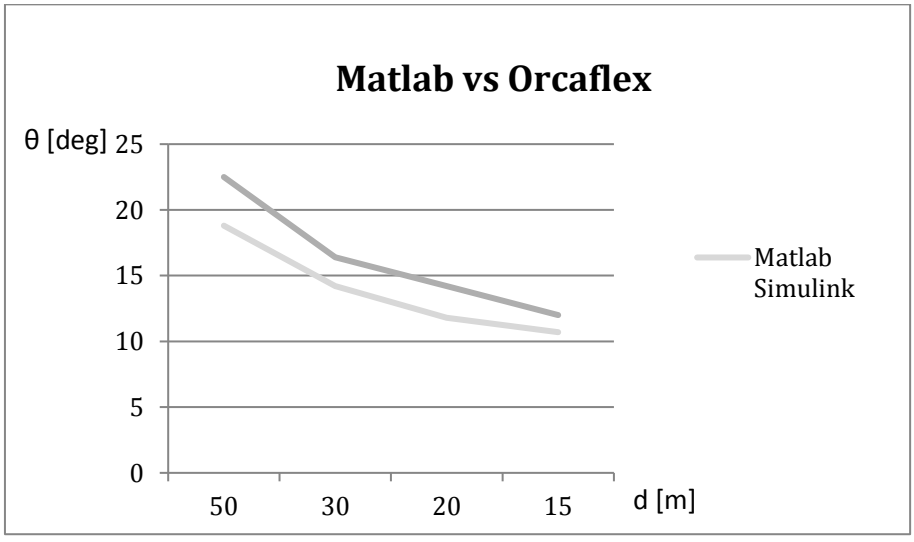

FIGURE 4-8 COMPARISON BETWEEN THE MATLAB SIMULINK MODEL AND THE ORCAFLEX MODEL FOR A FIXED L [M]

CONCLUSIONS

The main outcomes from this preliminary study of the submergence as a survivability strategy for the OWC spar buoy are the followings:

- A deep OWC submergence significantly reduces the excitation forces

- Structure integrity has to be guaranteed at high depth due to static pressure – necessity to know whether a higher static pressure represents a risk or not.

- The horizontal configuration presents some stability issues with mooring lines and buoyancy element

- A tilted configuration appears to be a promising solution for coping with horizontal stability issues

4.2. Engineering constraints and evaluation for large-scale applications

4.2.1. Engineering considerations for full-scale applications

Beyond the structural integrity challenges previously mentioned, other up-scaling issues can be foreseen. In particular, what transpires from the above preliminary conclusions is that a tradeoff between two core aspects must be found in order for the submergence as a survival strategy to be both technically feasible and economically viable:

- the effectiveness of the submergence strategy in terms of load reductions (and potentially savings in structural costs mostly because of thinner hull)
- the need to maintain the structural integrity while avoiding significant extra costs for implementation and use

In terms of the equipment and machinery that could provide the means to achieve the submergence, one can think of two methods to provide the pulling force required to submerge the floating structure:

1- Ballasting; by adding weight into the structure. For example, for the OWC spar buoy hollow structural sections of the floater, LTT and submerged mass could be designed to accommodate water or other ballasting material through a pumping mechanism.
2- By use of a winch fitted within the mooring system. Companies like MacGregor (see here) and AMGC (see here) offer a range of whinch solutions which have been used in other offshore industries.

As previously described, an iterative process using the 2-D model presented in Section 4.13 complemented with a more detailed time-domain analysis can determine the level of the pulling force required for full-scale applications. This information could be the starting point for the selection of the method (ballasting and/or winching) and associated equipment to be utilized for the submergence process.

Another critical issue to be addressed concerns the sealing considerations to protect all sensitive parts. As the WEC is being submerged, all electro-mechanical components and other parts not designed to be in contact with sea-water should be put in a waterproof position. One way to achieve this would be to design caissons with bearing and/or sliding bars which could accommodate the sensitive PTO and instrumentations components through active or passive control.

In any case, sealing should be achieved remotely avoiding the need for the intervention of a crew at the offshore location. For this reason, sensors and control instrumentation will have to be fitted on-board to ensure communication (with redundancy where possible) with the onshore O&M station. In this configuration, the responsiveness of the control systems to activate the ballasting/winching system as well as the sealing/protecting mechanism should not only be well coordinated but also be fast enough when compared to the anticipation time estimated by the weather forecast. Indeed, the main objective of submerging the floating WEC is to reduce the loads before 'too strong' environmental conditions hit the machine and jeopardize its integrity.

Having this additional on-board equipment will also require some power consumption. Integration of the power supply mechanism should also be appropriately designed to meet the standards of offshore applications. Proper sealing and redundancy requirements should be followed while respecting the health & safety standards.

In section 1.3, a mooring design for the reference design case of the OWC spar buoy is proposed. However, based on the preliminary feasibility assessment reported in the previous section, a new mooring design would be required to allow the submergence strategy to be successfully implemented. In particular, the fairlead positions should be carefully chosen to ensure stability is maintained in either floating operational position and submerged survival position. Mooring elements should also be selected and designed to facilitate the submergence process itself.

One critical component for floating offshore WECs is the umbilical dynamical electrical cable. This umbilical is required to transmit the electricity generated by the WEC from the generator in the WEC to the static cable or connection point on the seabed. Since these dynamic cables have very strict design and load requirements, this element should be carefully considered during submergence. For instance, maximum curvatures, bending loads and fatigue life requirements are key factors to take into account. To this extent, buoyancy elements and touch-down point of the umbilical should be chosen in a way that these requirements are met under both the operational (floating) and survival (submerged) modes.

Another important aspect to engineer when scaling up the submergence as a survival strategy is the recovery system. While one may intuitively assume that the exact reverse process of the submergence would be suitable, special care should be made when ensuring a suitable restoring force will be available to carry the WEC back to its operational mode. Beyond the hydrodynamic mechanical challenge for this process, remote re-activation of all PTO equipment and connection to the grid represents another critical issue.

At this stage, many unknowns remain related to the engineering challenges associated with a submergence strategy of an offshore WECs. More detailed analysis will be carried out to evaluate some of these issues within the WP3 of the WETFEET project. In turn, the submergence as a survivability strategy would only be worthwhile from a holistic perspective if:

- the benefits; structural loads reduction and potentially structural cost reductions, avoidance of marine operations, increase of productivity due to expected quicker on/off grid connection,

SURPASS,

- the drawbacks; increased overall system complexity (ballasting/winching equipment, mooring and umbilical design, power supply, sealing/protective mechanisms, etc…), additional cost due to on-board equipment

The attractiveness of the submergence as a survival strategy should also be discussed in the context of a benchmarking exercise against a reference configuration employing a more conventional survivability strategy. Looking back at the limited operational experience from floating WECs at sea, it appears that one survival strategy often applied in prevision of forthcoming harsh met-ocean conditions consists of towing back the device back to port (e.g Pelamis). While this method has the clear disadvantage of using the appropriate vessel and crew to allow the disconnection of the WEC in a timely-acceptable fashion, it does not require any fundamental design adaptations. Another configuration which can be considered for the benchmarking exercise would be to re-design the reference case assuming the loads can be sustained by the structure under extreme conditions. This would typically mean having a “reinforced” (likely to be stiffer and heavier) WEC and mooring design since it would need to survive by staying in operational configuration instead of being submerged.

4.2.2. Applications to other WECs and recommendations for future work

In principle, any other WEC structure moored to the seabed could design the submergence as a survival strategy. Furthermore, it may be noted that this submergence strategy should preferably be designed with a capsule for water-proofing and isolation of critical components. Some of the WEC design parameters that may influence the feasibility of implementing the submergence strategy (mostly in terms of required force) include the total mass and the water-plane area.

5. DIELECTRIC ELASTOMER GENERATORS AS POWER-TAKE-OFF FOR WAVE ENERGY CONVERSION

5.1. Introduction

This chapter provides insight on possible implementations and potential performance of Dielectric Elastomer Generator (DEG) PTOs for the two WECs investigated within WETFEET project, namely, OWC spar buoy and Symphony.
Dielectric Elastomers (DEs) represent a potential breakthrough for WEC technology, as they might drive towards reduction in costs and better adaptability to sea environment. Nonetheless, their effectiveness has to be first assessed by identifying possible architectures for their implementation, evaluating relevant parameters (involved amounts of DE material, performance) and analyzing engineering issues associated with this new technology (e.g., DEG survivability and lifetime, manufacturability of large DEGs stacks).
In the following, we present two case-studies in which a given DEG system is used as PTO respectively on a full-scale OWC spar buoy device and on an intermediate scale Symphony WEC (outer diameter 1.5 m). The DEG architecture chosen for both case studies is the so-called Circular Diaphragm DEG (CD-DEG), which has been extensively described in [72], [73]. This DEG is adaptable to different WECs and operating configurations. Specifically, it has been here assumed that the CD-DEG operates in air when installed in the OWC spar buoy, while it contacts sea water in case it is installed on the Symphony.
In the following, after a short recall on the DEG operation and model, results of the two case studies are presented and discussed. In the simulations, engineering constraints have been introduced, to optimize the lifetime of the DEG: the maximum applied electric field has been limited to enhance electrical fatigue lifetime and reduce losses, and, in the case of the OWC, a security valve model has been included in the simulations to prevent material overstretch.
Results show that the DEG is a promising solution, especially for OWCs.

5.2. Circular Diaphragm DEG

A CD-DEG is depicted in Figure 5-1. It consists of an equi-biaxially pre-stretched planar circular DE membrane (DEM) that is clamped along its perimeter to a fixed frame at radius e and with thickness t (whereas e_0 and t_0 indicate the radius and thickness of the DEM in its planar undeformed state). The ratio between the frame radius, e, and the membrane undeformed radius, e_0, is referred to as pre-stretch: $\lambda_p=e/e_0$. The DEM in undeformed and pre-stretched configuration is shown in Figure 5-1 (a) and Figure 5-1 (b) respectively. The membrane is made of insulating material while its faces are covered by deformable electrodes, to form a variable capacitor. In order to limit the applied voltage and to make the electric field within the generator more homogeneous, the membrane can be split in a stack of parallel connected membranes, each coated by a couple of compliant electrodes.
The opposing sides of the CD-DEG are subjected to the time variable differential pressure, either generated by pressurization/depressurization of an air volume beneath the CD-DEG or by displacement of a water volume contacting one of the faces of the CD-DEG. The CD-DEG undergoes an out of plane

axial-symmetric (bubble-like) deformation (area expansion). In Figure 5-1 (c), *h* identifies the resultant displacement of the CD-DEG tip.
The electro-mechanical response of the CD-DEG can be described using a simplified approach, which relies on an assumption on the deformation kinematics of the DEG [74]. In particular, it is hereby assumed that the CD-DEG deforms a thin spherical shell segment with tip height *h* and radius *R*.

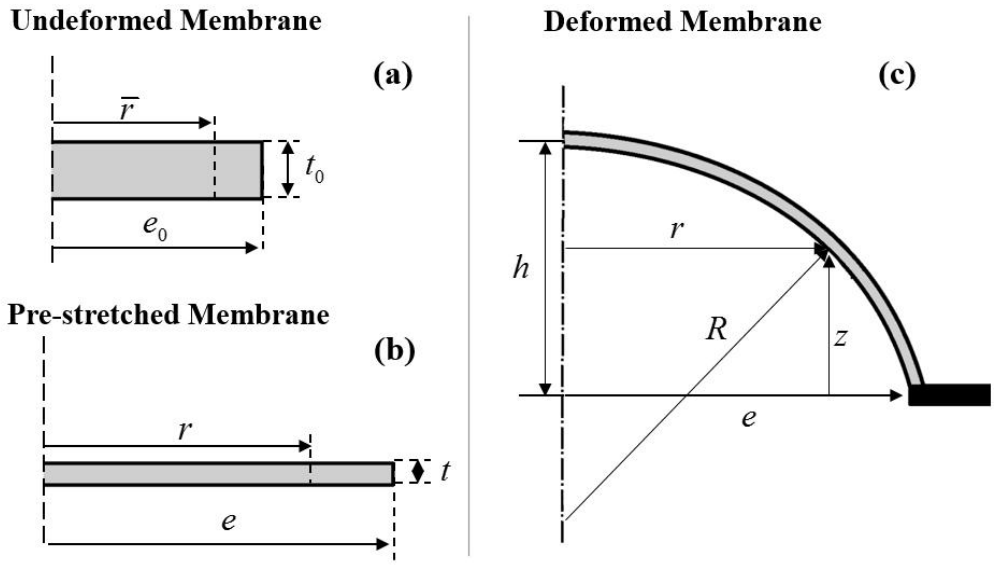

FIGURE 5-1. CIRCULAR DIAPHRAGM DIELECTRIC ELASTOMER GENERATOR (CD-DEG): (A) CD-DEG UNDEFORMED STATE, (B) CD-DEG PRE-STRETCHED STATE WITH NO DIFFERENTIAL PRESSURE AND ELECTRIC POTENTIAL, (C) CD-DEG DEFORMED STATE WITH DIFFERENTIAL PRESSURE AND/OR ELECTRIC POTENTIAL.

Other assumptions used to model the ICD (Inflated Circular Diaphragm)-DEG are:
- the ICD-DEG deformation is prevalently equi-biaxial, with the amount of deformation depending on *h* and varying with the radial distance *r*;
- the ICD-DEG capacitance is assumed to be equivalent to that of a planar circular capacitor with variable thickness;
- the DE material is assumed as an hyperelastic non-viscous solid [75].

As shown in [73], with the abovementioned assumptions, the principal stretches (circumferential and meridian) of an element of membrane located at a distance $\bar{r}$ from the axis in the undeformed configuration (Figure 5-1 (a)) read as:

$$\lambda\left(h,\bar{r}\right)=\lambda_1\left(h,\bar{r}\right)=\lambda_2\left(h,\bar{r}\right)=ee_0\left(h^2+e^2\right)\Big/\left(e^2e_0^2+h^2\bar{r}^2\right) \qquad \textbf{(5-1)}$$

Assuming the DE material is hyperelastic, the elastic energy per unit material volume can be expressed through a strain-energy function, $\psi=\psi\left(I_1,I_2\right)$, that depends on deformations invariants I_1 and I_2:

$$I_1=\lambda_1^{\,2}+\lambda_2^{\,2}+\lambda_1^{-2}\lambda_2^{-2}\quad;\quad I_2=\lambda_1^{-2}+\lambda_2^{-2}+\lambda_1^{\,2}\lambda_2^{\,2}. \qquad \textbf{(5-2)}$$

The overall elastic energy of the deformed DE material can be then expressed as

$$U_{el}\left(h\right)=\int_0^{e_0}2\pi t_0\bar{r}\psi d\bar{r} \qquad \textbf{(5-3)}$$

As regards the DEG capacitance, it can be shown [73] that it equals

$$C_e=\frac{\pi\varepsilon n^2ee_0}{3t_0}\lambda\left(\lambda^2+\frac{e}{e_0}\lambda+\frac{e^2}{e_0^2}\right), \qquad \textbf{(5-4)}$$

where ε is the elastomer dielectric constant and n is the number of parallel-connected layers into which the membrane thickness is split.
A way to relate the pressure difference between the CD-DEG faces to its deformation is considering the stress equilibrium at the membrane tip $(\bar{r}=0)$. Mechanical equilibrium of the CD-DEG tip leads to the following expression for the pressure:

$$p=\frac{4h}{h^2+e^2}\frac{t_0}{\lambda_T^{\,2}}\sigma, \quad \text{with} \quad \lambda_T=\lambda(h,0) \quad \text{and} \quad \sigma=\lambda_1\frac{\partial\psi}{\partial\lambda_1}-\varepsilon E_T^{\,2} \qquad \textbf{(5-5)}$$

Where E_T is the electric field at the membrane tip, which relates to the applied voltage, V_e, as follows:

$$E_T=n^2\lambda_T^{\,4}t_0^{-2}V_e^{\,2} \qquad \textbf{(5-6)}$$

5.3. OWC spar buoy-DEG: architecture definition and numerical assessment

A modified design for the OWC spar buoy, purposely conceived to house a DEG PTO, is shown in Figure 5-2. With respect to the base design, the submerged part of the device is unaltered, while an extension of the upper air chamber has been envisaged to place the DEGs PTO. In order to limit the dimensions of the DEGs and avoid excessively large membranes (requiring unconventional manufacturing), it is supposed that the PTO can be split in a number of independent DEGs, each one featuring a multi-layered architecture with several alternated dielectric and conductive layers.

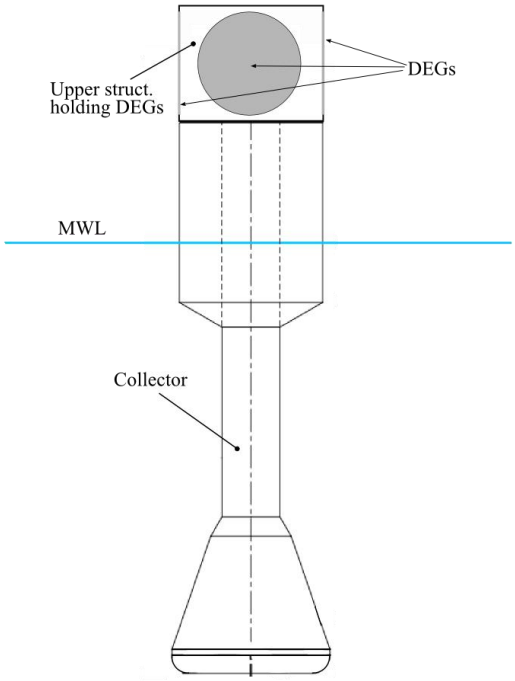

FIGURE 5-2. OWC SPAR BUOY WITH DEG AS PTO. THE COLLECTOR EMERGED PART IS SUPPOSED TO BE MODIFIED TO HOUSE THE DEGS.

The time-domain hydrodynamic model, based on frequency-domain hydrodynamic parameters and state space identification for the radiation, has been integrated with the Circular Diaphragm DEG model described in [72] and recalled in the previous section. That is, the CD-DEG deformation has been put in relation to the air pressure within the chamber using equation (5-5). Compression and expansion of the air volume in the closed chamber has been considered adiabatic.

The behavior of the system in irregular waves has been investigated using a Pierson-Moscowitz spectrum.
Simulations have been run with two different materials: a commercial styrene-based rubber [74], and a novel silicone matrix conceived for DEs application, adding 20 phr of silicone dielectric oil to a commercial silicone rubber [76]. This latter material features interesting properties in terms of dielectric constant, break-down strength and dielectric losses, and presents a reduced mechanical stiffness with respect to rubber.
The DEG is controlled according to the following strategy: when the capacitance rises (bubble-like outward deformation), no charge is present on the electrodes. The DEG is activated as its capacitance reaches a maximum and, as the capacitance decreases, voltage is controlled in a way that the electric field at the membrane tip is kept at a fixed percentage of the maximum allowed value (break-down), which is a known function of the deformation. As the DEG gets flat (minimum capacitance), it is discharged and the cycle is then restarted.
With respect to the simulation methodology described in [72], the following improvements have been introduced:
1) Basing on preliminary experimental tests on fatigue lifetime and leakage losses, a constraint on the maximum applied electric field has been introduced, that limits the electric field at the membrane tip to a fixed percentage of the break-down field. Experiments have indeed shown that keeping a certain security factor with respect to break-down positively influences the DEG lifetime increasing it up to one order of magnitude. Moreover, reduced applied electric field positively influences the leakage losses, which depend exponentially on the instant electric field.
2) Implementation of a relief valve model that prevents DEGs over-stretching in roughest seas. Brief details on such model are provided in the following.

Relief valve model
From a first-iteration simulation, a number of sea states have been identified, in correspondence of which the membrane features very large deformations (over the hemispherical out-of-plane deformation). Those sea states have been considered as "critical", and, whenever they occur, the membrane should operate in security mode with a relief valve partially open (with the aperture section properly chosen for each sea state). In practice, the aperture of the valve could be adjusted occasionally, basing on wave climate forecasts and setting it to the appropriate value for the foreseen sea conditions. Alternatively, the valve could be automatically adjusted quite frequently, basing on wave gauges acquisitions in the far-field of the devices.
The thermodynamic model of the air volume in case of open chamber has been formulated as in [77], assuming the system adiabatic. In particular, the following dynamic equation holds:

$$\dot{p} = -\frac{\gamma p_{atm}}{V}\left(1+\frac{p}{p_{atm}}\right)\left(\dot{Q}+\dot{V}\right) \qquad \textbf{(5-7)}$$

Where γ=1.4 is the adiabatic air ratio, and V is the volume of the air chamber (delimited by the membrane cap, the water column surface and the collector walls) and p_{atm} is the atmospheric pressure. The equation of the air volume flow rate, $\dot{Q}$, through the valve orifice has the following well-known form:

$$\dot{Q} = \mathrm{sgn}(p)\frac{CA_v}{\sqrt{1-\left(A_v/A_{OWC}\right)^2}}\left(2|p|/\rho\right)^{1/2} \qquad \textbf{(5-8)}$$

where p and $\rho = \rho_{atm}\left(1+p/p_{atm}\right)^{1/\gamma}$ are the instant air gauge pressure and density respectively (ρ_{atm} is atmospheric air density), A_v is the valve aperture section, A_{OWC} is a reference transversal section of the OWC, and C is a coefficient of discharge, usually taken equal to 0.5.

Parameter	Simulation 1	Simulation 2	Simulation 3
DE material	Synthetic rubber	Custom silicone with dielectric oil (20phr) **Error! Reference source not found.**	
Hyperelastic parameters - Mooney-Rivlin model $\psi = \sum_i A_i (I_1 - 3)^i + \sum_j B_j (I_2 - 3)^j$	A_1=1.03 MPa A_2=0.17 MPa A_3=-4.11 kPa B_1=-0.59 MPa B_2=1.84 kPa	A_1=0.23 MPa	
Dielectric constant, ε	2.7×8.85e-12 F/m	3.9×8.85e-12 F/m	
Break-down electric field, $E_{BD} = E_{BD,0}\lambda^R$	$E_{BD,0}$=100 MV/m R=1	$E_{BD,0}$=100 MV/m R=1	
Fraction of E_{BD} using during activation phase, α	0.8	0.8	
Number of DEGs, N_m	4	4	3
DEG diameter, e	3 m	3 m	3.5 m
DEG thickness, t	99.2 mm	83.3 mm	83.3 mm
Pre-stretch, λ_p	1.1	1.2	1.2
Foreseen stack architecture	4 modules by 50 layers each	4 modules by 40 layers each	

TABLE 5-1. RESUME OF THE PARAMETERS (MATERIAL PROPERTIES) EMPLOYED IN THE DIFFERENT SIMULATIONS.

Simulation 1

T_e (s) \ H_s (m)	0.5	1	1.5	2	2.5	3	3.5	4
6	0.1	0.2	0.3	0.4	0.5	0.5	0.6	0.8
7	0.3	0.9	1.8	2.0	3.0	3.5	4.7	6.6
8	0.9	2.2	4.6	6.2	9.2	14	18	21
9	1.1	3.2	6.5	12	18	22	29	34
10	1.3	4.5	9.4	16	23	24	32	82
11	1.6	5.7	11	13	20	51	57*	82
12	2.1	4.2	8.6	24	37	60	81	47
13	1.3	7.2	15	28	42	26	34	53*
14	2.2	7.4	15	12	18	57	55*	41*
15	2.0	3.4	7.0	23	35	60	50*	45*

Simulation 2

T_e (s) \ H_s (m)	0.5	1	1.5	2	2.5	3	3.5	4
6	0.1	0.2	0.4	0.5	0.7	0.8	0.9	1.2
7	0.4	1.1	2.2	2.8	4.2	5.5	7.3	9.9
8	1.1	3.0	6.4	10	15	21	28	33
9	1.4	5.1	11	18	27	36	48	56
10	2.0	6.3	14	26	39	41	55	76*
11	2.2	9.4	20	22	33	89	89*	111*
12	3.2	6.7	14	41	63	104	81*	76
13	2.0	11	24	48	73	42	57	67*
14	3.1	13	27	20	30	95	82*	59*
15	3.3	5.7	12	40	62	82	57*	52*

Simulation 3

T_e (s) \ H_s (m)	0.5	1	1.5	2	2.5	3	3.5	4
6	0.1	0.3	0.4	0.5	0.7	0.8	1.0	1.2
7	0.4	1.0	2.0	2.5	3.7	5.4	7.2	9.2
8	1.0	2.7	5.7	11	16	20	27	33
9	1.3	5.3	11	16	25	36	48	57
10	2.1	5.9	13	27	41	44	58	143
11	2.1	9.7	21	24	36	92	125	101*
12	3.2	7.7	16	43	66	107*	95*	79
13	2.3	11	25	59	92	45	60	89*
14	3.0	15	33	22	32	104	101*	68*
15	3.7	6.2	13	47	73	71	95	78*

FIGURE 5-3. POWER MATRICES RESULTS FOR THREE DIFFERENT SIMULATION SCENARIOS. POWERS ARE IN KW. CELLS WITH ASTERISKS REFER TO THE SEA STATES WERE THE RELIEF VALVE IS PARTIALLY OPEN AND THE DEVICE IS PARTIALLY DEPOWERED.

Simulation results

Overall, three different simulations have been run, varying the parameters as in Table 5-1. In the Table, the main DEG features are described, moreover, a plausible architecture for the DEG stacks implementation is proposed: it is assumed that each DEG is split into four independent modules (that can be replaced individually in case of failure), with a number of layers (n) such that the maximum output voltage is below 50 kV.

Simulation results (in terms of device power output) are shown in Figure 5-3. The matrices report the OWC spar buoy power output in kW for each sea state. For each simulation, the cases in which the relief valve is set to a partially open configuration to prevent over-deformation are marked with an asterisk.

Basing on preliminary fatigue tests, material exploitation at 70-80 % the break-down field improves the cyclic DEG lifetime up to one order of magnitude, increasing it from 10^6 to 10^7 cycle. Maximum applied electric field was thus limited to 80% of break-down value.

The presented results do not keep into account losses due to leakage (which should be anyway limited due to the restriction on electric field) and conditioning electronics efficiency.

Power output results give evidence of two resonance peaks of the device (approximately at T_e=13 and 15 s for significant height H_s=2.5 m), due to the two degrees of freedom of the system.

Results obtained with silicone are visibly better than those with synthetic rubber. Silicone appears to be more suitable for OWC spar buoy application, thanks to its larger dielectric constant and its lower rigidity, which becomes crucial as the OWC spar buoy PTO is in series to an air volume which tends to absorb part of the deformation induced by the free surface displacement.

Results obtained with silicone and the two different architectures are quite similar, even though the second solution provides slightly larger power output. In terms of implementation the first solution might be preferable, though, as it features lower diameters membrane, which are easier to manufacture, install and maintain.

5.4. Symphony-DEG: architecture definition and numerical assessment

Figure 5-4.a shows a modified architecture for the Symphony, which features a DEG PTO contacting the inner water volume on one side and sea water on the other. The following architectural assumptions have been made:

- The air vessel and the turbine of the base design are not present in this design. In static conditions, the task of holding the floating cylinder in place at the zero reference position is performed by the DEG that, in the equilibrium position, has a bias deformation.
- The geometry of the inner support membranes is unvaried, thus, the water volume that goes into (or away from) the DEG is given by the difference of the volumes flowing through the upper and the lower membranes cross section, and it equals the water volume through the turbine in the base case.

It can be shown that, with a few further assumptions, the inner fluid equilibrium pressure required to guarantee the static equilibrium of the device is the same of the base case (about 15 bar).

As regards the device dynamics, although the device geometry is slightly modified, the negative spring effect due to hydrostatic forces still provides a minimum negative stiffness close to $-\pi/4\,\rho g D_o^2$ (being D_o the outer cylinder diameter), which is achieved when vacuum is made in the volume under the outer cylinder tip. The positive stiffness of the air is replaced by the membrane (non-linear) stiffness.
The relatively large volumes of DE required in this application (to resist the high pressure difference and provide appropriate power output), combined with the relatively small diameters prescribed by the Symphony dimensions (outer diameter 1.5m) and kinematics (stroke approximately between -1 and +1 m), make it necessary to employ a very thick DEG. The best way to implement it is splitting the DEG in a number of independent modules (for easier handling and replacement), eventually separated by water to prevent friction among concurrent surfaces. Such a layout is shown in Figure 5-4.b.
A coupled DEG-Symphony model has been setup, integrating the following sub-models.

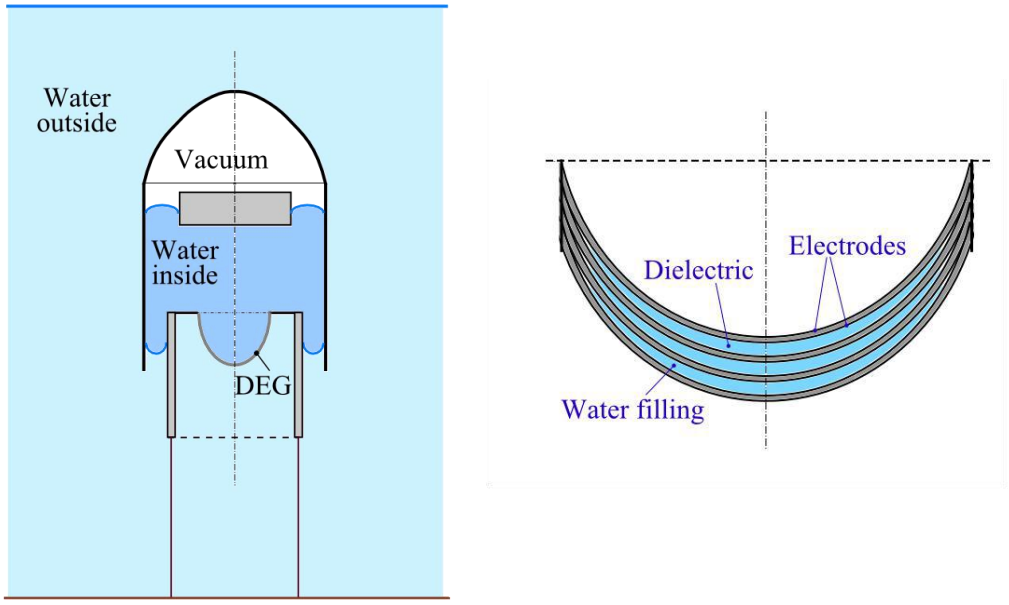

(a) (b)

FIGURE 5-4. (A) SCHEMATIC OF THE SYMPHONY FITTED WITH A DEG WITH WATER ON BOTH SIDES (SEA WATER ON THE BOTTOM, INNER OPERATIVE FLUID ON TOP). (B) ARCHITECTURE OF THE SYMPHONY DEG PTO. DUE TO THE LARGE REQUIRED VOLUMES OF POLYMER AND THE SMALL DIAMETER, THE DEG SHOULD BE IMPLEMENTED USING SEVERAL MODULES, EVENTUALLY SEPARATED BY WATER.

Hydrodynamic model

Hydrodynamic frequency-domain data for a 1.5m diameter Symphony have been provided by Teamwork Technology and they have been used to set up a time-domain model. Non-linear drag forces have been also included in the model, basing on Teamwork assessment of drag coefficient for up and downward floater motion (0.1 and 0.5 respectively).
Furthermore, a soft end-stops model has been implemented, to limit the oscillation amplitude of the floater to roughly ±1m, and strictly below ±2m. End-stops have been modelled as a spring-damper couple which provides force only when the slider position is above (below) +1m (-1m), thus providing a force as follows:

$$F_{ES} = \begin{cases} 0 & \text{if} \quad |z| < Z_{ES} \\ -\text{sign}(z)\cdot k_{ES}\left(|z| - Z_{ES}\right) - B_{ES}\dot{z} & \text{if} \quad |z| \geq Z_{ES} \end{cases} \qquad \textbf{(5-9)}$$

Where k_{ES} and B_{ES} are the end-stop stiffness and damping, and Z_{ES}=1 m.

DEG PTO model

The deformation kinematics assumed for the CD-DEG is that described in the previous section for the OWC spar buoy. The amount of inner water displaced per unitary displacement of the outer cylinder is known (dQ_v/dz=1 m³/m), and it allows to univocally relate the cylinder position (z) to a deformed shape of the membrane.

It can be easily shown, through an energy balance, that the total force on the outer cylinder due to the membrane reads as follows:

$$F_{DEG} = \left(p_{atm} + \rho g h_{DEG}\right)\frac{dQ_v}{dz} - \frac{dU_{el}}{dz} + F_{es}, \quad \text{with} \quad F_{es} = \frac{V_e^2}{2}\frac{dC_e}{dz} \qquad \textbf{(5-10)}$$

where h_{DEG} is the submergence of the membrane perimeter, U_{el} is the elastic energy of the DEG (known function of z), V_e is the instant voltage on the DEG and C_e its capacitance, given by equation (5-4), which depends on z too.

As regards the inertia of the DEG (and of the eventual embedded spacing fluid), it can be estimated and reduced to the degree of freedom of the floater as follows:

$$M_{DEG} = \rho_p \pi t_0 \left(\frac{dh}{dz}\right)^2 \int_0^{e_0}\left[\left(\frac{dr}{dh}\right)^2 + \left(\frac{dz}{dh}\right)^2\right]\bar{r}d\bar{r} \qquad \textbf{(5-11)}$$

where ρ_p is the polymer density, h is the membrane tip displacement (see Figure 5-1 (c)), which is univocally related to z, and r and z are the cylindrical coordinates describing the CD-DEG elements position (see Figure 5-1(c)) and they read as

$$r = \frac{e e_0\left(h^2 + e^2\right)\bar{r}}{\left(e^2 e_0^2 + h^2\bar{r}^2\right)}; \; z = \frac{e^2\left(e_0^2 - \bar{r}^2\right)h}{\left(e^2 e_0^2 + h^2\bar{r}^2\right)}. \qquad \textbf{(5-12)}$$

It is worth noticing that, although the involved mass of polymers are non-negligible with respect to the device inertia, the reduced DEG inertia is very low, due to the particular DEG kinematics in fact, most of the DE material is located nearby the DEG perimeter, where the displacements are rather small compared to z).

Control

Assuming that, due to kinematics, the membrane is always deformed downward with respect to the flat configuration, its capacitance decreases for upward motion. Therefore, the term dC_e/dz in equation (5-9) is always negative, and the electrostatic contribution to F_{DEG} is negative too. As a result, the DEG is capable of "damping" the WEC motion only while it moves upward ($\dot{z} > 0$), i.e, when the DEG capacitance decreases. Consequently, we chose to activate the DEG only when $\dot{z} > 0$.

Nevertheless, keeping the electric field at the maximum value over the whole activation phase (as done for the OWC spar buoy) would result, in this case, in an over-aggressive control, which would prevent the DEG from oscillating and would rather keep it stuck at the lower dead point position.

A different control strategy was then chosen, in which the voltage on the DEG is controlled to produce a damping force (proportional to the floater velocity), compatible with the operating limits of the DEG:

$$F_{es,ctrl} = \begin{cases} \max\left(-B_{PTO}\dot{z}\,,\; \dfrac{V_e^2}{2}\dfrac{dC_e}{dz}\right) & \text{if } \dot{z} \geq 0 \\ 0 & \text{if } \dot{z} < 0 \end{cases} \qquad \textbf{(5-13)}$$

The damping level, B_{PTO}, is changed for each sea state to maximize the mean power output.

Simulation results

A set of simulations were run, assuming a synthetic rubber as reference DE material (properties are in Table 5-2). Two different sets of simulations were performed, using two different hypothesis on the operating limits of the generator with respect to break-down: 1) maximum electric field is kept below 80% of the break-down value, 2) maximum electric field coincides with break-down condition. Results in the two cases are basically identical, with minor exceptions (of a few points percent) at the roughest sea states. This demonstrates that, with the chosen control strategy, sufficient damping can be provided even with limited electric field. For the same reason, in this case, the hypothetic replacement of synthetic rubber with a different DE with larger dielectric constant (e.g., silicone) was considered unnecessary, as the proposed DEG design already provides sufficient damping levels.

The negative stiffness due to hydrostatic is set to 70% of $-\pi/4\,\rho g D_o^2$ (i.e., the volume below the floater tip is in a condition close to vacuum).

The DEG response for the case in exam is shown in Figure 5-5. In particular Figure 5-5 (a) shows the CD-DEG tip displacement (h) as a function of the outer floating cylinder position (z), while Figure 5-5 (b) shows the PTO force profile (F_{DEG}) either in absence of electric field or at the maximum allowed electric field (in this case, $0.8E_{BD}$).

Parameter	**Value**
DE material	Synthetic rubber
Density, ρ_p	1000 kg m^{-3}
Hyperelastic parameters - Mooney-Rivlin model $\psi = \sum_i A_i (I_1 - 3)^i + \sum_j B_j (I_2 - 3)^j$	A_1=1.03 MPa A_2=0.17 MPa A_3=-4.11 kPa B_1=-0.59 MPa B_2=1.84 kPa
Dielectric constant, ε	2.7×8.85e-12 F/m
Break-down electric field, $E_{BD} = E_{BD,0}\lambda^R$	$E_{BD,0}$=100 MV/m R=1
Conductivity $\kappa(E) = \kappa_0 \exp(E/E_0)$	κ_0=6.4e-14 S/m E_0=51 MV/m
DEG diameter, e	0.55 m
DEG thickness (overall), t	625 mm
Pre-stretch, λ_p	1.1
Mass of water filling between the layers	20% of DE mass
Foreseen stack architecture	10 modules by 130 layers each
End-stop features	k_{ES}=1.78e5 N/m B_{ES}=5 t/s

TABLE 5-2. RESUME OF THE PARAMETERS (MATERIAL PROPERTIES) EMPLOYED IN THE DIFFERENT SIMULATIONS.

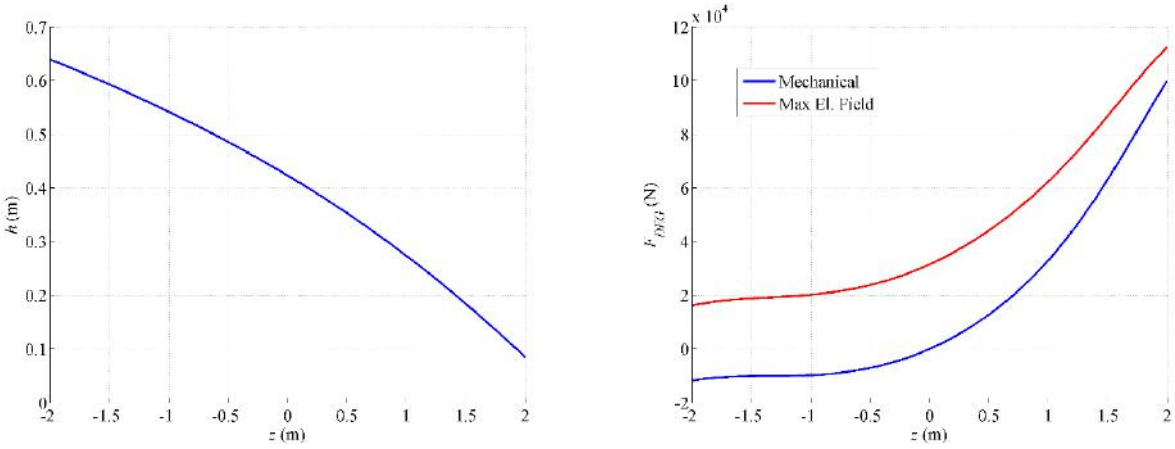

(a) **(b)**

FIGURE 5-5. (A)FLOATER DISPLACEMENT (Z) – DEG TIP DISPLACEMENT (H) CURVE FOR THE CASE STUDY CONFIGURATION. (B) FORCE OF THE DEG VS FLOATER DISPLACEMENT: THE BLUE CURVE IS THE PURELY MECHANICAL RESPONSE (NO ELECTRIC ACTIVATION), THE RED CURVE IS THE RESPONSE WHEN THE MAXIMUM ELECTRIC FIELD ($0.8E_{BD}$) IS APPLIED.

Power matrix

T_e (s) \ H_s (m)	0.5	1	1.5	2	2.5	3	3.5	4	4.5	5
6	0.0	0.3	0.6	1.0	1.3	1.6	1.9	2.3	2.7	3.0
7	0.0	0.4	0.8	1.1	1.5	1.8	2.3	2.3	2.6	3.0
8	0.1	0.4	0.7	1.1	1.4	1.8	2.2	2.5	2.9	3.3
9	0.1	0.4	0.7	1.0	1.4	1.7	2.0	2.4	2.9	3.2
10	0.1	0.4	0.8	1.1	1.5	1.8	2.2	2.6	2.9	2.9
11	0.1	0.4	0.7	1.0	1.3	1.6	1.9	2.2	2.5	3.1
12	0.1	0.4	0.7	1.0	1.3	1.6	1.9	2.3	2.6	2.7
13	0.1	0.4	0.6	0.9	1.2	1.4	1.7	2.0	2.2	2.5
14	0.1	0.4	0.7	0.9	1.2	1.5	1.7	2.0	2.3	2.6
15	0.1	0.4	0.6	0.9	1.1	1.4	1.6	1.9	2.2	2.5

Optimal damping factor

T_e (s) \ H_s (m)	0.5	1	1.5	2	2.5	3	3.5	4	4.5	5
6	5.0	5.0	10.0	10.0	10.0	10.0	10.0	15.0	15.0	15.0
7	5.0	5.0	10.0	10.0	10.0	15.0	15.0	15.0	15.0	20.0
8	5.0	5.0	10.0	10.0	10.0	15.0	15.0	20.0	15.0	20.0
9	5.0	10.0	10.0	10.0	15.0	15.0	20.0	20.0	20.0	25.0
10	5.0	10.0	10.0	15.0	15.0	20.0	20.0	20.0	25.0	30.0
11	5.0	10.0	15.0	20.0	15.0	20.0	20.0	30.0	35.0	30.0
12	5.0	10.0	10.0	15.0	15.0	20.0	20.0	25.0	30.0	25.0
13	5.0	10.0	15.0	20.0	25.0	30.0	30.0	35.0	35.0	40.0
14	10.0	10.0	15.0	15.0	20.0	25.0	30.0	30.0	35.0	40.0
15	5.0	15.0	15.0	20.0	20.0	25.0	30.0	35.0	40.0	45.0

FIGURE 5-6. UPPER. POWER MATRICES FOR THE REFERENCE SIMULATION SCENARIO. POWERS ARE IN KW. LOWER: MATRIX OF OPTIMAL DAMPING PARAMETER (B_{PTO}) FOR THE DIFFERENT SEA STATES. VALUES ARE IN TON/S.

Results are reported only for the case with maximum electric field of $0.8E_{BD}$ and they are shown in Figure 5-6. In particular, the upper matrix shows the device power matrix and the lower matrix reports the optimal damping factor, resulting from an optimization done on each sea condition. As expected, the optimal level of damping increases with increasing power in the incoming wave.
As for the OWC spar buoy, dielectric losses and electronics efficiency have not been included. It is worth noticing that, in this case, with the mentioned control strategy, electric field is much lower than the prescribed upper bound ($0.8E_{BD}$) during most of the device operation. Since losses decrease exponentially with decreasing electric field, this is likely to result is negligible leakage losses. On the other hand, though, material exploitation for the present case (e.g., cyclic converted energy per unit material weight) is much worse than for the OWC spar buoy, as a rather large volume of polymer is used to produce relatively low power outputs.

6. A NOVEL TETRA-RADIAL AIR TURBINE AS A POWER-TAKE-OFF WAVE ENERGY CONVERSION

The new tetra-radial turbine was conceived to solve the shortcomings presented by twin unidirectional turbines in OWC applications. As revealed by a numerical study [78], the efficiency of the twin unidirectional turbine is negatively affected by one of the twin turbines absorbing a non-insignificant part of the total flow while consuming some power from the generator (due to negative torque). For this reason, the novel tetra-radial air turbine has been proposed as a PTO system for wave energy conversion. The present chapter discusses the initial findings on the potential and challenges associated with this new air turbine.

6.1. Multidisciplinary assessment and design specifications of the tetra-radial air turbine

6.1.1. Description of the tetra-radial turbine

The new tetra-radial turbine consists of two sets of rotor blades mounted on a common shaft and axially offset from each other. Each set of rotor blades is complemented by a set of guide vanes, as in a conventional unidirectional turbine. This whole set of rotor blades and guide vanes (stator) may be regarded as forming two conventional single-stage turbines, T1 and T2 (**Error! Reference source not found.**). The turbine operates between spaces A (OWC air chamber) and B (atmosphere) at pressures p_A and p_B respectively. When $p_A > p_B$, the air should flow only through blade set T1. Conversely, when $p_A < p_B$, the air should flow only through blade-set T2. This is made possible by a double set of curved ducts arranged circumferentially and alternately open to space A and space B, as represented in **Error! Reference source not found.**, and, in perspective, in Figure 6-2. Each rotor is connected to the corresponding set of curved ducts by a bladeless space bounded by curved and plane walls of revolution. The radial extent of this bladeless space allows it to act as a diffuser, recovering part of the kinetic energy at rotor exit before flow entrance into the curved-duct manifold. The configuration of the new turbine makes it possible to install a three-position axially-sliding cylindrical valve that is operated to prevent air from flowing in the reverse direction or to completely block the flow between spaces A and B (**Error! Reference source not found.**). This is made easier by the relatively small size and stroke of the valve. The valve actuator may be pneumatic, electrical or of other type. In the case of flow blockage, if the valve actuator is fast enough (opening and closing times not exceeding a few tens of a second), then this provides away of phase-controlling the OWC plant by latching. Latching is known to be an effective way of substantially increasing the amount of energy absorbed from the waves by oscillating body devices. This could be enhanced by the new turbine proposed here.

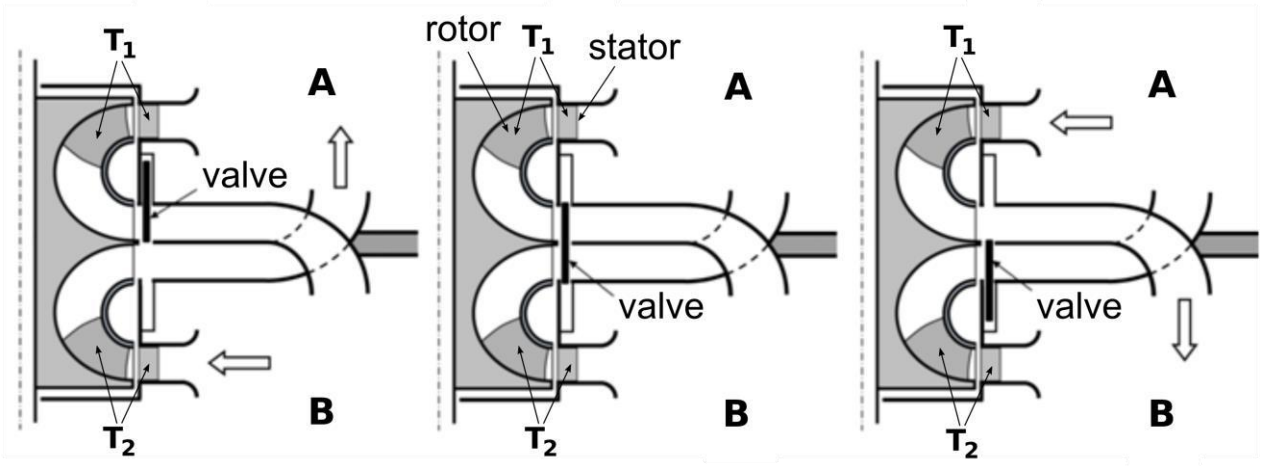

(A) (B) (C)

FIGURE 6-1 SCHEMATIC REPRESENTATION OF THE TETRA-RADIAL TURBINE CONFIGURATION WITH A THREE POSITION AXIALLY-SLIDING VALVE: (A) AIR FLOW FROM B TO A WITH BLOCKED REVERSE FLOW; (B) COMPLETE FLOW BLOCKAGE; (C) AIR FLOW FROM A TO B WITH REVERSE BLOCKAGE

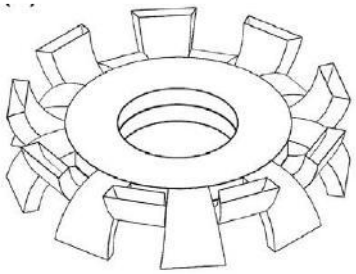

FIGURE 6-2 PERSPECTIVE REPRESENTATION OF THE CURVED-DUCT MANIFOLD, WITH TRAPEZOIDAL EXIT SECTION

6.1.2. Modeling approach for performance evaluation

The efficiency of the tetra radial turbine was investigated. A given geometry was adopted for the turbine rotor. Four geometries of the curved-duct manifold were analyzed (circular, elliptic, rectangular and trapezoidal). The radius ratio R_3/R_1 (Figure 6-3) was allowed to vary in order to investigate the effect of varying manifold-to-rotor size ratio upon the performance of the machine. Naturally, the geometry of the connecting axisymmetric duct has to be adequately adapted. It is assumed that p_A in space A is larger than the pressure p_B in space B, i.e. the pressure head available to the machine is $p_A - p_B > 0$.

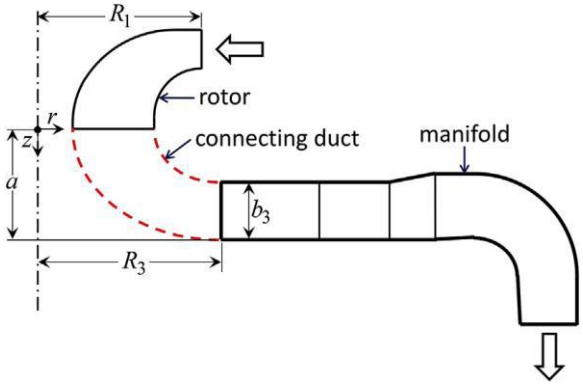

FIGURE 6-3 SCHEMATIC REPRESENTATION OF ROTOR, CURVED-DUCT MANIFOLD AND AXISYMMETRIC CONNECTING DUCT, USED FOR THE NUMERICAL SIMULATION OF THE TURBINE PERFORMANCE

Published experimental data for a conventional radial-inflow turbine were used. The tests had been carried out at low Mach numbers, as under conditions representative of wave energy applications. The turbine geometry is typical of a highly efficient radial-inflow gas turbine.

Computational fluid dynamics (CFD) was employed to model the flow and losses through the curved-duct manifold.

RADIAL-INFLOW TURBINE MODELING

The turbine geometry, the test rig and the experimental techniques and results are described in detail in [79]–[81], where the rotor is designated as the "conventional impeller". The design values of the specific speed N_s and specific diameter D_s (as usually defined in turbomachinery literature, see e.g. [82]) were $N_s = 0.6$ rad/s and $D_s = 3.3$ m. This gives a point in the well-known Balje diagram for 90° radial-inflow turbines [82], [83] close to the highest efficiency zone. The rig was of blow-down type. The air was sucked through a bellmouth into the turbine directly from the atmosphere. The flow rate was obtained from the static pressure relative to atmosphere measured at the bellmouth throat. The work done by the turbine was absorbed by an electrical motor-generator whose stator frame was cradle-

mounted, allowing the measurement of the torque with the help of a torque arm. The turbine rotor was mounted directly onto the generator shaft.

As in most radial-inflow gas turbines, the rotor was of open type (no shroud), Figure 6-4. Details in the rotor dimension can be found in [84]. Close to the rotor entrance there was an annular row of 31 streamlined guide vanes of 64 mm chord. The design flow angle at rotor entrance was 16° with respect to the circumferential direction.

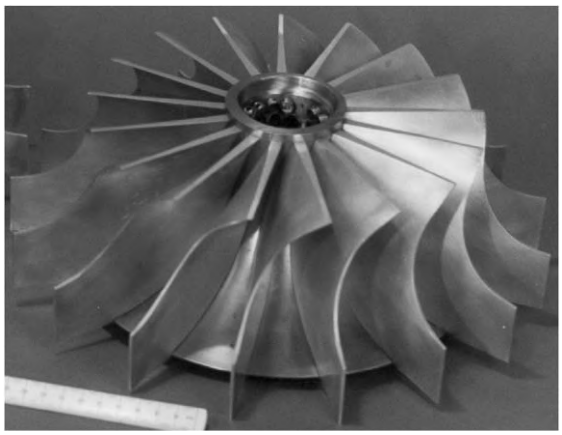

FIGURE 6-4 THE TURBINE ROTOR

Applying dimensional analysis, it is possible to plot characteristic curves of a turbine using dimensionless coefficients as the dimensionless power output Π and the dimensionless flow rate Φ

$$\Pi = \frac{P_t}{\rho \Omega^3 D^5}, \quad \Phi = \frac{Q}{\Omega D^3}. \tag{6-1}$$

Here P_t is the turbine power output, Q is the volume flow rate, Ω is the rotational speed (in radians per unit time), $D = 2R_1$ is the rotor outer diameter and ρ is the air density. Most of the measurements were performed at rotational speeds about 3000 rpm. The experimental data are well approximated by the polynomial (for details, see [84].)

$$\Pi(\Phi) = -2.0356\,\Phi^3 + 6.1343\,\Phi^2 - 0.0606\,\Phi - 0.0006. \tag{6-2}$$

So far, we have only considered the energy conversion in the air flow process that takes place between the machine entrance and the exit from the curved-duct manifold, with pressure head $p_A - p_B > 0$. It should not be forgotten that, during that time, windage losses take place at the other rotor mostly due to aerodynamic drag, even if the flow rate is zero as it should be if the sliding valve is moved into the right position. Such losses take place all the time, alternately at one and the other rotor, and should be accounted for. Not much information on this effect is available, since it is a situation of little practical interest for conventional turbines. The experiments on the radial-inflow turbine on whose results the present analysis is based did not include torque measurements at zero flow rate. However, an estimate of such torque can be made by extrapolation of experimental results. Such results are well approximated by the polynomial relationship in Eq. (6-2), which gives $\Pi_0 = 0.0006$ for the dimensionless value of the turbine power loss (at zero flow rate). The net power is $\Pi_{net}(\Phi) = \Pi(\Phi) - \Pi_0$. The relative windage power loss is important at relatively small flow rates and decreases rapidly with increasing Φ. It is about 5% under conditions close to maximum efficiency.

Detailed radial traverses were made with a three-hole probe at the rotor exit, close to the rotor trailing edges, for the measurements of the static pressure, axial velocity and circumferential (swirl) velocity. These measurements were performed for five values of the dimensionless flow rate. With this measurements it is possible to obtain the radially averaged pressure difference (between the pressure

in the space surrounding the turbine entrance and the static pressure) weighted by the elementary flow rate $(p_A - p_2)_{av}$, which allow us to compute the total-to-static efficiency of the turbine (see e.g. [82])

$$\eta_{ts} = P_t Q^{-1} (p_A - p_2)_{av}^{-1}. \quad (6\text{-}3)$$

The total-to-static efficiency η_{ts} was computed for the five dimensionless values of the flow rate, Φ_1 to Φ_5. The maximum value, $\eta_{ts} = 0.906$, occurs for $\Phi = 0.046$.

CURVED-DUCT MANIFOLD MODELING

What is essentially new in the turbine is the arrangement of curved ducts shown in Figure 6-2 and Figure 6-3. It is important to investigate the losses in that part of the machine in comparison with the power output of the turbine.

Since the curved-duct manifold is circumferentially periodic, only one part of the total flow space needs to be analyzed. Figure 6-5 represents the computation domain. There are Z ducts open to space A and equal number open to space B. The entrance into the domain is a segment of circular cylindrical surface of radius R_3 and width b_3, with area $A_3 = 2\pi R_3 b_3 / Z$. The following configuration was adopted: $Z = 9$, $b_3 = R_3/3$, area $A_3 = 0.2327\, R_3^2$. Four geometries were numerically modelled for the curved ducts, having exit sections of trapezoidal, rectangular (with rounded corners), elliptic and circular shapes. They are represented, together with their area A_4, in Figure 6-6.

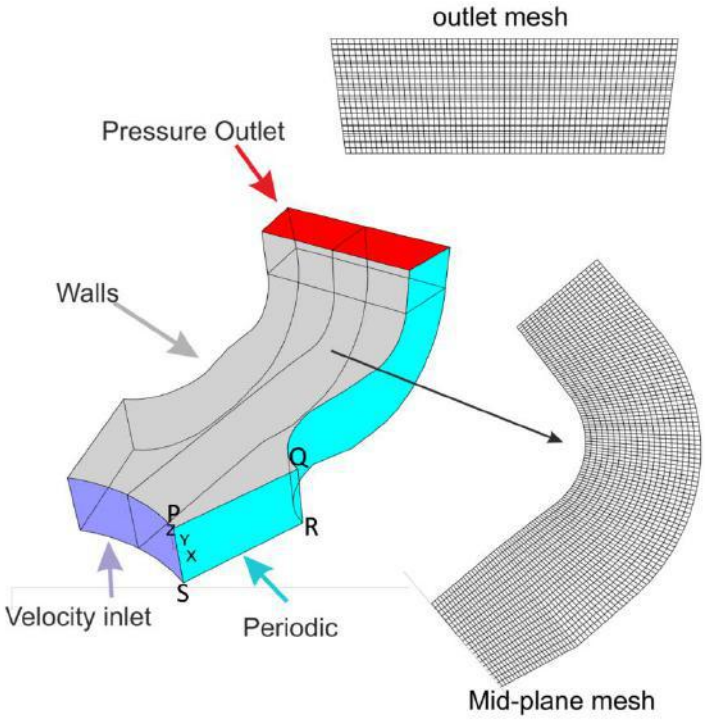

FIGURE 6-5 COMPUTATIONAL DOMAIN USED FOR THE FLOW ANALYSIS (CFD COMPUTATIONS) IN THE CURVED-DUCT MANIFOLD, MESH DETAILS AND BOUNDARY CONDITIONS

Computational fluid dynamics (CFD) based on the numerical integration of the Reynolds-averaged Navier-Stokes (RANS) equations was employed to simulate the flow through the curved-duct manifold. In the computations, it was assumed that the entrance flow at radial coordinate $r = R_3$ is axisymmetric with uniform radial velocity V_{3r}, uniform circumferential velocity $V_{3\theta}$ and zero axial velocity $V_{3z} = 0$. The angle of the entrance velocity vector with the radial direction is $\gamma = \arctan(V_{3\theta}/V_{3r})$. PQRS and the homologous surface (Figure 6-5) are open surfaces introduced to bound the circumferentially periodic flow space. The computations were performed for $R_3 = 0.450\ m$, $V_{3r} = 20$ m/s and $\gamma = 0°, 15°, 30°, 45°$.

The flow simulation was done with FLUENT v12, which employs the finite-volume numerical method for solving the RANS equations by using a segregated solver. The mesh was structured, totally composed of 3×10^5 hexahedrical cells and was built in GAMBIT 2.4. Some details can be seen in Fig. 19, that also shows the imposed boundary conditions: velocity at inlet and pressure at outlet. The realizable $k-\varepsilon$ turbulence model was used with the standard wall function. The y^+ values were in the correct range, over 95% of the cells were in the interval $30 \leq y^+ \leq 150$. The time-dependent term was approximated by a second-order implicit scheme. The pressure-velocity coupling was performed with the aid of the SIMPLE algorithm. The higher order Monotone Upwind Scheme for Conservation Laws (MUSCL) was used for convective term discretization and the classical central difference approximation for diffusion terms. The residuals were set to 10^{-5}, reached after approximately 2000 iterations.

The loss (including exit kinetic energy loss) per unit mass of air at the curved-duct manifold is computed from the pressure difference between the total pressure at section 3 and the exit pressure.

CONNECTING DUCT MODELING

We analyze the flow in the duct, formed by walls of revolution, that connects the rotor and the curved-duct manifold (Figure 6-3). The flow is assumed axisymmetric. We introduce radial coordinate r and axial coordinate z, and consider two points on a generic stream surface of revolution: point P_2 at the exit from the rotor $(r = x, z = 0)$ and point P_3 at the entrance to the curved-duct manifold $(r = R_3, z = a - y)$. The velocity components are $V_{2r} = 0, V_{2z}(x), V_{2\theta}(x)$ at point P_2, and $V_{3r}(y), V_{3z} = 0, V_{3\theta}(y)$ at point P_3.

We further assume ideal fluid flow (viscous losses are neglected), so that total pressure, as well as angular momentum per unit mass, are constant over a stream surface. Results from the radial-inflow turbine modeling shows that the pressure at rotor exit is almost invariant with the radial coordinate. It is not unreasonable to assume that the pressure p_3 at the curved-duct manifold inlet is approximately invariant with axial coordinate y.

Considering Bernoulli equation between points P_2 and P_3, the conservation of angular momentum and the continuity of flow rate between stream surfaces, we can obtain the correct value of pressure p_3 that satisfies the stated conditions for the adopted width b_3.

OVERALL PERFORMANCE

The overall efficiency of the machine is

$$\eta_{\mathrm{AB}} = \frac{\Pi_{\mathrm{net}}}{\Phi\Psi_{\mathrm{AB}}}, \tag{6-4}$$

where Π and Φ are defined as in Eq. 6-1, the subscript "net" means that windage power losses were subtracted, and

$$\Psi_{\mathrm{AB}} = \frac{p_{\mathrm{A}} - p_{\mathrm{B}}}{\rho\Omega^2 D^2}. \tag{6-5}$$

Here, as above, p_{A} is the pressure in space A surrounding the turbine inlet and p_{B} is the pressure in space B at the machine exit.

In the calculations, we assume that the inlet pressure p_{A}, the flow rate Q and the rotational speed Ω are fixed, and compute the value of the exit pressure p_{B}. Note that the dimensionless coefficient ε of losses in the curved-duct manifold, plotted in Figure 6-6, was computed assuming uniform values of the radial and circumferential components of the velocity at duct inlet. This is not the case: the values of V_{3r} and $V_{3\theta}$ are functions of the axial coordinate y, and so is the angle $\gamma = \arctan(V_{3\theta}/V_{3r})$. This difficulty is circumvented by taking the loss coefficient also as a function of y (and consequently of the radial coordinate x), the same happening with the computed value of the exit pressure p_{B}, which we denote as

$\hat{p}_B(x)$. Finally, we compute an average value for p_B by integration, taking the elementary flow rate as a weight function. Applying the same rational in dimensionless form, the value of Ψ_{AB} is obtained.

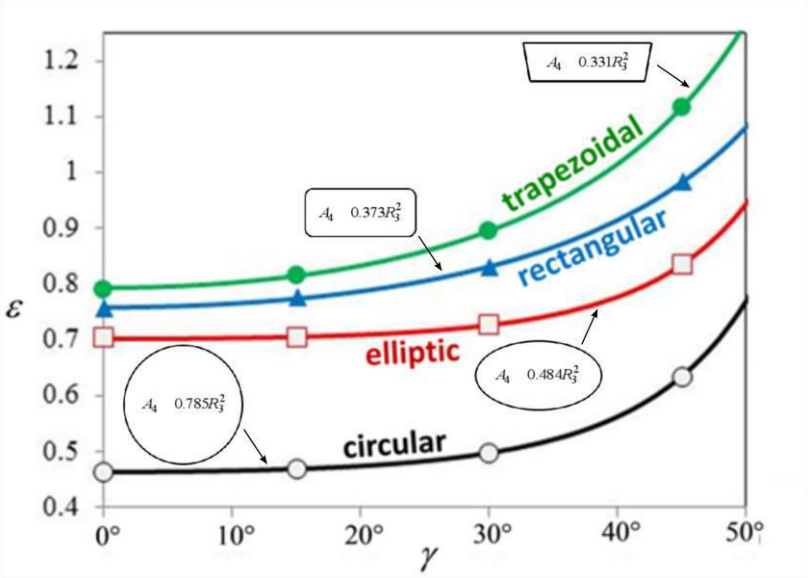

FIGURE 6-6 LOSS COEFFICIENT ε AT THE CURVED-DUCT MANIFOLD VERSUS ANGLE OF INCIDENCE γ FOR THE FOUR EXIT SECTION GEOMETRIES ($\gamma = 0$ MEANS PURELY RADIAL INLET FLOW). THE AREAS OF THE CURVED-DUCT-MANIFOLD EXIT SECTIONS ARE PRESENTED AT THE SAME SCALE

PERFORMANCE RESULTS AND COMPARISON WITH THE BI-RADIAL TURBINE

Numerical results were obtained for the performance of the whole machine operating between inlet pressure p_A and outlet pressure p_B. Results for the overall efficiency η_{AB} versus flow rate coefficient Φ are shown in Figure 6-7 for the rectangular exit section. Curves are shown for five values of the ratio $R_3/R_1 = 0.8, 1.0, 1.2, 1.4, 1.6$. In each figure, the curve of the total-to-static efficiency η_{ts} of the radial-inflow turbine alone (corrected for windage power losses) is also shown for comparison. We recall that, when radius R_3 is changed, all dimensions of the curved-duct manifold vary proportionally, i.e. the geometry (apart from size) is conserved.

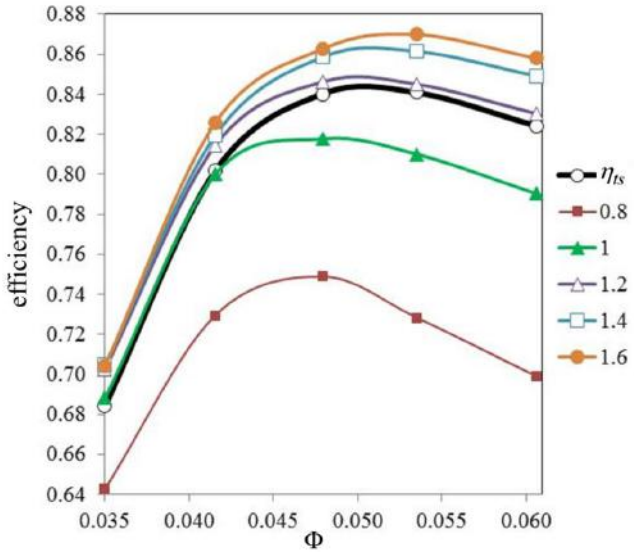

FIGURE 6-7 OVERALL EFFICIENCY η_{AB} AS A FUNTION OF THE FLOW RATE COEFFICIENT Φ, FOR $R_3/R_1 = 0.8, 1.0, 1.2, 1.4, 1.6$. THE EXIT SECTION OF THE CURVED-DUCT MANIFOLD IS CIRCULAR. ALL CURVES ARE CORRECTED FOR WINDAGE LOSSES.

The new tetra-radial turbine and the bi-radial turbine are both radial-flow turbines for bidirectional flows that have a two-position element that is moved in translation whenever the flow changes its direction. The element is a cylindrical valve in the new turbine and the twin set of guide vanes in the bi-radial turbine. It is interesting to compare the performance of both turbines, one of the reasons being that the peak efficiency, measured in model testing, of the bi-radial turbine seems to exceed that of any other self-rectifying air turbine. Information from model testing of the bi-radial turbine is available in [16]. In the comparison, the curved-duct manifold of the new turbine has a circular exit section and $R_3/R_1 = 1.2$. Figure 6-8 (a) shows that the peak efficiency of the new turbine exceeds that of the bi-radial turbine by about 8%. This peak occurs at a lower value of the flow rate coefficient $\Phi_{\eta_{\max}}$. However, the efficiencies are plotted versus the ratio $\Phi/\Phi_{\eta_{\max}}$, which provides an easier comparison of the two turbines close to their best efficiency conditions.

It is also of interest to know the ratios of rotor diameter, $D_{\text{new}}/D_{\text{birad}}$, and rotational speed, $\Omega_{\text{new}}/\Omega_{\text{birad}}$, of the new turbine and the bi-radial turbine, if the two turbines are to operate at peak efficiency under identical conditions of flow rate Q and pressure difference $p_{\text{A}} - p_{\text{B}}$. The values are $\Phi_{\text{new},\eta_{\max}} = 0.0517$, $\Psi_{\text{new},\eta_{\max}} = 0.264$ for the new tetra-radial turbine with circular exit section and $R_3/R_1 = 1.2$, and $\Phi_{\text{birad},\eta_{\max}} = 0.0963$, $\Psi_{\text{birad},\eta_{\max}} = 0.338$ for the bi-radial turbine. From the definitions of Φ and Ψ, we easily find $D_{\text{new}}/D_{\text{birad}} = 1.28$, $\Omega_{\text{new}}/\Omega_{\text{birad}} = 0.88$. For an identical application, the new turbine has a larger rotor and rotates at a lower rotational speed, as compared with the bi-radial turbine.

The turbine is to be mounted on an OWC wave energy converter and operate under real random wave conditions. A reasonable assumption is to assume that the oscillation in air pressure head $\Delta p = p_{\text{A}} - p_{\text{B}}$ is a Gaussian process with variance σ_p^2, whose probability density function is taken from [59].

The instantaneous power output of the turbine versus the pressure head is assumed known in dimensionless form as $\Pi_{\text{net}} = f_{\Pi}(\Psi_{\text{AB}})$. From the definitions of Ψ_{AB} and Π, we find that the instantaneous turbine net power output $P_{\text{t,net}}$ can be expressed as a function of the pressure head Δp. Knowing the pressure oscillation for a given sea state it is possible to compute the time-averaged turbine power output $\bar{P}_{\text{t,net}}$ and its dimensionless form $\overline{\Pi}_{\text{net}}$.

The average efficiency of the turbine is defined as $\bar{\eta}_{\text{AB}} = \bar{P}_{\text{t,net}}/\bar{P}_{\text{avai}} = \overline{\Pi}_{\text{net}}/\overline{\Pi}_{\text{avai}}$, where $\bar{P}_{\text{avai}}$ is the time-average of the power $P_{\text{avai}} = Q\Delta p$ available to the turbine, and $\overline{\Pi}_{\text{avai}}$ is its dimensionless form. The values of $\bar{P}_{\text{avai}}$ and $\overline{\Pi}_{\text{avai}}$ can be obtained by integration with respect to Δp and Ψ, respectively, as explained above for $\bar{P}_{\text{t,net}}$ and $\overline{\Pi}_{\text{net}}$. In the integrations, it is assumed that f_{Π} is an even function, and the infinite limits of integration are replaced by finite ones. It should be noted that extrapolated values of Ψ_{AB} versus Φ were used in the integrations.

Results for the average efficiency of the new turbine in random waves, together with values for the bi-radial turbine, are shown in Figure 6-8 (b). As in the comparison above for instantaneous values, the curved-duct manifold of the new turbine has a circular exit section and $R_3/R_1 = 1.2$. The maximum value of the average efficiency of the new turbine is 79.6% and occurs for $\sigma_\Psi \approx 0.22$. It exceeds the corresponding value of the bi-radial turbine by about 8%.

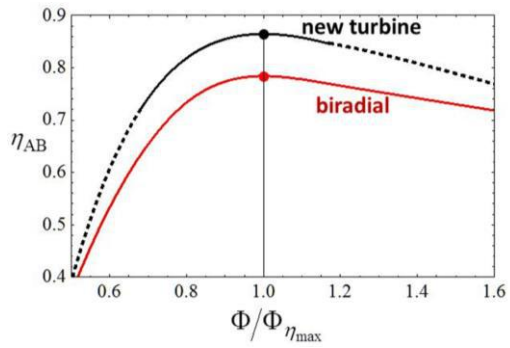

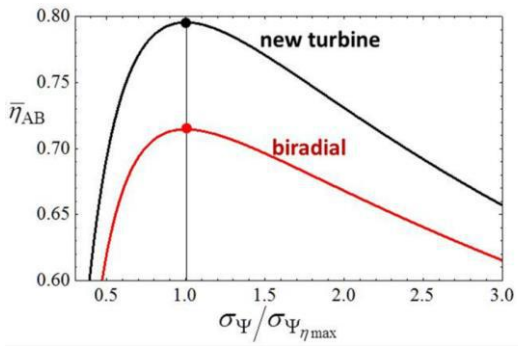

(A) (B)

FIGURE 6-8 COMPARISON OF EFFICIENCY BETWEEN THE TETRA-RADIAL (NEW TURBINE) AND THE BI-RADIAL TURBINE WITH SLIDING GUIDE VANES: (A) EFFICIENCY VERSUS FLOW RATE RATIO $\Phi/\Phi_{\eta_{max}}$, WHERE SUBSCRIPT η_{max} MEANS MAXIMUM EFFICIENCY CONDITIONS; (B) AVERAGE EFFICIENCY $\overline{\eta}_{AB}$ IN IRREGULAR WAVES VERSUS THE RATIO $\sigma_\Psi/\sigma_{\Psi_{\eta_{max}}}$, WHERE SUBSCRIPT η_{max} MEANS CONDITIONS AT MAXIMUM VALUE OF $\overline{\eta}_{AB}$ AND σ_Ψ IS DIMENSIONLESS ROOT MEAN SQUARE OF PRESSURE HEAD.

6.1.3. Concluding remarks

A new air turbine for bidirectional flow applications in wave energy conversion was presented. The numerical values of the performance of the whole machine are based on available experimental results for the gas turbine performance, together with CFD results for aerodynamic losses in the curved duct manifold. Four different geometries for the curved-duct manifold were numerically simulated. This was combined with five different sizes. As a consequence of detailed measured flow velocity and pressure data at gas turbine rotor exit being available only over a limited range of flow rates, results for the overall efficiency of the whole turbine could be computed only over the same range of flow rates. Extrapolation was used to compute average performance of the turbine in irregular waves.

Windage losses, that occur at the inactive rotor and are inherent to the machine conception, were found to be a major loss, reducing the overall efficiency close to best efficiency point by about 5%. The curved-duct manifold with circular cross section is the most efficient of the four tested geometries, because of its largest area, and presumably also because the rounded shape avoids secondary flow losses at corners. As should be expected, the overall performance depends on the size of the manifold, represented by the radius ratio R_3/R_1. It is only marginally improved for $R_3/R_1 > 1.4$, the range $R_3/R_1 = 1.0$ to 1.2 possibly being a good compromise between aerodynamic performance, overall machine size and cost.

Comparisons were presented between the new turbine (with $R_3/R_1 = 1.2$ and circular exit section) and the bi-radial turbine (sliding guide-vanes version), the latter being possibly the most efficient self-rectifying turbine model-tested so far. The new turbine was found to be more efficient, both in peak instantaneous efficiency and in maximum average efficiency in irregular waves, by a margin of about 8%.

For identical applications (same pressure head and flow rate), the new machine is larger than the bi-radial turbine, in terms of rotor diameter ($D_{new}/D_{birad} = 1.28$) and of overall diameter, and its rotational speed is lower ($\Omega_{new}/\Omega_{birad} = 0.88$) . Apart from the higher efficiency, the new machine has the advantage of the moving element being a simple axially-sliding cylindrical valve rather than the much heavier and mechanically more complex twin set of guide vanes.

6.2. Engineering constraints and evaluation for large-scale applications

The models used so far for the simulation of the tetra-radial turbine used a hybrid approach, applying very detailed numerical CFD codes for analyzing the flow in the curved-duct manifold and experimental data from a radial-inflow turbine. This approach does not solve the whole problem simultaneously yet it was able to display the large potential of this turbine, whose performance exceeds the one of the bi-radial turbine.

Future work, which will be developed within the framework of work-package 4, will include the experimental testing of the entire turbine. With this testing program, a more detailed analysis of the turbine will be carried out. Simulations will be done for steady and oscillatory flow. A three-dimensional representation of the test rig is depicted in Figure 6-9. The guides vanes used at the turbine entrance

are shown in Figure 6-10. The blades were made from resin using silicon molds, where the master piece was made from an aluminum alloy using a 3-axis CNC machine.

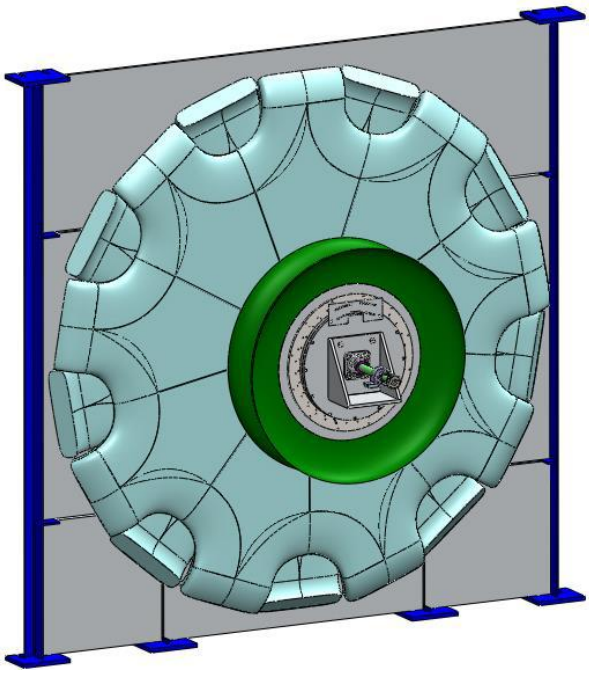

FIGURE 6-9 THREE-DIMENSIONAL REPRESENTATION OF THE TETRA-RADIAL TURBINE TEST RIG

FIGURE 6-10 THE THIRTY-ONE GUIDE VANES MADE FROM RESIN OF THE ENTRANCE STATOR

In a full-scale application, due to the particular geometry of the turbine, the curved-duct manifold may have to support the entire structural loads of the turbine and electrical generator. This problem can be circumvented by introducing an additional supporting structure connected to the equipment attached to the shaft. Since the curved duct manifold is exposed to the exterior environment it may also have to withstand possible green water loads and the high/low pressure oscillations inside the air chamber.

Special attention should also be given to the operation of the sliding cylindrical valve since it has to be actuated at every few seconds (about half the wave period). It should be understood how efficient and precise the valve has to be to prevent reverse flow and the loads required to perform this operation.

7. A NOVEL WATER TURBINE AS A POWER-TAKE-OFF FOR WAVE ENERGY CONVERSION

7.1. Multidisciplinary assessment of the potential of the water turbine

In the early decision process of the WETFEET project with respect to the choice of an appropriate PTO for the Symphony wave energy converter, the decision to use a water turbine (against a spindle drive or similar linear electro-mechanical options) was taken, as presented in Deliverable 2.2 [2].

Initial considerations about the type of the water turbine were presented, which were backed with more systematic work in the following project phase. The work presented in the following is largely provided by de Jong [85]. Major challenge for the design of a water turbine for the Symphony is that the flow speed inside the turbines is bi-directional and irregular. There is no off-the-shelf solution for these operational requirements, which is why a novel water turbine as part of the power take off for a Symphony WEC has to be developed. The turbine will be engineered, manufactured and tested within WP4 of the WETFEET project, using the Symphony WEC as a reference basis. Focus of the design exercise presented in the following is therefore to build first a prototype of the water turbine for a 1.5m diameter Symphony, while considerations for a full-scale device are included as a secondary objective.

The following questions reflect the starting point for this exercise with the main objective of finding the most suitable turbine for the Symphony WEC:

1. Which water pumps/turbines are currently used as PTO turbines and how is the PTO conversion mechanism achieved?
2. What are the requirements for the PTO turbine for the Symphony WEC?
3. Which currently available turbines are most suitable for adaptation to the PTO requirements of the Symphony WEC?
4. Which criteria influence the decision for the PTO turbine for the Symphony WEC?
5. Which turbine concept is the most suitable for the PTO turbine for the Symphony WEC?
6. What is the conceptual design of the PTO turbine for the Symphony WEC?

The work path to address these questions started from an in-depth analysis of WECs and existing PTOs, especially potential precedences. A description of the dynamics of the Symphony, and an analysis of existing hydro turbines, including the distinction between impulse and reaction turbines, and other differentiating operational aspects between turbine types was made [85]. The possibility of using a conventional pump design as a turbine (also referred to as a positive displacement turbine) is derived as an alternative, and systematically compared to three other potential candidates. After the turbine type is elected, a more detailed design exercise based on the expected flow data (detailed design, estimation of losses and a study to the slip (leakage) and flow pulsation of the choses turbines) provides the input to the work to be done in WP4.

7.1.1. Turbine design requirements and type choice

The operational nature of the Symphony induces some unconventional requirements for the turbine. Figure 7-1 shows a simplified scheme of the Symphony and the flow in the membrane. An oscillating force pushes the piston down. In one instance, a strong force is exerted, which reduces significantly several seconds. Due to these sharp forces variations, the pressure rise in the air spring tank is strong

enough to push the piston upwards during the low force period. If the flow of the water is synchronised, the water oscillates between the piston and air spring tank. In the theoretical case of the oscillation being without losses, the pressure rise in the air spring tank would increase during every oscillation, due to resonance. By placing a turbine between the two components, the motion is damped. In equilibrium conditions, the turbine extracts the amount of energy that is added by the piston. If the turbine extracted all fluid energy from the flow, the oscillation would stop. This is fundamentally different than a turbine in for example a hydroelectric dam, where the goal is to extract 100% of the energy in the water flow. Another difference is that the turbine in Figure 7-1 must extract energy in two directions.

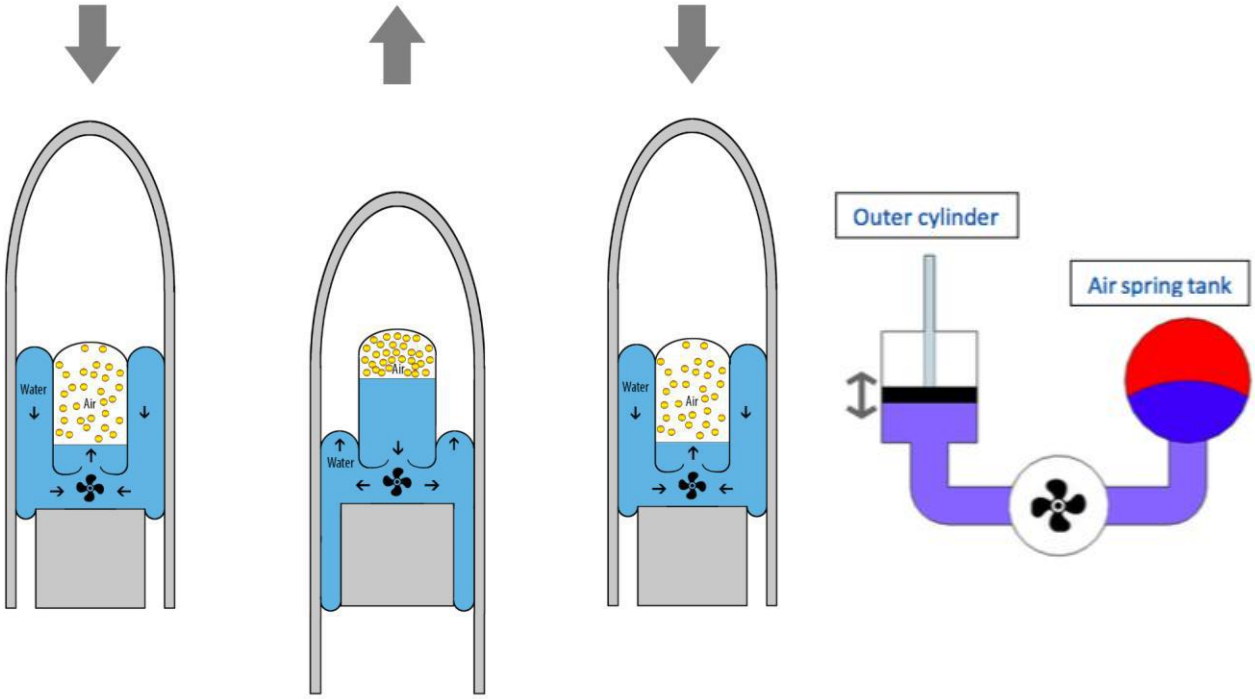

FIGURE 7-1 OPERATIONAL PRINCIPLE OF WATER TURBINE IN SYMPHONY (LEFT) AND TEST BENCH/LABORATORY SETUP VISION FOR CONTROLLED TESTING OF PROTOTYPE (RIGHT)

During each stroke, an amount of water is pushed through the turbine and pushed back through the same turbine. There are significant technical uncertainties related to this operational mode, especially the reciprocity of (incompressible) water flow within one wave cycle is without precedence in turbine technology. Turbulence is another issue and the fact that the turbine is inserted in a closed water body, which potentially will not be mixed sufficiently. Heat generated by turbulence – which is in principle more critical than for stationary flow – might thus build up in the turbine vicinity and cause cavitation or other issues. Developing and building a first prototype of the novel water turbine is therefore high priority, before the future prospects and further Symphony developments can be specified. Figure 7-1 on the right side shows a scheme for the prototype tests of the turbine for a 1.5m Symphony device to be developed in WP4 of WETFEET, and the requirements for the turbine based on the specifications and dimensions of the 1.5m diameter Symphony are shown in the following Figure 7-2.

REQUIREMENT	VALUE	UNIT
FLOW PER STROKE	2 x 413	l
WAVE PERIOD	10	s
MAXIMUM FLOW PER SECOND	130	l/s
PEAK PRESSURE DROP	25	meter head
PEAK POWER TAKE-OFF	32.5	kW
REQUIRED OPERATING TIME WITHOUT MAINTENANCE	6	years
ROTATIONAL VELOCITY	350	Rpm
SPECIFIC SPEED (PROTOTYPE)	36	-
SPECIFIC SPEED (FULL SCALE)	198	-
SPECIAL REQUIREMENTS		
Must be able to operate bidirectional due to the oscillating motion of the symphony		
Must be able to pump water to the membrane or air spring tank to be able to put the symphony in any vertical position		

FIGURE 7-2 REQUIREMENTS FOR 1.5M DIAMETER SYMPHONY TURBINE PROTOTYPE DESIGN

Following a comprehensive analysis of existing turbines including a literature study as part of [20], which is attached to this document as Appendix F, four concepts were filtered as most promising candidates for an adaption in Symphony:

1) Positive displacement turbine;
2) Impulse turbine;
3) Francis turbine;
4) Kaplan turbine.

These concepts are compared in a semi-quantitative assessment matrix where first selection criteria and weighting factors are defined whereupon scores were given.

7.1.2. Turbine type analysis

In order to design a turbine that meets the design requirements a turbine type analysis was set up (see extracts from de Jong, [85] in Appendix F), based on a score matrix with a selection of the turbine types that are expected to meet the requirements. The turbine design requirements together with the score matrix were setup in order to compare turbine concepts for both small scale and large scale PTO's. This is due to potentially changing preferences and challenges when moving from a small-scale prototype (like in the present design exercise for testing within WETFEET) to a serial device e.g. 4-5 times the diameter.

The selection criteria are based on efficiency, bidirectional, pump functionality, manufacturability, maintenance and reliability. Each concept receives a grade for every selection criterion. The weighting factor states how important a criterion is for the trade-off. It is hard and can be to a certain extent subject to bias to quantify the scores and weighting factors, especially because the design process is still in the conceptual phase. The reason for a high or low score and weighting factor are explained for every criterion. The exact scores are often given on engineering judgement and validated during technical consultation meetings within Teamwork.

- **Efficiency**

The efficiency of a turbine depends mainly on the specific speed N_s, which for turbines is the rotational speed where 1 kW power is generated per meter head input pressure [41].

$$N_s = \frac{N\sqrt{P}}{h^{5/4}}, \tag{7-1}$$

where N is the rotational speed in rpm, P is the power in kW, and h the head (pressure difference over the turbine plane). For pumps, the specific speed is not based on power, but on flow: it indicates the rotational speed where 1 m^3/s flow is pumped with a head rise of 1 meter water column.

$$N_s = \frac{N\sqrt{Q}}{(gh)^{3/4}}, \tag{7-2}$$

where Q is the flow in m^3/s and g the gravitational constant.

The formula for the specific speed is applied to the rotational speed (350 rpm) and pressure difference (25 m head) over the turbine, similar for the prototype and full scale model. The nominal power for the prototype is set to 32.5 kW, therefore the specific speed as a function of rotational speed, nominal power and pressure head is 36. For the prototype targeted in this exercise, a 1MW rating is assumed while rotational speed and pressure head remain, resulting in a specific speed of 198.

As can be seen in common turbine diagrams, the impulse type turbine is the best choice in the prototype situation. The Kaplan turbine scores the lowest and the Francis turbine scores halfway between the impulse and Kaplan turbine. For the full scale model, a high score for the Francis turbine is achieved, followed by the Kaplan turbine due to its reaction nature. The impulse and positive displacement turbine concept score the lowest.

The efficiency does not influence significantly the design for the prototype turbine. The prototype, used for testing, is allowed to generate energy with a lower efficiency, as priority is its basic functionality and identification of improvements. For the full scale model, the efficiency increases in importance, but because the differences are small the weighting factor only increases one point.

- **Bidirectionality**

The positive displacement turbine and impulse turbine can be operated bidirectional without any complex arrangements. Some efficiency might be lost for the impulse turbine because inflow and outflow must be identical and cannot be designed specifically for one purpose. This results in a high score for these concepts. The axial reaction turbine requires rotational blades to be able to operate under bidirectional flow. The radial reaction turbine needs a more complex design to be able to operate bidirectional and therefore receives a low score.

The ability of a concept to operate bidirectional is of great importance for the functioning of the system and therefore weighs heavier than almost all other criteria. This is equal for the prototype and the full-scale model. In principle, every turbine can be equipped with auxiliary equipment (valves, guide vanes, channels) to make use of bi-directional flow, even if the turbine cannot reverse rotational direction. Thus, it would be inappropriate to make this an exclusion criterion, however the score gets adjusted according to the difficulty to make such adjustments.

- **Pump functionality**

For the prototype, the pump functionality of a concept has a very high priority. The pump must be able to control the system accurately. Therefore, this criterion is the most important one for the prototype. For the full-scale model, the pump function is only a feature of the Symphony which enables the device

to start up after a period of rest. The turbine must be able to perform this function, but slip and low efficiency are allowed. Therefore, the influence of the pumping qualities of a concept is considered less important for the full-scale model.

The positive displacement turbine scores highest for this criterion. The blades of the axial reaction turbine can be positioned so that the turbine functions as a pump. This does not receive the highest score because adjustable blades are necessary for this function. The radial reaction turbine can pump the water only one way. However, if the assumption is made that the concept is made bidirectional, the concept will be able to pump water. The impulse turbine is not able to pump water. An additional provision must be made to enable this concept to pump water such as rotational turbine blades or an additional pump.

- **Manufacturing**

The number of products that need to be manufactured in future influences the score for this criterion. Only a single version of the prototype will be manufactured. The size of the prototype gives the option to manufacture a standard pump, or with relatively slight adjustments, without the need for an entirely new design. However, for the full-scale model, the volume flow and power are too large for standard pump types to be used as turbines. This means that a specially engineered pump must be assembled during the manufacturing process of the Symphony, which increases the complexity and costs. An impulse turbine only increases in size between the prototype and full scale model so the score will remain the same. The geometry of a radial reaction turbine is the most complex of all turbines, but the runner is just one piece which can be placed in the turbine quite easily. The complex geometry induces high costs for the prototype because only a single turbine can be produced. For the full-scale serial production, a mould can be used several times and runners can be ordered in batches, which will decrease the costs and therefore increase the score of this concept. The blades of the axial reaction turbine have a more complex shape than the reaction turbine and due to the rotating blades the assembly is more complex. Therefore this concept scores low for manufacturing.

The manufacturing complexity is important for the prototype mostly because of the limited budget available to design and manufacture the turbine. Nevertheless, a quality product is still required and a moderate weighting factor is therefore given. For large scale manufacturing, investments can be made in specialized tools and services to support the manufacturing process. This reduces the influence of this criterion and therefore the weighting factor.

- **Maintenance**

Maintenance is dependent on the number of moving parts and the internal stresses in the turbine. Especially the load on parts like gears is maximum due to the bidirectional nature of the turbine. This affects the positive displacement turbine the most and therefore the score for maintenance is low for this concept. The impulse turbine and radial reaction turbine both have no moving parts besides the runner and are scored high. The axial reaction turbine requires more than the radial and impulse turbine maintenance because of the rotating turbine blades.

The prototype will be used to prove the concept and measure the performance of the Symphony. The operating hours of the full-scale turbine will be a multiple of the operating hours of the prototype. Because the Symphony is installed under water attached to the ocean floor, maintenance is expensive and time consuming. It is very important that the Symphony is able to operate for years without requiring maintenance. However, this mainly applies to the full-scale, serial device. If maintenance is necessary for safe and reliable operation, the cocoon will be part of the solution for simple removal (see chapter **Error! Reference source not found.**. For the prototype, frequent maintenance and inspections are part of the program anyway, which is why the influence of maintenance is small.

- **Reliability**

Reliability is the most important factor for both development horizons (prototype and full-scale, serial device) of the Symphony. Maintenance intervals may decrease to increase the reliability of a concept. A simple explanation for this choice is that regular maintenance can be planned months, or maybe years, in advance and can be performed very efficient. In the case of damage parts during operation, an unplanned operation must be performed under short notice.

- **Scores and Conclusion of the turbine type analysis**

The criteria, weighting factors and scores for the prototype are given in Figure 7-3 and for the full scale device in Figure 7-4. The contribution score for one criterion per concept is the product of the weighting factor and the score. The positive displacement turbine concept scores clearly highest for the prototype. The trade-off for the full scale model is not explicit. The development of the power take-off system for this phase will not be continued at this moment, but resumes when prototype testing is finished.

Prototype
For the prototype, the pump as turbine concept is a clear winner. This results makes sense as this concept scores very high at pump functionality and reliability which are considered to be very important characteristics for the prototype. This report will continue with the elaboration of this concept up to the point where a reliable estimation can be made of the losses which will occur. The goal is to gain more knowledge about the operational behaviour of the Symphony wave energy converter by testing the prototype

Full scale device
The trade-off for the full scale model gives no undisputed winner. The pump as turbine concept receives a score of 66/90 and the axial reaction turbine 67/90. The axial turbine is more efficient than the pump as turbine but loses its preference because complex rotating blades are necessary to full use the capabilities of the axial turbine. The development of the power-take-off turbine for the full scale model will be halted for this phase of the project.. Knowledge from the prototype can be used to make a more solid turbine concept selection.

Following this evaluation exercise, a next level of design choice comparing different types of positive displacement pumps was made, where initially the lobe pump was identified as best option for the Symphony wave energy converter. The design of such a system must be in a way that the lobes are as close as possible to each other, but do not touch, for every moment in a full rotation. This and a pulsating flow pattern introducing vibration and mechanical wear made a similar concept, the External Circumferential Piston (ECP) pump, appear more suitable. The advantage of the ECP pump is that it has less slip, non- pulsating flow and less critical synchronization requirements.

		Positive displ.		Impulse		Francis		Kaplan		Ideal concept	
Selection criteria	Weighting factor	Score	Total	Score	Total	Score	Total	Score	Total	Score	Total
Efficiency	2	4	8	5	10	3	6	1	2	5	10
Bidirectional	4	5	20	4	16	1	4	3	12	5	20
Pump functionality	5	5	25	1	5	3	15	4	20	5	25
Manufacture	3	5	15	4	12	2	6	1	3	5	15
Maintenance	1	1	1	5	5	5	5	3	3	5	5
Reliability	5	5	25	2	10	1	5	5	25	5	25
Total			94		58		41		65		100

FIGURE 7-3 EVALUATION MATRIX FOR THE PROTOTYPE TURBINE FOR THE 1.5M SYMPHONY, USED FOR DECISION ON FURTHER DESIGN PROCESS WITHIN WETFEET

		Positive displ.		Impulse		Francis		Kaplan		Ideal concept	
Selection criteria	Weighting factor	Score	Total	Score	Total	Score	Total	Score	Total	Score	Total
Efficiency	3	2	6	1	3	5	15	4	12	5	15
Bidirectional	4	5	20	4	16	1	4	3	12	5	20
Pump functionality	2	5	10	1	2	3	6	4	8	5	10
Manufacture	1	2	2	4	4	5	2	1	1	5	5
Maintenance	3	1	3	5	15	5	15	3	9	5	15
Reliability	5	5	25	2	10	1	5	5	25	5	25
Total			66		50		47		67		90

FIGURE 7-4 EVALUATION MATRIX FOR THE FULL-SCALE MODEL, TO SUPPORT TECHNO-ECONOMIC EVALUATION OF FUTURE DEVELOPMENTS

7.1.3. The turbine design exercise

During the design process of evaluating the initial choice for a positive displacement system, a lobe turbine, a few disadvantages were found which could be solved by using an ECP turbine instead. To investigate whether this statement was true, the impacts of the design changes of replacing the lobe turbine for the ECP turbine were examined. Three major aspects were examined: Slip, the synchronization mechanism and flow pulsation. For slip reduction, the investigation included a CFD simulation study with the commercially available software Solidworks Flowsimulation for four different concepts [19]. Following this exercise, the required manufacturing tolerances are assessed. Finally the effect of water (and so the turbine itself) heating up through turbulence is assessed, as it leads to thermal expansion. During the final design of the turbine, a small gap must be placed between the parts to accommodate this expansion.

Due to the technical advantages of an ECP turbine in respect to the lobe turbine, it was decided to continue developing an ECP turbine. The following steps outline the continuation of developing a fully defined detailed turbine design:

- Design of the complete flow path (including inlet, outlet and exact pump house dimensions)
- Design of the runner geometry to reduce losses and optimize efficiencies
- Research labyrinth sealing options to reduce leakage in ECP turbine
- Design external runner synchronizing mechanism and generator interface

The required flow characteristics determine the size of the positive displacement turbine. To support this design step, a tool was made for creating the shape of the runners. The advantages of an ECP turbine in respect to a lobe turbine is quantified by CFD simulations (Solidworks Flowsimulation), comparing four models which represent the geometry as in a real turbine. Drawings for these geometries were made in [19], and the design process was taken further from this point, but both cannot be presented at this stage in a public deliverable due to ongoing IP protection processes:

1) Lobe model: A rounded surface moves along the inner surface of the casing. The slit size is the distance between the tip of the lobe and the casing. The distance between lobe and casing increases rapidly at both sides of the lobe tip. The result is that the water flow experiences the minimum slit size only at one point.
2) ECP model: This model reduces the slip by increasing the length of the slit. Instead of one point where the minimal slit size occurs, a path across 90 degrees of the circumference lessens the water flow. The longer path increases the friction forces on the fluid and should reduce the flow. Also the tortuous shape of the flow path influences the slip positively.
3) ECP model with labyrinth seal in casing: Small chambers are machined into the casing of the turbine. Water leaks through the slit from chamber to chamber. The pressure difference

between the high pressure side and the low pressure side of the turbine is distributed along these chambers. The pressure difference between every chamber is a small share from the total pressure difference. This should result in a lower flow through the slit.

4) ECP model with labyrinth seal in casing and runner: The labyrinth from the previous model is now machined alternately in the casing and runner.

FIGURE 7-5 LABYRINTH SEAL AS DESIGN OPTION TO REDUCE SLIP IN POSITIVE DISPLACEMENT PUMP; THE SMALL GREEN LINES INDICATE VORTICES CREATED IN THE FLOW IN THE VOIDS, RESPONSIBLE FOR A SIGNIFICANT PART OF HEAT (EFFICIENCY) LOSSES

- **Mesh settings**

Before running the CFD simulation, the fluid domain is divided into many small elements. The mesh of a model is refined until the results of the simulation do not change anymore with finer meshes. If the mesh is refined beyond this point, the simulation requires unnecessary processor time without any additional advantages. For this study, the model is simulated for a number of meshes with a mesh of n*n elements per unit x or y. The results of an initial two-dimensional simulation are used to determine the mass flow through the slit for a fixed height Z of 317 mm (the pump house height Z for a lobe turbine with a pump house length L of 500 mm).

To test which mesh setting must be used for the models above, the casing labyrinth model with a 0.1 mm slit size is used as test case. The small slit size and more complex labyrinth geometry represents the most complex model which will be simulated. The simulated is performed with values for n ranging from 50 to 500. Figure 7-6 shows the results of these simulations. The results stay within a 5% range of each other for n values higher than 170. For this estimation of slip, a deviation in results of 5% is considered stable. Therefore, a mesh setting of 200x200 was decided to be used for the simulations.

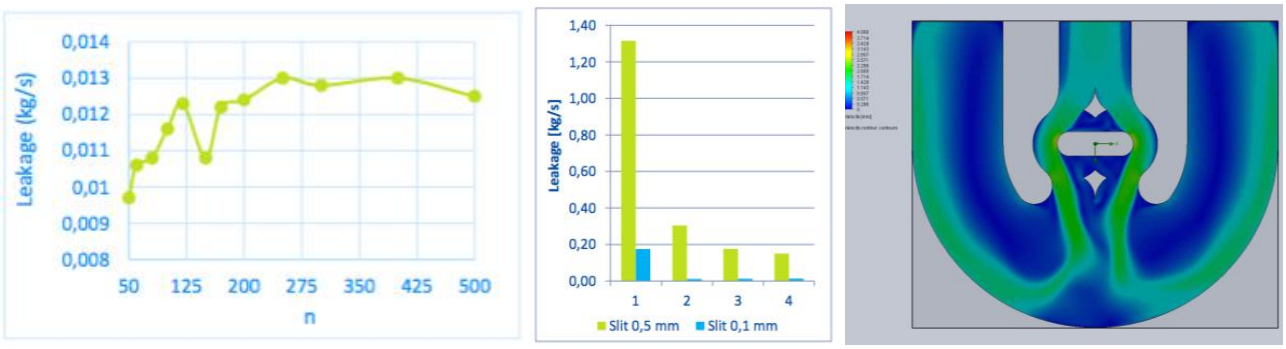

FIGURE 7-6 MESH SETTING VERIFICATION FOR CFD SIMULATION OF SLIP (LEFT), RESULTS OF THE SLIP COMPARISON FOR 4 CASES (CENTRE), EXEMPLARY FLOW SIMULATION RESULT OF TURBINE INLET WITHOUT RUNNERS (RIGHT)

Following the results depicted in Figure 7-6 (centre), an ECP model without labyrinth seal in casing/runner. The changes in efficiency (see vortices in Figure 7-5) are not worth in comparison to the effort of actually making a labyrinth with such tolerances.

- **Tolerances between parts**

Designing the turbine mechanically can start if the flow path is known. Mechanical limitations can force changes to the flow path. Manufacturing tolerances result in slip and backlash between parts. How tight the manufacturing tolerances must be must be determined during the manufacturing design phase, which is part of WP4 of the WETFEET project. Another important factor which influences the tolerances in a turbine is the thermal expansion of parts during operation. The thermal expansion is dependent on the temperature rise and used materials, which are not known yet, only estimates can be made.

- **Thermal expansion of the turbine**

The water in the Symphony operates in a closed circuit. This means that all energy losses (e.g. friction and turbine) result into an increasing temperature of the water repeatedly during every cycle. The amount of energy the Symphony is able to radiate to the ocean increases as the temperature difference between the ocean and water in the Symphony increases. If the energy added to the water by losses and energy radiated into the ocean are in equilibrium, a stable water temperature is reached. The water also increases the temperature of all internal parts of the Symphony, like the turbine. This may cause difficulties if the thermal expansion coefficient (C_{th}) of the used materials differ much. If the runner expands significant more than the casing, the runner could rub against the casing which causes damage to both casing and runner. Some assumptions are made to estimate the order of magnitude of the dissimilarity of the thermal expansion of the runner and casing of an exemplary positive displacement pump:

- ✓ Casing is made of stainless steel (AISI 316: $C_{th} = 1.6\ e^{-5}$)
- ✓ Runner is made of aluminium (1060: $C_{th} = 2.4\ e^{-5}$)
- ✓ Runner radius is 150 mm
- ✓ Pump house height Z is 317 mm
- ✓ Change in temperature is 20° C

The thermal expansion of a part is defined as the product of the initial dimension, the change in temperature and the thermal expansion coefficient. The new dimension in heated condition is the sum of initial dimension and the thermal expansion of R and Z for the runner and casing, respectively. These results must be used when the tolerances of the turbine parts are specified:

- ➢ R expands by 0.048mm for the casing and 0.072mm for the runner (difference 0.024mm)
- ➢ Z expands by 0.101mm for the casing and 0.152mm for the runner (difference 0.051mm)

7.1.4. Conclusions

The final result of this project, and answer to the main research question, is that the ECP turbine is considered the best power take-off device for the Symphony wave energy converter. The advantage of the ECP pump in respect to the lobe turbine is that the ECP turbine has less slip, a non-pulsating flow and less critical synchronization requirements. The slip reduction is the result of a longer seal between runner and casing. The pulsation is gone due to the constant position of the sealing point between a runner and the axis of the other runner. This sealing method between runners makes the

synchronization system for the two runners less critical. The project will continue with working towards a manufacturing design for the ECP turbine.

A special challenge for this is the inlet and outlet geometry of the turbine, to enable an as smooth as possible flow to limit turbulence (heat) losses. Figure 7-7 shows a late version of the asymmetrical runner ECP turbine design to be engineered and manufactured and tested within WP4 of WETFEET. This design has been registered for patent protection as outcome of the work within WP2.

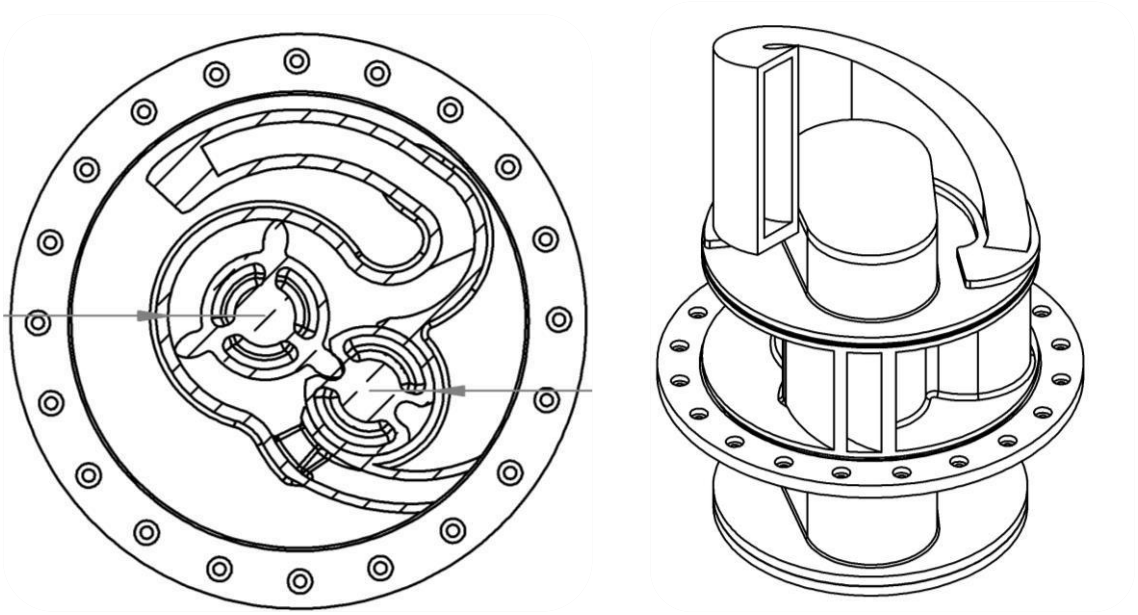

FIGURE 7-7 CROSS-SECTION OF TURBINE AND HOUSING (LEFT) AND 3D VIEW OF TURBINE (RIGHT)

7.2. Engineering constraints and evaluation for large-scale applications

7.2.1. Engineering challenges and up-scaling issues

Significant difficulties for designing and building this turbine have been detected only in the phase of elaborating the manufacture-ready calculations and drawings for the prototype. Especially the demand for a **high pressure** certification makes the building not only expensive, but especially time-consuming for the first device (before serial manufacture can be implemented).

But also for the generic purpose of size increase in up-scaling, pressures inside the turbine will increase further. Among the most likely solutions to counter this challenge is the use of different materials and strengthening the current design

Another generic challenge due to the relatively limited options to limit temperature (closed circuit) is the **high flow speeds** causing more turbulence and losses. The most obvious solution to this problem would be the increase of relative turbine size in order to reduce flow speeds. However this would contradict the logic of other up-scaling solutions as discussed in section 8.2.1: for up-scaling the membrane, increasing the diameter is a strong issue due to manufacture limitations. A trade-off needs to be found at later stage of design and/or more focus needs to be put into the temperature stabilization of the water volume (e.g. active cooling).

Further, the **manufacture method** of the turbine is an issue for up-scaling. For the prototype dimension, it is planned to make the turbine out of NI-resist using casting techniques. When the size of

the WEC increases, the pressure inside the turbine will become higher. The moulds are made with a 3d printer, and in addition to the intrinsic size limitation of such machinery, the high-pressure demands will be increasingly difficult to meet.

In general, the following issues need to be carefully considered for future considerations about the turbine:

The **overall efficiency** of the turbine will be very low in comparison to a turbine which is built e.g. for a hydroelectric power station. The reason for this low efficiency is that extracting too much energy from the flow will disturb the cyclic (ideally resonant) motion of the damped mass-spring system that represents the Symphony. The goal is to create a pressure drop over the turbine of a maximum of 2.5 bar, while the inlet flow is usually 15 bar. If the three sub-efficiencies (hydraulic, volumetric and mechanical) are analysed, an explanation can be given for where the turbine may lose its efficiency. The goal is to maximize the mechanical efficiency as for every other turbine. High mechanical efficiency can be achieved by, for example, minimizing bearing losses as well as minimizing the weight of the turbine. Mechanical losses are energy transformed to heat, energy which cannot be recovered by the system. There are two possibilities to reach the 'controlled' low turbine efficiency. The hydraulic efficiency can be reduced using small turbine blade angles. Another method is to reduce the volumetric efficiency of the turbine. This means that a part of the water volume flows through the turbine without interacting with its runner. Caution must be taken that this solution does not disturb the free flow extensively. Another option is to split the efficiency compensation between the volumetric and hydraulic efficiencies. The most important factor for the efficiency is that a turbine does not produce heat (from drag and friction) during power generation.

The water flow through the Symphony changes direction every half wave period (about 5 seconds). The turbine assembly must be **bidirectional**, i.e. able to handle this flow from two directions. In the ideal situation, the turbine is able to operate under both flow directions without changing anything mechanical, the complexity needs to be kept small for this part.

Another important feature of the turbine in addition to energy conversion is its **pumping function**, i.e. the ability to induce a volume flow in order to function as a starter motor for the Symphony. Especially for the early phase of technology implementation, the turbine must be able to pump water (using the generator as an electro-motor) with only minor adjustments.

The complexity of **manufacturing** is based on the number of parts and the number of specialized parts or tooling required for the assembly. A complex assembly with a high number of parts which are tailor-made, will be more expensive to manufacture.

The Symphony is a device which operates several meters beneath the water surface in a sea or ocean. This makes **maintenance** to the device a costly and time consuming task. The entire device would benefit from a turbine assembly which requires minimal maintenance to minimize downtime. In addition, it must be guaranteed that the turbine casing fits into the control cocoon (see chapter **Error! Reference source not found.**) for ensuring in-situ removal.

The **reliability** is a term which includes addressing all factors which may compromise the performance of the turbine. Two of the most important questions to assess this criterion are: (i) how much does the performance degrade and components wear when operating outside the ideal theoretical conditions? (ii) how sensitive is this concept to electro-mechanical failure?

7.2.2. Application in other device types

The feasibility of implementing the water turbine developed for Symphony in other device types depends highly on other modifications of such systems. As is, no other concept uses water as medium

for the PTO, except the overtopping device (e.g. Wave Dragon) and the bulge wave converter (e.g. Anaconda). While in overtopping devices quite different turbine types are used (one direction, free water surface flow, low-head turbines), for bulge wave converters this turbine could in principle be used with adaptations according to the design specifications of such devices. As these are also in rather early stage and no operational experience has been reported, no further detail can be assessed here.

For all other devices, this possibility must be evaluated including the implementation of a high pressure water body (and – most likely – a structural membrane) as PTO fluid. In section 8.2.2, the 8 common device types to date as presented by the AquaRET project (www.aquaret.com) are discussed with respect to the benefits that a structural membrane and/or a water turbine PTO could have for each of them. The benefit of using either 'breakthrough component' – membrane or turbine – in other systems increases when both are used as a system, as it is the combination of characteristics that makes such a solution interesting.

8. THE STRUCTURAL MEMBRANE

8.1. Multidisciplinary assessment of the potential of the structural membrane

The Symphony consists of two parts separated by a membrane (see e.g. Figure 1-26 and Figure 8-1). The hydrostatic pressure of passing waves pushes the upper part (Outer cylinder) down. This results in a decreasing inner volume of the Symphony. The decreasing volume creates an internal water flow through a turbine driving a generator. At the same time the inner pressure in the Spring Chamber builds up due to the decreasing volume. The counter movement, the Outer Cylinder moves up again, happens under a wave through as the inner pressure is larger than the hydrostatic pressure. The internal water flow is reversed through the turbine.

Although the primary function of the membrane is the separation between the two parts of the Symphony, its overall functionality is much more. While acting as a seal to enclose the inner pressure/volume, it also acts as a bearing for the cylinder. More precisely, the membrane is the variable volume 'breathing' under the waves. The inner volume changes due to the difference in the width in which the upper and lower part of the membrane roll up and down. Due to a specially designed (inner) hull shape, the membrane also acts as end stop.

8.1.1. Functional requirements

The following 3 main functions are to be fulfilled by the membrane:

- ✓ Sealing: the membrane acts as a sealing, protecting the internal components from the ocean water and preventing water to flow in the upper part of the hull.
- ✓ Bearing: the membrane functions as a bearing in-between the moving hull and the fixed compensation tank. It is important that the membrane centers the hull radially to exclude possible collision between the hull and the compensation tank.
- ✓ End stop: The membrane will be used as an end stop. The end stop will be realised by narrowing the wall geometry on the inner (static) side of the contact area.

Not all of these issues could be addressed to the same extent within the work scope in this phase. In particular, the bearing function of the membrane could only be addressed in a simplified way, which must be enhanced by further work before design steps. The lateral force on the membrane imposed by (surge) wave motions has been assumed to be evenly distributed over the hull in this exercise. For this situation, the restoring (centering) force of the membrane has shown to be good. However in reality the

surge forces are higher towards the water surface, therefore a bending moment will be introduced into the membrane plane. To which extent this moment can be critical needs to be assessed with additional data, partly expected to be obtained in the further course of the WETFEET project.

In the following, the specification exercise of the membrane for the Symphony is described. Whenever dimensions are involved, these refer to the 1.5m diameter prototype, as this is the membrane actually to be manufactured and tested in WP3. The specifications in this report have been composed before the engineering phase of the membrane has started. The specifications described are based on the functionality and dimensions of the membrane. Material specifications and detailed specifications of the connections are not included. These considerations were used as a starting point of the engineering of the membrane.

- **Operating conditions**

One of the key challenges for the membrane is the vast number of load cycles during life time. Per year, the membrane rolls up and down the stroke approximately 2 to 3 million times (fully or partly; according to the wave periods and heights, respectively). In Figure 8-1, the different positions (down–centre–up) of the membrane are indicated. As the sleeve (outer cylinder) is being pushed down, the roll membrane starts to roll down. As the membrane rolls down the volume inside the membrane becomes less and forces the water into the spring room trough a turbine. As the built-up pressure in the spring room forces the water back, it is pushed in the membrane which rolls up with the outer cylinder. Operational pressures from 10 to 20 bar are expected during the cycle.

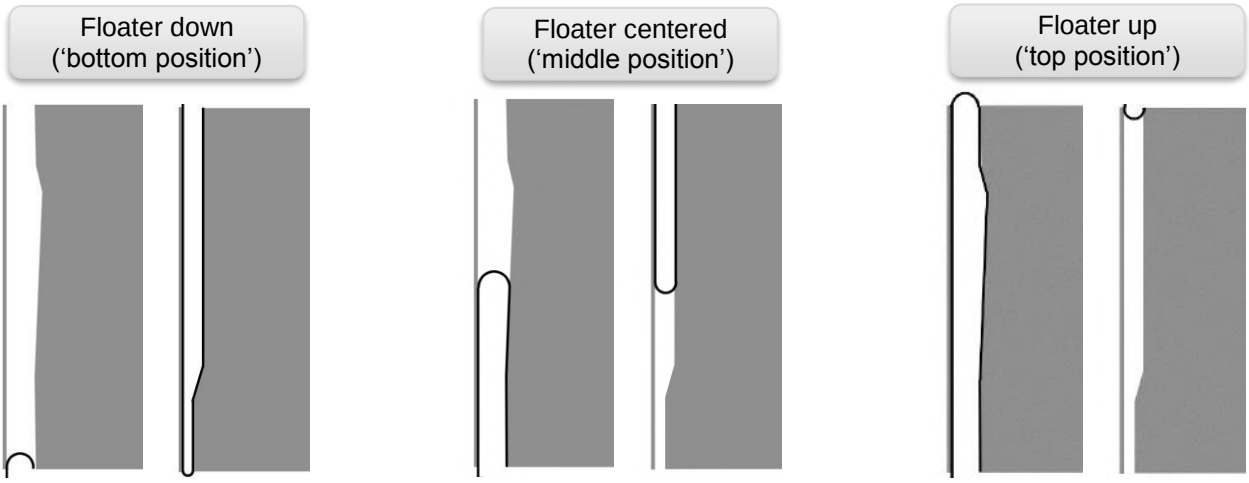

FIGURE 8-1 SCHEMATIC VIEW OF THE MOST RELEVANT FLOATER POSITIONS AND THE RESPECTIVE POSITION OF THE MEMBRANE ON THE HULL WALLS. LEFT: SITUATION WHEN FLOATER IS DOWN; CENTRE: SITUATION WHEN FLOATER IS IN MID-POSITION AND RIGHT: SITUATION WHEN FLOATER IS UP. THE LEFT SIDE OF EACH PAIR ABOVE REPRESENTS THE UPPER MEMBRANE, RIGHT IS THE LOWER MEMBRANE.

The design of the membrane and choice of material is a complex task, as the membrane on one hand has to withstand the high (fluctuating) pressures, guarantee tightness over its life time, and at the same time maintain sufficient flexibility, in order to not become brittle or obstruct the floater movement. Additional difficulty is implied by the requirement of having a seamless, round, three-dimensional shape. On one hand, its shape and behaviour under pressure must be assessed in different situations, and on the other hand it must be taken account for the different diameters over the stroke length, causing a risk of the membrane to wrinkle/crease.

8.1.2. Determination of the shapes that the membrane attain under pressure

In the following, an assessment of the shape of the membranes during the operational stages is presented. The membrane will be made of fibre-reinforced rubber sheet. It is assumed that the membrane is made of a tube of constant inner and outer diameter. The outer part is folded back over the inner part and the rim is stretched and attached to the outer cylinder (see figure 8-2). In operation the space between the two membranes is filled with water under pressure that forces the outer membrane against the outer cylinder. This section investigates how the shape of the membranes evolves during this process: this is important for determining the vertical force exerted by the membranes on the moving part.

- **Membrane type**

In several scoping sessions involving the WETFEET partner Trelleborg, it was concluded that the preferred material for the membrane is fiber reinforced rubber. The fibers are inserted under an angle α with the horizontal direction Figure 8-2). It is assumed that the fibers are so stiff compared to the rubber that the strain in the fiber direction is negligible. This means that the fibers only rotate but do not increase in length. Figure 8-2 shows what happens when the sheet is stretched in the y - direction. The rotation of the fibers causes a reduction of the width of the strip.

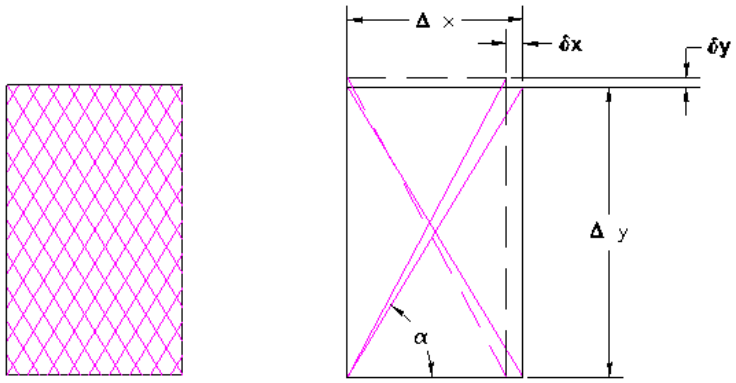

FIGURE 8-2 SCHEMATIC VIEW ON FIBRE-REINFORCED MEMBRANE SHEET (LEFT), EFFECT OF STRETCH IN Y-DIRECTION (CENTRE), THE PINK LINES INDICATE THE FIBRES. THE CALCULATION BASIS FOR RESULTING ELONGATION ε IN X- AND Y- DIRECTIONS IS OUTLINED IN THE TEXT BELOW THIS FIGURE.

Figure 8-2 shows that with purely vertical fibers, horizontal stretching does not cause vertical stretch. For an angle α = 90 degrees, the strain in y-direction is zero, independent of the strain in the x-direction. If angle α = 45 degrees, the strain in y-direction is equal to that in x-direction but opposite in sign. In-between these two values the strain ratio varies.

$$\varepsilon_x = \frac{\delta_x}{\Delta x} \; ; \; \varepsilon_y = \frac{\delta_y}{\Delta y} \; ; \tag{8-1}$$

$$\Delta y = \Delta x \; tg(\alpha) \; ; \tag{8-2}$$

$$\delta_x = -\delta_y \; tg(\alpha) \; ; \tag{8-3}$$

$$\varepsilon_y = \frac{\delta_y}{\Delta y}\frac{\Delta x}{\delta_x}\varepsilon_x = \frac{-\varepsilon_x}{tg(\alpha)^2} \quad (8\text{-}4)$$

Where ε_x *and* ε_y are the relative stretch in x- and y- direction, respectively (being Δx *and* Δy the side lengths of the sheet segment and δ_x and δ_y the deformation/stretch in the respective direction); α is the stretching angle.

- Calculation of the shape of the membrane

The shape of the membrane is calculated using a dedicated Matlab code developed in-house for this task. The code is based on an energy principle: the water can blow up the membrane until the deformation energy of the membrane (strain and bending) exceeds the energy provided by the water:

$$E = V_{membr} * p_{water} - E_{strain} - E_{bending} \quad (8\text{-}5)$$

Where:

- V_{membr} = the water volume in the membrane
- p_{water} = the water pressure in the membrane
- E_{strain} = the energy required to stretch the membrane to fill the space between the two cylinders
- $E_{bending}$ = the energy required to bend the original flat membrane in the curved shape

The Matlab function fmincon (determination minimum under constraints), already provided by the program, has been considered a suitable routine for this task, as it allows to implement the above physical problem into a relatively simple calculation procedure. It is used in the code determining the shape of the membrane. The shape is varied within the given limits to find the maximum of E.

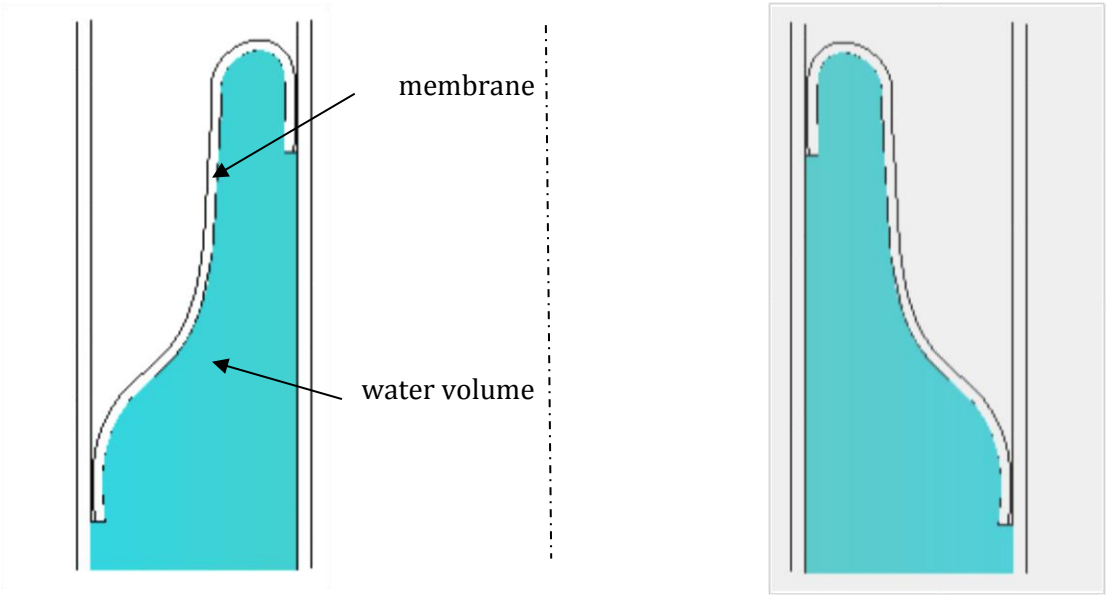

FIGURE 8-3 EXEMPLARY VIEW ON THE MEMBRANE SHAPE WITH LIMITED AMOUNT OF INSIDE PRESSURE;

The deformation energy of the membrane is divided into:

strain energy:

$$E_{strain} = \frac{Eh}{2(1-\nu^2)}\left[\left(e_{xx}+e_{yy}\right)^2 - 2(1-\nu) * \left(e_{xx}e_{yy} - e_{xx}e_{yy}\right)\right]\Delta x\,\Delta y \qquad (8\text{-}6)$$

bending energy:

$$E_{bending} = \frac{Eh^3}{24(1-\nu^2)}\left[\left(e_{xx}+e_{yy}\right)^2 - 2(1-\nu) * \left(e_{xx}e_{yy} - e_{xx}e_{yy}\right)\right]\Delta x\,\Delta y \qquad (8\text{-}7)$$

Where:

- E = the young's modulus (used 15.4 106 N/m2 for the rubber)
- h = the membrane thickness
- e = the strain
- ν = the Poisson ratio (0.5 for rubber)

Among the objectives of these calculations is to find out about the membrane's shape/behaviour in relation to the fiber orientation chosen.

- **Results**

The code was run for different pressures and different fiber enforcement angles. Figure 8-4 shows the results for a fiber angle parallel to the vertical. This means that in vertical direction no strain is possible

due to the stiff fibers. It is also shown that for most pressures the shape is the same. Only for the lowest pressure can be seen that the membrane is being blown up.

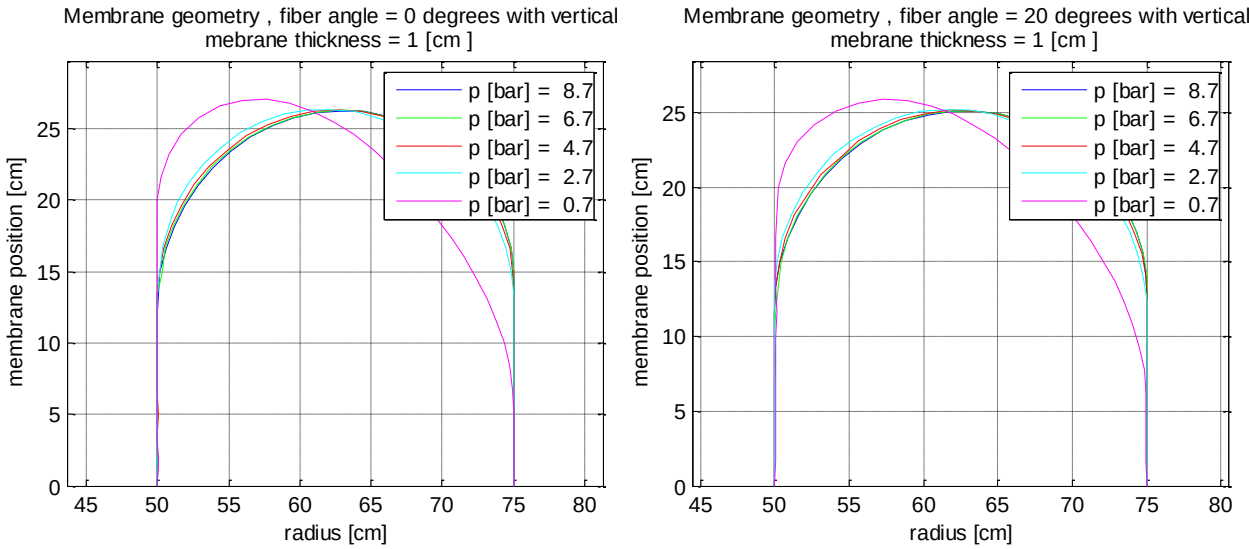

FIGURE 8-4 RESULTING MEMBRANE SHAPE FOR DIFFERENT INSIDE PRESSURES FOR A FIBER ANGLE PARALLEL TO THE VERTICAL (LEFT) AND IN A 20º ANGLE (RIGHT).

Figure 8-6 shows that the segments along the membrane keep the same length when fiber angles are parallel to the vertical, but changes when the fibers are placed with a 20º angle. Now the circumferential stretching of the membrane causes shortening of the segments in radial direction along the membrane.

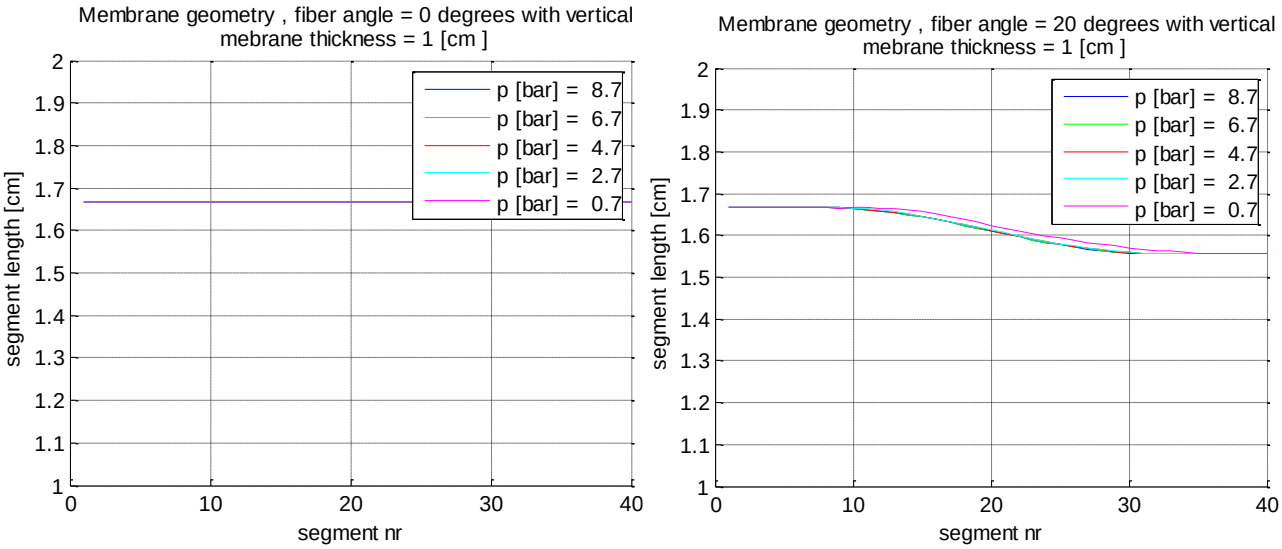

FIGURE 8-5 RESULTING FIBER SEGMENT LENGTH FOR DIFFERENT INSIDE PRESSURES FOR A FIBER ANGLE PARALLEL TO THE VERTICAL (LEFT) AND IN A 20º ANGLE (RIGHT).

From Figure 8-6 it can be interpreted that for higher pressures the top of the membrane lies approximately in the middle of the gap, the radius increasing slowly with the pressure.

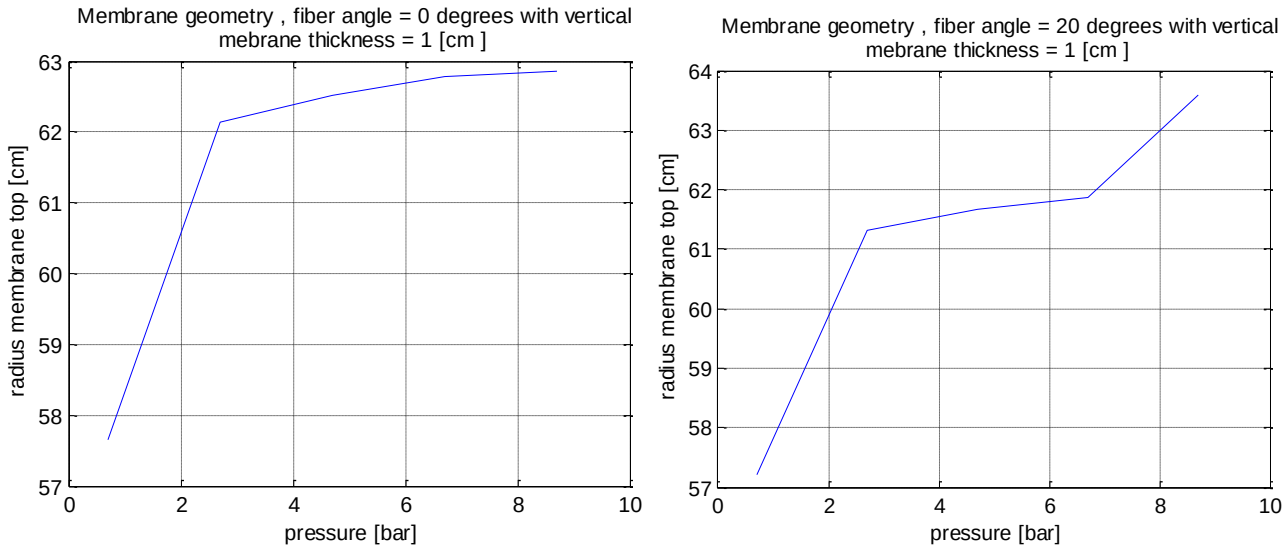

FIGURE 8-6 RESULTING RADIUS OF MEMBRANE TOP FOR A FIBER ANGLE PARALLEL TO THE VERTICAL (LEFT) AND IN A 20º ANGLE (RIGHT).

8.1.3. Behaviour of membrane with a larger initial inner diameter than inner cylinder

Among the concerns for the membrane design is the behaviour of a membrane with an inner initially unloaded diameter when pressurized. If the membrane tends to crease (wrinkle), the lifetime could be significantly reduced, or even operational malfunctions occur. The membrane Matlab code presented above was adapted to compute the behaviour of the inner wall of this membrane when it is blown up with water. The same formula and data were used for computing the membrane deformation energy.

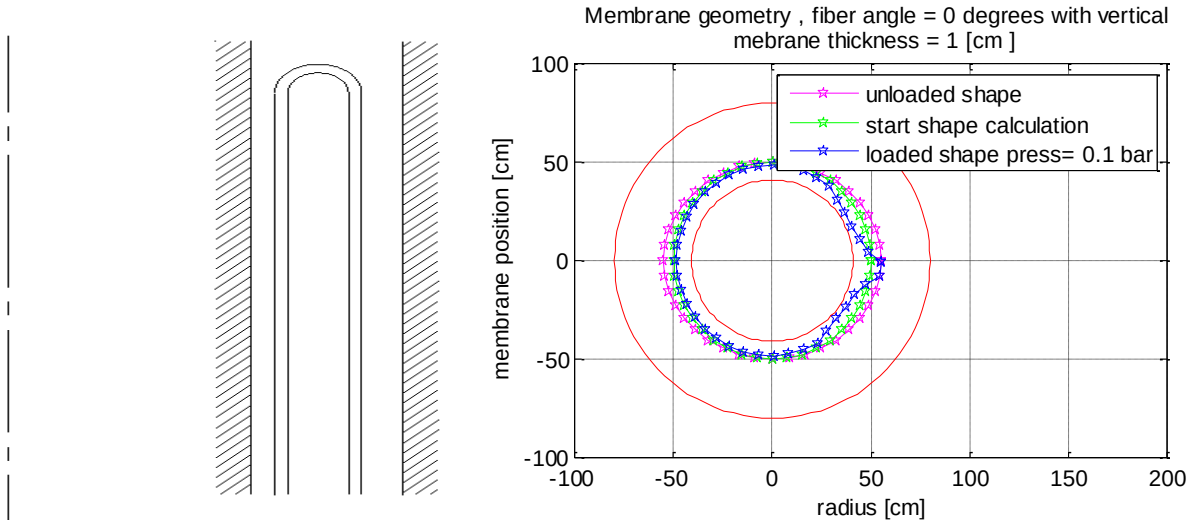

FIGURE 8-7 UNLOADED MEMBRANE SHAPE CROSS-SECTIONAL VIEW (LEFT); MEMBRANE FOLDED INWARD AROUND INNER CYLINDER AT LOW PRESSURE (RIGHT)

A low pressure folds the membrane around the inner tube and the excess membrane material forms a crease. Increasing the pressure later does not change this situation. The membrane is only pressed more

firmly together. It is not expected to be an issue during operation as normal operating pressures will be much higher.

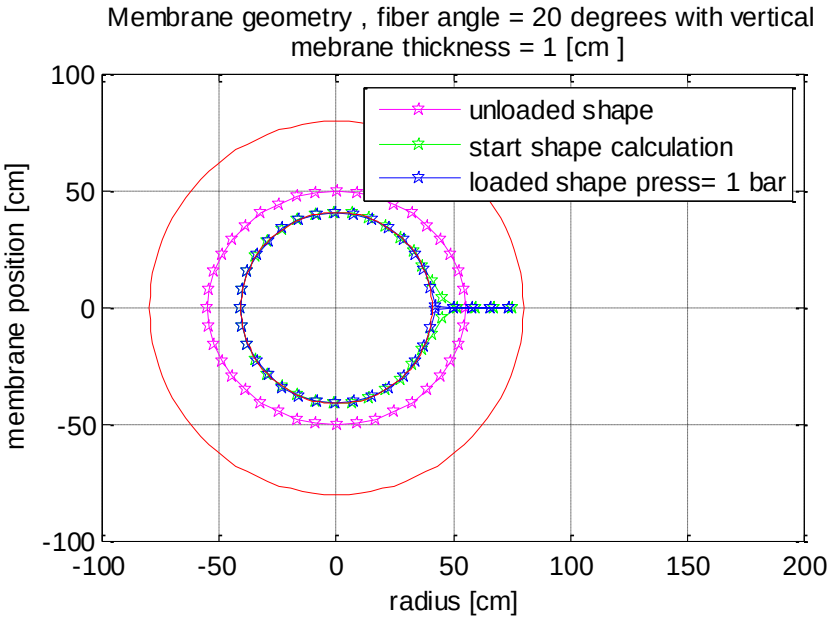

FIGURE 8-8 MEMBRANE FOLDED INWARD AROUND INNER CYLINDER AT HIGHER PRESSURE

Due to this behaviour, it appears most appropriate to start with a membrane that in unloaded situation fits around the inner tube. Then no creases can occur. The behaviour of the outer layer of the membrane is different as it is loaded from the inside. It is neatly blown up against the inside the outer tube without creases (see Figure 8-9 and Figure 8-10).

These observations help to initiate the engineering design of the membrane, and to elaborate the technical specifications for this component presented in Section 8.1.4.

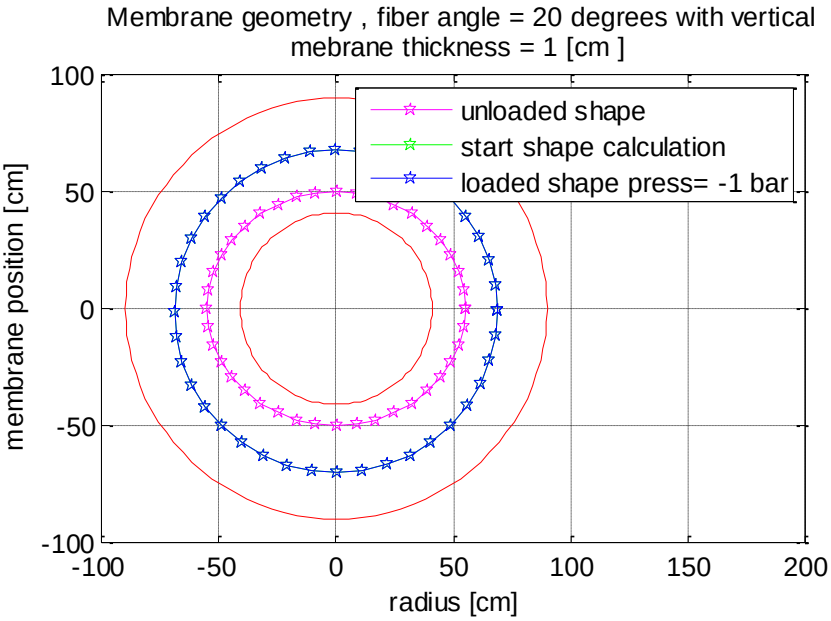

FIGURE 8-9 OUTER WALL MEMBRANE BLOWN OUTWARD, NOT YET FULLY STRETCHED AGAINST OUTER CYLINDER (NEGATIVE PRESSURE INDICATES PRESSURE DIRECTED OUTWARDS)

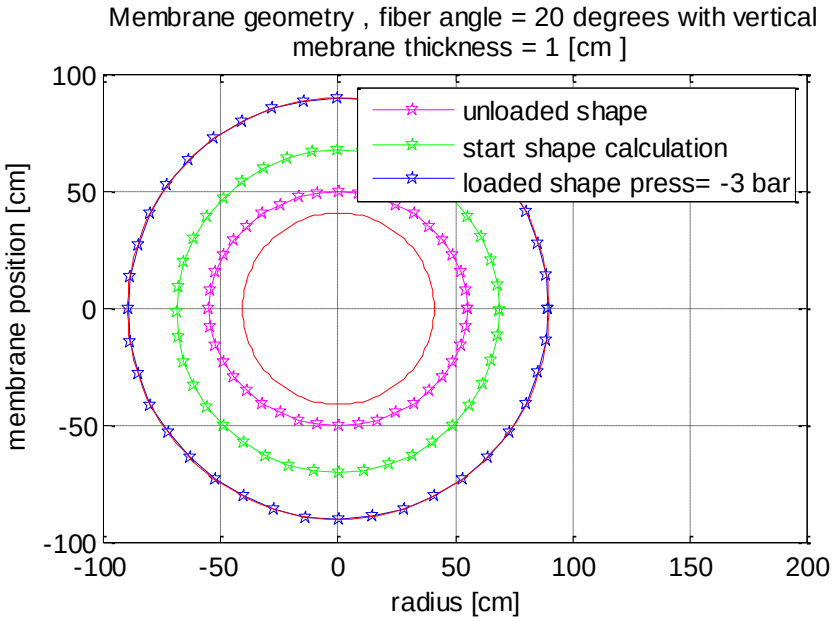

FIGURE 8-10 OUTER WALL MEMBRANE BLOWN OUTWARD, NOW FULLY STRETCHED AGAINST OUTER CYLINDER (NEGATIVE PRESSURE INDICATES PRESSURE DIRECTED OUTWARDS)

8.1.4. Membrane specifications

- **General specifications**

The inside wall geometry acts as a negative spring that linearizes the air spring. The membrane must be able to function at different diameters, since the inner diameter changes due to optimisation of the spring. The membrane must be built with properties that enable full functionality if the inner diameter of the upper wall geometry changes by 20%. The inside wall geometry of the Symphony is modular. After the device is built, the wall geometry might be changed in order to optimise the system, or correct inefficiencies. If the inside wall geometry is changed, the membrane will have more or less overspan in comparison to the original state. The membrane will have a different contact surfaces. Therefore the membrane must be adjustable in length. The air spring has a low spring stiffness of around 800 N/m displacement If the membrane rolls along the surface, the membrane's material will compress or expand. The membrane must be demountable for maintenance purposes.

TABLE 8-1 MEMBRANE SPECIFICATIONS

Medium inside membrane:	Water
Lower membrane external exposure:	Ocean water
Upper membrane external exposure:	Air (at with a relative vacuum of 80%)
Operational stroke [m]:	2
Full stroke [m] (including braking area):	4

Part	No.	Dimensions(l*d*t)	Material	Weight	Supplier
Upper membrane	1	2487*1500*+/-10 mm	Aramid fiber reinforced rubber	+/- 164 kg**	Trelleborg
Lower membrane	1	2440*1500*+/-10 mm	Aramid fiber reinforced rubber	+/-161 kg**	Trelleborg

* The final thickness can differ due to the production method ** Estimated density of the rubber composite: 1400[kg/m^3]	Max pressure: 30 bar Lifespan: 10 years

Membrane material specifications

* The final thickness can differ due to the production method ** Estimated density of the rubber composite: 1400[kg/m^3]	Max pressure: 30 bar Lifespan: 10 years

Membrane material	Aramid fiber reinforced rubber composite
Number of aramid fiber layers	1
Fiber orientation	+/- 10 degrees
Breaking strength of aramid component	3100-3600 GPa
Stiffness of aramid component	60-180 GPa
Failure strain of aramid component	1.7 %
Density of the aramid fibers	1540 kg/m^3
Young's modulus of rubber component	+/- 4-5 Mpa

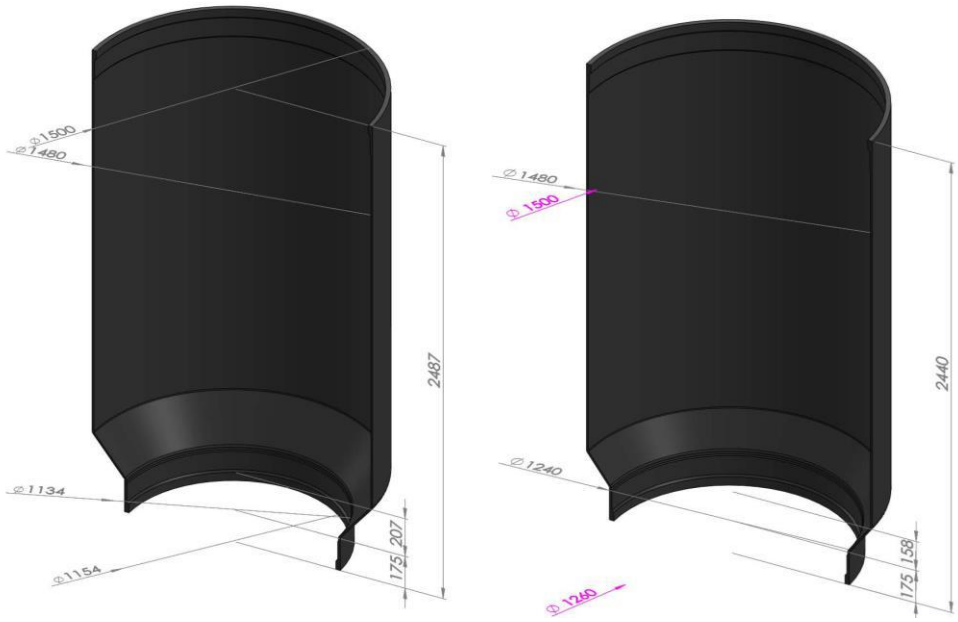

FIGURE 8-11 CUT OUT OF THE UPPER MEMBRANE (LEFT) , LOWER MEMBRANE (RIGHT)

- **Membrane connections**

In addition to the complex exercise of designing and dimensioning the membrane itself, a significant technical challenge lies in its connection to the device. As mentioned before, the membrane is subject to 2-3 million wave cycles, and as it also functions as end stop, it may experience large instantaneous stretch loads, especially at the connection points. The membrane is the only connection point between inner and outer cylinder, and it must keep fully tight for pressure differences in the range of 20 bars. Its vital function for the Symphony device operation makes it potentially the most critical element in the system. If the membrane fails, the device becomes inoperative and needs to be removed for repair. The methodology for fixing the membrane to the device has been largely discussed with the WETFEET partner Trelleborg, especially the preference for a non-destructive/intrusive way of fixing. Any punch hole in the membrane would increase the risk of bearing stress and rupture. Also gluing was found to be inappropriate in an early phase, due the materials and specific demands to the connection area. More importantly, a glue would be very difficult to apply and especially to remove in case of the need of disassembly. Being demountable is one of the key requirements for the connection. The solution elaborated is a number of clamps that are mounted successively from the outside to hold the membrane.

TABLE 8-2 MEMBRANE CONNECTOR SPECIFICATIONS

Part	No.	Dimensions (l*d*t)	Material	Weight	Supplier
Lower inner membrane connector	24	240*164*42	steel	8 kg	tbd
outer membrane connector	48	240*196*42	steel	8 kg	tbd
upper inner membrane connector	24	240*146*42	steel	8 kg	tbd

By clamping the membrane via a number of single clamps fixed from the outside, the demands of being demountable and non-destructive are met, and in addition this procedure gives confidence and

possibilities of intervention/replacement from outside in case of unexpected failures, due to its modularity.

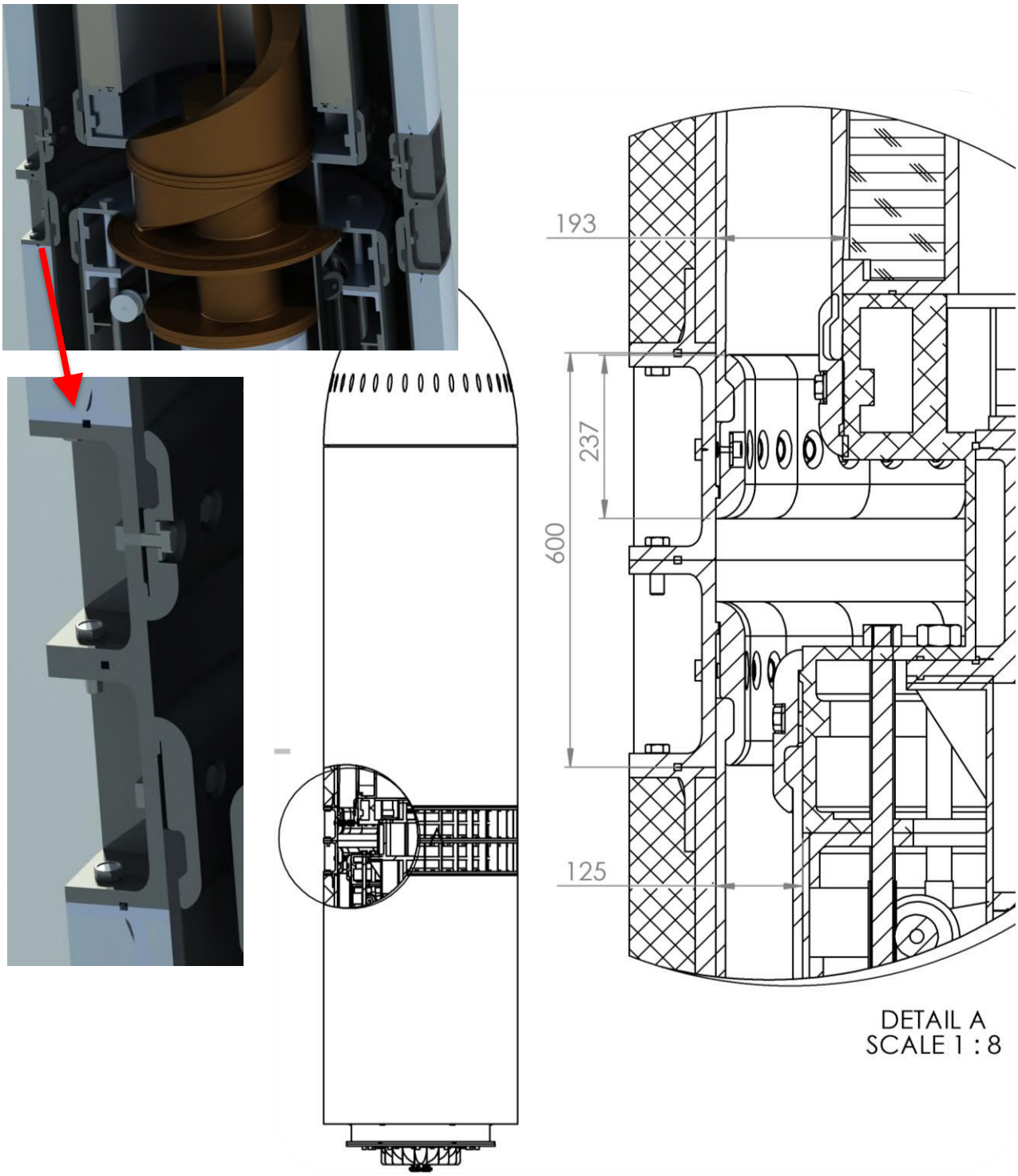

FIGURE 8-12 CROSS-SECTION OF 3D VIEW OF TURBINE HOUSING AND (UPPER AND LOWER) MEMBRANE CONNECTION CLAMPS (LEFT, ABOVE); ZOOM OF OUTER CONNECTION CLAMPS (LEFT, BELOW); LOCATION AND CUT-OUT DETAIL OF THE FIXING OF THE UPPER AND LOWER MEMBRANE (CENTRE AND RIGHT).

8.2. Engineering constraints and evaluation for large-scale applications

8.2.1. Challenges for future developments

The membrane is a key component for the Symphony technology, and may bring significant advantages to other SPDD type WEC. At the same time it is a very specific material (reinforced rubber), which has been used in specialized offshore solutions, but no significant experience data or widespread design and manufacture know-how exists, as well as no standards. Currently only one manufacturer (the WETFEET partner Trelleborg) that could be identified by the Symphony team to have the ability to produce the aramid fiber reinforced membrane to the required specifications. The maximum diameter of their production line is 4m, limiting the potential diameter of a future device Further, the production line is also used for other projects, and therefore not always available. If large scale WEC's are required or multiple devices are being built in a relative small amount of time, this could become a limitation in size and production speed.

However, for utility-scale devices – which is the probable main future market – 6m, and more likely 10-12m will be required, which is why this can be considered the strongest bottleneck according to present technically available manufacture capacities. It is expected that the Symphony technology will be initially commercialised with smaller diameters (3-4m), and in niche applications.

It is likely that such a development, in which larger devices, especially for large-scale electricity production (and feed-in to the grid), are produced, is still a relative future scenario. It is likely that a market path of 5-10 years until the first (still smaller) grid-connected devices will be manufactured, at which stage the diameter is likely not to exceed 6m. At the same time, a market demand can be sufficiently well assessed, making it possible that the manufacturer invests into larger production capacities. It is also possible that new methods will be available by that time. The same logic should be applicable for the following up-scaling phases, which is why this limitation is not necessarily going to be a show-stopper.

Potential solutions to approach the problem in case it persists in the next development steps are:

(i) Increase PTO pressure in order to have the same power with a smaller PTO system.
(ii) Start a new, dedicated production line for large diameter membranes.

Another challenge for future development is the high pressure the membrane is subject to (which would be further increased in case of the first solution indicated for the previous challenge). When the size of the WEC increases, the pressure inside the membrane will become higher. The membrane and connections are exposed to greater forces. The current type of membrane connectors clamps the membrane using bolts. When pressures become greater this type of connector is likely to be non-sufficient.

A potential solution to this challenge is the dedicated development of a new type of membrane connector, differing from the currently used clamping mechanism. There are other options, like in particular winding the fibers to a fixed component. In order to strengthen further the rubber composite membrane component in this situation, the following is suggested: currently only one layer of aramid fiber reinforcement is used for the reinforcement of the membrane. It is possible to use multiple layers of aramid fiber reinforcement. Further research to delamination need to be done before making this type of membrane, but in general strength limits can be pushed further with this method.

8.2.2. Application in other device types

Being the key component for a 'breakthrough' in SPDD technology, the membrane is especially required due to the status of full, continuous submergence of the device. The combination of the membrane with its functions and the turbine, enables a new approach to SPDD WECs in the view of the Symphony team.

For floating WECs, or other types of submerged devices, different solutions may be more efficient to ensure functionality.

However, in connection with the internal water pressure, and in particular with the inner shape as end stop, the membrane could be an interesting alternative for all linear heaving devices, especially when the relative movement occurs under water. Ideally, the membrane is combined with the water turbine, and the joint unit can offset more complex or economically less promising combinations of components.

In the following, 8 common WEC types are discussed separately, with respect to the benefits that a structural membrane and/or a water turbine PTO (as presented in chapter **Error! Reference source not found.**) could have for each of them. It appears more appropriate to include the turbine PTO here, as opposed to discuss it separately in chapter **Error! Reference source not found.**, as typically the benefit increases when a structural membrane and a turbine are both used.

8 WEC device types corresponding to the classification by the AquaRET project (www.aquaret.com), and are outlined below:

1) Attenuators

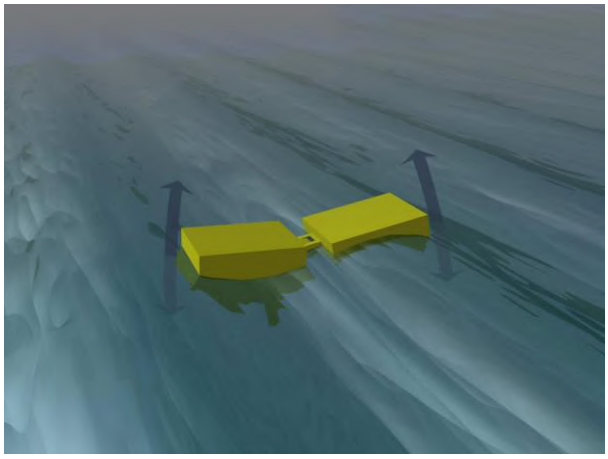

FIGURE 8-13 ATTENUATOR (WWW.AQUARET.COM).

In attenuators, typically the relative movement of two or more floating bodies is converted. In the past the only method proposed (or practised) was hydraulic cylinders. Due to their geometry, their operation mode and typically small seals due to externally mounted (linear) PTO components, it is difficult to picture the use of a structural membrane and water turbine in this device type.

Potentially the joints could be replaced by a specially shaped pressurised water volume enclosed by a membrane, which would make the result similar to the bulge wave technology, with the difference of combining rigid bodies with flexible parts. In such a scenario, a water turbine could be incorporated.

2) Surface point absorbers

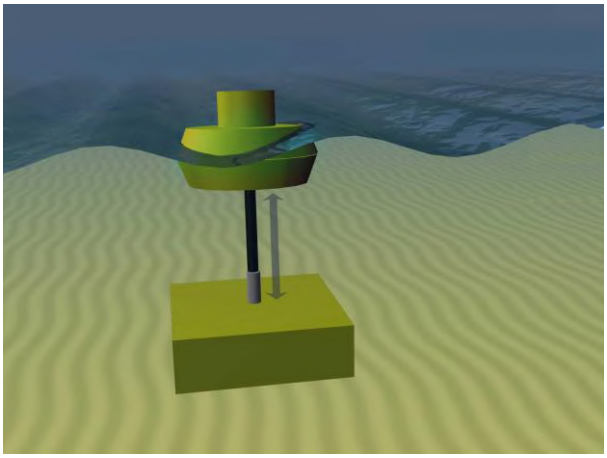

FIGURE 8-14 SURFACE POINT ABSORBER (WWW.AQUARET.COM).

A surface point absorber is typically a heaving device, which means that the movement characteristics are similar to an SPDD like the Symphony. The use of a membrane would not be as essential and ground-braking like for the SPDD, as the seals have smaller dimensions and can be located above water surface. However, knowing the fundamental challenges that point absorbers have with end stops and (linear) PTO implementation, the combination of membrane and turbine could be competitive for these devices. Especially the intrinsic end stop function of the membrane with a shaped wall could bring significant improvements to some systems. Using only the membrane with another PTO is conceivable.

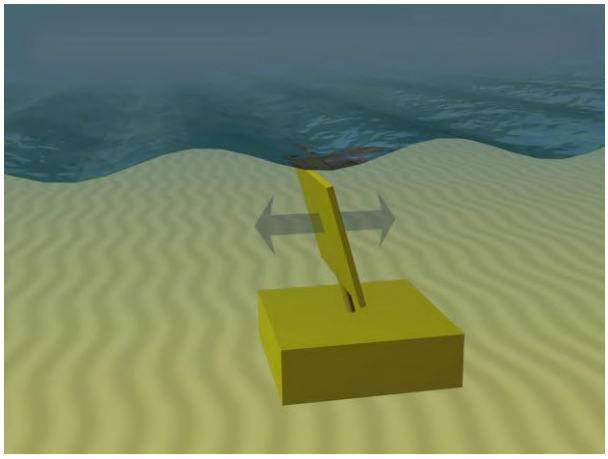

3) Oscillating wave surge converters (OWSC)

Similar to the attenuators, the OWSC do not appear to be a natural candidate for implementation of the membrane and/or the water turbine. In similar fashion like the attenuator, for this type of device it is also difficult to picture how a membrane could improve functionality, unless significant changes in the prime mover transmission are made. The movements on the bottom are transmitted with a relatively high moment but small displacement. With a specially designed asymmetric geometry, a membrane could be used to drive a high pressure water turbine, however its use as end stop is difficult to imagine.

FIGURE 8-15 OSCILLATING WAVE SURGE CONVERTERS (OWSC) (WWW.AQUARET.COM**).**

4) Oscillating Water Column (OWC)

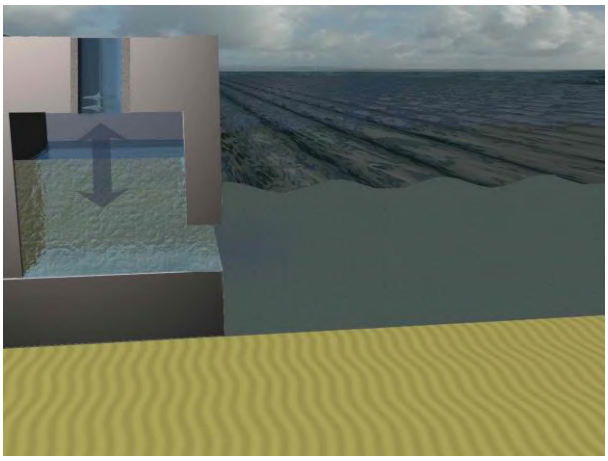

The working principle of an OWC is specific to this device type, and no structural parts move against each other (only the turbine rotates inside the air duct). There is no added value that the concept of a structural membrane could bring to the OWC operation principle.

Similarly, it is also unlikely that the water turbine brings any improvement to OWC systems, except if the entire surface of the water column is captured and funnelled through a small turbine duct. It appears more likely that improvements in air turbine design and operation will lead to better technology economics of this device type.

FIGURE 8-16 OSCILLATING WATER COLUMN (OWC) (WWW.AQUARET.COM**).**

5) Overtopping device

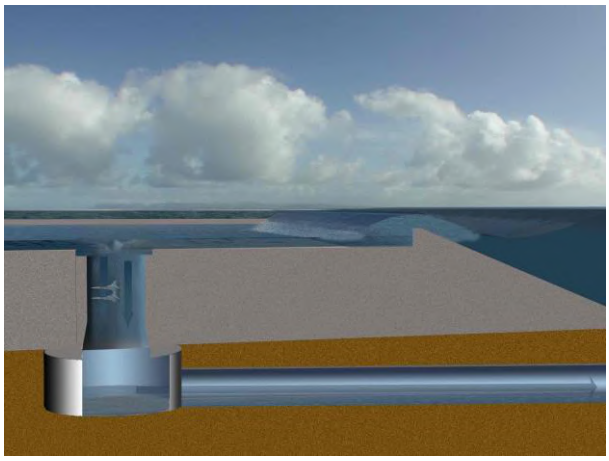

Similar to the OWC, the overtopping device has no critical issues with two bodies moving against each other as prime energy conversion step. As such, the membrane could not bring any added value to overtopping devices. The water turbine on the other hand, is in principle applicable to overtopping devices, which are the only WEC using water turbines to date. However, the operational environment is substantially different to the Symphony, where high pressures and reciprocating flow exist. Overtopping devices use one-directional low-head turbines.

FIGURE 8-17 OVERTOPPING DEVICE (WWW.AQUARET.COM).

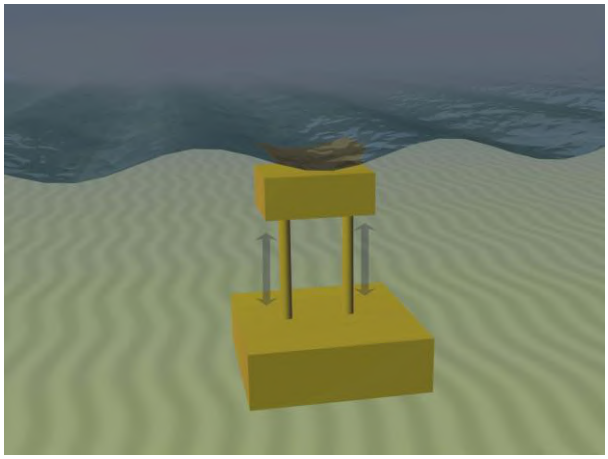

FIGURE 8-18 SPDD (WWW.AQUARET.COM).

6) SPDD

The reason why the membrane and its functions where introduced and are considered as breakthrough components is that the Symphony team believes this can turn the SPDD principle into a commercially viable WEC type, which otherwise would be difficult to achieve. Also the turbine is part of this approach, as by the combination of shaped inner wall, membrane and water turbine, the seal and bearing simultaneously drive the PTO.

Both membrane and water turbine are highly relevant for application in SPDD, and the WETFEET project aims at demonstrating their functionality in general

7) Bulge wave technology

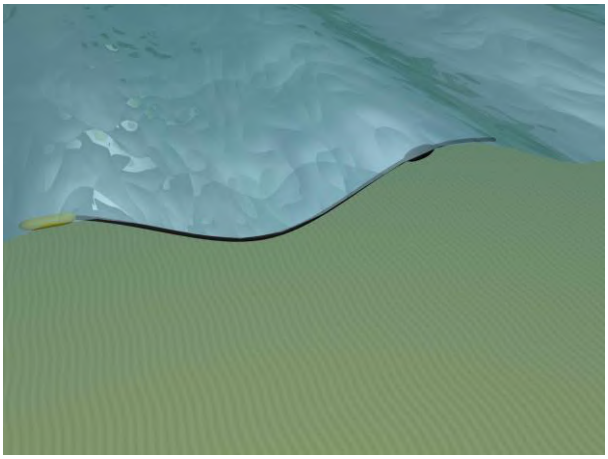

FIGURE 8-19 BULGE WEC (WWW.AQUARET.COM).

This relatively recent WEC concept bases on an entirely different functional principle then Symphony, however its structure consists mainly of a special (rubber) membrane, which pushes water through a turbine. In a way, it is a way to use a water turbine and a structural membrane without the rigid parts of Symphony, and without two bodies reacting against each other. The membrane is already the core of this concept, and the water turbine could become an interesting alternative to models used at present, once functional parameters are confirmed.

8) Rotating mass

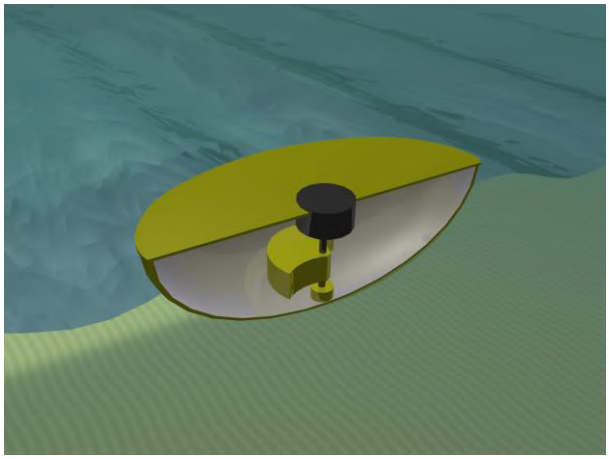

Similar to the OWC and the overtopping device, the rotating mass device has no issues with sealing a moving surface from the surrounding sea, which is why the membrane will not bring additional value to this device type.

Also a water turbine is difficult to picture in this type of device, as its functional principle is the free swinging mass, excited by the movements of the hull.

The potential relevance of the Symphony breakthroughs to this device type are possibly the lowest among all 8 types.

FIGURE 8-20 ROTATING MASS (WWW.AQUARET.COM).

Summarising these comparisons, it can be concluded that the structural membrane is highly relevant for heaving devices in general. While it was developed for SPDD and will be a breakthrough for this device type if meeting the expectations, its combined functions of bearing, seal and end stop can be an attractive alternative for heaving point absorbers, too. In particular when combined with the water turbine, this setup can offset more complex and vulnerable components in such devices.

More fantasy is required to take the vision of a structural membrane (and water turbine) a step further in pivoting devices like attenuators and Oscillating Wave Surge Converters, however it is not an impossible scenario, which under certain circumstances and with significant structural changes could be implemented and bring advantages.

No relevance of membrane and turbine can be identified for the device types OWC, overtopping, wave bulge and rotating mass, with the exception that the water turbine developed for Symphony could be interesting for the wave bulge device, depending on existing design parameters.

9. CONTROL COCOON FOR CONTINUOUS SUBMERGENCE AS AN O&M STRATEGY

9.1. Multidisciplinary assessment of the potential of the control cocoon for continuous submergence as an O&M strategy

9.1.1. Introductory note

One of the main "unique selling points" of an SPDD like Symphony is its full submergence. While having theoretically similar primary power conversion efficiency in average when compared to floating devices, the permanent submergence can have positive effects, like e.g. strongly reduced jerking loads and smoother (heave) movements, the absence of visual impacts, protection from wave slamming and the most destructive forces in extreme sea states and – despite what might be assumed at first sight – potential advantages for O&M. The latter is due to the fact that for docking and personnel transfer of two independent (typically floating) bodies, small wave motions are sufficient to introduce significant risks of damage and injuries. This has been a significant issue for the early phase of offshore wind farms, although the turbines stay still and only the service vessel moves. In case of two independently moving bodies, the challenge is increased. The Symphony team expects that either personnel transfer or diving near the water surface will be required for floating WECs, as it appears a very costly strategy to lift the entire device on deck or even tow it into shore for minor inspection and maintenance works. When the structure is submerged, divers might be required, however once in the water the access is easier further down in the water column, due to decreasing movements, and due to the fact that only one floating body is subject to water surface movements. At the same time, an automated servicing scheme based on ROVs (Remotely Operated Vehicles) or AUVs (Autonomous Underwater Vehicles) are a realistic vision at present stage of development. Especially if the operation is only required for simple procedures, like releasing parts of the system under water in order to transport them to the vessel or tow them to land.

The control cocoon is an approach to turn such a maintenance strategy into reality, by placing all critical equipment (electric parts, mechanical/moving items and auxiliary equipment) into one fully insulated cylindrical unit at the bottom of the device, from where it can be pulled out when required. By this means, the cocoon turns an otherwise difficult to access system – the SPDD– into a device type with a relative straight-forward maintenance methodology, suited for the marine environment.

As opposed to the turbine and the membrane, the functional verification of the cocoon is not by itself a challenge, and it only has an auxiliary function to the device's operation. However exchanging and re-inserting the cocoon is potentially the most challenging operational task to tackle, once the full prototype is built for deployment and marine operations are planned. The conceptual sequence has been indicated in [2], and the cocoon and mooring design of Symphony must respect the requirements for this operation. It is anticipated that the cocoon can be pulled down by an incorporated winch along the taut mooring line in a controlled manner, before it is disconnected from the pulling system and brought on deck or in towing position. For such an intervention, a team of two divers and a light work vessel are anticipated. Further work and a detailed description of how this process is going to be implemented has not been focus of the initial work within this WP, as at this stage it must first be investigated if and how the required control and power equipment fits into the cocoon, as well as how the interfaces from the cocoon must be specified.

In the following, a conceptual view on how the required components are envisaged in being placed in the cocoon, together with an indicative overview of dimensions, main functions and interfaces.

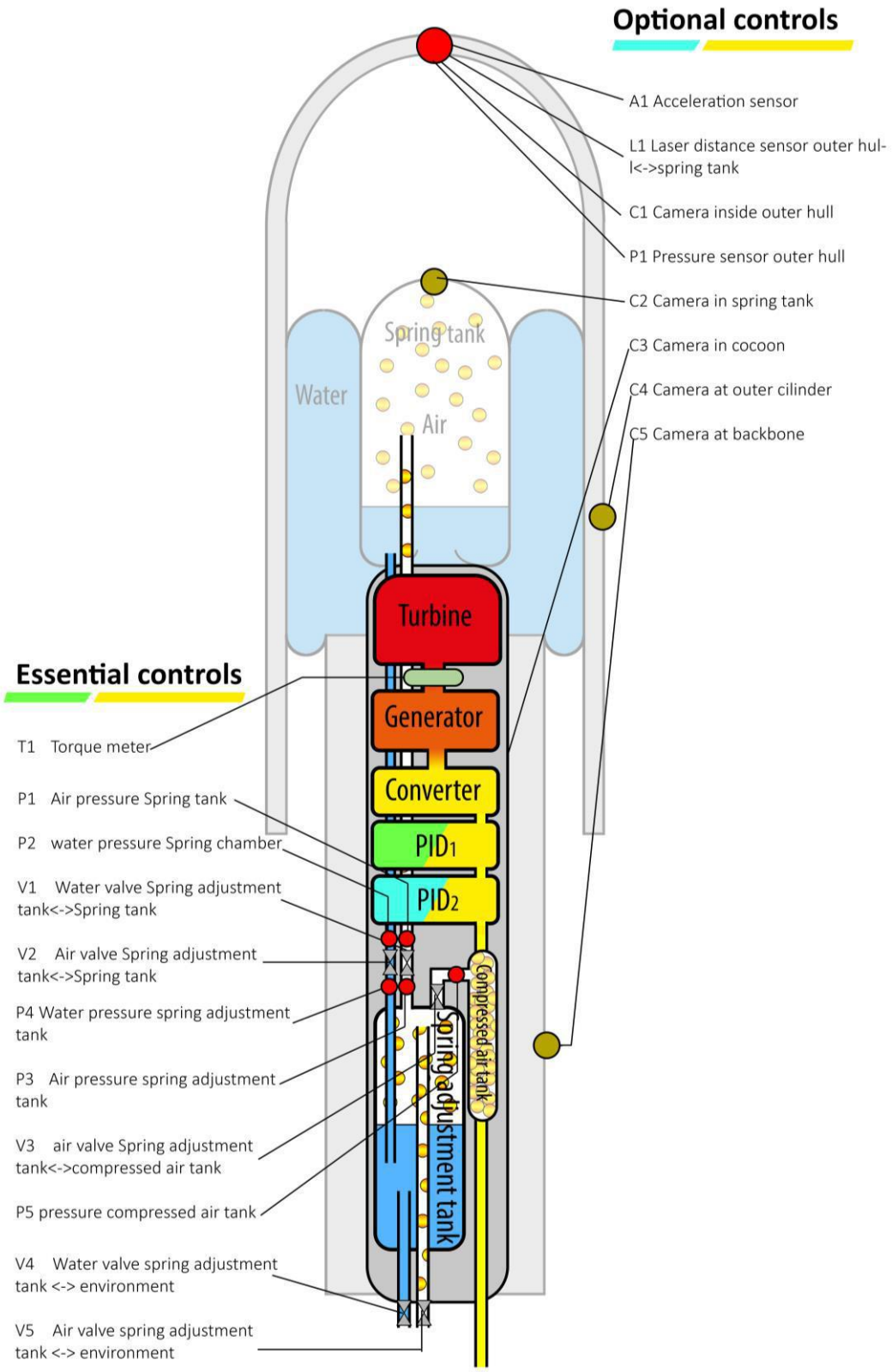

FIGURE 9-1 CROSS-SECTION OF SYMPHONY, DETAILING THE FUNCTIONALITIES AND INTERFACES OF THE COMPONENTS TO BE ACCOMMODATED IN THE COCOON: MAJOR COMPONENTS ARE (I) TURBINE, (II) GENERATOR, (III) ELECTRONICS (CONVERTER AND PID - PROPORTIONAL–INTEGRAL–DERIVATIVE CONTROLLER), (IV) SPRING ADJUSTMENT TANK WITH (IV) COMPRESSED AIR TANK.

The engineering realisation of the cocoon, its components and its connections (seals to the turbine chamber; potentially underwater electrical connectors to the hull) is demanding, and involves several adaptations to existing equipment. However the key for the feasibility assessment of the cocoon is its integration into the overall concept. It would be over-ambitious and beyond the scope of the WETFEET project to build a prototype of the cocoon, which is why the project work focuses on the following the three major issues to be solved:

(i) to fit the components into the available space;
(ii) to design a feasible guidance and docking methodology, allowing to safely remove and re-insert the cocoon;
(iii) to demonstrate the feasibility of the Symphony device to keep station without the cocoon (when the cocoon is removed for maintenance).

While the last aspect is addressed by hydrodynamic tank tests with a small-scale model in WP3 of WETFEET, the first two aspects are discussed based on the findings for the 1.5m prototype device. These serve as baseline for the future work presently being prepared with respect to larger diameters, in particular the 6m WETFEET reference case. In Figure 9-1, the cocoon and its components is sketched.

9.1.2. Design considerations

From the subcomponents of the cocoon summarized in Figure 9-1, most items are not critical with respect to space requirement, which is the first challenge for the cocoon design to be evaluated. The major components to be integrated in the limited space of the cocoon are summarised in the following, including an assessment of their space requirements:

- **Turbine**

A new custom bi-directional asymmetrical pump is used as a part of the PTO of the Symphony, as presented in chapter 7. The housing of the turbine is used to guide the water into the runners. The turbine also functions as an end stop and its housing as platform for seals to the cocoon, as the turbine is the part that connects the sealed cocoon area with the high-pressure water/air volume between structural membrane and spring tank. This is the most critical part with respect to the cocoon. The turbine diameter is adapted to the overall design of the Symphony, and in case of the 1.5m diameter prototype the housing diameter is significantly smaller, fitting into the cocoon. This is one of the intrinsic design demands for the turbine, which is why i tis not further discussed at this stage.

- **Generator**

The axis of the turbine is connected to a generator, which could be used to drive the turbine axis, too. It is sealed in the interior of the cocoon and has no critical interfaces to the outside. The final choice of a generator is not concluded at this stage, however the requirements would be appropriately met by a permanent magnet generator, directly connected to the turbine shaft. An exemplary device for the current PTO is a back-to-back controlled generator of the make Alxion, making it able to generate energy and drive the turbine. The generator is cooled using an external cooling system. This system is connected to the inlet and outlet of the turbine which creates a pressure differential when operational.

TABLE 9-1 GENERATOR SPECIFICATIONS FOR SYMPHONY PROTOTYPE (EXEMPLARY)

Parameter	*Lower limit*	*Upper limit*	*Unit*
Rated speed	80	400	Rpm
Rated Power	2823	22678	W
Input torque at rated speed	478	611	Nm
Efficiency at rated power	71	89	%
Current at rated power	7.3	56.3	Amps
Voltage at rated power	231	238	V
Rated power at half speed	911	10009	W
Input torque at half speed	366	582	N/m
Efficiency at half speed	60	82	%
Number of poles		48(24)	n
Cogging torque		5.5	
Phase resistance at 20C	6.45	0.2	Ohm
Phase inductance	31	0.94	mH
Voltage at no load (Back EMF)	342	299	V
Rotor intertia		1270	
Weight		55	
Power cable square section	4*1.5	4*10	mm2
Power cable diameter	⌀8.6	4*⌀9.5	mm

- **Electronics and control system**

The electronics (converter, PID1, PID2) will be placed in a sealed box, from where the winch (for tidal adjustments), generator and valves of the pressure systems are controlled. This is the core part of the device control, and might be placed closer to the end of the cocoon for easier access. Slight over-pressure is being considered for additional protection. Critical physical interfaces to the outside (unless going through winch) do not exist, also their dimensions will be easily fit into the cocoon.

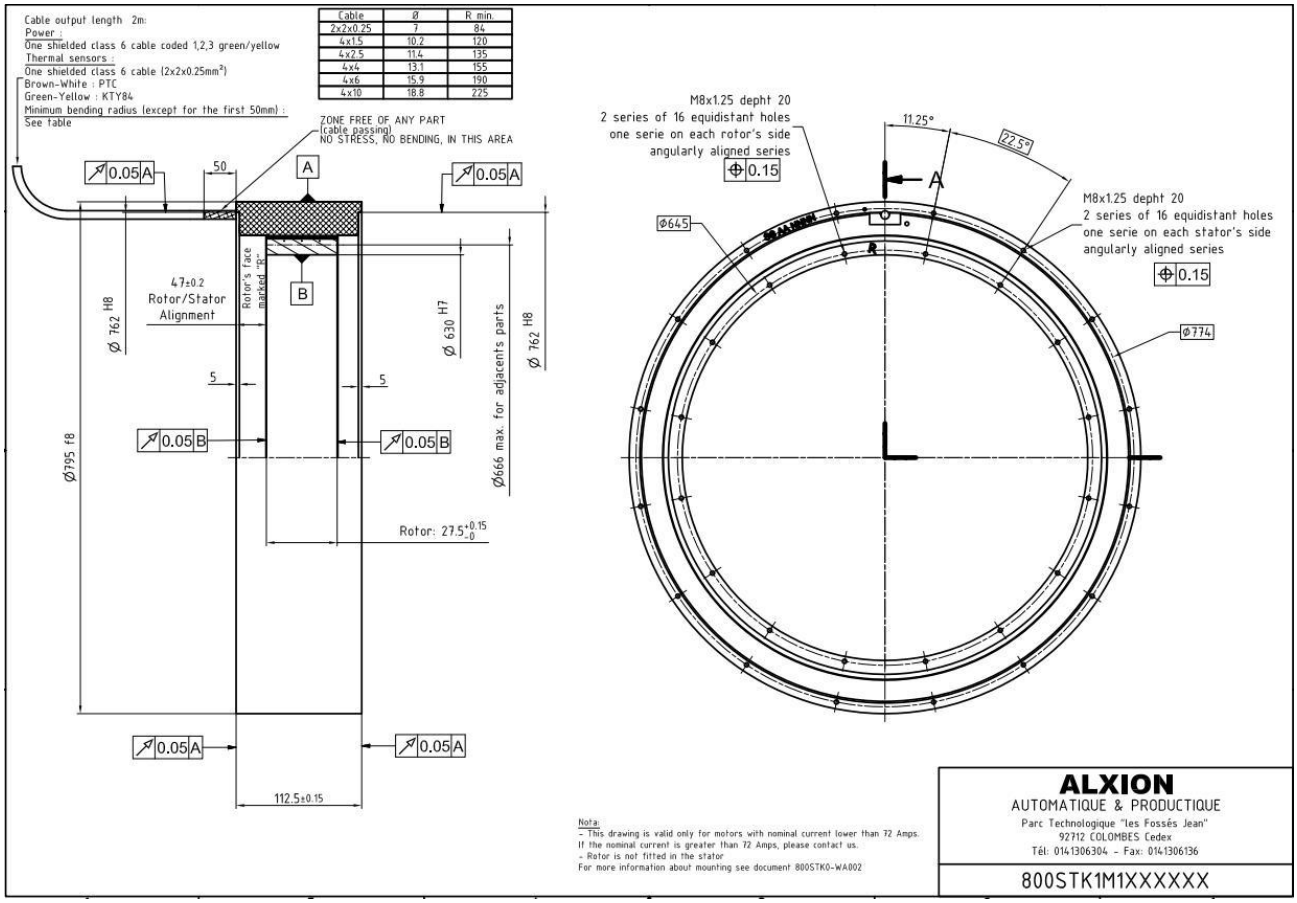

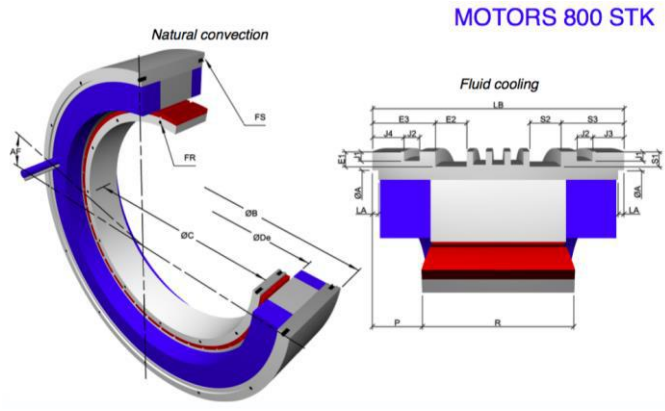

DIMENSIONS FOR ALL 800 STK		
Housing internal centering diameter	A H8	762
Angle wire output / tapped holes	AF	11.25°
Housing external centering diameter (fluid cooling)	B f8	795
Housing external centering diameter (natural convection)	B f8	795
Rotoric internal centering diameter	C H7	630
Housing internal diameter	De	689
Depth of fluid front input / output groove	E1	8
Width of fluid front input / output groove	E2	15.5
Position of fluid front I/O groove	E3	28 (68)
Rotoric fixation holes	FR	16xM8 sur Ø645
Housing fixation holes	FS	16xM8 sur Ø774

FIGURE 9-2 DIMENSION SPECIFICATION: GENERATOR TYPE: 800STK1M NK, AN APPROPRIATE MODEL FOR MATCHING THE REQUIREMENTS OF A 1.5M DIAMETER SYMPHONY PROTOTYPE (WWW.ALXION.COM)

- **Spring tank tuning system**

Spring adjustment tank: this unit is required to integrate the tuning of the air spring. If a limited unwanted pressure drop/raise occurs in the spring chamber due to leakage or temperature changes, the spring adjustment tank is used to compensate. The pressure inside the spring adjustment tank will be the same as the neutral pressure of the spring chamber which is around 15 bars(g).

Compressed air tank: a compressed air tank with control valves is placed in the cocoon in pressurize the spring adjustment tank. The pressure inside the compressed air tank will be 100 to 200 bar(g), to be specified at later stage.

These two units and auxiliary equipment form the spring tank tuning system, which is a support system for the spring tank function inside the Symphony (acting as a spring and medium carrier for the PTO). The water/air ratio inside the spring tank influences the system's mass spring characteristics. During temperature changes the water/air ratio needs to be tuned in order to optimise the WEC's efficiency. An illustrative drawing of the required system is shown in Figure 9-3; the spring tank, the compensation (spring adjustment) tank, the compressed air tank, connection pipes for air and water from the compensation tank to the spring tank and the outside, and the required valves (red cross when closed): the compensation tank is used to tune the spring tank. The neutral position pressure inside the spring tank is 15 bar. The neutral pressure is regulated using the compressed air tank and air outlet. The Neutral pressure the spring tank is also 15 bar g. The pressure inside the spring tank fluctuates between 10-20 bar each wave cycle. The pressure differential between the spring tank and the compensation tank is used to pump water or air between the two tanks. The different valve positions according to certain operational modes required are sketched in Figure 9-4.

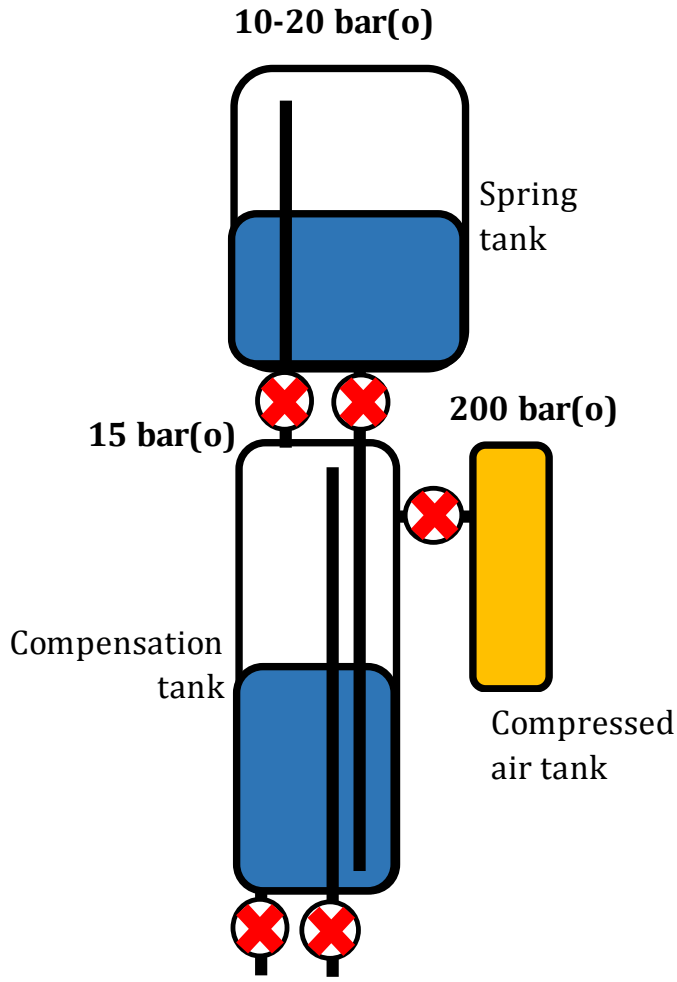

FIGURE 9-3 SPRING ADJUSTMENT SYSTEM SCHEME WITH THE MAIN PARTS COMPENSATION TANK AND COMPRESSED AIR TANK; AND THE CONNECTIONS (I) COMPRESSED AIR CONNECTION FROM COMPRESSED AIR TANK TO COMPENSATION TANK, (II) AIR CONNECTION FROM COMPENSATION TANK TO SPRING TANK, (III) WATER CONNECTION FROM COMPENSATION TANK TO SPRING TANK, (IV) WATER INLET/OUTLET, AND AIR INLET/OUTLET. THE RESPECTIVE VALVES ARE ALL DEPICTED IN CLOSED POSITION (CROSS), WHEREAS OPEN POSITION INDICATES 'OPEN'.

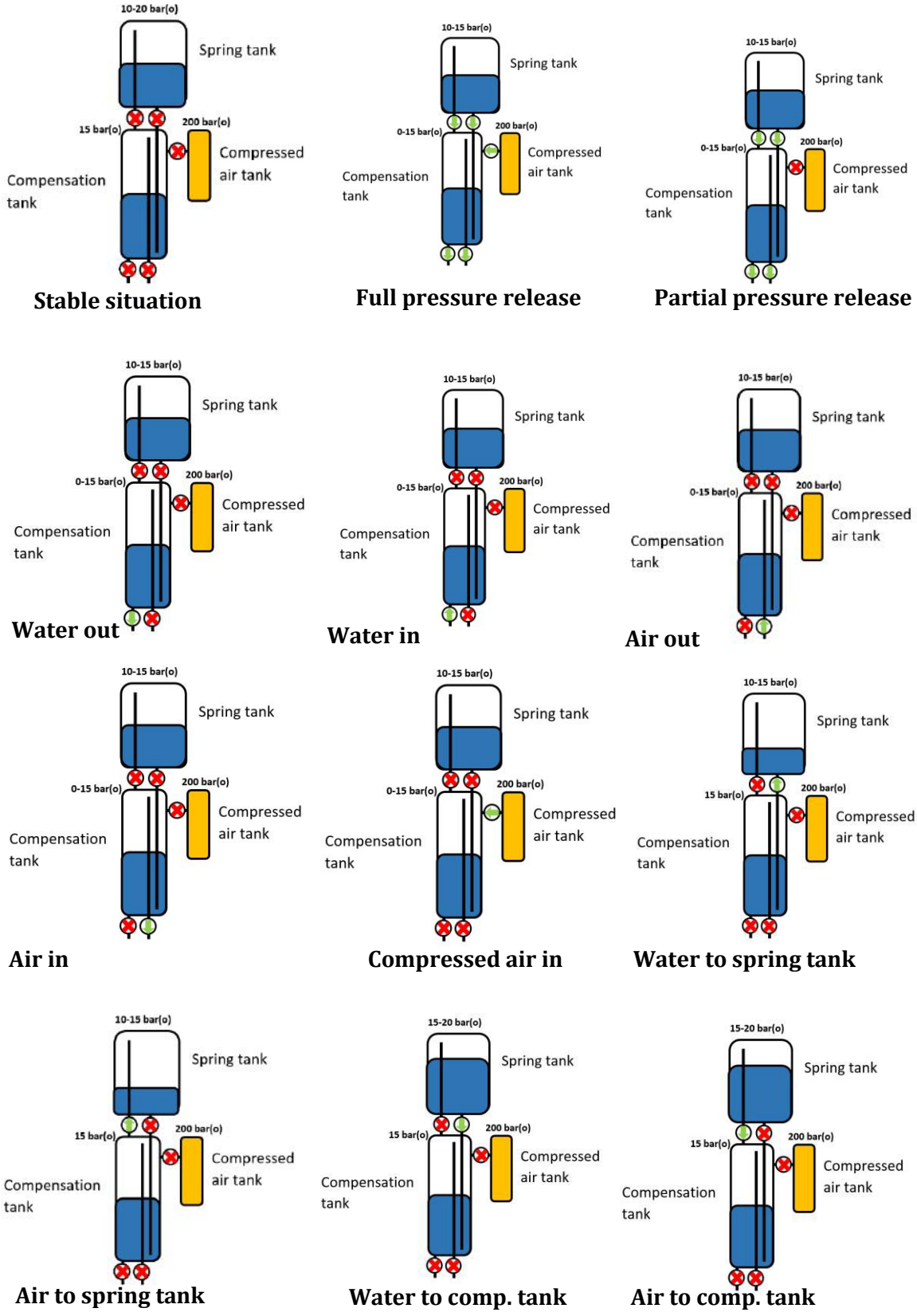

FIGURE 9-4 TUNING SITUATIONS REQUIRED TO BE COVERED BY THE COMPENSATION TANK SYSTEM.

The dimensions required for the compensation tank are possibly the most critical for the inclusion of the cocoon, as the demand to compensate air temperature variations may imply large volumes. The dimensions required depend on the specification to which extent the temperature needs to be compensated, which is partly empirical. The compensation tank is used to tune the spring tank. For the first prototype, a relative small compensation is placed with a high pressure compressed air tank. This setup can change the spring characteristics but only for a limited amount of time (here called "passive tuning"; note that passive/active tuning might not be the proper wording since it is used for different purposes in control techniques).

In case the average temperature inside the spring tank changes, the properties of the air spring changes. The volume inside the compensation is designed to be able to compensate for this matter. The design of the Symphony is made to have a maximum average temperature change of 25 degrees Celsius. This value needs to be benchmarked with measurements in the turbine tests in WP4 and future studies dedicated to this task, as it is a critical obstacle to PTO feasibility if the real value is a multiple of this assumed temperature change range. The resulting dimensions of the compensation tank are the following:

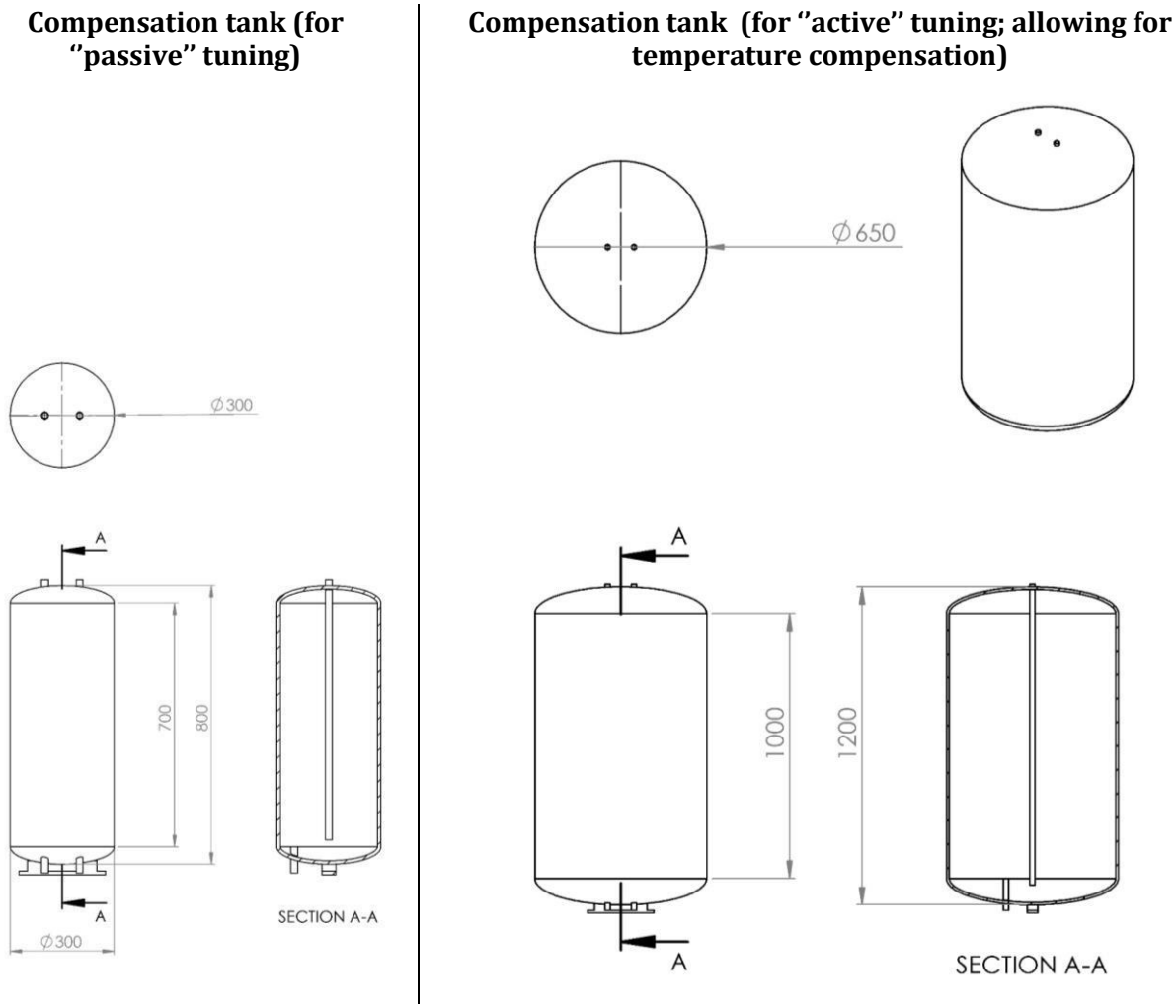

FIGURE 9-5 REQUIRED COMPENSATION TANK REQUIREMENTS FOR "ACTIVE" AND "PASSIVE" TUNING OF THE AIR SPRING.

TABLE 9-2 TECHNICAL SPECIFICATIONS COMPENSATION TANK

"Passive" tuning	*Value*	*Unit*
Neutral operation pressure	15	[bar]
Max operation pressure	20	[bar]
Minimum operation pressure	10	[bar]
Total tank volume	0.050	[m^3]
Water volume	0.025	[m^3]
Air volume	0.025	[m^3]
Material type	Stainless steel AISI 304	
"Active" tuning		
Neutral operation pressure	15	[bar]
Max operation pressure	20	[bar]
Minimum operation pressure	10	[bar]
Total tank volume	0.36	[m^3]
Water volume	0.18	[m^3]
Air volume	0.18	[m^3]
Material type	Stainless steel AISI 304	
Technical specifications compressed air tank		
Max operation pressure	200	[bar]
Minimum operation pressure	15	[bar]
Air volume	0.25	[m^3]

- **Torque meter, valves and connection pipes**

The auxiliary equipment for essential measurements (torque meter between turbine and generator) and providing the connections and controls between the different air/water volumes of the spring tank tuning system are uncritical with respect to their dimensions and fitting into the cocoon. The choice of models will be undertaken at later stage, due to the fast development in this area.

- **Cocoon locking system and Winch**

For tide compensation and survivability mode under severe sea conditions, a winch unit is placed on the bottom part of the cocoon, which will pull the Symphony down. It will equally be used for maintenance removal of the cocoon. Interfaces exist to the upper part of the cocoon and/or outside of device, it is however expected that these can be uncritical.

- **Cocoon guidance system and seals**

In order to remove the cocoon smoothly from the hull, a guidance system must be implemented. The conceptual design of this system foresees rolling rails on the outside of the cocoon, which must be included in the dimensioning considerations but is considered uncritical for the total dimensions. Figure 9-6 shows the conceptual design of the guidance rail and expected overall dimensions.

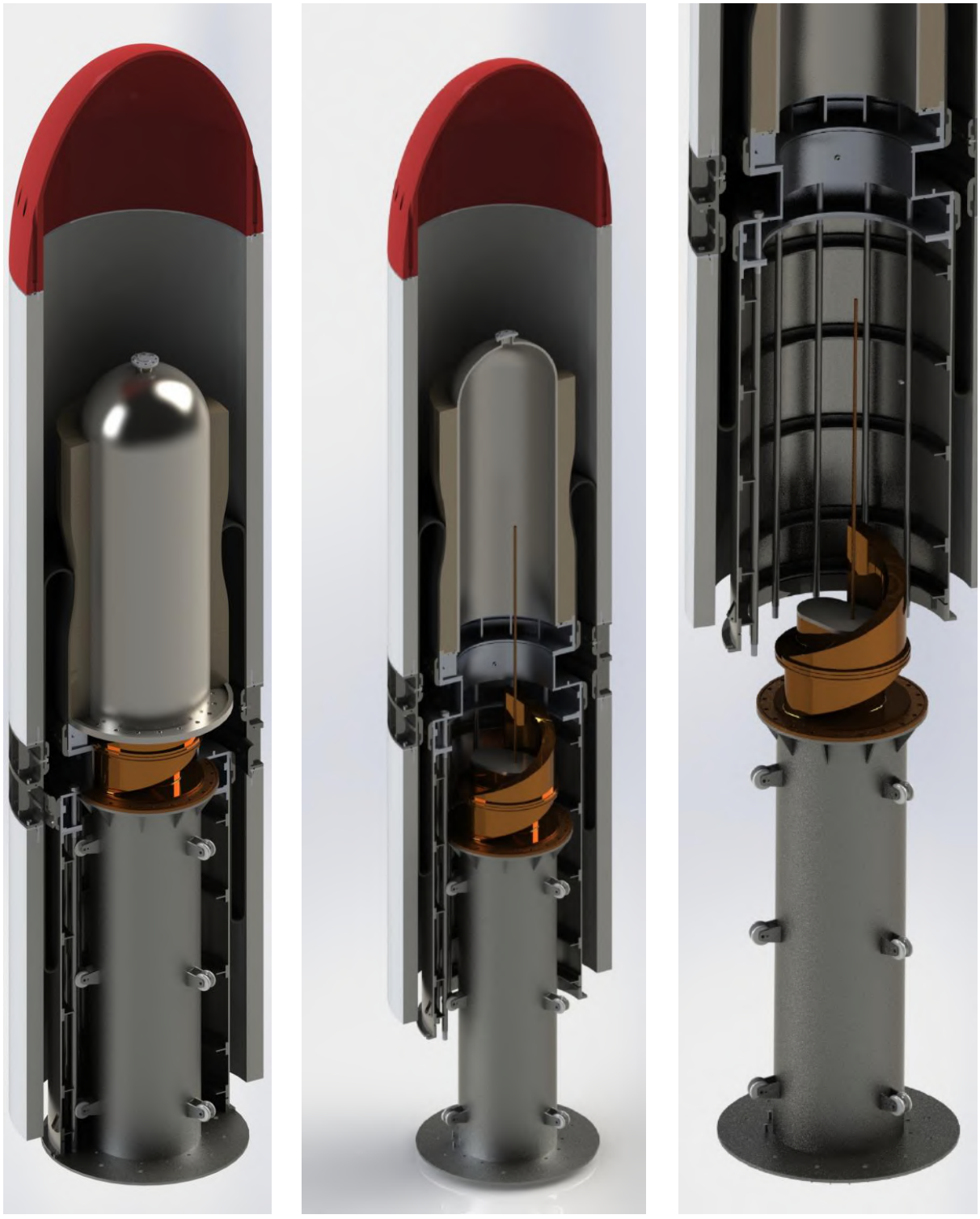

FIGURE 9-6 GUIDANCE RAIL SYSTEM FOR COCOON REMOVAL; LEFT: SPRING TANK, TURBINE HOUSING AND COCOON HOUSING AS INSERTED IN THE HULL, CENTRE: CROSS-SECTION OF SPRING TANK AND TURBINE HOUSING; RIGHT: COCOON PARTLY REMOVED.

The exploded view in Figure 9-7 outlines the conceptual design of the cocoon components at present stage of development. More detailed design and choice of manufacturers/models will be made at stage of cocoon prototype development, which is out of scope for WETFEET.

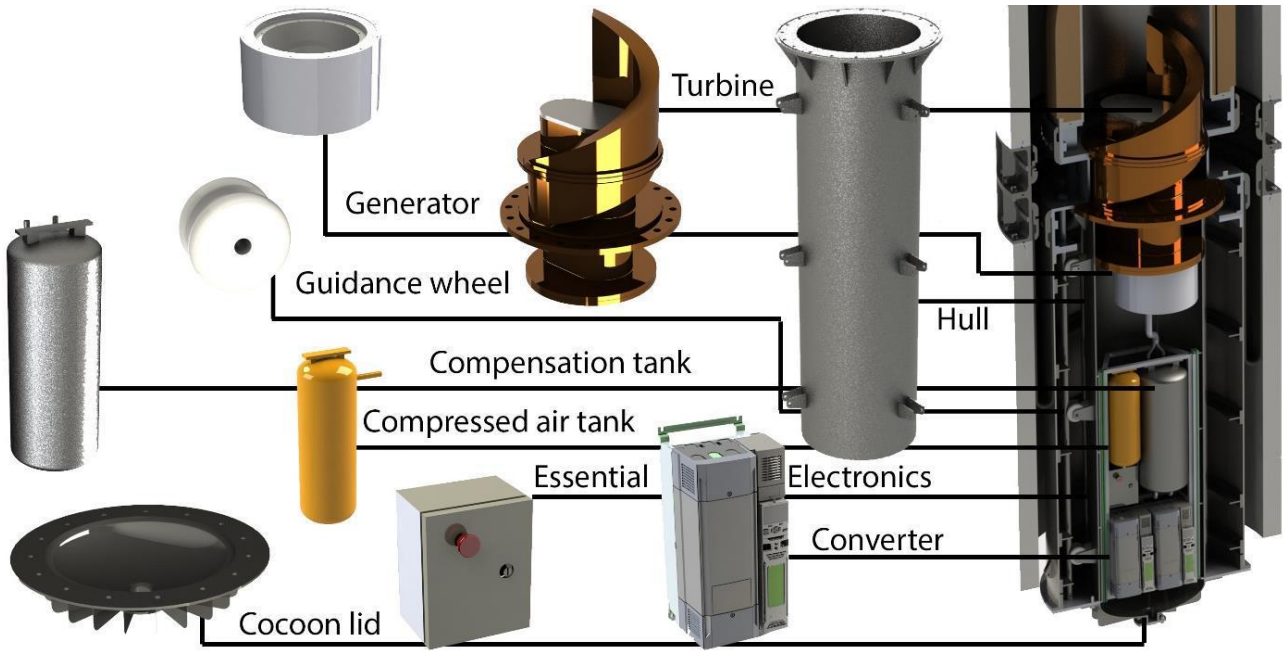

FIGURE 9-7 REQUIRED COMPENSATION TANK REQUIREMENTS FOR "ACTIVE" AND "PASSIVE" TUNING OF THE AIR SPRING.

9.2. Engineering constraints and evaluation for large-scale applications

9.2.1. Up-scaling issues regarding the cocoon

As the WECs becomes bigger, the control **cocoon becomes bigger and he**avier. Sea operations costs (installation, inspection, maintenance, decommissioning operations) are a relative big expense in offshore renewables, and also the mere handling of large units becomes increasingly complex. This might impose physical limits to the up-scaling of Symphony devices with control cocoon. For relative big WECs or wave farms it becomes increasingly important to reduce the weight of the control cocoon, also due to economic feasibility. The weight and size of the control cocoon can be minimised by moving a part of the components to a central control station. The central control station becomes more interesting in case of a wave farm.

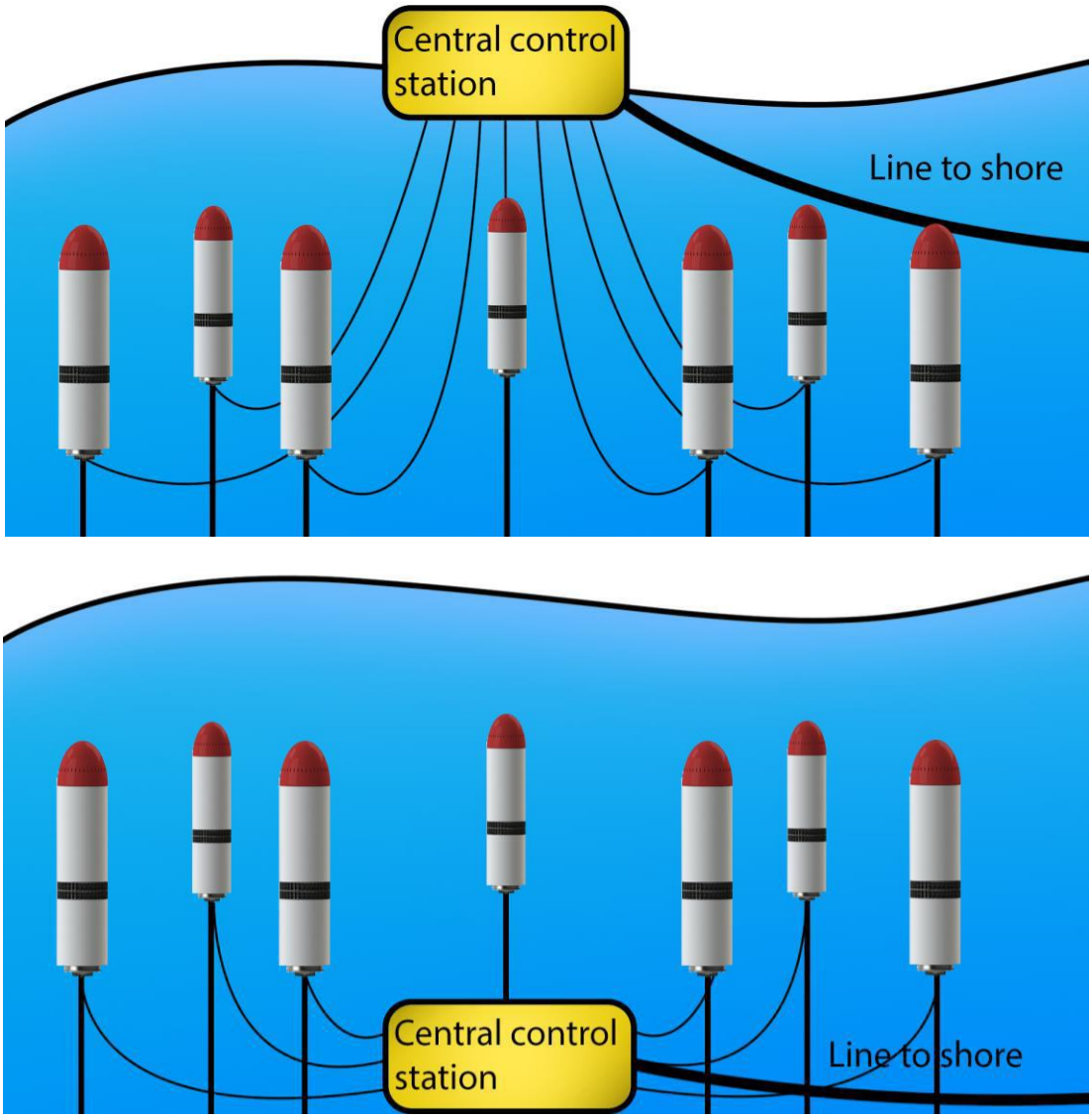

FIGURE 9-8 VISION FOR JOINING SIGNIFICANT PARTS OF THE CONTROL COCOON INSIDE CENTRAL UNITS. THE VERSION OF A FLOATING UNIT RESEMBLES THE APPROACH TAKEN IN OFFSHORE (FIXED) WIND FARMS, HOWEVER MIGHT BECOME A SIGNIFICANT TECHNICAL CHALLENGE (FLOATING UNITS WITH DYNAMIC POWER CABLES). LOCATION ON THE SEABED APPEARS A MORE FEASIBLE SOLUTION.

Although such a central unit would not replace all parts of the cocoon (turbine and generator would need to be kept within each device), such a solution could significantly contribute to mitigate up-scaling issues with increasing dimensions.

The maximum depth of the Symphony 1.5 m prototype is less than 30 meters during maintenance, allowing the use of divers. For bigger devices, the control cocoon at the bottom part of the construction, **diving operations become increasingly challenging**, due to deeper bottom part. At this stage, an automated control cocoon removal & placement system is essential for a sound operation and maintenance strategy. Also, the placement of the control cocoon on top of the device is a potential solution to this challenge.

The current generator is a permanent magnet generator. The **efficiency of a permanent magnet generator drops when it is used in partial loads** due to iron losses. From an efficiency point of view, a relatively low rated power is required but for controllability during heavy sea states a high rated power is required. This aspect is a general problem for wave energy, because of extreme high peaks. It would be better explained including graphs about regular (non-PM) generators and why they are not suitable either, but this is beyond the scope of this contribution. In this context, a hybrid generator type might be the best option, or potentially the use of more than one PTO per device (several small turbine-generator units.

9.2.2. Application in other device types

The control cocoon was specifically developed for SPDD technology, and is a feature that could mitigate one major issue of submerged devices, the accessibility and maintenance operations. Depending on the geometry and potential access for removal/placing on the bottom (or sideways in a submerged area), the control cocoon could become an interesting option for other device types, especially point absorbers.

As not only the submerged access for removal but mainly the joining of essential parts of the WEC inside one removable unit is the philosophy of a control cocoon, partly implementations of control cocoon in other devices will make sense. It goes beyond the scope of this report to elaborate more detailed visions, also because of the high diversity of existing concepts and possibilities to transfer this approach.

10. CONCLUSIONS AND FUTURE WORK

This deliverable compiles the main findings of the preliminary feasibility assessment of 8 proposed breakthroughs. Table 10-1 below summarizes the main conclusions that can be drawn from the work presented herein along with the prospect to future analysis in the upcoming tasks of the WETFEET project.

TABLE 10-1 SUMMARY OF MAIN FINDINGS FOR EACH BREAKTHROUGH CONCEPT & FUTURE WORK AS PART OF THE WETFEET PROJECT

Breakthrough idea	Feasibility & potential	Challenges & issues	Future work
Negative springs	Both the IVV and the HNS methods have demonstrated their potential to shift the resonance frequency of resonant WEC through	The IVV method requires a large extra structure to accommodate the volume which appears very challenging	Tank testing of the HNS method will undergo in WP3 Further numerical analysis (including

	analytical and frequency-domain analysis	No significant issues were identified for the HNS method	AEP assessment) will be carried out
Enhanced added-mass	It was shown that the shape of the submerged-mass can vary depending on the objective function of the optimization routine The EAM concept has potential to contribute to stability of spar-like structure	Manufacturing complexity due to the EAM may lead to	No further numerical nor experimental modelling is currently envisaged
Submergence as a survivability strategy	Conceptual benefit of using a remote-controlled submergence was highlighted Hydrodynamic load reductions potential was quantified	Many major engineering issues were identified, e.g increased overall system complexity (ballasting/winching equipment, mooring and umbilical design, power supply, sealing/protective mechanisms, etc…), additional cost due to on-board equipment Increased hydrostatic loads with submergence depth and dynamic stability is also a big challenge	Experimental tank-testing of the submergence strategy for an OWC spar buoy prototype will be carried out in WP3 More in-depth numerical and engineering analysis will also be carried out in WP3 to further investigate the issues identified
Dielectric Elastomer Generators	Feasibility of using DEG for PTO into two different WECs was exhibited Potential gain in terms of PTO simplicity and power production was shown	Generic issues related to manufacturability and installation were made in [1], [2] Fatigue life of DEG and, in particular, submerged DEG-PTO systems remains largely unknown	Wet-run test of a DEG membrane PTO (scale between 1:15 and 1:30) will be carried out in WP5 Sensing system for monitoring and control of DEG-PTO will also be developed in WP5
Tetra-radial air turbine	Numerical evidence of the improved efficiency of the novel air turbine when compared to state-of-the-art air turbines for WEC was provided	Special care to the structural integrity of the turbine should be done. Curved-duct manifold and sliding cylindrical vanes are two components which	Experimental dry-testing of the full turbine in a relevant setup environment will be carried out as part of WP4

		would require special care	
Novel water turbine	The characteristics of a customized water-turbine capable of providing the best trade-off for applications in a SPDD-WEC type were detailed	Beyond the requirements in terms of high-pressure and high-flow speeds, manufacturing and reliability were highlighted	Experimental dry-testing of the full turbine in a relevant setup environment will be carried out as part of WP4
Structural membrane	The functional requirements and behavior of a rubber membrane to provide sealing and spring to a SPDD-WEC type were presented and appear like a promising solution	Manufacturability of a membrane for large-scale applications emerges as the main issue Ability to handle the sideway forces are also a concern	Experimental dry-testing of the 1.5m diameter membrane under static loads will be carried out as part of WP4
Control cocoon as an O&M strategy	Design considerations to develop a capsule accommodating all critical PTO parts of a submerged-WEC were proposed The possibility of detaching the control cocoon to facilitate O&M interventions appear like an attractive alternative to underwater or port maintenance strategies	Controllability and power-efficiency of the control cocoon system for large-scale applications are considered to be the two main concerns	Simplified tank-testing of the control cocoon for a Symphony prototype will be carried out in WP3

The most promising breakthrough ideas will also go through a more in-depth multi-disciplinary assessment within the frame of WP7. This will involve dedicated considerations with respects to techno-economic performance, supply-chain analysis of critical components, logistical and marine operations issues, environmental impact assessment, life-cycle and carbon-footprint analysis as well as a macro socio-economic impact study. Beyond this WP7 scope, the TPL framework as conceived by Weber [29] will be applied. A scenario featuring one breakthrough will be benchmarked in terms of TPL against the reference design cases presented in this report.

BIBLIOGRAPHY

[1] B. Teillant, Y. Debruyne, A. Sarmento, M. Silva, T. Simas, R. P. F. Gomes, J. C. C. Henriques, M. Philippe, A. Combourieu, and M. Fontana, "WETFEET Deliverable 2.1 - Designs and specifications of an OWC able to integrate the negative spring," 2016.

[2] R. Schuitema, H. Van Noorloos, and F. Neumann, "WETFEET Deliverable 2.2 - Report with designs and specifications of a Symphony able to integrate the control cocoon , electro-mechanic PTO , structural membrane and dielectric generators," 2016.

[3] "EMEC - TRL." [Online]. Available: http://www.emec.org.uk/services/pathway-to-emec/technology-readiness-levels/. [Accessed: 01-Jan-2016].

[4] R. P. F. Gomes, J. C. C. Henriques, L. M. C. Gato, and a. F. O. Falcão, "Hydrodynamic optimization of an axisymmetric floating oscillating water column for wave energy conversion," *Renew. Energy*, vol. 44, pp. 328–339, 2012.

[5] Massachuset Institute Technology, "WAMIT." 2015.

[6] Orcina, "OrcaFlex." 2016.

[7] J. N. Newman, *Marine Hydodynamics*. The MIT Press Cambridge, 1999.

[8] INNOSEA, "Preliminary Structural Assessment of the OWC Spar-Buoy. WETFEET WP2 internal report.," 2016.

[9] Det Norske Veritas (DNV), "DNV-OS-C106: Structural Design of Deep Draught Floating Units / Spars," 2012.

[10] Det Norske Veritas, "DNV-RP-F205 Global Performance Analysis of Deepwater Floating Structures, vol. DNV-RP-F20," 2009.

[11] Det Norske Veritas, "DNV-OS-C101 Design of Offshore Steel Structures - General (LRFD Method)," 2011.

[12] Det Norske Veritas, "DNV-RP-C202 Buckling Strength of Shells, vol. DNV-RP-C20.," 2013.

[13] IST, "Conceptual Design of the OWC Spar-Buoy. WETFEET WP2 internal report," 2015.

[14] WavEC Offshore Renewables, "Leixões environmental conditions. WETFEET internal report," 2015.

[15] INNOSEA, "Analysis of hydrodynamic loads assessment results provided by WavEC V4. WETFEET internal report," 2016.

[16] A. F. D. O. Falcão, L. M. C. Gato, and E. P. a S. Nunes, "A novel radial self-rectifying air turbine for use in wave energy converters. Part 2. Results from model testing," *Renew. Energy*, vol. 53, pp. 159–164, 2013.

[17] J. C. C. Henriques, M. F. P. Lopes, R. P. F. Gomes, L. M. C. Gato, and A. F. O. Falcão, "On the annual wave energy absorption by two-body heaving WECs with latching control," *Renew. Energy*, vol. 45, pp. 31–40, 2012.

[18] T. Perez and T. I. Fossen, "A Matlab toolbox for parametric identification of radiation-force models of ships and offshore structures," *Model. Identif. Control*, vol. 30, no. 1, pp. 1–15, 2009.

[19] J. N. Newman and C. H. Lee, *WAMIT User Manual*. \url{http://www.wamit.com/manual.htm}: WAMIT Inc., 2004.

[20] C. H. Lee and J. N. Newman, "Computation of wave effects using the panel method," in *Numerical models in fluid-structure interaction*, 2004.

[21] S. L. Dixon and C. A. Hall, *Fluid mechanics and thermodynamics of turbomachinery*, 7th Editio. Oxford: Butterworth-Heinemann, 2013.

[22] E. Tedeschi, M. Carraro, M. Molinas, and P. Mattavelli, "Effect of control strategies and power take-off efficiency on the power capture from sea waves," *IEEE Trans. Energy Convers.*, vol. 26, no. 4, pp. 1088–1098, 2011.

[23] A. F. de O. Falcão, "Control of an oscillating-water-column wave power plant for maximum energy production," *Appl. Ocean Res.*, vol. 24, no. 2, pp. 73–82, 2002.

[24] J. C. C. Henriques, J. C. C. Portillo, L. M. C. Gato, R. P. F. Gomes, D. N. Ferreira, and A. F. O. Falcão, "Design of oscillating-water-column wave energy converters with an application to self-powered sensor buoys," *Energy*, vol. 112, pp. 852–867, 2016.

[25] A. Combourieu, "Technical note - Preliminary motion analysis of the Symphony device. PROJECT: WETFEET," 2016.

[26] N. Leitjens, "Optimal Buffer Design for the Symphony Wave Power System.," Faculty of Engineering Technology, 2016.

[27] R. van Schie, "Physical model testing for characterizing the AWS," in *3rd European Wave Energy Conference*, 1998, pp. 192–199.

[28] M. Prado, F. Neumann, M. Damen, and F. Gardner, "AWS results of pilot plant testing 2004," in *6th European Wave & Tidal Energy Conference*, 2005, pp. 401–407.

[29] J. Weber and D. Laird, "Structured innovation of high performance Wave Energy Converter technology," in *11th European Wave and Tidal Energy Conference*, 2015, pp. 1–7.

[30] J. Fitzgerald, "Evolution of the AWS waveswing TM MkII concept," in *2nd International Conference on Ocean Energy*, 2008, no. October, pp. 1–9.

[31] M. I. Marei, M. Mokhtar, and A. A. El-Sattar, "MPPT strategy based on speed control for AWS-based wave energy conversion system," *Renew. Energy*, vol. 83, 2015.

[32] F. Wu, X. P. Zhang, S. Member, P. Ju, and M. J. H. Sterling, "Optimal control for AWS-based wave energy conversion system," *IEEE Trans. Power Syst.*, vol. 24, no. 4, pp. 1747–1755, 2009.

[33] J. Sá da Costa, J. Pinto, A. Sarmento, and F. Gardner, "Modelling and simulation of AWS: a wave energy extractor," in *4th IMACS Symposium on Mathematical Modelling.*, 2003, pp. 161–170.

[34] A. Sarmento, A. Luís, and D. Lopes, "Frequency-Domain Analysis of the AWS," in *3rd European Wave Energy Conference*, 1998, pp. 15–22.

[35] H. Polinder, M. Damen, and F. Gardner, "Linear PM generator system for wave energy conversion in the AWS.," *IEEE Trans. Energy Convers.*, vol. 19, pp. 583–589, 2004.

[36] H. Polinder and M. Damen, "Design, modelling and test results of the AWS PM linear generator," in *European Transactions on Electrical Power*, 2005, pp. 245–256.

[37] "Archimedes Wave Swing Ltd." .

[38] D. Valério, P. Beirão, and J. Sá da Costa, "Optimisation of wave energy extraction with the Archimedes Wave Swing.," *Ocean Eng.*, vol. 34, pp. 2330–2344, 2007.

[39] J. Sá da Costa, A. Sarmento, F. Gardner, and P. Beirão, "Time domain model of the Archimedes

Wave Swing wave energy converter.," in *6th European Wave and Tidal Energy Conference*, 2005, pp. 91–97.

[40] J. Pinkster, "Computations for Archimedes Wave Swing," Delft, The Netherlands, 1997.

[41] D. Albady and C. Öhman, "Characterization of a Cascade Gear Box for a Wave Energy Converter.," KTH Royal Institute of Technolog, 2003.

[42] J. Cruz and A. Sarmento, "Wave Energy Absorption by a Submerged Sphere of Variable Radius With a Swinging Single Point Moored Tension Line.," in *14th International Offshore and Polar Engineering*, 2004.

[43] J. Hals Todalshaug, "Wave Energy Convertor," WO 2015107158 A1, 2015.

[44] "CorPower Ocean," 2015. [Online]. Available: http://www.corpowerocean.com. [Accessed: 01-Dec-2015].

[45] J. Hals Todalshaug, G. Steinn Àsgeirsson, E. Hjálmarsson, P. Pires, M. Guérinel, J. Maillet, M. Lopes, and P. Möller, "Tank testing of an inherently phase controlled Wave Energy Converter .," in *11th European Wave and Tidal Energy Conference*, 2015.

[46] S. Peretta, P. Ruol, L. Martinelli, A. Tetu, and J. P. Kofoed, "Effect of a negative stiffness mechanism on the performance of the WEPTOS rotors," in *6th International Conference on Computational Methods in Marine Engineering*, 2015.

[47] X. Zhang and J. Yang, "Power capture performance of an oscillating-body WEC with nonlinear snap through PTO systems in irregular waves," *Appl. Ocean Res.*, vol. 52, no. AUGUST, pp. 261–273, 2015.

[48] X. Zhang, J. Yang, and L. Xiao, "Numerical Study of an Oscillating Wave Energy Converter with Nonlinear Snap - Through Power - Take - Off Systems in Regular Waves," in *33rd International Conference on Ocean Offshore Arctic Engineering*, 2014, pp. 225–230.

[49] J. Cordonnier, F. Gorintin, a. De Cagny, A. Clément, and a. Babarit, "SEAREV: Case study of the development of a wave energy converter," *Renew. Energy*, vol. 80, pp. 40–52, 2015.

[50] R. P. F. Gomes, J. C. C. Henriques, L. M. C. Gato, and A. F. de O. Falcão, "IPS 2-body wave energy converter: acceleration tube optimization," *Int. J. Offshore Polar Eng.*, vol. 20, pp. 247–255, 2010.

[51] S. Ribeiro e Silva, R. P. F. Gomes, and A. F. O. Falcão, "Hydrodynamic optimization of the UGEN: Wave energy converter with U-shaped interior oscillating water column," *Int. J. Mar. Energy*, 2016.

[52] M. J. D. Powell, "A direct seach optimization method that models the objective and constraint functions by linear interpolation," in *Advances in Optimization and Numerical Analysis*, S. Gomez and J.-P. Hennart, Eds. Dordrecht: Kluwer Academic, 1994, pp. 51–67.

[53] M. J. D. Powell, "Direct search algorithms for optimization calculations," *Acta Numer.*, vol. 7, pp. 287–336, 1998.

[54] C. H. Lee, J. N. Newman, and F. G. Nielsen, "Wave Interactions with an Oscillating Water Column," in *Proceedings of the 6th International Conference on Offshore and Polar Engineering*, 1996.

[55] A. J. N. A. Sarmento and A. F. de O. Falcão, "Wave generation by an oscillating surface-pressure and its application in wave energy extraction," *J. Fluid Mech.*, vol. 150, pp. 467–485, 1985.

[56] A. F. de O. Falcão and P. A. . Justino, "OWC Wave energy devices with air-flow control," *Ocean Eng.*, vol. 26, pp. 1275–1295, 1999.

[57] A. F. O. O. Falcão, J. C. C. C. Henriques, L. M. C. C. Gato, and R. P. F. F. Gomes, "Air turbine choice and optimization for floating oscillating-water-column wave energy converter," *Ocean Eng.*, vol. 75, pp. 148–156, 2014.

[58] A. F. O. Falcão and L. M. C. Gato, "Ocean Energy: Air Turbines," in *Comprehensive Renewable Energy*, vol. 8, A. A. Sayigh, Ed. Elsevier, 2012, pp. 111–149.

[59] A. F. de O. Falcão and R. J. A. Rodrigues, "Stochastic modelling of OWC wave power plant performance," *Appl. Ocean Res.*, vol. 24, no. 2, pp. 59–71, 2002.

[60] M. S. Longuet-Higgins, "On the statistical distribution of the heights of sea waves," *J. Mar. Res.*, vol. 11, pp. 245–266, 1952.

[61] M. S. Longuet-Higgins, "The statistical analysis of a random, moving surface," *Phil. Trans. R. Soc. Lond. A*, vol. 249, pp. 321–387, 1957.

[62] T. Sarpkaya and M. Isaacson, *Mechanics of wave forces on offshore structures*. New York, USA: Van Nostrand Reinhold, 1981.

[63] Y. Goda, *Random Seas and Design of Maritime Structures*, 3$^\mathrm. Singapore: World Scientific, 2010.

[64] L. S. Borgman, "Spectral Analysis of Ocean Wave Forces on Piling," *J. Waterw. Harb. Div.*, vol. 93, pp. 129–156, 1967.

[65] R. P. F. F. Gomes, J. C. C. C. Henriques, L. M. C. C. Gato, and A. F. de O. Falcão, "Wave power extraction of a heaving fl oating oscillating water column in a wave channel," *Renew. Energy*, vol. 99, pp. 1262–1275, 2016.

[66] O. E. Systems and IEA-OES, "International LCOE for Ocean Energy Technologies," techreport, 2015.

[67] R. P. Galvão, "Technical and economical viability study of floating {C}oaxial {D}ucted {OWC}," mastersthesis, Instituto Superior T{é}cnico, Universidade de Lisboa, 2015.

[68] R. P. F. Gomes, "Wave energy extraction from oscillating systems: numerical modelling and experimental testing," phdthesis, Instituto Superior Técnico, Universidade de Lisboa, 2013.

[69] J. D. C. Malvar Ferreira, "Experimental study of the dynamic instability in the oscillating water column spar buoy," mastersthesis, Instituto Superior T{é}cnico, Universidade de Lisboa, 2016.

[70] K. Tarrant and C. Meskell, "Investigation on parametrically excited motions of point absorbers in regular waves," *Ocean Eng.*, vol. 111, 2016.

[71] R. P. F. Gomes, J. C. C. Henriques, L. M. C. Gato, and A. F. O. Falcão, "Multi-point aerodynamic optimization of the rotor blade sections of an axial-flow impulse air turbine for wave energy conversion," *Energy*, vol. 45, no. 1, pp. 570–580, 2012.

[72] G. Moretti, G. Pietro Rosati Papini, M. Alves, M. Grases, R. Vertechy, and M. Fontana, "Analysis And Design Of An Oscillating Water Column Wave Energy Converter With Dielectric Elastomer Power Take-Off," in *Proceedings of the ASME 2015 34th International Conference on Ocean, Offshore and Arctic Engineering OMAE*, 2015.

[73] R. Vertechy, G. P. Rosati Papini, and M. Fontana, "Reduced Model and Application of Inflating Circular Diaphragm Dielectric Elastomer Generators for Wave Energy Harvesting," *J. Vib. Acoust.*, vol. 137, no. 1, 2014.

[74] R. Vertechy and M. Fontana, "Electromechanical characterization of a new synthetic rubber

membrane for dielectric elastomer transducers," in *SPIE Smart Structures and Materials+ Nondestructive Evaluation and Health Monitoring*, 2015.

[75] P. Steinmann, M. Hossain, and G. Possart, "Hyperelastic models for rubber-like materials: Consistent tangent operators and suitability for Treloar's data," *Arch. Appl. Mech.*, vol. 82, no. 9, pp. 1183–1217, 2012.

[76] F. B. Madsen, L. Yu, P. S. Mazurek, and A. L. Skov, "A simple method for reducing inevitable dielectric loss in high-permittivity dielectric elastomers," *Smart Mater. Struct.*, vol. 25, 2016.

[77] A. F. de O. Falcão and P. A. . Justino, "OWC Wave energy devices with air-flow control," *Ocean Eng.*, vol. 26, no. 9, pp. 1275–1295, 1999.

[78] B. Pereiras, P. Valdez, and F. Castro, "Numerical analysis of a unidirectional axial turbine for twin turbine configuration," *Appl. Ocean Res.*, vol. 47, pp. 1–8, 2014.

[79] J. E. Borges, "Three-dimensional Design of Turbomachinery," phdthesis, University of Cambridge, UK, 1986.

[80] J. E. Borges, "A Three-Dimensional Inverse Method for Turbomachinery: Part I-theory," *J. Turbomachinery, Trans. ASME*, vol. 112, no. 3, pp. 346–354, 1990.

[81] J. E. Borges, "A Three-Dimensional Inverse Method for Turbomachinery: Part II-experimental verification," *J. Turbomachinery, Trans. ASME*, vol. 112, no. 3, pp. 355–361, 1990.

[82] S. A. Korpela, *Principles of Turbomachinery*. Hoboken, NJ: Wiley, 2011.

[83] O. E. Balje, *Turbomachines*. New York: Wiley, 1981.

[84] A. F. O. Falcão, L. M. C. C. Gato, J. C. C. C. Henriques, J. E. Borges, B. Pereiras, and F. Castro, "A novel twin-rotor radial-inflow air turbine for oscillating-water-column wave energy converters," *Energy*, vol. 93, pp. 2116–2125, 2015.

[85] J. de Jong, "Design of Power Take Off Turbine for the Symphony Wave Energy Converter.," Hogeschool INHOLLAND Delft HBO, 2015.

[86] J. Falnes, *Ocean Waves and Oscillating Systems*. Cambridge University Press, 2002.

APPENDICES

A. Scantlings of the OWC spar buoy reference designs

Design #0:

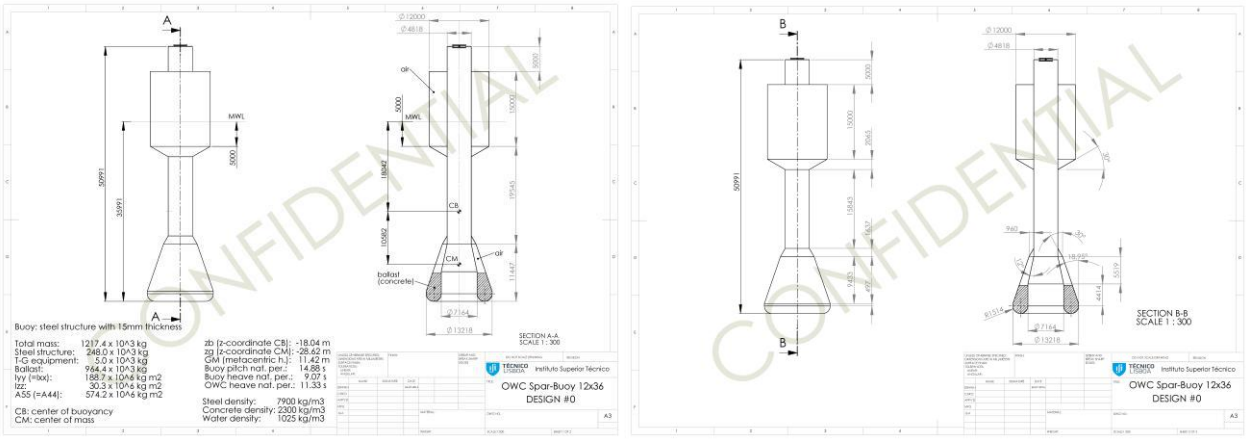

FIGURE A-0-1 SCANTLING OF THE OWC SAPR BUOY REFERENCE DESIGN #0

Design #2:

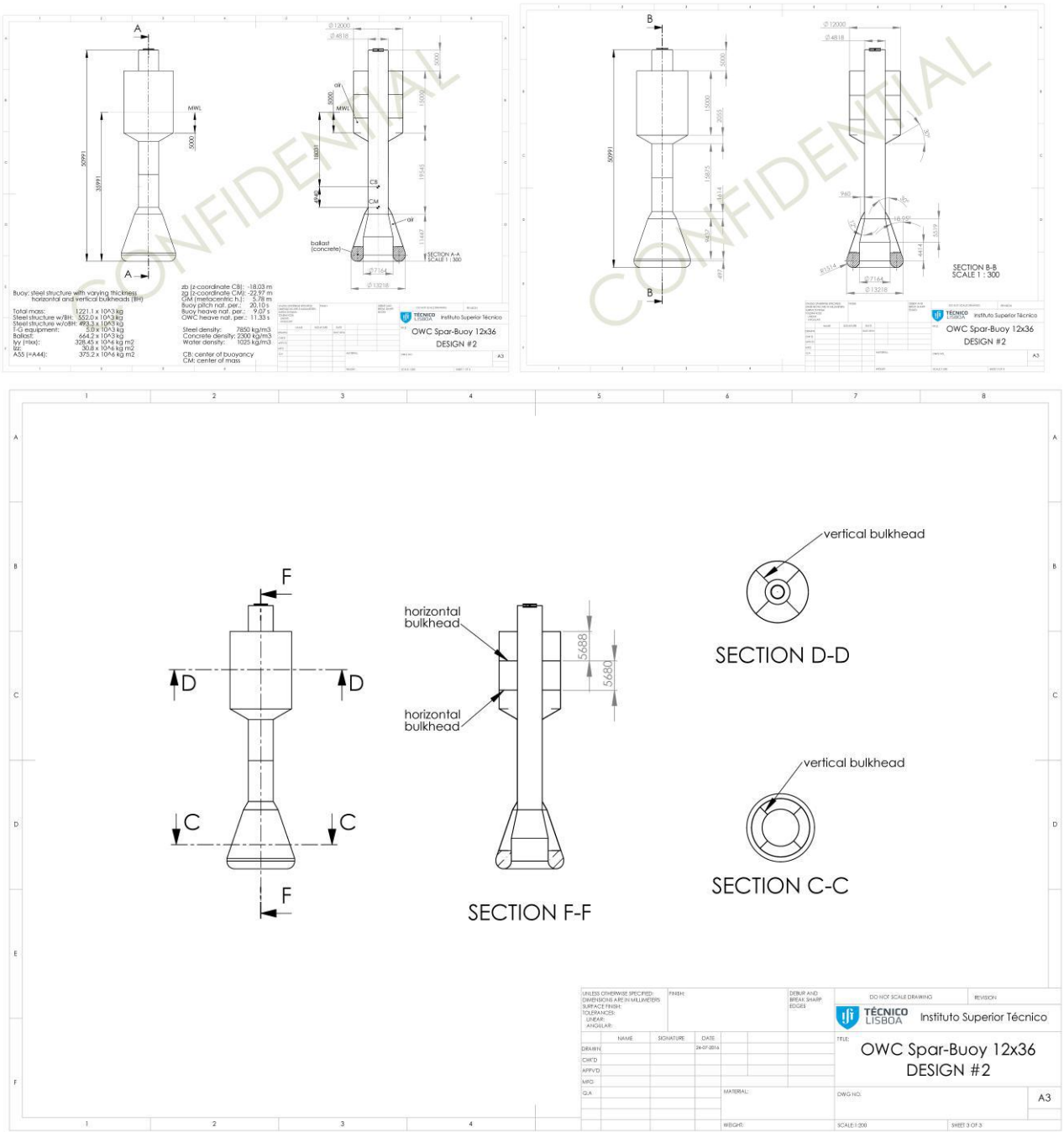

FIGURE A-0-2 SCANTLING OF THE OWC SPAR BUOY REFERENCE DESIGN #2

Design #3:

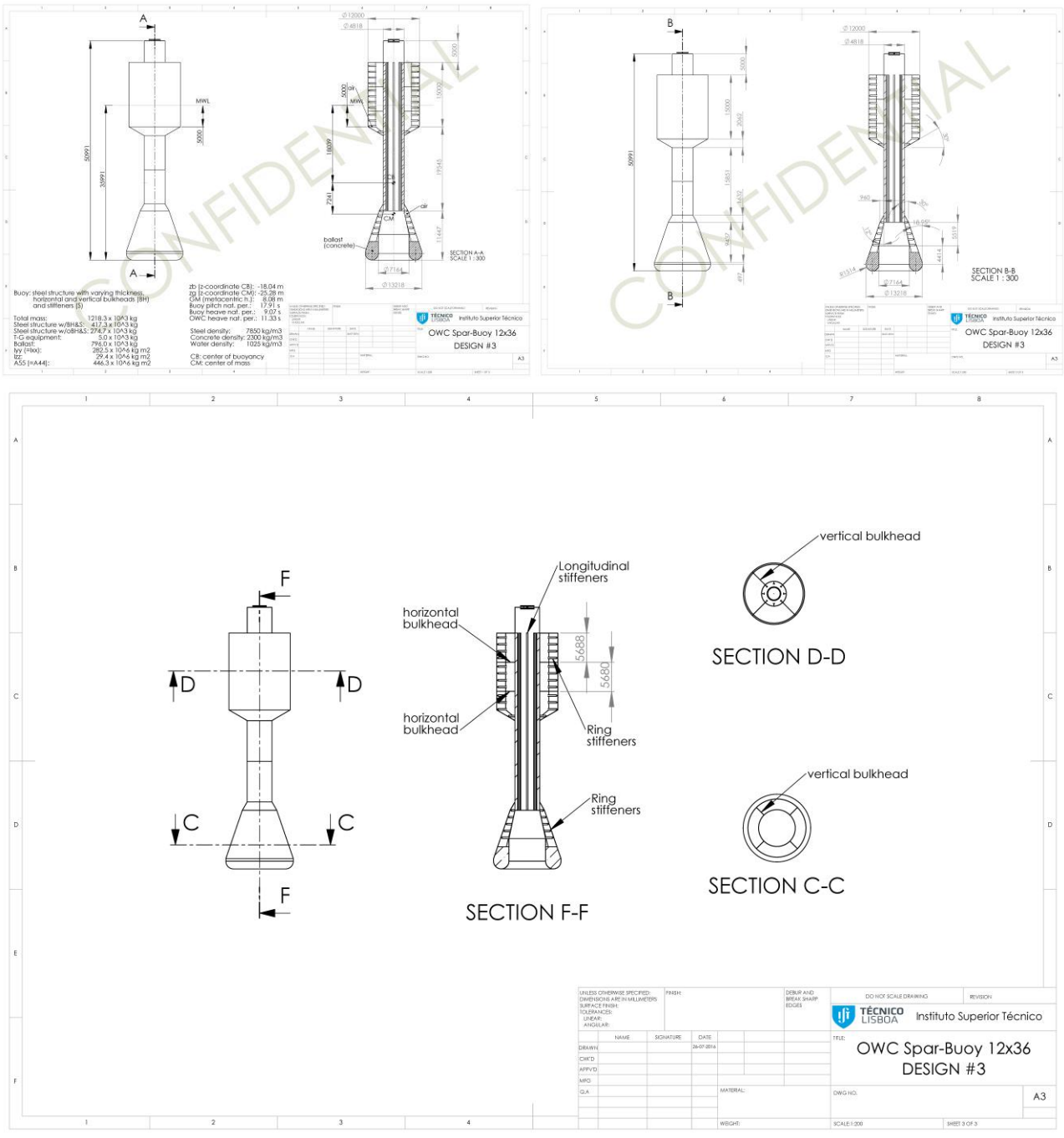

FIGURE A-0-3 SCANTLING OF THE OWC SPAR BUOY REFERENCE DESIGN #3

This appendix summarizes the verification procedure deployed to ensure that the

- **Surge force verification:**

The total forces F_1 acting on the structure in the general X – direction are taken as follows:

$$F_1 = Wave_{1GX} + AD_{GX} + Hyrdostatic_{GX} + Connections_{GX} \quad \text{(B-0-1)}$$

Where the subscript $_1$refers to the global force and GX corresponds to the surge direction. $Wave$, AD, $Hydrostatic$ and $Connections$ respectively correspond to the contribution from the excitation and diffracted hydrodynamic forces ($Wave$), the added-mass and damping (AD), the hydrostatic component and the mooring force.

The inertia force in surge F_{1M} is computed by:

$$F_{1M} = m * at_{GX} \quad \text{(B-0-2)}$$

With m the total dry mass of the WEC and at its translational acceleration.

The following figure presents the time-series of F_1 and F_{1M}, showing that they are equal.

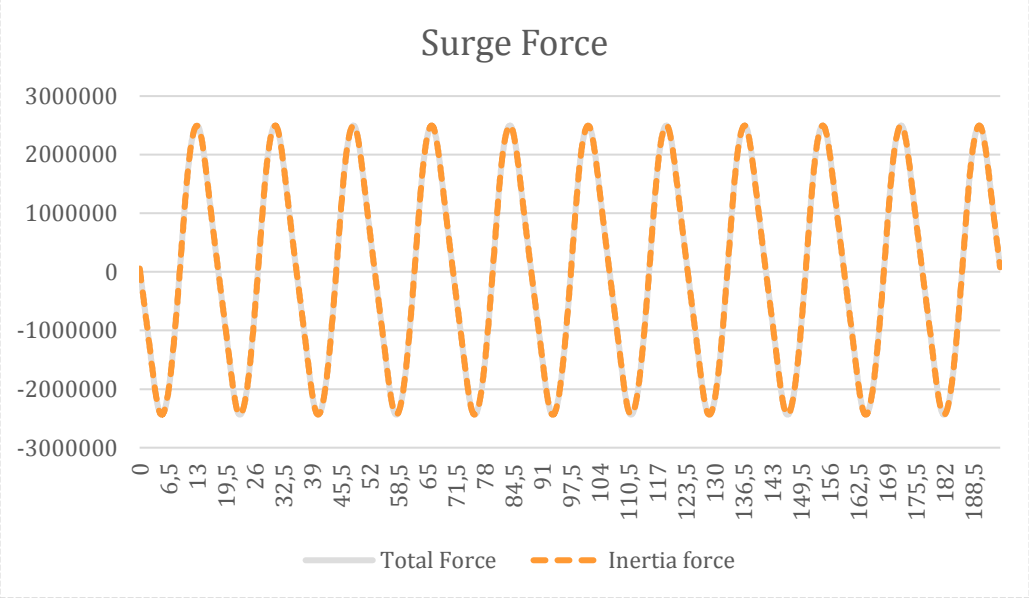

FIGURE 0-4: SURGE FORCE COMPUTATION VERIFICATION

- **Heave force verification:**

As for the surge mode, the total forces acting on the structure in the general Z – direction are calculated as:

$$F_3 = Wave_{1GZ} + AD_{GZ} + Hydrostatic_{GZ} + Connections_{GZ}$$

The inertia force in heave is computed by:

$$F_{3M} = m * at_{GZ}$$

In the following figure, one can see that F_3 and F_3M are equal.

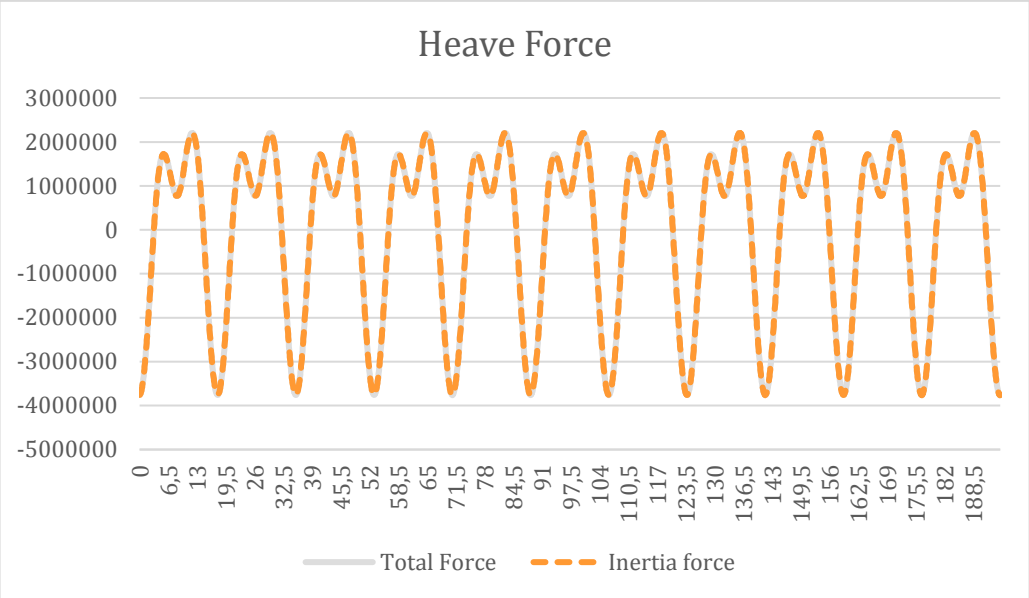

Figure 0-5: Heave force computation verification

- **Pitch moment verification:**

The pitch moment is computed considering all the forces and moments acting on the structure, and as a result we have:

$$M_5 = Wave_{1MtLy} + AD_{LMy} + Hydrostatic_{MtLy} + TotalConnections_{MtLy} + (t_{GZ} - t_{GZ_{Cg}}) * F_1 - (t_{GX} - t_{GX_{Cg}}) * F_3$$

The moment of inertia in pitch is obtained by:

$$M_{5M} = I_{yy} * ar_{GY}$$

Here also, M_5 and M_{5M} are equal, thus ensuring the balance between the moments acting on the structure and the inertia moment.

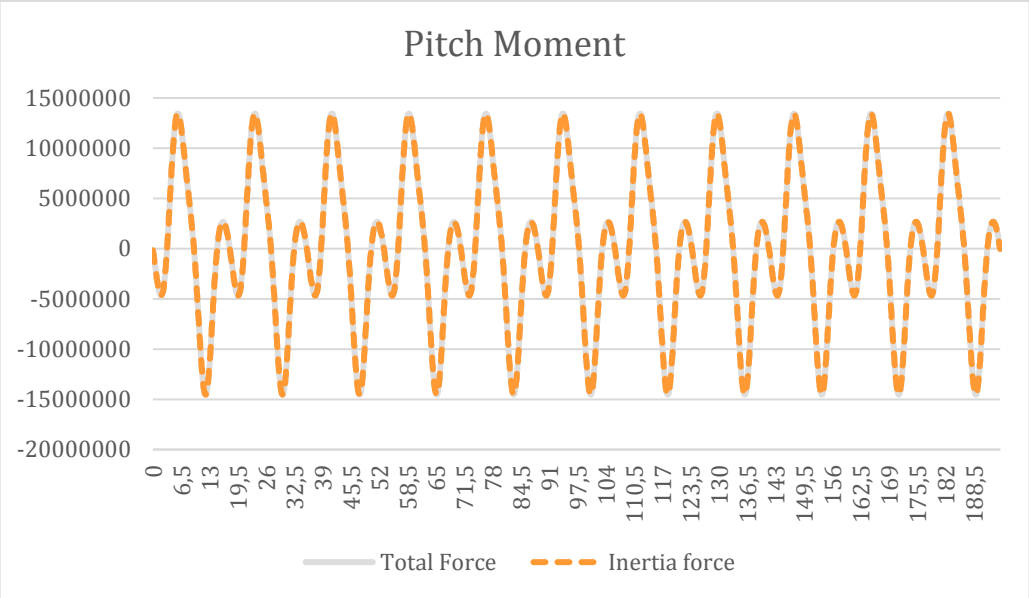

FIGURE 0-6: PITCH MOMENT COMPUTATION VERIFICATION

c. The two-body WEC

Building upon the theoretical foundation laid out by J. Falnes [86], a two-body floating WEC oscillating only in heave is considered. In such a system, the two bodies are coupled via their hydrodynamics and by their mechanics, the latter representing the PTO used for energy extraction by their relative motion. The system is illustrated below in Figure C-1:

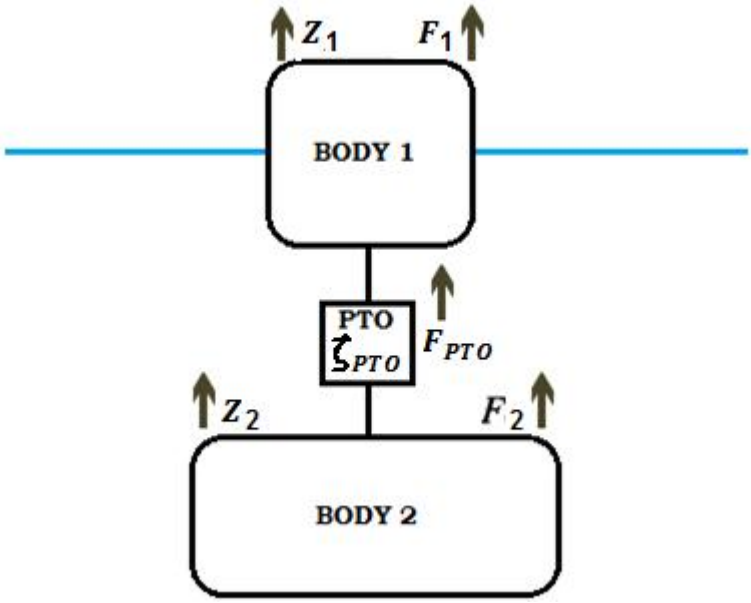

FIGURE C-1 THE TWO BODIES OF THE WEC, COUPLED BY THEIR HYDRODYNAMICS AND THE PTO.

The time-dependent vertical positions and wave-induced forces of Bodies 1 & 2 are denoted by $\{z_1(t), f_1(t)\}$ and $\{z_2(t), f_2(t)\}$, respectively. By taking the Fourier transform of these quantities, the corresponding frequency-dependent complex amplitudes of the vertical position and excitation force of Bodies 1 & 2 are denoted by $\{ Z_1, F_1 \}$ and $\{ Z_2, F_2 \}$, respectively. The radiated waves from one body act on the other body, and the PTO reaction force is dependent on the bodies' relative motion.

In the context of linear water wave theory in the frequency-domain, the hydrostatic restoring force on Body *j*, may be modelled as a function of its weight and its buoyancy:

$$F_{HS\,j} = -W + B = -\rho g V_{0j} + \rho g\{V_{0j} - S_j Z_j\} = -\rho g S_j Z_j = -C_j Z_j \qquad \text{(C-1)}$$

where {j = 1,2}, $V_{0\,j}$ is the volume of the water displaced by Body *j*, ρ is the density of the seawater, g is the acceleration due to gravity, and S_j is the wetted cross-sectional area of Body *j*.

The radiation force from the waves generated by a body can be modeled by hydrodynamic damping and added mass terms. In the context of a two-body system,

$$F_{jk} = (\omega^2 A_{jk} - i\omega B_{jk}) Z_k \qquad \text{(C-2)}$$

where {j,k = 1,2}, and F_{jk} denotes the radiation force on Body *j* from the waves generated by Body *k*. In a two-body system, each body is acted upon by the radiation force from its own generated waves, and by the waves generated from the other body. The latter phenomenon represents the bodies' hydrodynamic coupling.

The PTO reaction force on Body *j* is given by the relative velocity of the two-body system:

$$F_{PTO\ j} = -i\omega\zeta_{PTO}(Z_j - Z_k) \tag{C-3}$$

where {j,k = 1,2}, and ζ_{PTO} is the load impedance of the PTO, as shown in Figure C-1.

The viscous effects on Body *j* may be modelled by the following relation**:**

$$F_{V\,j} = -i\omega D_j Z_j \tag{C-4}$$

where {j = 1,2}. The term $F_{V\,j}$ denotes the complex amplitude of viscous forces on Body *j*, where D_j is its own drag coefficient.

Newton's Second Law in the frequency-domain models the sum of all the aforementioned forces acting on Bodies 1 & 2, respectively:

$$\{-\omega^2(m_1 + A_{11}) + i\omega(B_{11}+D_1) + C_1\}Z_1 + \{-\omega^2 A_{12} + i\omega B_{12}\}Z_2 \tag{C-5}$$
$$+i\omega\zeta_{PTO}(Z_1 - Z_2) = F_{E,1}$$

$$\{-\omega^2(m_2 + A_{22}) + i\omega(B_{22}+D_2) + C_2\}Z_2 + \{-\omega^2 A_{21} + i\omega B_{21}\}Z_1 \tag{C-6}$$
$$-i\omega\zeta_{PTO}(Z_1 - Z_2) = F_{E,2}.$$

The cross terms in Eq. (C-5 & C-6) represent the hydrodynamic coupling between the two bodies. These terms quantify how the waves radiated by one body affect the motion of the other body, and it should therefore be noted that $A_{12} = A_{21}$ and $B_{12} = B_{21}$.

D. Preliminary motion analysis of the symphony device”

Simplified hydrodynamic analysis for Symphony:

INNOSEA
“Preliminary motion analysis of the symphony device”
Ref.: 163-P_BURD 163042015 WETFEET Revision No.2; PROJECT: WETFEET
Date: 01/06/2016

INNOSEA
Marine Energy Engineering

Technical note

Preliminary motion analysis of the Symphony device

Project: WETFEET
Work Package 2

This page was intentionally left blank

Cette page est intentionnellement vide

Technical note

Preliminary motion analysis of the symphony device

PROJECT: WETFEET

INNOSEA

Ref.: 163-P_BURD 163042015 WETFEET

Revision No.2

Date: 01/06/2016

Document N°: 163-P_BURD 163042015 WETFEET_WP2_TechnicalNote_Symphony

Versioning

Version	Author	Check	Reviewer	Validation
1	Adrien Combourieu	Valentin ARRAMOUNET	Adrien Combourieu	Maxime PHILIPPE
2 Addition of mooring chain properties and comment on results.	Adrien Combourieu		Adrien Combourieu	Maxime PHILIPPE

Preliminary documents

N°	Reference document	Transmitted (date):	Recipient

Table of contents

Table of figures

List of tables

1 Reference documents

1.1 Project documents

[1] *WETFEET Deliverable 2.2D - Report with designs and specifications of a Symphony able to integrate the control cocoon, electro-mechanic PTO, structural membrane and dielectric generators*, 29/01/2016.

1.2 Exchanged documents

[2] *SY_MOO-2015-1_Mooring motion analysis specifications_V1.2.docx*, received from TeamWork, 15/12/2015.
[3] *Inertia data symphony.docx*, received from TeamWork, 26/01/2015.

1.3 Rules and standard

[4] DNV-RP-C205 Environmental Conditions and Environmental Loads, April 2014.

1.4 Other documents

[5] Orcaflex User Guide.

Executive summary

The aim of this document is to present the preliminary motion analysis of the Symphony device performed in the frame of WP2 of WETFEET project. Specifications of the system, environmental conditions and calculation cases were specified by TeamWork in [2]. Main input data for the simulations is recalled in part 2. The methodology used for the calculation was described in [1] and was slightly modified in the present study. Therefore, the methodology actually used is highlighted in part 3. Finally, main results are presented in part 4 and all result data is provided in attachment of this document.

2 Test cases definition

2.1 Floater configurations

As specified by TeamWork in [2], in this study the floater is considered in its lower position and the internal articulation of the system is not modelled.

In this section, the two system configurations defined by TeamWork for the motion analysis carried out by INNOSEA are recalled.

Configuration	Floater position	Draft	COG position	Fairlead position
Operational	lower	39m	-28m	-35m
Survival	lower	50m	-39m	-46m

Table 1 Floater position for both configurations, as specified in [3]

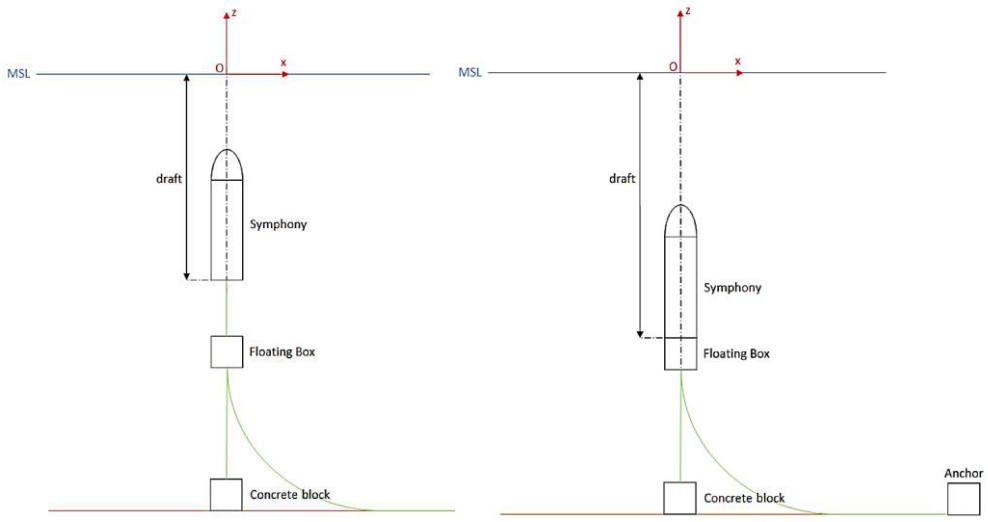

Figure 1 Operational configuration (left) and survival configuration (right)

Mass of the system is not precisely defined: 650 tons are mentioned in [1] and 600 tons in [2].

In this study, for both configurations, the mass of the floater is taken as 600 tons, and the inertia matrix at center of gravity is taken from [2] and presented in Table 2.

28250	0	0
0	28250	0
0	0	2607

Table 2 Inertia matrix of Symphony floater at its center of gravity [kg.m²]

2.2 Environmental conditions

Irregular wave conditions are considered and modelled with a JONSWAP spectrum. Two different sea states are considered for operational (DCC1) and survival conditions (DCC2). They were defined in [2] and are recalled in Table 3. The frequency spreading γ was not specified and chosen to a classical offshore value (3.3).

Configuration	DCC1	DCC2
Hs [m]	5	15
Tp [s]	12	18
γ	3.3	3.3
Wave direction	In line with 1 mooring line (see Figure 2)	In line with 1 mooring line (see Figure 2)
Duration [s]	3600	3600

Table 3 Wave conditions considered for DCC1 and DCC2

The wave propagation direction is in line with one mooring line as shown in Figure 2.

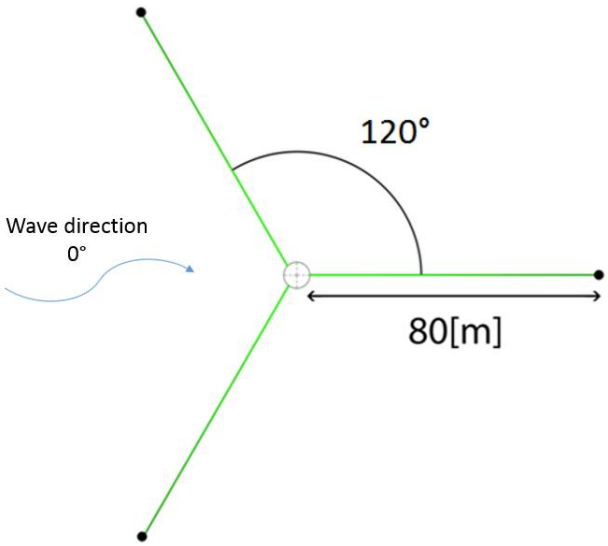

Figure 2 Wave direction considered (0°)

2.3 Mooring chain properties

Basic mooring chains properties were provided by TeamWork in [2] and are recalled in Table 4.

Line	Line type	Chain bar diameter D [m]	Stud type	Break load [kN]
vertical	chain	0.042	studlink	1400
spread	chain	0.034	studlink	937

Table 4 Basic mooring chains properties from [2]

From this data, additional chain properties is derived from Orcaflex chain catalogue [5]. In particular. Some important data that will impact the numerical model are highlighted in Table 5.

Line	Lineic mass [kg/m]	Young modulus E [kN/m²]	Section area A [m²]	Axial stiffness EA [kN]
vertical	39	6.40E+07	2.78E-03	1.78E+05
spread	25	6.40E+07	1.82E-03	1.17E+05

Table 5 Additional chain properties derived by Orcaflex

In particular, the axial stiffness is the constant slope of the line relating chain tension to chain strain. This slope is the equivalent EA value for the line, where E is Young's modulus and A is the cross section area of the chain. It equals the force required to double the length of any given piece of chain, assuming perfectly linear elastic behaviour. In practice, of course, lines would yield before such a tension was reached.

The Orcaflex catalogue [5] also gives the value for the Young's Modulus of the studlink chain, that has been deduced from stress-strain relationships in which the cross sectional area of two bars is taken to be the load bearing area $A = 2*\pi D^2/4$.

3 Modelling methodology

Symphony floater motions were computed using InWave, INNOSEA's in-house multibody offshore system modelling software. InWave mechanical solver is a nonlinear time domain solver. This section presents the methodology used for the preliminary motion analysis of the Symphony floater under wave loads.

3.1 Load modelling

3.1.1 Hydrostatic loads

Hydrostatic loads are calculated using an instantaneous hydrostatic pressure integration method. Hydrostatic force is calculated integrating the contribution of hydrostatic pressure over the hull surface. Instantaneous position of the hull is used for hydrostatic load calculation.

It can be noted that in the particular case of a fully submerged system, the hydrostatic global load on the floater is constant.

3.1.2 Hydrodynamic loads

Hydrodynamic loads on offshore structures are usually computed using Morison formulation, potential flow theory or a combination of both. It depends on which physical effect is dominating (drag, inertia, Froude-Krylov or diffraction).

Keulegan-Carpenter parameter is used to quantify which phenomenon is important, and therefore which hydrodynamic theory to use. Values of this parameter is shown in Table 6.

DCC	Kc
1	3.7
2	17

Table 6 Keulegan-Carpenter for DCC1 and DCC2

In this case, a mix of linear potential flow theory and Morison formulation is considered to compute the wave load. In practice, linear potential flow theory is used and the drag part of Morison formulation is added. Drag is accounted for based on the relative velocity between the Symphony floater and the fluid.

3.1.2.1 Linear wave loads

It is assumed that linear potential flow theory is applicable. This is a strong assumption for the Symphony system in large waves, which may have large motion amplitudes. Also, in extreme sea states, the size of Symphony floater becomes smaller in comparison with the wave. Diffraction/radiation might not be the dominating hydrodynamic contribution in such cases. Drag is added on top of potential flow theory for this reason.

The diffraction/radiation coefficients are obtained from InWave based on a surfacic mesh obtained from the floater geometry. A convergence study on mesh size was performed and the final mesh used contains 658 faces. It is shown in Figure 3.

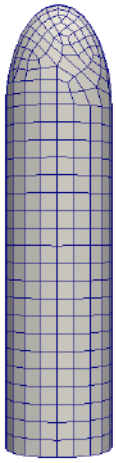

Figure 3 Mesh of the Symphony hull

3.1.2.2 Drag loads

Viscous drag is added using relative velocity Morison formulation. This formulation relies on the drag coefficient, which needs to be calibrated with experimental measurements.

Drag coefficients depend on the shape of the system, the surface roughness, the motion of the system and the wave conditions. These coefficients are not known in the frame of this study. They were therefore estimated based on [4] using an equivalent vertical cylinder of 6m diameter and smooth surface roughness. Retained drag coefficients are listed in Table 7.

	Cd
DCC1	0.31
DCC2	0.65

Table 7 Drag coefficients used for DCC1 and DCC2

Only radial drag is considered and axial drag is neglected. On this specific topic, more investigation will be needed at a further stage.

The equivalent cylinder is then discretized into 50 nodes along the height of the cylinder. Drag loads are assed locally at these nodes. Local drag loads are provided in the local frame described in Figure 4. In this frame, radial drag loads are expressed along X axis only. Figure 4 also shows the numbering of the local elements used.

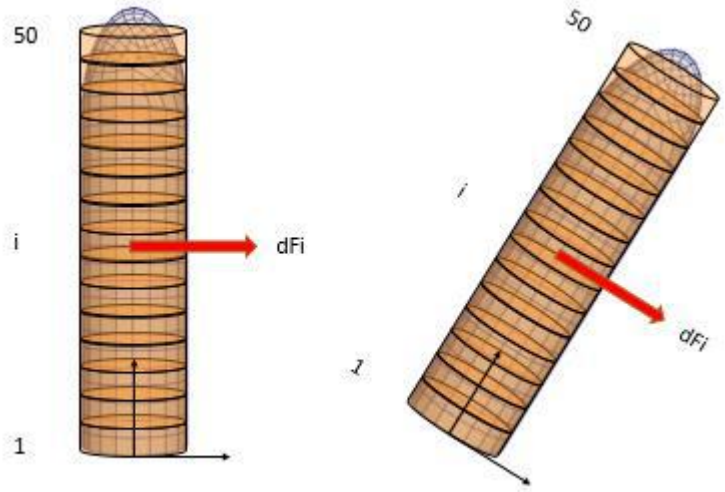

Figure 4 Illustration of Morison elements used for drag calculation

3.1.3 Mooring loads

As mentioned in [1], it is assumed that quasi-static mooring theory applies. This is a strong assumption considering the mooring system considered at this stage. As the dynamics of the lines is not modelled, dynamic effects such (e.g. resulting from snap loads) are not considered in the analysis. Those are likely to happen given the fact that vertical lines are taut.

The only external loads considered on the mooring lines are weight and buoyancy. Neglecting hydrodynamics on the mooring system is also a strong assumption in the case of the Symphony system. In particular, hydrodynamic loads on the floating box are not considered.

Quasi-static mooring model assumes that mooring lines are at static equilibrium at each time step. In particular, it means that the mooring force at fairlead will only depend on fairlead position.

A slight modification of the methodology for quasistatic mooring loads calculation has been introduced compared to what was presented in [1]. In this study, instead of using a quasistatic mooring model, mooring loads are precomputed for a set of predetermined fairlead positions with Orcaflex software. This choice have been made to be able to account for the presence of the floating box more accurately. Doing so, a database of mooring force at fairlead is built for different fairlead position, before the time domain simulations with InWave. During the simulations, InWave gets the mooring load at fairlead by reading the precomputed force value at the instantaneous fairlead position. Fo a given instantaneous position of the fairlead, the value of the force for the closest position in the database is taken. This modelling is still based on the quasistatic approach as the dynamics of the lines is not accounted for.

In Orcaflex, the five mooring lines and the floating box are represented (see Figure 5). The floater is slowly forced to move and covers the range of predetermined fairlead positions. Mooring force at fairlead is recorded at each position.

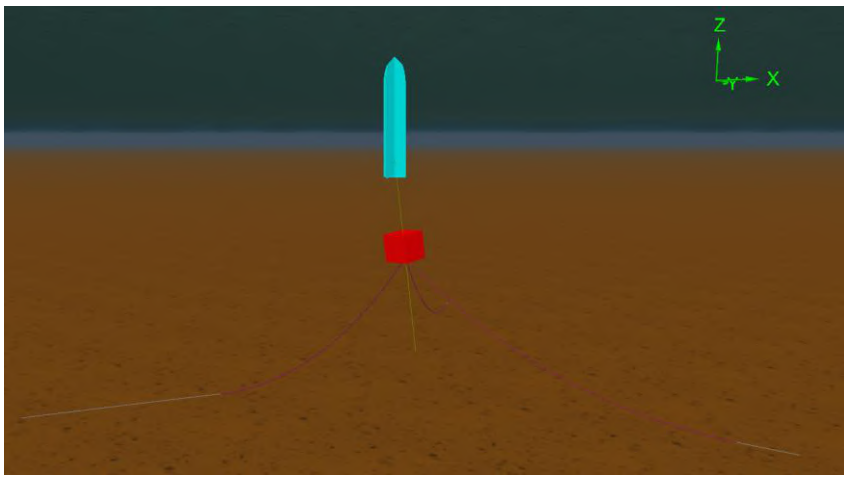

Figure 5 Visualization of the mooring model in Orcaflex

An example of the mooring force in function of surge offset (for a fixed value of heave and sway) is given in Figure 6 and Figure 7.

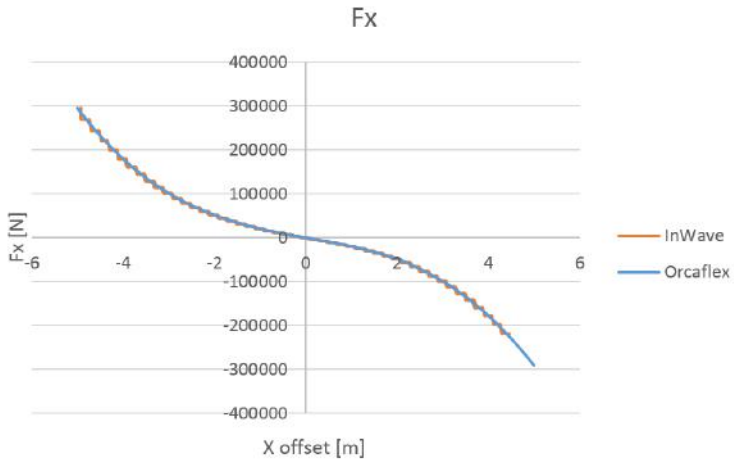

Figure 6 Quasistatic mooring force along X in function of fairlead X position (for fairlead at Z=-34.8m and Y=0m)

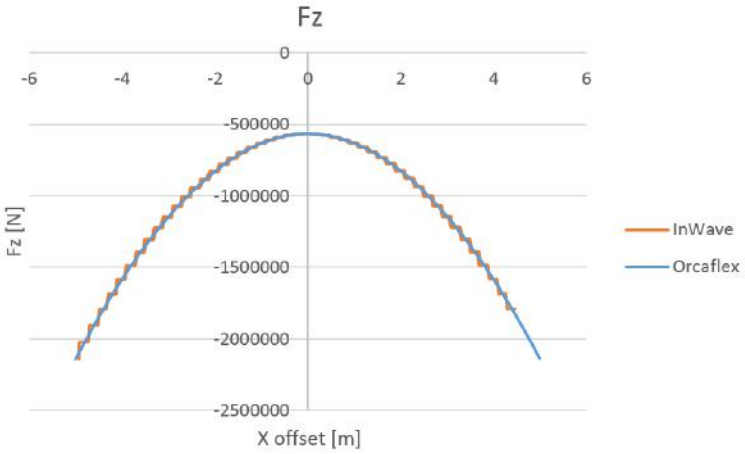

Figure 7 Quasistatic mooring force along Z in function of fairlead X position (for fairlead at Z=-34.8m and Y=0m)

These figures show several things:

- The mooring stiffness in surge is increasing with surge offset.
- When the fairlead shifts horizontally, the mooring pulls the floater down.
- The pretension in the mooring line is important leading to a large vertical force, which is increasing quickly with horizontal motion of the fairlead.

3.2 Surface pressure on hull: linear reconstruction

Surface pressure on the hull is reconstructed by post-processing the simulations.

Dynamic pressure is obtained from linear potential flow theory:

- Incident and diffracted pressure are calculated at the equilibrium position of the system. They do not depend on system motion.
- Radiation pressure is calculated at the equilibrium position of the system. It is dependent on system motion.

Hydrostatic pressure is taken at the instantaneous position of the system. It is therefore dependent on system position.

As the system is fully submerged at a significant immersion, it can be expected that hydrostatic pressure (which increases with immersion) will be larger than dynamic pressure (which is decreasing with immersion).

3.3 Limitations

Some assumptions and limitations of the modelling methodology exposed previously are summarized in Table 8, their impact shall be addressed in future studies.

	Theory	Hypothesis	Limitations for Symphony system
Ocean loads model	Linear Potential Flow	- Non-rotational flow. - Inviscid flow (viscous drag forces neglected). - Linear waves: wave amplitude small compared to wavelength. - Wave amplitude small compared to body dimensions. - Motion of the body are small relative to the body dimensions. - 2nd order wave effect are not taken into account in this study.	- Viscous drag might appear in practice due to the small dimensions of the floater compared to extreme waves. Morison hydrodynamic drag is applied to account for that (see below). - Low frequency wave load are usually important to consider for catenary moored floating systems. - High frequency wave load are usually important for taut mooring systems.
	Morison equations (drag)	- Body small compared to wavelength. - Cylindrical structures. - Only radial drag considered.	- Validity relies on the accuracy of drag coefficients provided. - Such coefficients should be determined experimentally. - Axial drag may appear on Symphony floater due to sharp edges at the bottom of the floater.
Mooring system model	Quasi-static mooring	- Lines in static equilibrium at each time step. - Hydrodynamic loads on lines neglected. - Lines assumed infinitely elastics. - Torsion stiffness neglected. - Internal friction neglected.	- Dynamic of the line is not captured (e.g. snap loads) which might lead to underestimation of maximum tension in the lines. - Hydrodynamics on the mooring system is neglected, in particular on the floating box. - Tension might get above maximum allowable tensions. Breaking of the lines is not simulated.

Table 8 Assumptions and limitations of the modelling methodology

4 Results

4.1 Preliminary results

4.1.1 Static equilibrium position

The system has an excess of buoyancy and is kept in position by the mooring system (see Table 9).

Weight [N]	-5.89E+06
Buoyancy [N]	6.40E+06
Excess of buoyancy [N]	5.12E+05

Table 9 Weight and buoyancy of the system

At equilibrium, the mooring system applies a vertical force that counteracts the excess of buoyancy of the system. The vertical mooring lines are in tension in static equilibrium. Note that tension in the line at equilibrium is not verified in this study. However, it would be interesting to check that this static tension is below maximum allowable tension.

The static equilibrium position found is Z=-27.87m for DCC1.

The static equilibrium position found is Z=-38.89m for DCC2.

4.1.2 Hydrodynamic database

The hydrodynamic database contains for both DCC:

- The wave excitation force amplitude and phase.
- The radiation damping.
- The added mass.

Figure 8 shows the wave excitation force in surge and heave for both operational immersions of DCC1 and DCC2. As expected, the wave excitation loads decrease when immersion of the system increases.

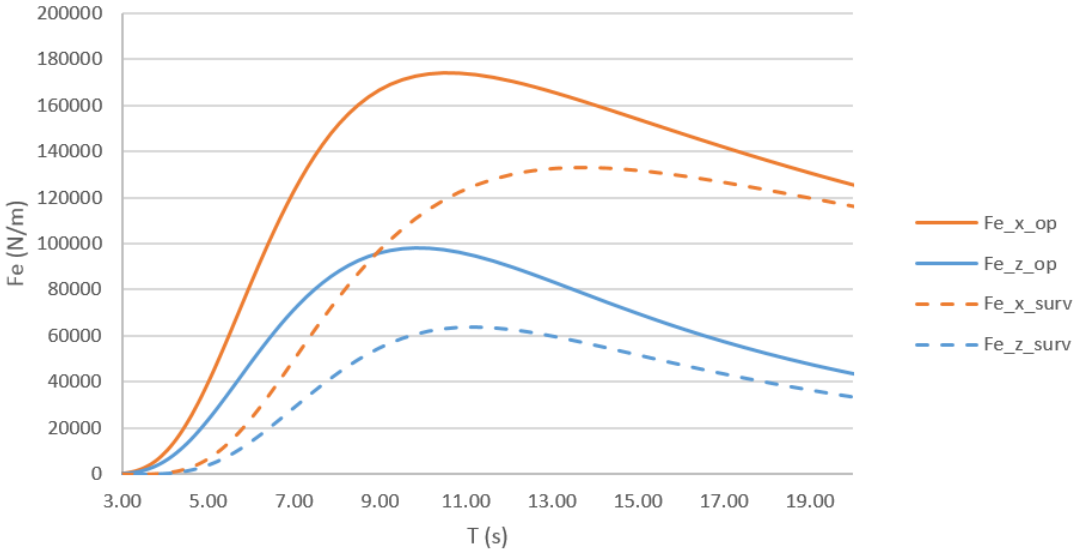

Figure 8 Wave excitation force RAO in surge and heave for DCC1 and DCC2

4.1.3 Decay tests

Decay tests are simple tests where the system is offset from its equilibrium position along one DOF and released. The oscillations back to equilibrium allow to measure the natural period of the system for the corresponding DOF. It gives also insight on the damping of the system.

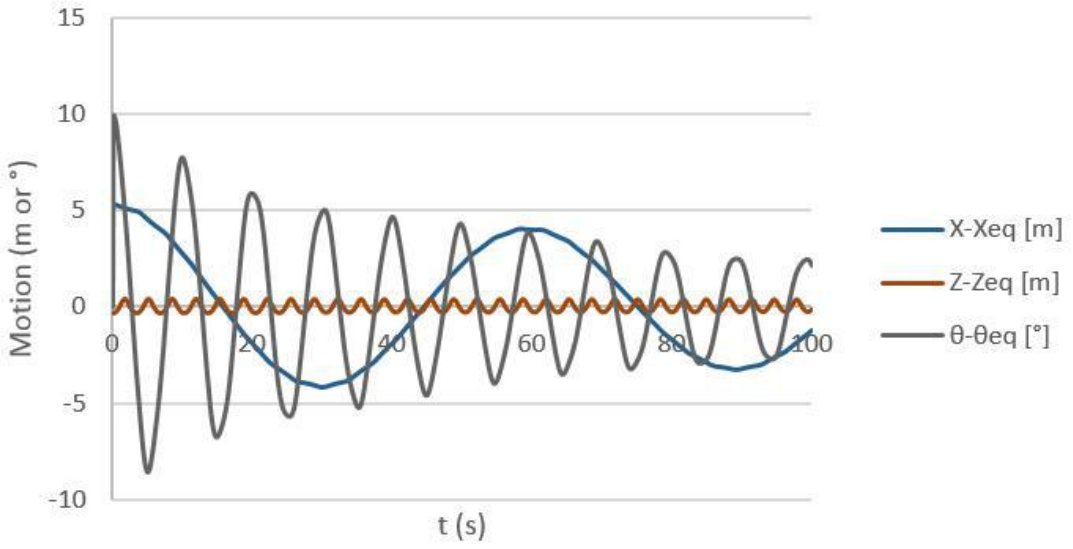

Figure 9 Decay tests for DCC1

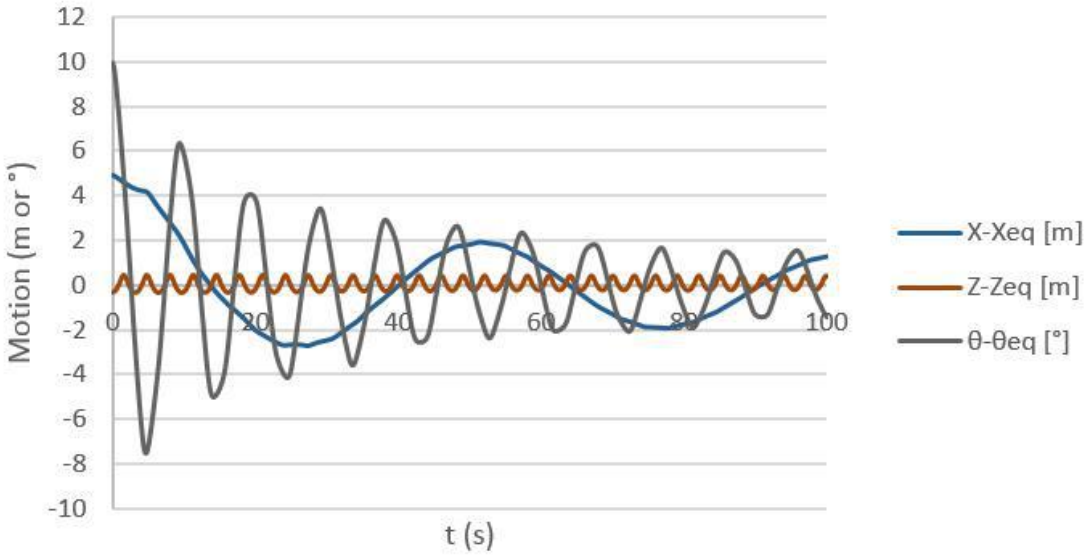

Figure 10 Decay tests for DCC2

Offset used for decay tests and natural periods obtained are highlighted in Table 10.

DOF	Offset [m or °]	Natural period [s] DCC1	Natural period [s] DCC2
Surge	5	59.8	53.0
Heave	-0.5	3.4	3.2
Pitch	10	10.4	10.1

Table 10 Natural periods of the system in both configurations

Natural periods are not much affected by change of immersion.

Surge natural period (>50s) is larger than wave periods. Low frequency second order wave loads might result in large low frequency surge motion. This is not accounted for in this preliminary study.

Pitch natural period (10s) is within typical wave periods. Large pitch motion might be observed under waves when the system is in the lower position considered in this study.

Heave natural period (approx. 3s) is below wave periods. High frequency second order wave loads might result in heave resonance. This is not accounted for in this preliminary study.

It can be noted on heave decay results that when pushed down of 0.5m the system is oscillating and able to go up higher than equilibrium position. This is due to the elasticity of the lines, which are supposed to be infinitely elastic. Linear behavior of vertical lines in extension can be observed on Figure 11.

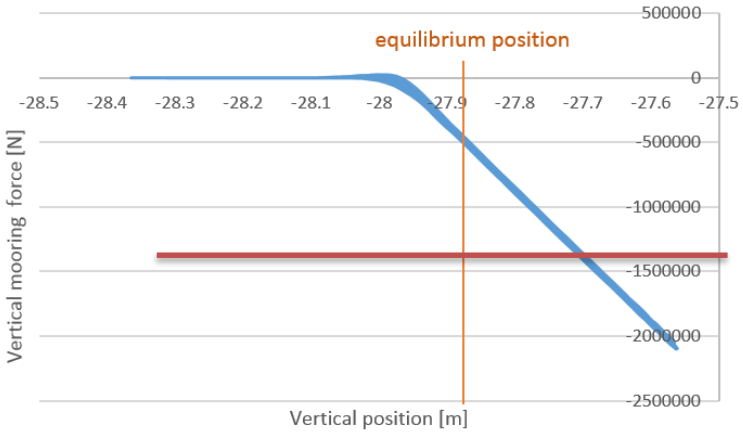

Figure 11 Vertical mooring force in function of vertical position during heave decay test for operational configuration

In red: break load of the vertical chains

Stiffness of the lines is directly linked to their axial stiffness *EA* and therefore to their section area. Increasing the section would increase the line stiffness. Also, it should again be recalled that that once in tension, lines are assumed infinitely elastic. Therefore the line tension can exceed the maximum allowable tension in the lines, which is not verified in this study. In this heave decay test, it can be seen that the total vertical mooring load applied on the floater is often above the vertical chains break load, which is likely to mean that vertical chains would actually not withstand.

4.2 Design configuration cases results

Three distinct simulations of 1300s are performed, using three different random seeds for wave elevation generation. On each simulation, the first 100s are discarded, to remove transient effects. Therefore in total, 3600s (1h) of simulations were performed for DCC1 and for DCC2, as required in [2].

All output data (motion, loads and pressure) time series are attached with this report, and formatted as explained in Appendix.

In this section, some results are provided along with statistics.

4.2.1 Motion

Figure 12 and Figure 13 show time series of wave elevation and respectively surge and heave motion for DCC2.

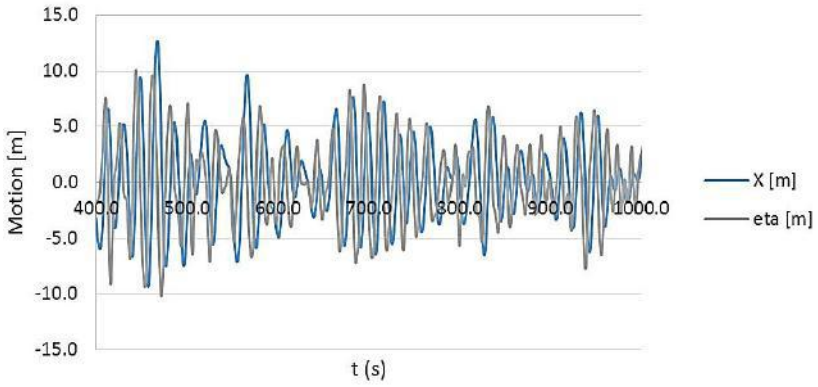

Figure 12 Wave elevation and surge motion for DCC2 (seed 1)

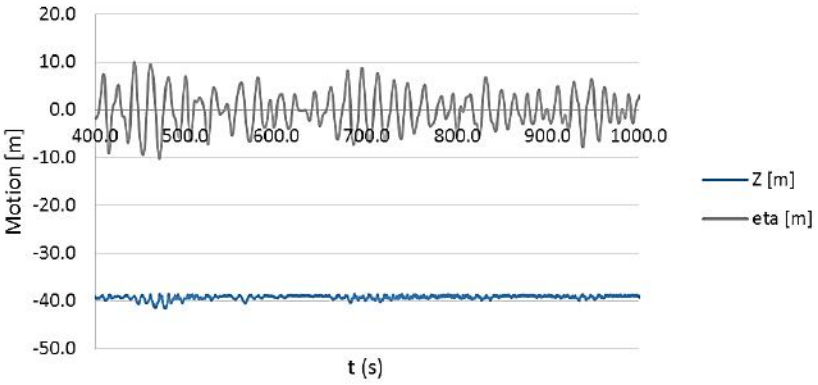

Figure 13 Wave elevation and heave motion for DCC2 (seed 1)

Motion statistics are presented for the different seeds of DCC1 and DCC2 respectively in Table 11 and Table 12.

	Seed 1				Seed 2				Seed 3			
	η [m]	X [m]	Z [m]	θ [°]	η [m]	X [m]	Z [m]	θ [°]	η [m]	X [m]	Z [m]	θ [°]
mean	0.0	0.0	-28.0	0.3	0.0	0.0	-28.0	0.3	0.0	0.0	-28.0	0.4
max	4.0	2.3	-27.7	20.3	3.7	1.9	-27.8	21.7	4.8	2.5	**-27.2**	23.2
min	-3.4	-2.2	-28.5	-18.0	-4.0	-1.9	-28.6	-17.6	-4.2	-2.0	**-30.5**	-19.8
std	1.3	0.7	0.1	7.7	1.3	0.7	0.1	7.8	1.3	0.7	0.3	7.8

Table 11 Motion statistics for 3 seeds of DCC1

	Seed 1				Seed 2				Seed 3			
	η [m]	X [m]	Z [m]	θ [°]	η [m]	X [m]	Z [m]	θ [°]	η [m]	X [m]	Z [m]	θ [°]
mean	0.0	0.2	-39.2	0.1	0.0	0.2	-39.3	0.1	0.0	0.2	-39.2	0.1
max	11.5	**12.7**	**-38.6**	**18.4**	11.2	11.2	-38.4	17.9	10.4	10.2	-38.5	17.7
min	-10.1	**-9.3**	-41.6	**-20.9**	-12.0	-9.0	**-42.9**	-19.6	-11.7	-8.4	-41.4	-16.2
std	3.8	3.8	0.4	6.3	3.9	3.8	0.5	6.4	3.5	3.4	0.4	6.0

Table 12 Motion statistics for 3 seeds of DCC2

It can be seen that for the large and long waves considered, the system is following the wave in surge, showing quite large motion. In heave, the system is constrained. It can hardly move up due to line tension. It can move down in large waves. This will cause the line to become slack, and induce large loads when the floater comes back to its position and the line becomes suddenly taut again (snap loads). This phenomenon is observed in the present study but not accurately modeled as it is a highly dynamic phenomenon. At a later stage of the system development, a more complete methodology should be elaborated for the motions and mooring load assessment.

Also, these results show that surge and heave motion are more important for DCC2 that for DCC1. Pitch motion are similar between both DCC.

4.2.2 Mooring force at fairlead

Figure 14 and Figure 15 show time series of mooring force in surge and heave for DCC2.

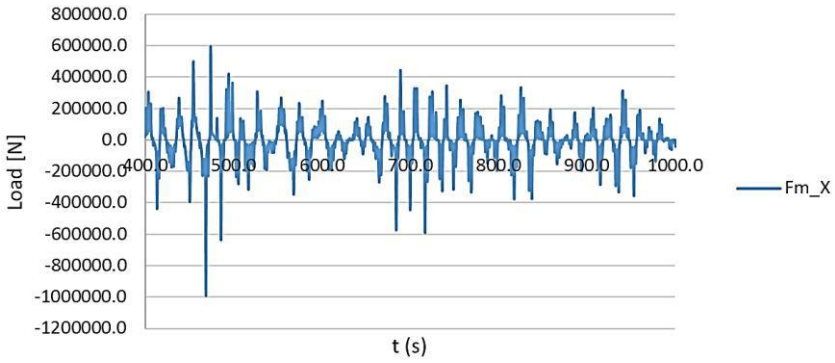

Figure 14 Mooring force in surge for DCC2 (seed 1)

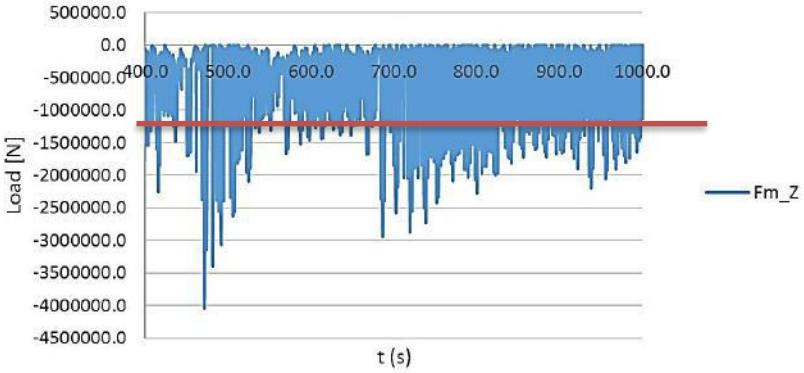

Figure 15 Mooring force in heave for DCC2 (seed 1)

In red: the vertical chain break load

Mooring load statistics are presented for the different seeds of DCC1 and DCC2 respectively in Table 13 and Table 14.

	Seed 1			Seed 2			Seed 3		
	Fm_X [N]	Fm_Z [N]	Fm_θ [N.m]	Fm_X [N]	Fm_Z [N]	Fm_θ [N.m]	Fm_X [N]	Fm_Z [N]	Fm_θ [N.m]
mean	-3.8E+02	-5.4E+05	3.6E+04	-4.6E+02	-5.4E+05	3.8E+04	-8.5E+02	-5.4E+05	4.3E+04
max	7.2E+04	-6.9E+03	2.1E+06	7.6E+04	-1.1E+04	2.0E+06	1.8E+05	-4.5E+03	7.6E+06
min	-8.9E+04	-1.3E+06	-1.7E+06	-8.7E+04	-1.2E+06	-1.5E+06	-2.6E+05	**-4.4E+06**	-6.2E+06
std	2.3E+04	2.1E+05	6.1E+05	2.3E+04	1.9E+05	6.1E+05	2.5E+04	3.3E+05	6.9E+05

Table 13 Mooring force statistics for 3 seeds of DCC1

	Seed 1			Seed 2			Seed 3		
	Fm_X [N]	Fm_Z [N]	Fm_θ [N.m]	Fm_X [N]	Fm_Z [N]	Fm_θ [N.m]	Fm_X [N]	Fm_Z [N]	Fm_θ [N.m]
mean	-3.5E+03	-5.2E+05	2.6E+04	-3.8E+03	-5.3E+05	2.9E+04	-3.2E+03	-5.3E+05	2.6E+04
max	6.0E+05	-7.1E+02	7.6E+06	**1.4E+06**	-7.1E+02	1.7E+07	6.1E+05	-7.1E+02	5.8E+06
min	-9.8E+05	-4.0E+06	-4.6E+06	-8.7E+05	**-6.7E+06**	-1.7E+07	-6.7E+05	-3.4E+06	-4.9E+06
std	1.0E+05	5.4E+05	7.5E+05	1.1E+05	5.9E+05	8.9E+05	9.7E+04	6.1E+05	7.6E+05

Table 14 Mooring force statistics for 3 seeds of DCC2

These results show that maximum instantaneous mooring force in heave can be much larger (1 order of magnitude) than the mean vertical force at equilibrium.

In heave, the system is constrained. It can hardly move up due to line tension. It can move down in large waves. This will cause the line to become slack, and induce large loads when the floater comes back to its position and the line becomes suddenly taut again (snap loads). Such loads are visible in Figure 15 but it should be recalled that this is a dynamic phenomenon. Such phenomenon is not modelled accurately with quasistatic mooring theory. At a later stage of the system development, a more complete methodology should be elaborated for the motions and mooring load assessment.

Also, these results show that mooring tensions are more important for DCC2 than for DCC1. It has to be kept in mind that mooring tensions are not accurately estimated (e.g. due to the fact that dynamic of the lines and hydrodynamic second order effects are not accounted for).

Finally, it should again be recalled that once in tension, lines are assumed infinitely elastic. Therefore the line tension can exceed the maximum allowable tension in the lines, which is not verified in this study. For DCC2, it can be seen that the total vertical mooring load applied on the floater is often above the vertical chains break load, which is likely to mean that vertical chains would actually not withstand in that case.

4.2.3 Wave force on hull

4.2.3.1 Global force

Figure 16 shows a time series of linear wave force in surge for DCC1.

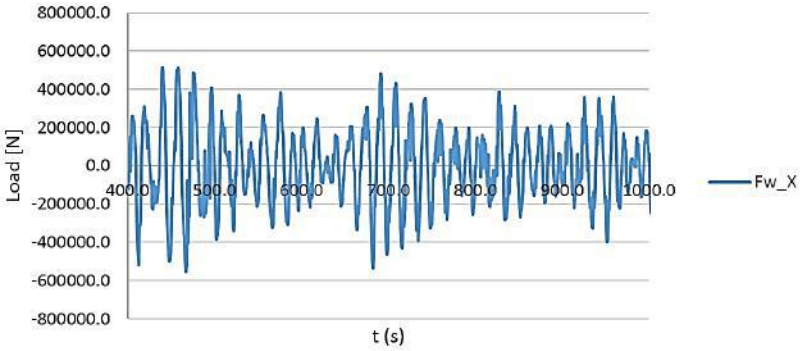

Figure 16 Total linear wave force in surge (diffraction and radiation) for DCC2 (seed 1)

Linear wave force statistics are presented for all the different seeds for DCC1 and DCC2 in Table 15 and Table 16.

	Seed 1			Seed 2			Seed 3		
	Fw_X [N]	Fw_Z [N]	Fw_θ [N.m]	Fw_X [N]	Fw_Z [N]	Fw_θ [N.m]	Fw_X [N]	Fw_Z [N]	Fw_θ [N.m]
mean	5.4E+02	-8.9E+00	-8.1E+02	-1.6E+02	7.7E+00	-6.3E+01	3.0E+02	-2.0E+01	1.3E+03
max	2.8E+05	3.1E+05	2.4E+06	3.0E+05	3.5E+05	2.5E+06	3.2E+05	6.6E+05	7.6E+06
min	-3.0E+05	-3.6E+05	-2.9E+06	-3.2E+05	-3.6E+05	-2.6E+06	-4.2E+05	-4.1E+05	-8.3E+06
std	9.4E+04	1.1E+05	1.0E+06	9.4E+04	1.1E+05	1.0E+06	9.6E+04	1.2E+05	1.1E+06

Table 15 Total linear wave force statistics for 3 seeds of DCC1

	Seed 1	Seed 2	Seed 3

	Fw_X [N]	Fw_Z [N]	Fw_θ [N.m]	Fw_X [N]	Fw_Z [N]	Fw_θ [N.m]	Fw_X [N]	Fw_Z [N]	Fw_θ [N.m]
mean	1.1E+03	-8.0E+01	3.8E+02	-1.1E+03	1.8E+02	-9.4E+02	-3.5E+02	4.4E+02	2.6E+03
max	5.7E+05	7.4E+05	5.2E+06	**6.5E+05**	**1.2E+06**	**1.5E+07**	6.5E+05	7.8E+05	5.7E+06
min	-5.5E+05	-4.7E+05	-7.1E+06	**-7.9E+05**	**-5.7E+05**	**-1.5E+07**	-6.1E+05	-5.2E+05	-5.1E+06
std	2.0E+05	1.8E+05	8.8E+05	2.0E+05	1.8E+05	1.0E+06	1.8E+05	1.7E+05	9.2E+05

Table 16 Total linear wave force statistics for 3 seeds of DCC2

These results show that wave loads in surge and heave are greater for DCC2 than for DCC1, despite the fact that immersion is greater in DCC2. Regarding the wave loads, the increasing wave conditions from DCC1 to DCC2 is not fully compensated by the immersion.

4.2.3.2 Pressure on hull

Dynamic pressure on hull are calculated based on potential flow theory. An example of dynamic pressure is depicted in Figure 17.

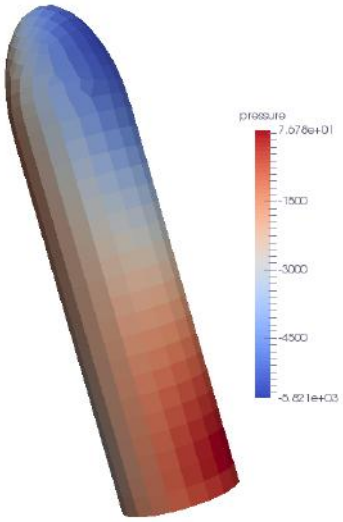

Figure 17 Visualization of dynamic pressure on hull for DCC1 (seed 1)

Extremum hydrostatic and hydrodynamic pressures are displayed for all seeds of both DCC in Table 17.

Extremum pressure (Pa)			**DCC 1**	**DCC 2**
Seed 1	dynamic	max	2.5E+04	8.0E+04
		min	-2.4E+04	-8.4E+04
	static	max	4.0E+05	5.3E+05
		min	1.4E+05	2.5E+05
Seed 2	dynamic	max	2.4E+04	7.7E+04
		min	-2.5E+04	-1.0E+05
	static	max	4.0E+05	5.4E+05
		min	1.4E+05	2.5E+05
Seed 3	dynamic	max	3.1E+04	**8.2E+04**

		min	-3.2E+04	**-1.1E+05**
	static	max	4.2E+05	**5.6E+05**
		min	1.3E+05	**2.5E+05**

Table 17 Extremum static and dynamic pressure for DCC1 and DCC2

It can be noticed that for DCC1, static pressure is one order of magnitude greater than dynamic pressure. For DCC2, static pressure is larger but of the same order of magnitude than static pressure.

4.2.4 Drag force on hull

Figure 18 shows a time series of drag force in surge for DCC2.

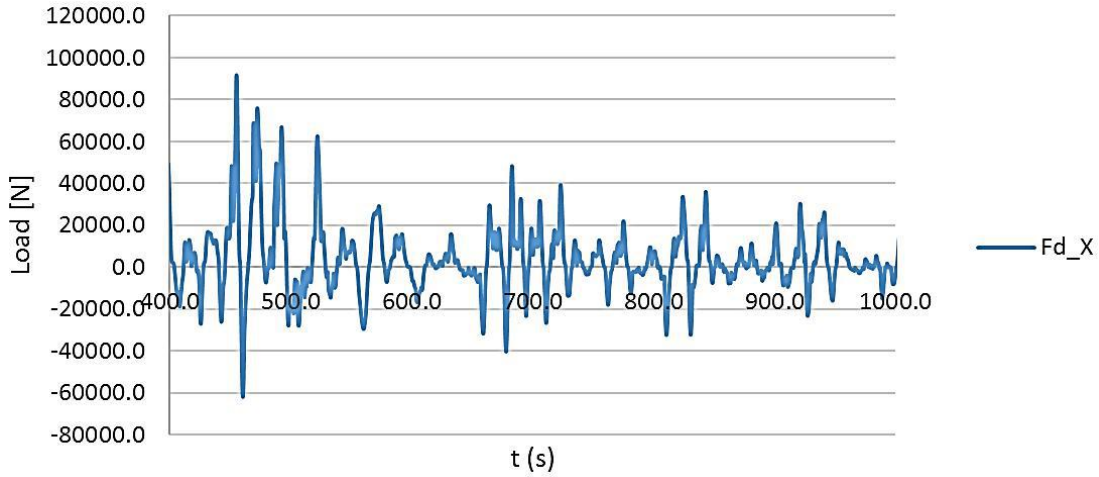

Figure 18 Total drag force in surge for DCC2 (seed 1)

Drag force statistics are presented for all seeds of each DCC in Table 18 and Table 19.

	Seed 1			Seed 2			Seed 3		
	Fd_X [N]	Fd_Z [N]	Fd_θ [N.m]	Fd_X [N]	Fd_Z [N]	Fd_θ [N.m]	Fd_X [N]	Fd_Z [N]	Fd_θ [N.m]
mean	5.1E+01	-2.3E+00	-4.8E+02	4.9E+01	-7.6E-01	-4.1E+02	1.5E+02	-9.3E+00	-4.8E+02
max	1.6E+04	2.5E+03	5.6E+05	2.0E+04	3.5E+03	5.9E+05	3.3E+04	4.1E+03	7.7E+05
min	-1.1E+04	-3.2E+03	-4.7E+05	-1.4E+04	-4.5E+03	-4.8E+05	-1.9E+04	-9.0E+03	-9.4E+05
std	2.7E+03	3.5E+02	1.2E+05	2.9E+03	4.0E+02	1.3E+05	3.5E+03	5.9E+02	1.4E+05

Table 18 Total drag force statistics for 3 seeds of DCC1

	Seed 1			Seed 2			Seed 3		
	Fd_X [N]	Fd_Z [N]	Fd_θ [N.m]	Fd_X [N]	Fd_Z [N]	Fd_θ [N.m]	Fd_X [N]	Fd_Z [N]	Fd_θ [N.m]
mean	4.1E+03	-1.6E+02	1.6E+04	4.0E+03	-1.2E+02	1.4E+04	3.4E+03	-1.2E+02	1.4E+04
max	**9.5E+04**	**2.2E+04**	1.1E+06	9.3E+04	1.5E+04	**1.4E+06**	7.8E+04	1.1E+04	1.1E+06
min	**-6.2E+04**	**-1.4E+04**	-1.0E+06	-5.7E+04	-1.2E+04	**-4.4E+06**	-4.5E+04	-1.3E+04	-9.7E+05
std	1.6E+04	2.1E+03	1.8E+05	1.5E+04	1.8E+03	2.2E+05	1.3E+04	1.6E+03	1.7E+05

Table 19 Total drag force statistics for 3 seeds of DCC2

These results show that drag force is at least one order of magnitude smaller than other loads.

4.2.5 Load summary

To get a quick insight on loads order of magnitude, static loads and extremum (absolute) dynamic loads for each DCC are summarized in Table 20 and Table 21.

Load	Fx [N]	Fz [N]	Fθ [N.m]
Weight	0	-5.89E+06	0
Buoyancy	0	6.40E+06	0
Mooring load	2.6E+05	4.4E+06	6.2E+06
Linear wave load	4.2E+05	6.6E+05	8.3E+06
Drag load	3.3E+04	9.0E+03	9.4E+05

Table 20 Extreme load summary for DCC1 (absolute values)

Load	Fx [N]	Fz [N]	Fθ [N.m]
Weight	0	-5.89E+06	0
Buoyancy	0	6.40E+06	0
Mooring load	9.8E+05	6.7E+06	1.7E+07
Linear wave load	7.9E+05	1.2E+06	1.5E+07
Drag load	9.5E+04	2.2E+04	4.4E+06

Table 21 Extreme load summary for DCC2 (absolute values)

5 Appendix

Along with this report, one result folder is provided for each DCC.

The data contained in such folder is described in the following.

5.1 DCCX.xls

5.1.1 Global_loads_DCCX

This tab contains global data time series and their statistics:

- Time vector *t*
- Wave elevation at point (0, 0) *eta*
- Surge motion *X*
- Heave motion *Z*
- Pitch motion θ
- Mooring loads at fairlead *Fm*
- Linear wave load *Fw*
- Drag loads *Fd*

This data is provided from t=100s to t=1300s, without transient time, and for each seed.

5.1.2 Local_drag_loads_seedX

These tabs contain the local drag load in each Morison element. Each column corresponds to an element, numbered as shown in Figure 19. The local frame depicted in Figure 19 is used to express local loads, so that only the components along X in this frame is non-zero.

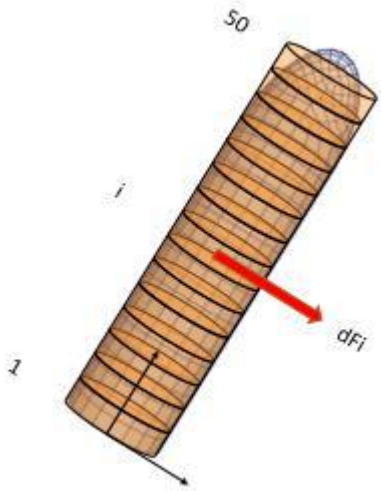

Figure 19 Morison elements and local frame used for local drag loads

5.2 Hull_pressure

This folder contains a subfolder for each seed considered for the DCC at stake. The files provided in these folders are described in the following.

5.2.1 Phydro_static_i.txt

There is a file for each time step, *i* being the time step number.

This file contains a header on the first line.

On the second line, the time value is provided.

Then, there is 1 line for each face in the mesh:

- The first 3 columns are the instantaneous position of the face center.
- The last column is the value of the hydrostatic pressure on the face. This value takes into account the instantaneous face position.

5.2.2 Phydro_dynamic_i.txt

There is a file for each time step, *i* being the time step number.

This file contain a header on the first line.

On the second line, the time value is provided.

Then, there is 1 line for each face in the mesh:

- The first 3 columns are the instantaneous position of the face center.
- The last column is the value of the hydrodynamic pressure on the face.

E. Background document for the TDM of Symphony:

Niels Leitjens:
“Optimal Buffer Design for the Symphony Wave Power System”

Faculty of Engineering Technology, Engineering Fluid Dynamics; EFD-247;
Graduation Report 21 October 2016

(Includes description of Symphony TDM and bibliography)

EFD-247

UNIVERSITY OF TWENTE.

Faculty of Engineering Technology,
Engineering Fluid Dynamics

Optimal Buffer Design for the Symphony Wave Power System

Niels Leijtens

Graduation Report
21 October 2016

Graduation committee:
Prof. dr. ir. C.H. Venner (chairman)
Dr. ir. R. Hagmeijer (mentor)
Ing. F. Gardner (Teamwork Technology)
Dr. ir. P.C. Roos (external member)

Contents

Preface

The use of water as a source of energy is known for centuries. The Romans have already been using systems with watermills, and these fundamentals can still be seen today in hydroelectric stations. These systems were always placed along rivers and coasts. Since the last few decades researchers are aiming to develop an energy system that can extract energy in the open sea. The Symphony is one of such systems that is under current development.

This project aims to further crystallise the buffer system of the Symphony and was performed as graduation thesis at the engineering department at the University of Twente.

During the design process I was supported by the team of Teamwork Technology and the Faculty Fluid Dynamics at the University of Twente. I would like to thank Fred Gardner and Bauke Vriesema from Teamwork Technology for mentoring me during my research. It was great to be a part of Teamwork Technology where I have never been the 'student' but always part of the team. Secondly, I would like to thank Rob Hagmeijer for our weekly meetings and supportive mentoring. This benefited not only my work, but also the joy in doing this research. At last I would like to thank all the persons that read my report and provided comments. Especially I would like to thank Laura de Ruijter who scarified a lot of evenings for reading and checking the present report.

Summary

Renewable energy is a hot topic these days. Wind farms are popping up all over the world and more and more solar panels start to produce electricity. Then why are we not producing energy from the sea? It is proven that the ocean could be a powerful energy source. However, the main problem is the diversity in wave heights. Most wave heights are low and easy to use for energy extraction, while a few times the ocean is rough and sea waves can become three times as high.

The Symphony is a wave power system which generates power from sea waves by an oscillating floater. This motion pumps water through a turbine. The main goal of the present research is to design the most optimal buffer system which mechanically limits the motion of the Symphony. An optimal buffer design is defined by optimal energy extraction in calm weather conditions, while the motion is controlled during rough weather conditions.

The natural frequency of the system is designed such that it is close to the most probable wave frequency. By oscillating around the equilibrium position at the natural frequency, an optimal power output is generated. It is shown that by adding a negative spring to a positive spring the combined spring has a low natural frequency and high bandwidth which is ideal for a wave power system such as the Symphony.

The optimal spring design for the Symphony has a larger spring force on both ends for control of high sea waves, while in the mid-section a tuned linear spring is present, which is ideal for low sea waves that have the highest probability. In between an S-curve is made to make the geometry more smooth. Together with the control system it restricts the floater motion within an allowable range for 95% of the weather conditions and optimally extracts energy in calm sea states.

Chapter 1

Research field

1.1 Project motivation

Over the last centuries researchers and engineers have been working on wave energy to find a solution to collect energy from the ocean. The global power potential represented by waves has been estimated around 2 TW [1]. Fig.1.1 gives an overview of the annual mean power density $[KW/m]$ per location in the world. In the high density areas wave power devices could be beneficial for energy production. For a constant supply of renewable energy it is important to have a wide variety of sources. When one renewable energy source is low due to bad weather another source could step in to keep the total production constant. Wave energy can play a role in this.

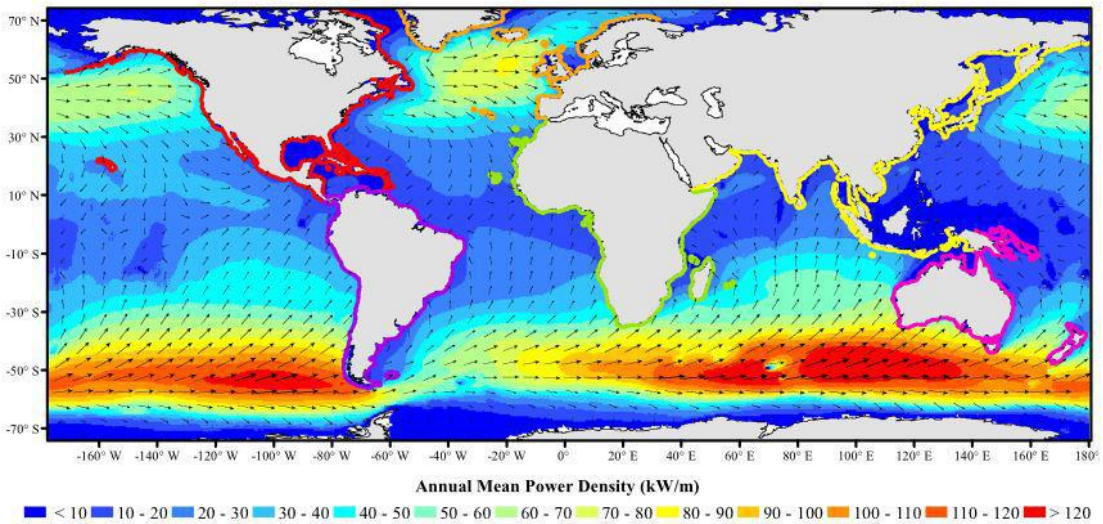

Figure 1.1: Annual mean power density on world scale [1]

One of the big advantages of wave energy over wind energy is that there is more kinetic energy available in water than in wind, as the density of water is much higher. However, wave energy is very underdeveloped compared to other renewable energy techniques. While wind farms and sun panels are popping up all over the world, wave energy is still in its development stage due to its complexity. First of all, the extremely rough oceanic weather conditions make the survivability of the system hard to engineer. Moreover, compared to wind energy for which the one important

factor is wind speed, wave energy has two important factors: the height and period of the waves. Teamwork Technology, the design team of the Symphony, has worked on several wave energy technologies. One of these was the Archimedes Wave Swing which was developed from 1993 to 2008 and was tested in Portugal in 2004 [2]. NUON was a partner in this project, which later on resulted in the company AWS Ocean Energy ltd. From the experiences of the Archimedes Wave Swing, Teamwork Technology has developed a new concept in wave energy, the Symphony [3]. The concept looks similar to the first AWS but is upgraded in several ways to reduce cost and to increase efficiency. One of the sponsors is the WETFEET project. This project is funded under EUs Horizon 2020 Framework program and addresses the major constraints that have been delaying wave energy's progress by identifying and developing components, systems and processes to improve the sector as a whole. This subsidy provides the possibility to develop the Symphony into a scale model will be used for testing in 2017 [3].
The present report aims to set a next step towards a world with more renewable energy from different devices.

1.2 Principles of wave power systems

(a) pitching body *(b)* surging body *(c)* floating heaving body *(d)* overtopping

(e) submerged heaving body *(f)* oscilating water column *(g)* rubber body

Figure 1.2: different devices in wave power (moves by clicking in the digital version) [3]

1.2.1 Categories of wave power systems

Wave energy technology has a wide variety of different ways of energy absorption [2]. This results in different locations and conditions of use per design. The current wave energy technologies can be split into three groups: Oscillating Body Devices (OBD), the overtopping technology and Oscillating Water Column (OWC).
The first category is the oscillating body devices (OBD). The oscillation of a body can be realised in several ways: pitching, surging, heaving and expanding one of the bodies, see Fig.1.2(a,b,c,d,g).

The similarity between these OBDs is that they all produce energy by reacting against the sea bottom or another oscillating body. These offshore devices lay in more energy dense waters but have additional problems with mooring, accessibility and long electrical cables [2]. This makes them more complex but in the end hopefully more beneficial. The Symphony is a good example of an expanding body with heaving motion, and is the subject of research in this project.
The second category concerns the overtopping converters, see Fig.1.2(d). These converters capture water that is close to the wave crest and bring it into a reservoir by overspilling it. In this way it is stored at a height above the average sea level. The potential energy is converted by hydraulic turbines. These devices are strongly non-linear and cannot be addressed by a linear water wave theory. An example is the Seawave Slot-Cone Generator (SSG) that is currently been tested for several years in Norway [2].
The third category concerns the Oscillating Water Column system (OWC) (Fig.1.2(f)), which is open at the bottom and compresses the trapped air between the water surface and the system. The oscillating motion makes the air flow through a turbine which drives the electrical generator [2]. A good example of this concept is the Spar-Buoy. The principle is straightforward: the axisymmetric device, which consists of a submerged vertical tail tube that is open at both ends and fixed to a floater, moves essentially in a heave motion [4]. This concept is possibly one of the simplest concepts for a floating energy converter.

1.3 Description of the Symphony

1.3.1 Classification

The Symphony is an OBD and can be classified in the subcategory of point absorbers. ”A point absorbing buoy is defined as a body with a characteristic length that is much smaller than the typical wave length of ocean waves.” [5]. When the frequency of the wave is close to the natural frequency of the oscillating system, the amplitude of the system will rise above the amplitude of the wave. This is necessary for the optimal absorption. Returning energy back into the sea could be needed during small fractions of each oscillation cycle to support the oscillating mode, options for this are reactive control or latching phase control [2].

1.3.2 Working principle

The Symphony is an OBD with an expanding volume from which the top floater can move up and down from its base, the cocoon. Its working principle can be best explained step by step a graphical interpretation can be seen in Fig.1.3.

1. The Symphony starts in its equilibrium position and a wave is coming in.
2. Water starts getting lifted on top of the Symphony. Due to the raising hydrostatic pressure the floater experiences a downward force and the floater starts moving downwards.
3. Due to the downward movement, water inside is forced by the membranes through the turbine into the gas chamber, where pressure is build up.
4. The sea water is at the top of the wave. The gas pressure inside creates a force on the membranes that is higher than the hydrostatic force of the wave, which starts to decelerate the floater.
5. After deceleration, the movement switches from direction and the pressure in the gas chamber starts to decrease.
6. The upward movement will start to decelerate when the second wave starts to come on top of the floater. The hydrostatic pressure and force starts to raise again.
7. After deceleration, the movement switches from direction and the floater will start to move down to its equilibrium position. Which brings the situation back to step 1.

This cycle results in a sinusoid movement of the floater over time. Where water is pushed through the turbine two times per cycle. The rotating turbine shaft is connected to a generator which transforms the torque in electricity.

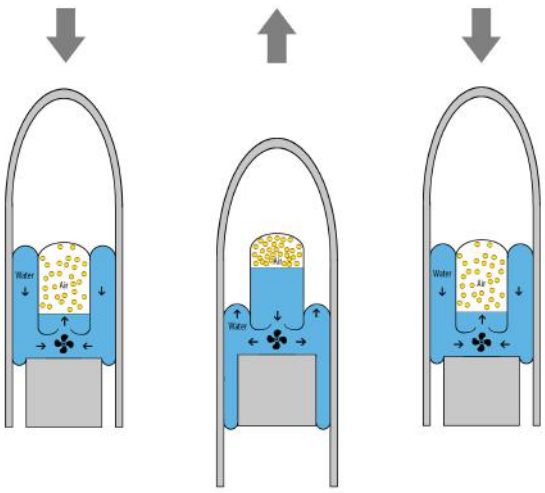

Figure 1.3: Schematic work principle of the Symphony [3]

1.3.3 Components

The device can be split into five components: the rubber membrane, spring chamber, power take off, control components and the floater.

Rubber membrane and Spring chamber

The rubber membrane is one of the key innovations of the Symphony. It seals the water inside the Symphony from the other components and sea water, because it is connected to the floater and cocoon. By moving the floater, the membranes are rolling over the outside wall of the cocoon. This movement presses water through the turbine. Since the membrane is fully around the cocoon it also centre the cocoon in the floater and gives the floater a full heave motion.

Power Take Off

The Power Take Off (PTO) consists of a turbine, generator and smaller electronic components. The turbine is designed and patented by Teamwork Technology, see Fig.1.4(b). The turbine is designed so that one rotor transports the flow while the other rotor creates a barrier. The input and output is brought in line with the flow direction and the channels toward the turbine are designed so that a large part of the kinetic energy is converted into pressure. It can be seen that both rotors never touch, which creates a small leak but limits the friction. The generator, gearbox and other smaller electrical components are currently under construction.

Control Components

The main function of the control components (Fig.1.5) regulate the pressure and volume of water and air within the Symphony. These conditions can change due to leaks or small failures in the system. The control components are not made for motion regulation of the floater but only maintain the pressures. At last a winch is attached to the Symphony so the total device can be brought to the bottom of the sea when rough weather conditions are expected. These components are being designed at this very moment and a final design will be finished not long after this report.

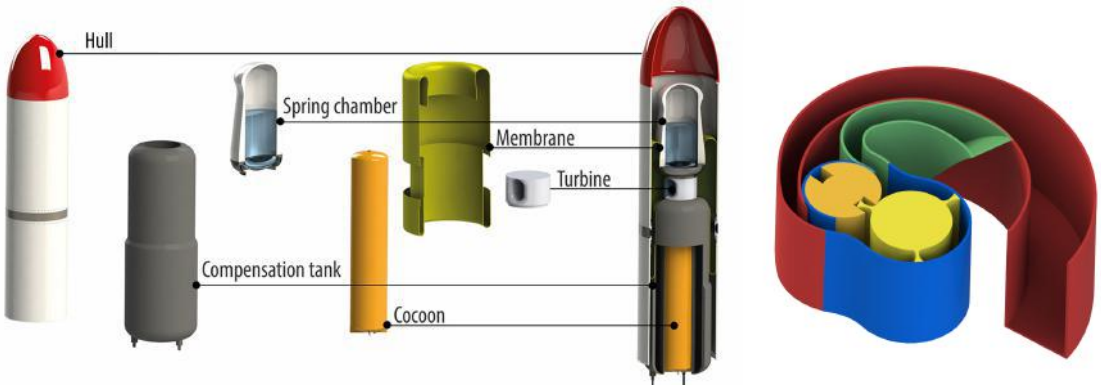

(a) Exploded view of the Symphony *(b)* Turbine design

Figure 1.4: Components of the Symphony [3]

Floater

The floater of the Symphony is the oscillating component of the design. It has two functions: varying the volume by rolling up the membrane, and to create an air chamber in the top of the Symphony that provides a big part of its buoyancy force. The top of the floater is streamlined so the floater experiences less resistance when it moves through the water.

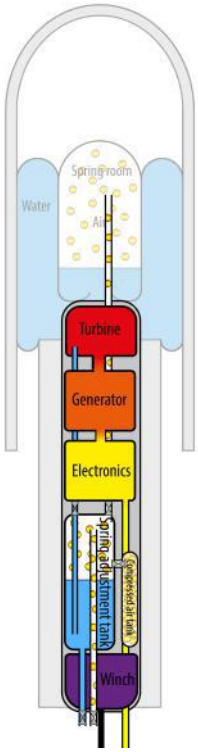

(a) Symphony cocoon

(b) Symphony working principle with power output (moves by clicking in digital version) [3]

Figure 1.5: Cocoon configuration [3]

1.4 Research objective and scope

Research objective

For this report the following research objective has been specified with the corresponding sub-questions.

- Design the most optimal inner geometry of buffer system that controls the Symphony wave power system during rough weather conditions and subtracts most optimal power during normal weather conditions.
  - Which boundary conditions, size, force and weather conditions, are significant?
  - What defines the most optimal buffer design?

Scope

This research is focusing on the 1.5m Symphony wave power prototype. In particular on the Floater, PTO, gas spring and membranes. The current configuration of all the components will be kept intact. This prototype will be placed near the coast of Leixoes, Portugal. The buffer design will be optimised for this location, but the overall conclusions should keep intact for other designs and locations.

Chapter 2

Principle of concept

2.1 Introduction

To prove the principle of concept, a comparison is made between the Symphony and another point absorber: the Corpower. Both wave power projects are in the same state of development and make use of the same basic principle, a positive spring combined with a negative spring. To gain a maximum amount of energy from the sea waves, a system is required with a low natural frequency, to keep it in resonance with the incident wave. By adding a negative spring stiffness to a positive spring stiffness this low natural frequency can be realised [2]. This section investigates the most important parameters for a maximum power output based on a linear model, giving a simplification of the actual situation.

2.2 Basic principles simplified model

2.2.1 Linear second order system

Starting with a basic analysis, it is useful to simplify the point absorber to a second order system. A graphical interpretation can be seen in Fig.2.1. The basic equation for a second order system is:

$$m\frac{d^2x(t)}{dt^2} + c\frac{dx(t)}{dt} + kx(t) = F_0\ \cos(\omega t), \tag{2.1}$$

which consists of a mass m $[kg]$, displacement of the mass $x(t)$ $[m]$, a damper with the damping constant c $[kg/s]$ and a spring with a spring constant k $[kg/s^2]$. An oscillating force $F = F_0\ \cos(\omega t)$ is applied on the system, where F_0 is the amplitude of the force $[N]$, ω the frequency of the force $[1/s]$ and t time $[s]$. The non-dimensional form of this equation is:

$$\tilde{\omega}^2\frac{d^2\chi(\tau)}{d\tau^2} + \tilde{\omega}\beta\frac{d\chi(\tau)}{d\tau} + \chi(\tau) = \digamma\ \cos(\tau), \tag{2.2}$$

$$\tau = \omega\ t, \qquad \chi = \frac{x}{x_0}, \qquad \tilde{\omega} = \frac{\omega}{\sqrt{\frac{k}{m}}},$$

$$\beta = \frac{c}{m\ \sqrt{\frac{k}{m}}}, \qquad \digamma = \frac{F_0}{k\ x_0}.$$

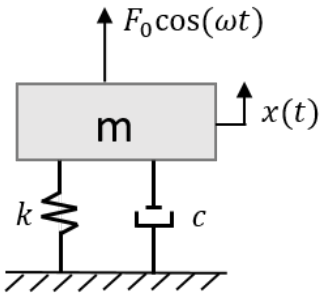

Figure 2.1: Basic second order system

The homogeneous solution is: $\chi_h = A_1 e^{\lambda_1} + A_2 e^{\lambda_2}$ and lead to: $\lambda_{1,2} = -\frac{\beta}{2\tilde{\omega}} \pm \frac{1}{2\tilde{\omega}}\sqrt{\beta^2 - 4}$ with A_1 and A_2 left undefined. Since the system is forced we use for the particular solution: $\chi_p = B\sin(\tau + \phi)$ where ϕ is the phase shift of the system [6]. Substitution χ_p into Eq. 2.2 yields:

$$(1 - \tilde{\omega}^2)\ B\ \sin(\tau + \phi) + \tilde{\omega}\ \beta\ B\ \cos(\tau + \phi) - F\ \cos(\tau + \phi) = 0. \tag{2.3}$$

By using $\cos(x - y) = \cos(x)\cos(y) + \sin(x)\sin(y)$ where $x = \tau + \phi$ and $y = \phi$ one obtains:

$$\Big(\tilde{\omega}\ \beta\ B - F\cos(\phi)\Big)\cos(\tau + \phi) + \Big(B(1 - \tilde{\omega}^2) - F\sin(\phi)\Big)\sin(\tau + \phi) = 0. \tag{2.4}$$

This equation has to hold for all values of τ, so:

$$F\cos(\phi) = B\ \beta\ \tilde{\omega} \qquad \text{and} \qquad F\sin(\phi) = B(1 - \tilde{\omega}^2), \tag{2.5}$$

which is rewritten in:

$$\boxed{B = \frac{F\cos(\phi)}{\beta\tilde{\omega}}} \qquad \text{and} \qquad \boxed{\tan(\phi) = \frac{1 - \tilde{\omega}^2}{\beta\tilde{\omega}}}. \tag{2.6}$$

The effect of the parameters can be investigated more closely by starting with the spring stiffness of both systems. This further examined in paragraph 2.4 and 2.5.

2.2.2 Negative spring

Suppose we have a spring that is stretched over a distance $x\ [m]$ and produces a reaction force $F(x)\ [N]$, with $F(0) = 0$. Then the spring stiffness is defined as:

$$k \equiv -\frac{dF(x)}{dx}. \tag{2.7}$$

If $k > 0$ then $\frac{dF(x)}{dx} < 0$ which means that the stretch and force have opposite signs. The spring will force the mass to its equilibrium position $x = 0$ which indicates a stable equilibrium point. If $k < 0$ the stretch and force have equal signs which indicates an instable situation and the system will be forced away from its equilibrium point, also known as a negative spring(Fig.2.2).
An example of a negative spring force is the hydrostatic force on a submerged balloon with a mass. Lets take its equilibrium point a certain length under the water surface. Here the buoyancy force of the balloon is equal to the gravity force of the mass. When the balloon moves slightly upwards

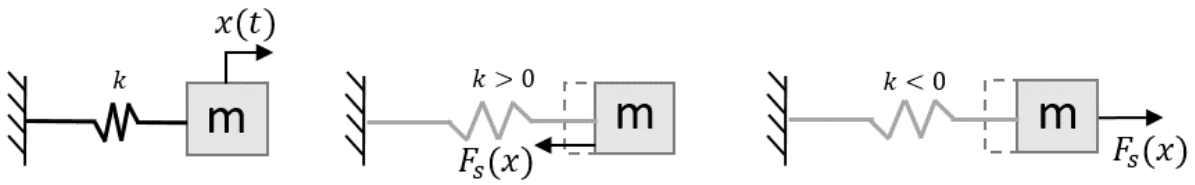

(a) Equilibrium position *(b)* Positive spring *(c)* Negative spring

Figure 2.2: Spring force by extraction of the spring

the balloon will expand by less surrounding pressure and the buoyancy force will increase. This causes the balloon to move even more upwards until the surface is reached. When the balloon is moved slightly down the surrounding pressure will suppress the balloon and the buoyancy force will decrease which causes the balloon to move even more down.

2.3 Optimisation of energy absorption

How long energy persists in a system is described by the Q-factor [7]. The higher the Q-factor, the more energy is extracted from the natural frequency motion, but at the same time less energy is extracted from motions with frequencies close to the natural frequency motion. This is also known as a low bandwidth. The Q-factor is defined as [7]:

$$Q \equiv \frac{\omega_n}{\Delta\omega}, \tag{2.8}$$

where $\Delta\omega$ is the frequency interval in which 50% of the maximum power is extracted $[1/s]$ and ω_n is the natural frequency $[1/s]$. For the Symphony and CorPower it is important to consider the benefits of a large interval $\Delta\omega_n$ versus extracting maximum energy at the natural frequency. Since the maximum energy extraction is limited by the boundaries of the system, the Q-factor should slightly be above these boundaries. In this case the maximum energy possible is extracted and the frequency domain is as large as possible. To estimate $\Delta\omega$ it is important to estimate the extracted power by the system. The average power is computed as:

$$P_{ave} = \frac{1}{t_P}\int_0^{t_P} P(t)dt = \frac{1}{t_P}\int_0^{t_P} F(t)v(t)dt, \tag{2.9}$$

where P_{ave} is the average power over time $[W]$, t_p is the total time $[s]$ and t is time $[s]$. By substituting this in Eq.2.1 with the known values for B, Eq.2.6, the following dimensionless equation is found:

$$\tilde{P}_{ave} = \frac{1}{\tau_P}\int_0^{\tau_P} F\ \cos(\tau)\ B\tilde{\omega}\ \cos(\tau+\phi)\ d\tau. \tag{2.10}$$

By using: $\cos(x+y) = \cos\ x\ \cos\ y - \sin\ x\ \sin\ y$ one obtains:

$$\tilde{P}_{ave} = \frac{F B\tilde{\omega}}{\tau_P}\left[\cos(\phi)\int_0^{\tau_P}\cos^2(\tau)\ d\tau - \sin(\phi)\int_0^{\tau_P}\cos(\tau)\sin(\tau)\ d\tau\right]. \tag{2.11}$$

It is evident that for a big τ_P, $\frac{1}{\tau_P}\int_0^{\tau_P}\sin(\tau)\cos(\tau)\,d\tau = 0$ and $\frac{1}{\tau_P}\int_0^{\tau_P}\cos^2(\tau)\,d\tau = \frac{1}{2}$. This leads to:

$$\tilde{P}_{ave} = \frac{F B\tilde{\omega}\,\cos(\phi)}{2}, \tag{2.12}$$

By applying: $\cos^2(\phi) = \frac{1}{1+\tan^2(\phi)}$ and substituting this in Eq.2.12 with the results from Eq.2.6 leads to:

$$\tilde{P}_{ave} = \frac{F B\tilde{\omega}}{2}\cos(\phi) = \frac{F^2}{2\beta}\cos^2(\phi) = \frac{F^2\,\tilde{\omega}^2\,\beta}{2\beta^2\tilde{\omega}^2 + 2(1-\tilde{\omega}^2)^2}. \tag{2.13}$$

A graphical interpretation of $\tilde{P}_{ave}$ (Fig.2.3) shows that at $\tilde{P}_{ave}(1) = max(\tilde{P})$ the power extraction is at its maximum. The bandwidth of the system $\Delta\omega$ is reflected in the length between both stars, when $Q = 1$. The bandwidth is the area where $P_{ave}(\omega) \geq 1/2P_{ave}(\omega_n)$. The boundary of the

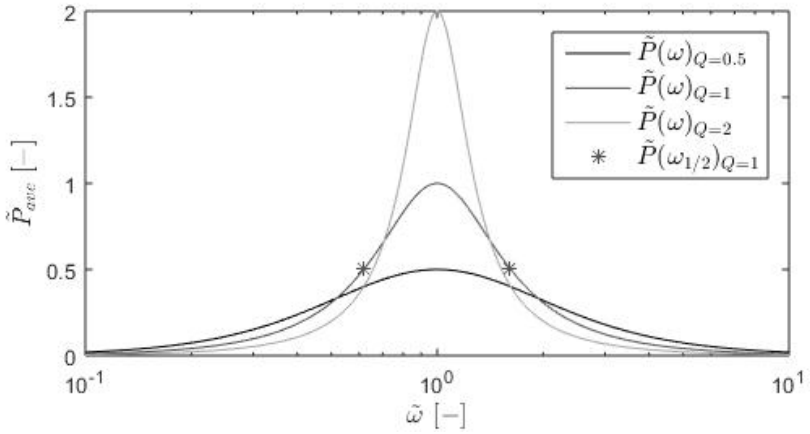

Figure 2.3: Power distribution with respect to the dimensionless frequency with both half power points as stars

bandwidth can be found by combining Eq. 2.13 with $\tilde{P}_{ave}(\omega_{1/2}) = 1/2\tilde{P}_{ave}(1)$:

$$\frac{F^2\tilde{\omega}_{1/2}^2\beta}{2\tilde{\omega}_{1/2}^2\beta^2 + 2(1-\tilde{\omega}_{1/2}^2)^2} = \frac{1}{2}\frac{F^2\,\beta}{2\beta^2}. \tag{2.14}$$

This can be simplified to:

$$\tilde{\omega}_{1/2}^4 - (\beta^2+2)\tilde{\omega}_{1/2}^2 + 1 = 0. \tag{2.15}$$

Solving this equation leads to four solutions:

$$\left.\begin{aligned}\tilde{\omega}_{1/2} &= \frac{1}{2}\sqrt{\beta^2+4} - \frac{1}{2}\beta\\ \tilde{\omega}_{1/2} &= \frac{1}{2}\sqrt{\beta^2+4} + \frac{1}{2}\beta\end{aligned}\right\} > 0, \qquad \left.\begin{aligned}\tilde{\omega}_{1/2} &= -\frac{1}{2}\sqrt{\beta^2+4} - \frac{1}{2}\beta\\ \tilde{\omega}_{1/2} &= -\frac{1}{2}\sqrt{\beta^2+4} + \frac{1}{2}\beta\end{aligned}\right\} < 0.$$

Since $\sqrt{\beta^2+4} > \beta$, it can be concluded that $\tilde{\omega}_{1/2} > 0$ for both left equations. On the other side can be seen that $\tilde{\omega}_{1/2} < 0$ for both right equations. Since a negative frequency is not possible, both right solutions are unsuitable for this topic. The possible solutions:

$$\tilde{\omega}_{1/2} = \frac{1}{2}\sqrt{\beta^2+4} \pm \frac{1}{2}\beta. \tag{2.16}$$

The domain between both solutions is the length of the bandwidth $\Delta\tilde{\omega} = \beta = \frac{c}{m\omega_n}$. Returning to the definition of the Q-factor from Eq. 2.8:

$$Q = \frac{\omega_n}{\Delta\omega} = \frac{\omega_n m}{c} = \frac{\sqrt{km}}{c} = \beta^{-1}. \tag{2.17}$$

It can be concluded the Q-factor is only a function of the damping factor c, spring constant k and total mass m. When a low natural frequency is needed two options are available: increasing the mass or lowering the spring stiffness. The side effect of increasing the mass is a lower bandwidth. This could be compensated by the damping factor c, however the report of A. Kooiman [8] has shown that this should be equal to two times the external losses of the system, for a point absorber. Since this factor is already given also this is no option. The last option is lowering the spring constant k then the bandwidth stays constant and for this reason a negative spring is a good option point absorbers to extract optimal energy from the sea.
In the next section, a comparison is made between the use of a negative spring by the Symphony and by the CorPower Wave Spring.

2.4 Simplified model of the Symphony

Spring forces

The report "Adjustments of the gas spring in the Symphony Wave Power Device" by A. Kooiman [8] shows that the model of the Symphony can be made up by two major forces: F_{hs} the hydrostatic force on top of the floater and F_{gas} the force created by the compression of the gas. Both forces can be seen in Fig. 2.4.

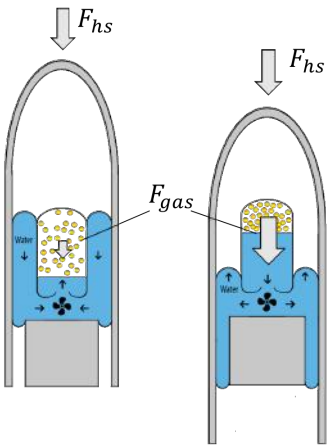

Figure 2.4: VLC symphony

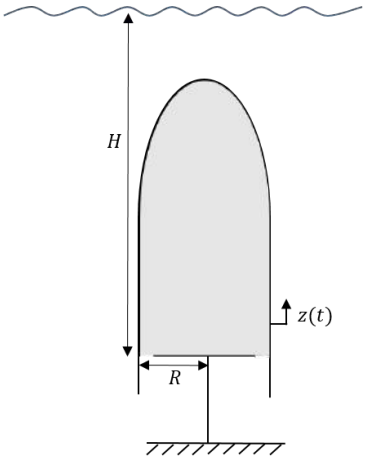

Figure 2.5: Symphony simplified to 2D

With for $F_{gas}(\zeta) = \zeta^{-\gamma}$ and $F_{hs}(\zeta) = \pi_1(\zeta - 1) - 1$, the dimensionless equation yields:

$$\tilde{F}_{sym}(\zeta) = F_{gas}(\zeta) + F_{hs}(\zeta) = \zeta^{-\gamma} + \pi_1(\zeta - 1) - 1, \tag{2.18}$$

where $\tilde{F}_{sym} = \frac{F}{AP_0}$, $\zeta = \frac{z}{z_0}$ and $\pi_1 = \frac{z_0}{H - z_0}$. The area of the piston is represented by $A\ [m^2]$, P_0 is the equilibrium pressure $[Pa]$, z the moved distance of the piston $[m]$, z_0 the equilibrium position

of the piston $[m]$ and H the height of the water which is above the piston when no extension takes place $[m]$. The simplified situation can be seen in Fig.2.5. A graphical interpretation of Eq.2.18 can be seen in Fig.2.6.

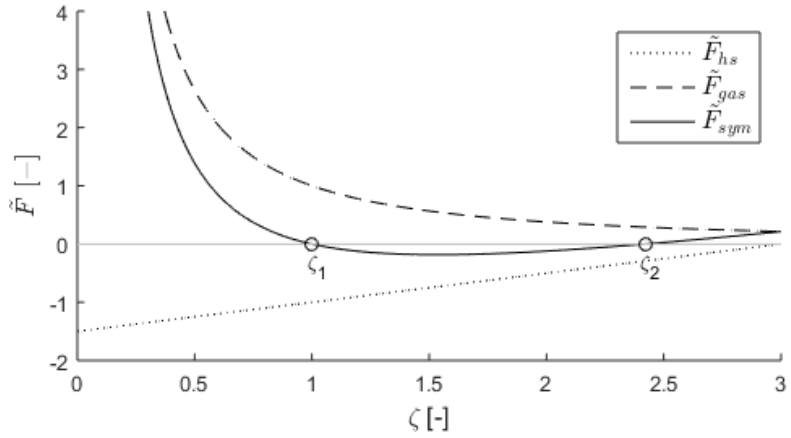

Figure 2.6: Symphony's spring force with $\pi_1 = 0.5$ and $\gamma = 1.4$ see Eq.

This figure shows that $\frac{F_{hs}(\zeta)}{d\zeta} > 0$, which follows the definition of a negative spring. In this situation the equilibrium position of F_{hs} with $\pi_1 = \frac{1}{2}$, is at $\zeta = 3$, being the position of the water surface. Also can be seen that $F_{sym}(\zeta_1) = F_{sym}(\zeta_2) = 0$ which marks both equilibrium positions. From the direction of the force can be concluded that ζ_1 is a stable equilibrium position with a net positive spring, while ζ_2 is an unstable equilibrium point with a net negative spring.

Added mass

When moving an object under water, not only the weight of this object is needed, but also the so called "added mass". The added mass is a virtual mass that is added to a system due to an acceleration or deceleration of a body through a fluid. This is due to the fact that liquid has a higher density, which results in the need for more power to move an object, through a liquid than through air. The equation of a mass for a submerged cylinder is:

$$m = \rho_{sym} 2H\pi R^2 + m_{added}, \tag{2.19}$$

with the added mass as a constant m_{added} $[kg]$ depending on the outer surface of the system. The non-dimensional form of this equation is:

$$\tilde{m} = \frac{m}{\rho_w \pi R^2 H} = 2\frac{\rho_{sym}}{\rho_w} + \tilde{m}_{added} \tag{2.20}$$

Natural Frequency

For small perturbations around the stable equilibrium position the local natural frequency can be calculated from the dynamic equation: $\omega_n^2 = \frac{k}{m}$. The stiffness of the system k in equilibrium point ζ_1 is found by looking at small perturbations, $\zeta - \zeta_1 << 1$, around this position:

$$F_{sym}(\zeta) \approx \cancel{F_{sym}}(\zeta_1) + \frac{dF_{sym}}{d\zeta}(\zeta_1)(\zeta - \zeta_1) + \mathcal{O}\big((\zeta - \zeta_1)^2\big) \tag{2.21}$$

Since $F_{sym}(\zeta_1) = 0$ the definition for the stiffness is obtained:

$$\tilde{k}_1 \equiv -\frac{d\tilde{F}_{sym}(\zeta_1)}{d\zeta} = \gamma\zeta_1^{-1-\gamma} - \pi_1. \tag{2.22}$$

From this natural frequency can be found:

$$\tilde{\omega}_n^2 = \frac{\tilde{k}_1}{\tilde{m}} = \frac{\gamma\zeta_1^{-1-\gamma} - \pi_1}{2\frac{\rho_{sym}}{\rho_w} + \tilde{m}_{added}}. \tag{2.23}$$

It can be concluded that the natural frequency is reduced by using the negative spring of the hydrostatic force π_1. When one calculates the natural frequency for ζ_2 it can be found that it is imaginary. This was expected since this point is unstable and it will not oscillate around this position but instead drift away from the equilibrium exponentially.

2.5 Simplified model of the CorPower

Both the Symphony and CorPower make use of a combined negative and positive spring. In the CorPower, the buoyancy force is the positive spring force while the mechanical springs are working as a negative spring, both in vertical direction. These mechanical springs are installed in precompressed condition and shown in Fig.2.7 [7].

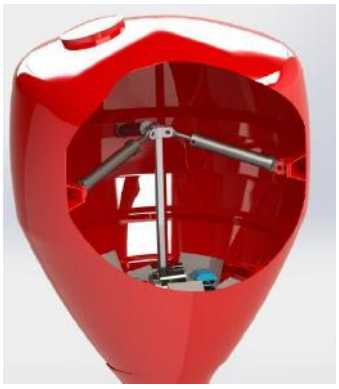

Figure 2.7: CorPower [9]

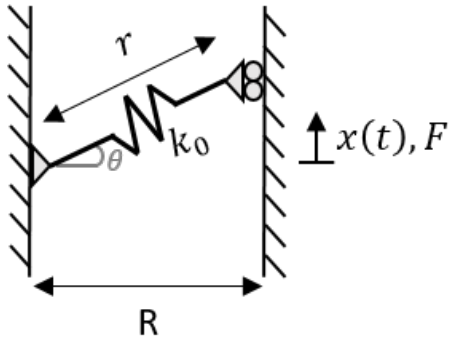

Figure 2.8: CorPower simplified to 2D

Spring forces

Since all three springs contribute equally to the total vertical spring force and so they can be modelled as one, see Fig.2.8. Since the spring is rotating the spring stiffness can be rewritten in a horizontal and vertical component. Due to symmetry all horizontal components cancel out. The diagonal spring force is:

$$F(r) = -k_0(r - r_0), \tag{2.24}$$

From this equation the vertical spring force is:

$$F_s(x) = F(r)\,\frac{x}{r} = -k_0(r - r_0)\,\frac{x}{r} = -k_0 x(1 - \frac{r_0}{r}). \tag{2.25}$$

where,

$$r = \sqrt{R^2 + x^2} \qquad \text{and} \qquad r_0 = \sqrt{R^2 + x_0^2},$$

with r is the diagonal $[m]$ and R is the horizontal distance between the middle point and the wall $[m]$. The stiffness of the system in vertical direction can be obtained as:

$$k_s(x) = -\frac{dF_s(x)}{dx} = -k_0\left(1 - \frac{\sqrt{R^2 + x_0^2}}{\sqrt{R^2 + x^2}}\right), \tag{2.26}$$

with the spring stiffness k_0 $[N/m]$ of the mechanical spring and x_0 is the vertical distance to the spring its equilibrium position $[m]$. A graphical interpretation of the non-dimensional stiffness k_s/k_0 and $F_s[N]$ is shown in Fig.2.9.

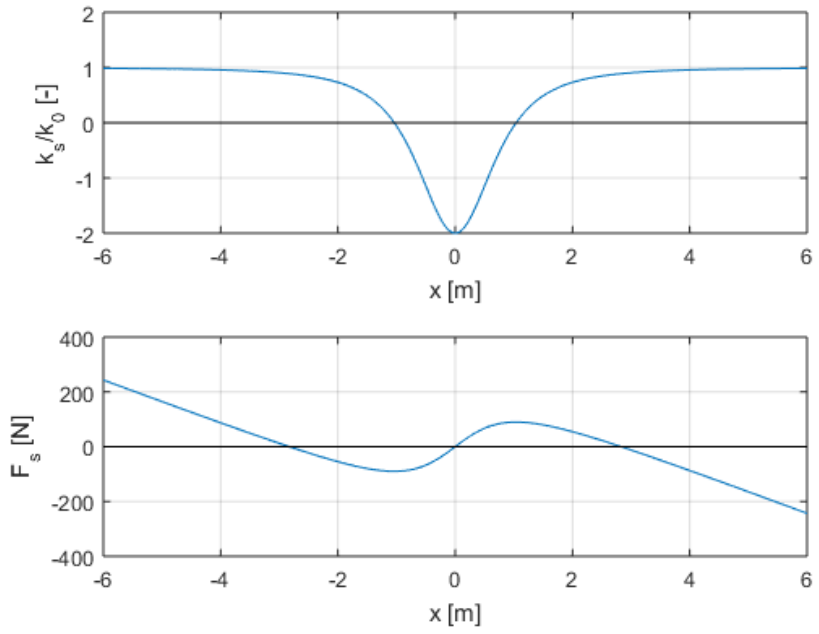

Figure 2.9: $k_s(x)$ and $F_s(x)$ are plotted with $k_0 = 2N/m$, $R = 1m$ and $r_0 = 3m$

It can be seen that for $|x| >> 1$, $k_s = k_0$. In this case spring stiffness acts as the original spring. However, for $-1 < x < 1$ the sign of k changes which indicates a negative spring. As mentioned before, the spring force is added to the buoyancy of the buoy which is known as [10]:

$$F_b = \rho_w g h A - \rho_{cor} 2HA = g\pi R^2(\rho_w H - \rho_w x - \rho_{cor} 2H), \tag{2.27}$$

where ρ_w is the density of the water $[kg/m^3]$, g the gravitation constant $[m/s^2]$, h under water height of the CorPower $[m]$, A area of the piston $[m^2]$, ρ_{cor} the average density of the Corpower

$[kg/m^3]$ and $2H$ the height of the piston $[m]$. The water level is at $x = 0$. The total force is obtained as:

$$F_{cor} = F_s + F_b = -k_0 x\left(1 - \frac{\sqrt{R^2 + x_0^2}}{\sqrt{R^2 + x^2}}\right) + g\pi R^2(\rho_w H - \rho_w x - \rho_{cor} 2H). \tag{2.28}$$

The non-dimensional form of this equation is:

$$\tilde{F}_{cor} = -\alpha\xi\left(1 - \frac{\sqrt{\xi_0^2 + \delta^2}}{\sqrt{\xi^2 + \delta^2}}\right) + (1 - \xi - 2\tilde{\rho}), \tag{2.29}$$

with

$$\tilde{F}_{cor} = \frac{F_{cor}}{\rho_w g H R^2 \pi} = \frac{F_{cor}}{P_0 \pi R^2}, \qquad \xi = \frac{x}{H}, \qquad \xi_0 = \frac{x_0}{H},$$
$$\alpha = \frac{k_0}{\rho_w g R^2 \pi}, \qquad \delta = \frac{R}{H}, \qquad \tilde{\rho} = \frac{\rho_{cor}}{\rho_w}.$$

A graphical interpretation of this equation can be seen in Fig. 2.10.

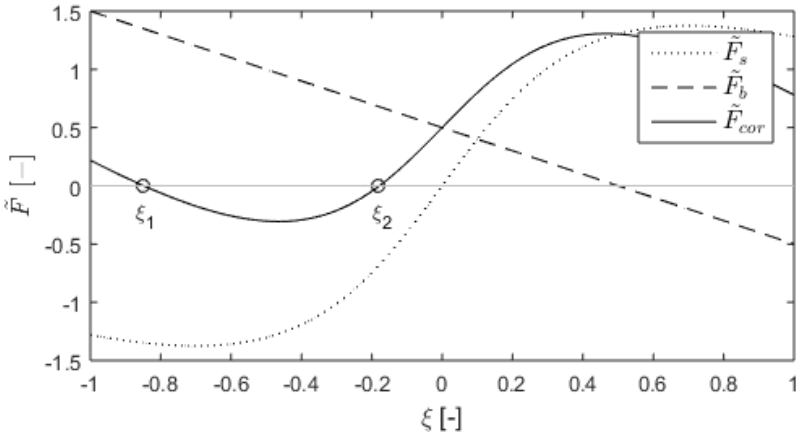

Figure 2.10: Total spring force on the CorPower with $\xi_0 = 2\frac{1}{2}$, $\delta = \frac{1}{2}$, $\tilde{\rho} = \frac{1}{4}$ and $\alpha = 1$.
At $\xi = -1$: the buoy is full underwater, $\xi = 1$: the buoy is fully floating.

Natural Frequency

By applying a similar procedure as for the Symphony, the natural frequency and added mass of the CorPower can be calculated. In Fig.2.10 can be seen that the CorPower has two equilibrium positions, ξ_1 and ξ_2. For the stable equilibrium position ξ_1, the stiffness of the system is:

$$\tilde{k} = -\frac{F(\xi_1)}{d\xi} = -\alpha + \alpha\left(\frac{\sqrt{\xi_0^2 + \delta^2}}{\sqrt{\xi_1^2 + \delta^2}}\right)\left(1 - \frac{\xi_1^2}{\xi_1^2 + \delta^2}\right) - 1. \tag{2.30}$$

This results in a natural frequency:

$$\tilde{\omega}_n^2 = \frac{1}{2\tilde{\rho} + \tilde{m}_{added}}\left(-\alpha + \alpha\left(\frac{\sqrt{\xi_0^2 + \delta^2}}{\sqrt{\xi_1^2 + \delta^2}}\right)\left(1 - \frac{\xi_1^2}{\xi_1^2 + \delta^2}\right) - 1\right) \tag{2.31}$$

The first equilibrium position, ξ_1, is a stable position since $\frac{F(\xi_1)}{d\xi} < 0$. For this a natural frequency can be found which can be tuned by the parameters δ and ξ_0 which can lead to the best position and frequency of the spring. The second equilibrium position, ξ_2, is unstable since $\frac{F(\xi_2)}{d\xi} > 0$.

2.6 Comparison of two working principles

In both working principles the total spring force crosses the zero line two times during the extraction. This means that both systems have more than one equilibrium point, in contrast to a standard positive spring.
For the Symphony, the spring of the system itself forces the Symphony to its stable equilibrium point at ζ_1, when $\zeta < \zeta_2$. In case $\zeta > \zeta_2$ the spring will force the Symphony away in positive direction from its unstable equilibrium point at ζ_2. Hereby the slope is lowered around position ζ_1 and by tuning the gas spring a perfect fit can be made to the natural frequency and wave frequency in order to extract maximum power. It must be noted that this is a simplified situation in which the Symphony is not modified to control this instability yet.
The CorPower system also has two equilibrium positions. The negative spring is instead of the surrounding water, the system itself. By adding a strong positive spring with a slightly weaker negative spring a weak spring is created. By changing the systems parameters this weak spring can be tuned to the perfect fit with the wave frequency.
In this section is shown that the natural frequency of a positive spring can be lowered by adding a negative spring. The other option to lower a natural frequency is applying a higher mass.

2.7 Conclusion

In conclusion, a negative spring is defined by: $k \equiv -\frac{dF(x)}{dx}$ when $k < 0$. When a negative spring is stretched, the spring force increases and pointing from its equilibrium position which forces the systems excitation to increase, leading to an instable situation. This can be solved by adding a negative spring to a stronger positive spring force, creating a weak spring with a low natural frequency. This combination benefits from low natural frequency and a large frequency bandwidth.

Chapter 3

Validation of the simplified model

3.1 Introduction

The principle of the Symphony has been proven based on its major forces, F_{Gas} and F_{hs}. In order to create an optimal design for the Symphony's spring force, first it is researched what the best suitable method is for calculating the power output based on the sea state and Symphony. This chapter looks into two different methods: simulating the system by a Time Domain Model and linearisation of the model. Simulation over time is a method which calculates the movement of the floater resulting in a precise power output. On the other hand, linearisation is a less time consuming method giving an algebraic solution for the spring force design.

3.2 Time Domain Model

The motion of the floater of the Symphony can be calculated by the Time Domain Model. This model is described as:

$$m\ddot{z}(t) = F_{Wave}(t) + \underbrace{F_G + F_{hs}(z) + F_{Gas}(z) + F_{AirTop}(z)}_{\text{Spring component}} + \underbrace{F_D(\dot{z})}_{\text{Damping}} + \underbrace{F_{PTO}(\dot{z}, z)}_{\text{Control}} + \cancel{F_{Rad}(\ddot{z})} \quad (3.1)$$

This model calculates the motion by submitting all important forces and calculate from this the acceleration, velocity and distance. A wave pattern over time is used as input and the movement of the floater as output. A more detailed description of this model can be found in Appendix A. As can be seen in Eq.3.1 the forces in the Time domain model can be categorized to a second order system as described in Eq.2.1. In this equation the gas spring force F_{Gas}, gravity force F_g, hydrostatic force F_{hs} and gas force from the top chamber are all dependent on z, combining them gives the spring component of the floater. The damping component is given by the drag force F_D. The system is controlled by the turbine resistance created by the control system, which results in F_{PTO}. For the design process, the radiation force is found too small compared to all other forces and is neglected during this report. The radiation force depends the model of the Symphony and is only been neglected in the present report.

Wave forces

For simulating the Symphony behaviour over time input of the sea is needed. There are two types of wave patterns that have been used in the simulation: Monochromatic waves and 'random' waves from the Bretschneider spectrum. A Monochromatic wave means that the sea waves are made from a single sinusoid. The only needed input is the amplitude, period and phase difference, Fig.3.1(a). These waves are important to simulate the behaviour of the Symphony on a specific wave. Of course the sea is not a perfect sinusoid and a more realistic sea state can be simulated by using the Bretschneider spectrum. The sea state uses the Bretschneider spectrum to pick waves from different heights and lengths to create a full sea state. The Bretschneider spectrum gives the arising probability of a certain wave. Here the specific height H_s is needed with the energy period T_e, Fig.3.1(b). A more detailed description is given in Appendix A.7.

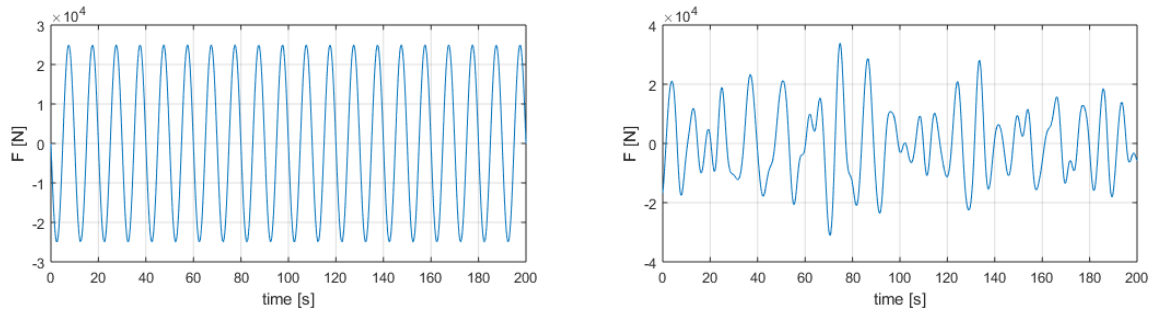

(a) Monochromatic wave with: $A = 2m\ T = 10s$

(b) Sea state $H_s = 4m\ T_e = 10s$

Figure 3.1: Spring force profile and corresponding diameter per length of the S-curve

Due to the difference in height of waves, a force is created. When the wave is on top of the Symphony the water pressure increases surrounding the Symphony. This creates a force on the surface of the Symphony. In vertical direction the pressure creates a force on top of the floater which points downwards. On the bottom of the Symphony the force is captured by two different areas: the bottom area of the floater and the bottom area of the cocoon. For the floater this means that a downwards force increases when a wave is on top of the floater and decreases when the wave is moving away from the floater. This is described in more detail in Appendix A.7.

Spring forces

As been written before the gas spring force F_{Gas}, hydrostatic force F_{hs} and gas force from the top chamber F_{AirTop} are all dependent on z. From which F_g, F_{hs} and F_{AirTop} are given by the design of the symphony. On the other hand the gas spring force is still variable. By changing the inner geometry at which the membranes are rolling the volume floating through the turbine changes. By this the pressure difference in the gas chamber changes. The geometry is calculated by choosing the resulting spring force of all mentioned spring forces. The exact calculation is described in more detail in Appendix B. The advantage is that all effects of the individual forces can be countered and if needed a full linear spring can be created. This resulting spring force is used to create the different geometries to solve the research question of this project.

Damping forces

The only major damping force the Symphony is experiencing is the drag force. This is the force due to movement of the submerged system through surrounding water. This effect is described in more detail in Appendix A.6. The equation for the drag force is a quadratic equation so this is a non-linear force. Also the drag coefficient is different per direction, since the top of the floater is far more streamlined in top direction than in bottom direction.

Control forces

By moving the floater up and down water is flowing by the membranes through the turbine. By adding resistance at the turbine rotation, the PTO force is created. This resistance is directly coupled to the power output of the Symphony and is used to control the motion of the Symphony. The added pressure is calculated by multiplying the output of the control system times the velocity. The input of the control system is calculated by the total kinetic and potential energy minus the maximum potential energy in the system. The outcome is the overcapacity of energy in the system by multiplying this with the P-controller the turbine is subtracting energy from the system. Only a P-controller is used since this is the most basic controller and is not influencing with the performances.
Now the system has been reduced to a forced non-linear second order system, an analysis is needed to see if and how this system can be estimated as a linear system. In order to make sure all conclusions from the earlier section can be used to design the air spring and control system.

3.3 Linearisation of the model

Two possible linearisation methods have been investigated in this section. The Describing Function Method which is a commonly used method in the control design and the Least Squares Method which optimises the minimal error over a distance. Both linearisation methods calculate the optimal linear force which should be representable for the non-linear force.

3.3.1 Describing Function Method

The sinusoidal-input describing function method (DFM) is the most widely known and used method for linearisation of a nonlinear element [11]. This method is subjected to a sinusoidal input:

$$x(t) = X\sin(\omega t + \phi), \tag{3.2}$$

where X is the amplitude of the input $[m]$, ω the frequency $[rad/s]$ and ϕ the phase angle $[rad]$. To emphasize the fact that $y(t)$ depends on $x(t)$ in some way, the current value of $x(t)$ and its derivative shall be indicated in the notation:

$$y(t) = y[x(t), \dot{x}(t)] = y[X\ \sin(\tau), X\omega\ \cos(\tau)], \tag{3.3}$$

with $\tau = \omega t + \phi$. Since the only unknown parameter τ has a periodic behaviour, it can be integrated over the range of $0 - 2\pi$. The probability density function for this uniformly distributed variable is $1/2\pi$. This leads to the following equations:

$$n_p = \frac{1}{\pi X} \int_0^{2\pi} y(X\sin(\tau), X\omega\cos(\tau))\sin(\tau)d\tau, \tag{3.4}$$

and

$$n_q = \frac{1}{\pi X} \int_0^{2\pi} y(X\sin(\tau), X\omega\cos(\tau))\cos(\tau)d\tau. \tag{3.5}$$

It can be seen that Eq. 3.4 and 3.5 are both the first order Fourier coefficients divided by X. These equations can be filled in the form derived by Krylov and Bogoliubov from the Fourier series:

$$\ddot{x} + \frac{n_q(X,\omega)}{\omega}\dot{x} + n_p(X,\omega)x = 0 \tag{3.6}$$

By using the Describing Function Method for the non-linear spring and the non-linear damping, a linear model can be derived.

Non-linear spring

Two continues non-linear spring forces have been used for analysing. The force of the non-linear spring is given by: $F = k_0 x + \beta x^3$ and $F_v = k_0 x + \beta x^7$. Both forces will be introduced in more detail later in Chapter 4 but for now they will be the test case for linearisation process. With the DFM we find:

$$\begin{aligned}
&y(X\sin(\tau), X\omega\cos(\tau)) = k_0 x + \beta x^3, \\
&n_p = \frac{1}{\pi X}\int_0^{2\pi} y(X\sin(\tau), X\omega\cos(\tau))\sin(\tau)d\tau, \\
&\quad = \frac{1}{\pi X}\int_0^{2\pi} k_0 X\sin^2(\tau)d\tau + \int_0^{2\pi}\beta X^3\sin^4(\tau)d\tau = (k_0 + \frac{3}{4}\beta X^2), \\
&n_q = \frac{1}{\pi X}\int_0^{2\pi} y(X\sin(\tau), X\omega\cos(\tau))\cos(\tau)d\tau = ...\int_0^{2\pi} ...\cos(\tau)\sin(\tau)d\tau = 0.
\end{aligned}$$

For $F_v = k_0 x + \beta x^7$ the same method is used for:

$$\begin{aligned}
&y(X\sin(\tau), X\omega\cos(\tau)) = k_0 x + \beta x^7, \\
&n_p = \frac{1}{\pi X}\int_0^{2\pi} y(X\sin(\tau), X\omega\cos(\tau))\sin(\tau)d\tau = (k_0 + \frac{35}{64}\beta X^6), \\
&n_q = \frac{1}{\pi X}\int_0^{2\pi} y(X\sin(\tau), X\omega\cos(\tau))\cos(\tau)d\tau = ...\int_0^{2\pi} ...\cos(\tau)\sin(\tau)d\tau = 0.
\end{aligned}$$

Which leads to the linear spring force:

$$\boxed{k = (k_0 + \frac{3}{4}\beta X^2)}, \tag{3.7}$$

and for $F_v = k_0 x + \beta x^7$:

$$\boxed{k = (k_0 + \frac{35}{64}\beta X^6)}. \tag{3.8}$$

3.3.2 Least Squares Method

Another method to find a characteristic spring constant that is representative for the non-linear behaviour of the Symphony consists of minimises the difference between the linear spring force and nonlinear spring force in the interval $[-X, X]$ is called the Least Squares Method (LSM). This can be found by subtracting the original equation $F_v = k_0x + \beta x^3$ from the to estimate linear equation $F_v = kx$. By taking the square, the error gets positive and all small errors are getting less important. Then taking the integral over the domain of the Symphony, which is the maximum of the stroke in both directions. The error ψ can be estimated by:

$$\psi(k) = \int_{-X}^{X} [k_0x + \beta x^3 - kx]^2 dx. \tag{3.9}$$

The optimal value of k minimize $\psi(k)$ and therefore $\frac{d\psi}{dk} = 0$ find the minimum error for a certain k the derivative of k is taken over the system. When this derivative is zero the error is minimized.

$$min(\psi) => \frac{d}{dk} \int_{-X}^{X} [k_0x + \beta x^3 - kx]^2 dx = 0. \tag{3.10}$$

For $F_v = kx + \beta x^3$ this leads to:

$$k = \frac{\int_{-X}^{X} [k_0x^2 + \beta x^4] dx}{\int_{-X}^{X} x^2 dx} = \boxed{k_0 + \frac{3}{5}\beta X^2}, \tag{3.11}$$

and for $F_v = kx + \beta x^7$ the same method can be used.

$$k = \frac{\int_{-X}^{X} [k_0x + \beta x^8] dx}{\int_{-X}^{X} x^2 dx} = \boxed{k_0 + \frac{3}{9}\beta X^6}. \tag{3.12}$$

3.4 Comparison

For the comparison of the DFM, LSM and the Time Domain Model a monochromatic sea wave analyses is made. This means that all four linear spring forces have been modelled in the time domain model and simulated with the input of a constant sinusoidal sea wave: $z_w = \frac{H}{2}\sin(\frac{t}{T})$. Here H is the wave height $[m]$ and T the period time of the wave $[s]$. Afterwards the results are compared to the non-linear spring. For this situation a larger stroke is allowed. In case of small waves the system uses the higher stiffness of the non-linear spring and the non-linearity can be compared to the linear-spring. This analyse is performed over a broad spectrum but for readability only a part of the results is shown in Fig.3.2 & 3.3.

In Fig.3.2(a) the power output can be seen for the third power spring with a wave height of 3 meter. All three springs are similar but the natural frequency is slightly lowered. An explanation for this is that the spring stiffness of the linear springs is higher than for the non-linear spring in its mid section. It also explains why both linear springs are extracting less energy. This pattern is found for wave heights $H < 4.5m$. When reaching higher wave heights, the linear spring is getting more distant from the non-linear solution. This can be seen in Fig.3.2(b). In which the power extraction at the highest possible wave height is visible $H = 6m$. It is clear that the linear models are not

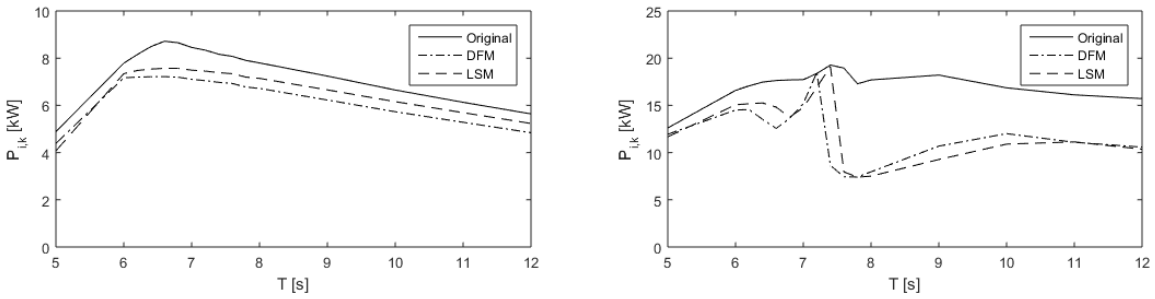

(a) $H = 3m$ *(b)* $H = 6m$

Figure 3.2: Power output,$P_{i,k}$, for spring force $F = k_0x + \beta x^3$, per method

representative for the non-linear model, because the linear model has no increased force at the end of the stroke. Since the PTO is controlling the system it is only controlling the system and cannot extract at the ideal moments.

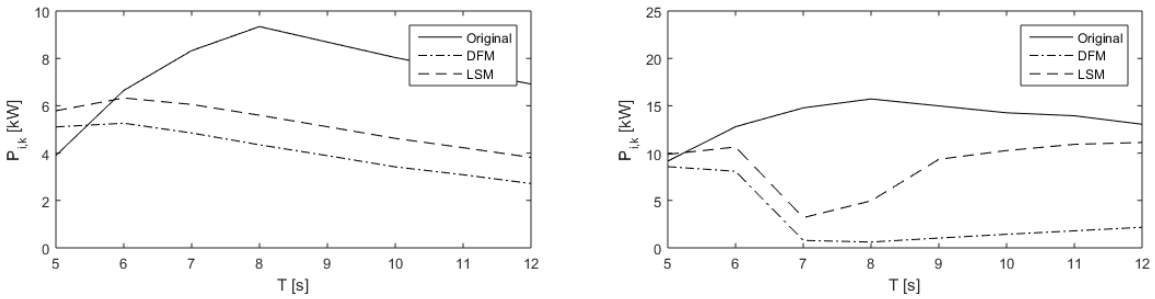

(a) $H = 3m$ *(b)* $H = 5m$

Figure 3.3: Power output,$P_{i,k}$, for spring force $F = k_0x + \beta x^7$, per method

Fig.3.3 depicts the power output for the non-linear spring with the seventh order with the same wave heights. The non-linear spring needs to compensate heavily for the seventh order This makes the spring a lot stiffer and causes the natural frequency to lower even more as is shown in Fig.3.3(a). Also the extracted power is much lower since this new natural frequency is far from the desired frequency. For all high sea waves, $H > 4m$, the linear model has no comparable pattern, Fig.3.3(b). Also the floater is not following the optimal route for extracting optimal power.

3.5 Conclusion

In conclusion, linearisation based on the Describing Function method and Least Square method only gives a crude estimate of the power output. For an exact solution the Time Domain Model is still needed. When the non-linearity of the original spring force increases, the error due to linearisation increases too. The error is also high near the maximum controlled wave height, for which linearisation does not give a realistic solution. The difference between both linearisations is small but the LSM is performing better overall. The overall conclusion is: linearisation only gives an order of magnitude of the exact solution when no extreme conditions are used.

Chapter 4

Design of the Buffer system

4.1 Introduction

Based on the model of the movement of the floater, design parameters of the spring can be determined. For this not only the floater but the full system needs to be analysed. After determining the design parameters, profile designs can be made and tested. After this the selected profile can be optimized by a detailed design.

4.2 Design Parameters

Maximum Spring forces

In earlier sections, it was assumed that the cocoon was clamped to the bottom of the sea, while in reality the vertical position of the cocoon section is retained by two forces: the buoyancy force and the gravitational force from the anchor. In Fig.4.1 the working forces on the cocoon are displayed in a sinusoid displacement.

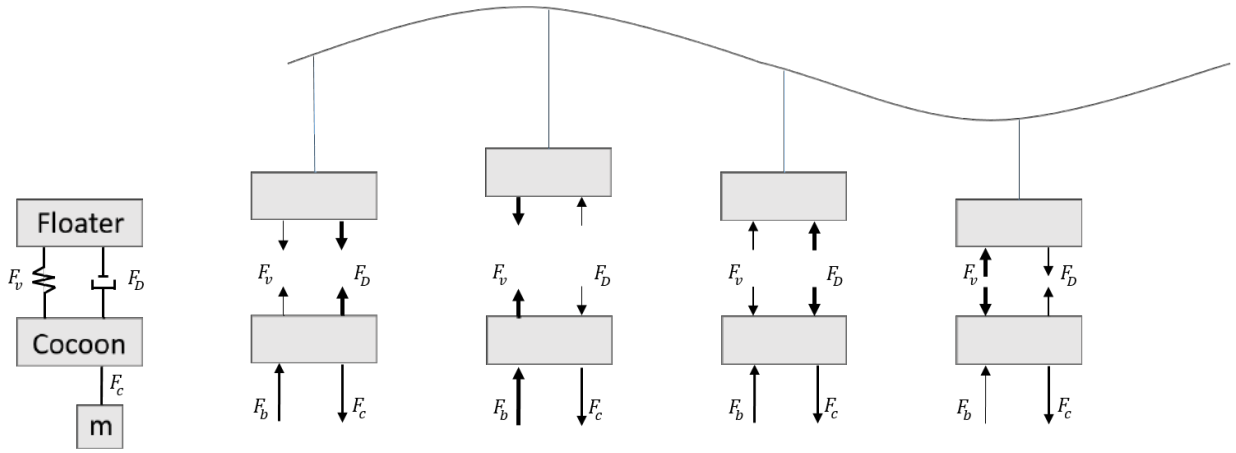

Figure 4.1: VLS for a small time step after the equilibrium, top and bottom position

The four different positions of the floater show that there is a phase delay of 90 degrees between

the damping force and spring force. The buoyancy force F_b has been taken as:

$$F_b(z) = \rho_w V_{SYM}(z) \cdot g - m_{SYM} \cdot g, \tag{4.1}$$

with ρ_w the density of water $[kg/m^3]$, V_{SYM} the volume of the Symphony $[m^3]$, g the gravitational constant $[m/s^2]$ and m_{SYM} the mass of the Symphony $[kg]$. When z increases overtime V_{SYM} will increases while m_{SYM} stays constant. This leads to F_b increases during an upward stroke. This is for the current design $F_b = 30kN$ in bottom position and $F_b = 80kN$ in top position.
The gravitational force from the anchor is called the chain force F_c. It results from the spring force, damping force and buoyancy force:

$$F_c = F_b(z) + F_{vc}(z) + F_D(t, \dot{z}) \quad \text{with} \quad 0 < F_c < F_{c_{max}}. \tag{4.2}$$

The maximum chain force, $F_{c_{max}}$, is limited to gravitational force of the anchor, and the maximum tension force of the cable. It is assumed that the allowed tension force is much higher than the gravitational force of the anchor. Also the chain can only hold tension forces and no compression forces. These both limitations result in $0 < F_c < F_{c_{max}}$. Which can be written for the cocoon as:

$$-F_b(z) < F_{vc}(z) < F_{c_{max}} - F_b(z) \tag{4.3}$$

The limitations on the spring force working on the cocoon $F_{vc}(z)$ should have opposite signs when considering the floater $F_v(z)$. Then the floater restrictions are:

$$F_b(z) - F_{c_{max}} < F_v(z) < F_b(z), \tag{4.4}$$

with $F_D(t, 0) = 0$. If the spring force on the floater is smaller than the restricting forces, the anchor is pulled up and will fall back again with big vibrations through the system. On the other hand when the spring force is bigger than the buoyancy force the chain will go slack and the full system will go down, also accompanied by big vibrations. A graphical impression of these design parameters is given in Fig.4.2 with the corresponding consequences.

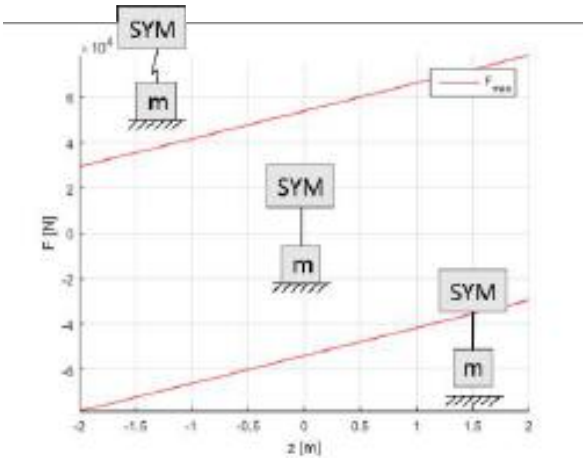

Figure 4.2: Maximum spring force on the floater and consequence

Avoiding wear

The second design parameter concerns additional wear over the membranes. The spring force can be designed by the shape of outer wall of the cocoon, over which the membrane is rolling. As this membrane goes over the walls every ten seconds, any sharp corners or discontinuities should be avoided to prevent additional wear.

Controlling without electrical demand

The last design parameter concerns the damping of the system in case all damping from the generator fades out and with this the resistance on the turbine. In exceptional conditions it can happen that the electrical grid stops demanding electricity. For example during a failure in software in or outside the Symphony, but also when other energy producing systems feeding to much energy to the grid and the production is higher than the demand. To deal with such situations the spring force should control the Symphony in its maximum stroke also without the generator resistance involved.

4.3 Profile designs

From the restrictions on the spring force five possible designs have been developed. For readability the geometries are called G1-G5 during the project. These designs all have a (quasi-) linear section in the middle of the stroke and an increased force at the both ends of the stroke. The designs are described by:

$$G1: \ F_v(z) = k \cdot z + \beta \cdot z^3, \tag{4.5}$$

$$G2: \ F_v(z) = k \cdot z + \frac{\beta}{z_{max}^2} \cdot z^5, \tag{4.6}$$

$$G3: \ F_v(z) = k \cdot z + \frac{\beta}{z_{max}^4} \cdot z^7, \tag{4.7}$$

$$G4: \ F_v(z) = \begin{cases} F_b(-z_{max}) - F_{c_{max}} & \text{if } -z_{max} < z < -z_{lin}, \\ k \cdot z & \text{if } -z_{lin} < z < z_{lin}, \\ F_b(z_{max}) & \text{if } z_{lin} < z < z_{max}, \end{cases} \tag{4.8}$$

$$G5: \ F_v(z) = \begin{cases} F_b(z) - F_{c_{max}} & \text{if } -z_{max} < z < -z_{lin}, \\ k \cdot z & \text{if } -z_{lin} < z < z_{lin}, \\ F_b(z) & \text{if } z_{lin} < z < z_{max}. \end{cases} \tag{4.9}$$

where F_v is the spring force $[N]$, k is the optimal stiffness which leads to the optimal natural frequency for the linear stroke $[N/m]$, β added stiffness for the non-linear part of the stroke $[N/m^3]$, z_{lin} length of the linear stroke $[m]$ and z_{max} maximum allowed stroke. All described geometries can been seen in Fig.4.3. The red dotted lines give the boundaries to the design described in section 4.2.

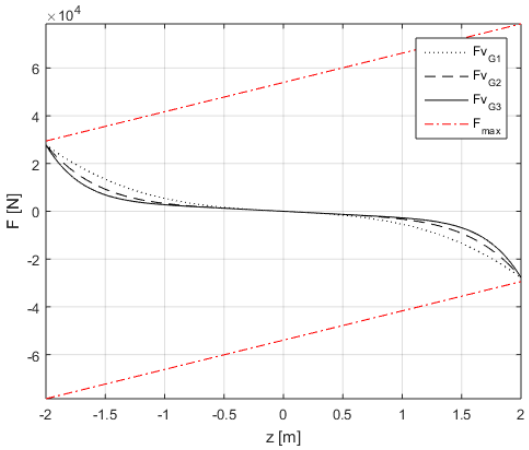

(a) G1,G2,G3

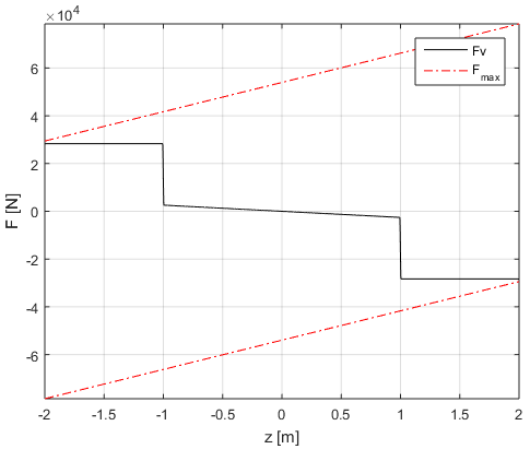

(b) G4,G5

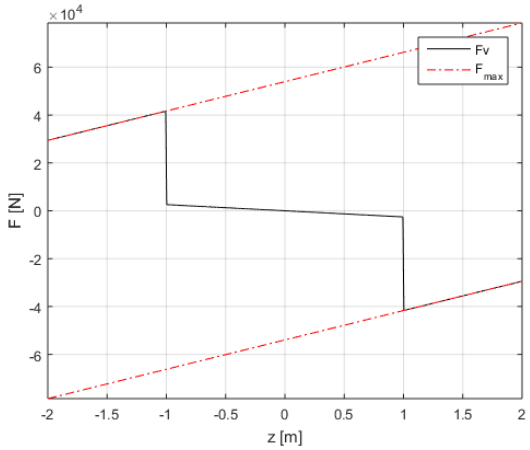

(c) G5

Figure 4.3: Design profiles of the spring forces during the stroke

The designs G1-G3 all have a continues force profile, which means the membrane can roll comfortable over the geometry. They have a quasi-linear section in $-z_{lin} < z < z_{lin}$ since also the higher order part of the function has influence on this section. The other two profiles, G4 and G5, are not continues. If these profiles would be chosen all sharp corners should be rounded off later on in the design process. They both have a perfect linear section in the middle and an abrupt increase to the ends. The difference is that the profile G4 has a constant maximum force at the end of the stroke and G5 has a maximum force that follows the change in buoyancy force during the stroke.

The spring stiffness k is chosen to create a natural frequency with the best performance. This is equal to the spring stiffness described in the report of Aart Kooiman [8].

4.4 Profile performance and selection

To test the performance of each profile design a simulation is performed, with all possible sea state conditions. For this analyse the sea conditions of Leixous, Portugal, have been used since this is the place where the first prototype of the Symphony will be tested. Each sea state has two important parameters: the energy period, T_e, and the significant height, H_s. These two parameters, together with the Bretschneider spectrum, give the wave spectrum. The wave spectrum gives on its turn a time dependent sea model which contains multiple waves heights and periods. A more detailed procedure description is given in Appendix A.7.2.
Each profile has been analysed with the Time Domain Model for all sea states. From this model an average power output can be obtained for each individual sea state $P_{i,k}$. The power output is set to zero in case the geometry is not able to keep the Symphony within its maximum stroke, z_{max}. The average power $< P > \ [W]$ can be found by:

$$< P >= \int_0^\infty \int_0^\infty P(H_s, T_e) \cdot \lambda(H_s, T_e) \, dT_e \, dH_s, \tag{4.10}$$

where λ is the probability density of a certain sea state $[m^{-1}s^{-1}]$. Where the total density is given by: $\int_0^\infty \int_0^\infty \lambda(H_s, T_e) \, dH_s dT_e = 1$. For Leixous a scatter diagram is given in the Appendix in table D.1. Here the probability of a wave belongs to $\Omega_{i,k}$ is defined by:

$$\eta_{i,k} = \iint_{\Omega_{i,k}} \lambda(H_s, T_e) \, dT_e \, dH_s, \qquad \begin{cases} \text{for } i = 1, 2, ...I \\ \text{for } k = 1, 2, ...K \end{cases} \tag{4.11}$$

where i is the index number for the energy period and k the index number for the wave height. $P_{i,k}$ is defined as the power output at the mid position in the area $\Omega_{i,k}$. Which results to an exact solution with an error of the second order. This leads to:

$$< P > \approx \sum_{i=1}^{I} \sum_{k=1}^{K} P_{i,k} \cdot \eta_{i,k}. \tag{4.12}$$

This finally leads to the equation for the power density per wave height:

$$P_k \approx \sum_{i=1}^{I} P_{i,k} \cdot \eta_{i,k}. \tag{4.13}$$

Results of P_k are listed in table 4.1. The first conclusion is the fact that the biggest contribution to the average power is extracted from waves with the range $1.5m < H_s < 3m$. The reason for this is that 58.4% of the annual waves in Leixous are within this range.
Moreover it shows that geometries G2-G5 extract almost the same energy for low wave heights ($H_s < 3.5m$), only negligible differences can be seen. On the other hand geometry G1 extracts less energy, because of a shorter linear spring in the mid section of the geometry ($-z_{lin} < z < z_{lin}$) as can be seen in Fig.4.3. In contrast to the fifth and seventh order in G2 and G3, the third order factor in G1 causes the geometry to deviate earlier in the stroke from the desired linear spring force. This conclusion only regards low wave heights since the PTO can control the system in its boundaries without the need for buffers from the spring force.

H_s	η_k	P_{k-G1}	P_{k-G2}	P_{k-G3}	P_{k-G4}	P_{k-G5}
$<$0.5m						
0.5 - 1.0m	5,0 %	11W	16W	15W	15W	15W
1.0 - 1.5m	23.0 %	168W	197W	194W	196W	195W
1.5 - 2.0m	24.1 %	303W	344W	342W	340W	339W
2.0 - 2.5m	16.9 %	314W	336W	334W	336W	331W
2.5 - 3.0m	10.7 %	243W	268W	270W	265W	266W
3.0 - 3.5m	6.7 %	195W	201W	202W	198W	200W
3.5 - 4.0m	4.7 %	150W	111W	101W	165W	164W
4.0 - 4.5m	2.9 %	105W	64W		116W	86W
4.5 - 5.0m	2.4 %	28W		5W	6W	103W
5.0 - 6.0m	2.2 %					18W
$>$6m	1.4 %					
Total	100 %	1517W	1536W	1465W	1637W	1720W
$max(H_s)$ if $F_{PTO} = 0$		0.5m	0.3m	0.25m	1.3m	1.5m

Table 4.1: P_k, Power per H_s per Geometry

The third conclusion concerns the maximum significant wave height H_s at which the system can still extract energy. The more energy can be stored in the spring of the system, the higher the maximum allowed wave force can be. This force directly coupled to the height of the wave. The values of P_{k-G3} show that G3 has the lowest maximum wave height, because the buffer comes up at almost the end of the stroke. In G1 and G2 the added buffer is beginning earlier in the stroke. For G4 and G5 the buffer is rising instantly after a distance z_{lin} which gives a long high buffer range. Since $F_{v-G5}(z_{lin}) > F_{v-G4}(z_{lin})$, G5 can reach a higher wave height.
Also the survivability per geometries was investigated. Geometry G5 has the highest survivability of all geometries this is since it has the highest spring force at the end of the linear stroke. A wave height of max 1.5m gives the probability of 25% it will survive when the PTO disappears for some time. This is unacceptable and another solution needs to be found.
Overall it can be concluded that geometry G5 is the optimal geometry. It has two major advantages, first it has a perfect tuned linear spring in the mid section of the stroke. Secondly it has the highest maximum allowed wave height by a high spring force at $F_{v-G5}(z_{lin})$. The major disadvantage is the non-continuity of the spring which result in higher wear on the membranes. A solution for this will be found later in the design process.

4.5 Detailed Design

4.5.1 Avoiding wear

It is important that the membranes follow the inner wall during the stroke. For this a continues profile without any big bumps or sharp corners is needed. The chosen profile G5 does not satisfy this condition, as can be seen in Fig.4.4(a,d). For this an analyse is done on how to smooth the profile. It is important to keep in mind smoothing the profile could cancel the advantage of a high instant spring force and the profile could become less productive than best continues profile G2.

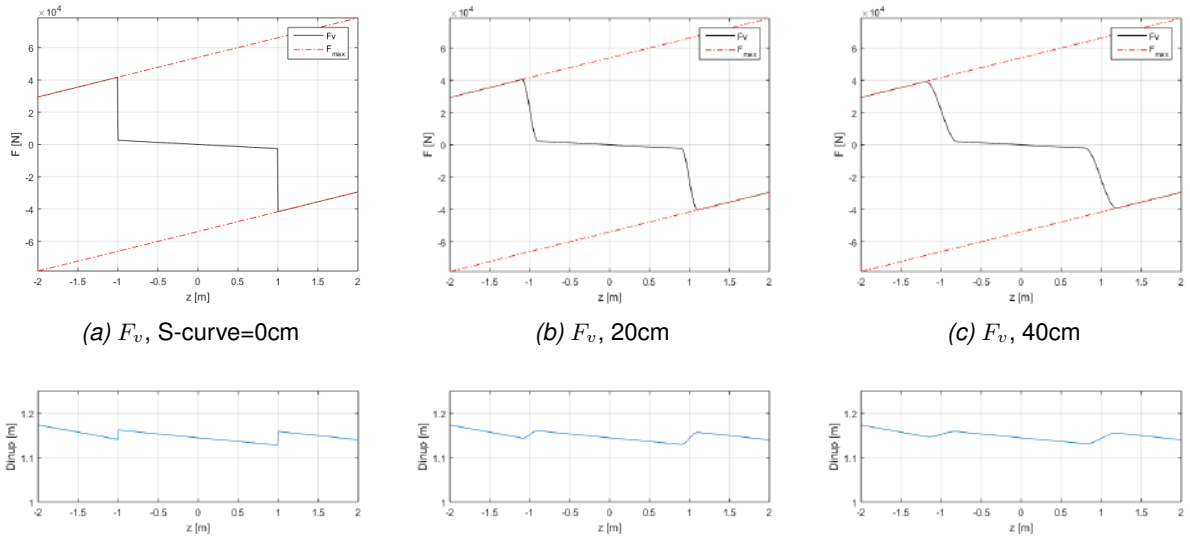

(a) F_v, S-curve=0cm *(b)* F_v, 20cm *(c)* F_v, 40cm

(d) D_{inup}, 0cm *(e)* D_{inup}, 20cm *(f)* D_{inup}, 40cm

Figure 4.4: Spring force profile and corresponding diameter per length of the S-curve

To smooth the sharp corners, an S-curve is introduced an interval Δz. This S-curve is made by a cubic spline interpolation, which results in a continues function in the first and second derivative [12]. Which results in a smooth surface for the membrane, Fig.4.4(b,c,e,f). Five different S-curves are tested following similar procedure as in previous section. The performances are shown in table 4.2.

H_s	η_k	$\Delta z = 0cm$	$10cm$	$20cm$	$30cm$	$40cm$
<0.5m						
0.5 - 1.0m	5,0 %	15W	16W	17W	17W	19W
1.0 - 1.5m	23.0 %	195W	196W	196W	204W	202W
1.5 - 2.0m	24.1 %	339W	341W	343W	337W	335W
2.0 - 2.5m	16.9 %	331W	331W	325W	322W	312W
2.5 - 3.0m	10.7 %	266W	260W	255W	252W	245W
3.0 - 3.5m	6.7 %	200W	197W	192W	187W	184W
3.5 - 4.0m	4.7 %	164W	159W	155W	153W	151W
4.0 - 4.5m	2.9 %	86W	114W	110W	108W	106W
4.5 - 5.0m	2.4 %	103W	71W	76W	82W	92W
5.0 - 6.0m	2.2 %	19W	19W	20W		
>6m	1.4 %					
Total	100 %	1720W	1705W	1689W	1662W	1646W
Loss		-	-0.9%	-1.8%	-3.4%	4.3%

Table 4.2: P_k, Power times probability per length of the S-curve

By implementing an S-curve the average power production of the system decreases as can be seen in table 4.2. The S-curve lowers the maximum force at $F_v(z_{lin})$ which result in a lower maximum wave height. Also for the sea states with $2.5m < Hs < 4m$ the power output decreases by increasing length of the S-curve. This comes due to the shorter linear spring in the mid section of the stroke. This leads directly to the rise of the system stiffness and with this the natural frequency. For $H_s < 2m$ the energy production is almost constant, here the floater is not influenced by the non-linear buffer system.
At this point the exact effect of the wall on the wear of the membranes is not known. It can be assumed that the S-curve with a length of 20cm is smooth enough for the membrane. The electricity loss of this profile is only 1.8% compared to original G5 geometry. The loss of 1.8% electricity is an acceptable solution and is still more productive then profiles G1-G3 which were already continues functions. For this reason this profile is selected for further design.

4.5.2 Optimization of the profile

The next and last step in the design process is the optimization of the profile for the energy production. By increasing the length of the linear stroke, z_{lin}, the floater is allowed to make a longer stroke which gives the floater a higher maximum speed which allows the system to extract more energy on the smaller waves. The disadvantage is that the maximum wave height is lowered. Since the lower waves are the most frequent waves it can be expected that the total extracted energy. The geometries of the optimization can be seen in Fig.4.5 and results in table 4.3.

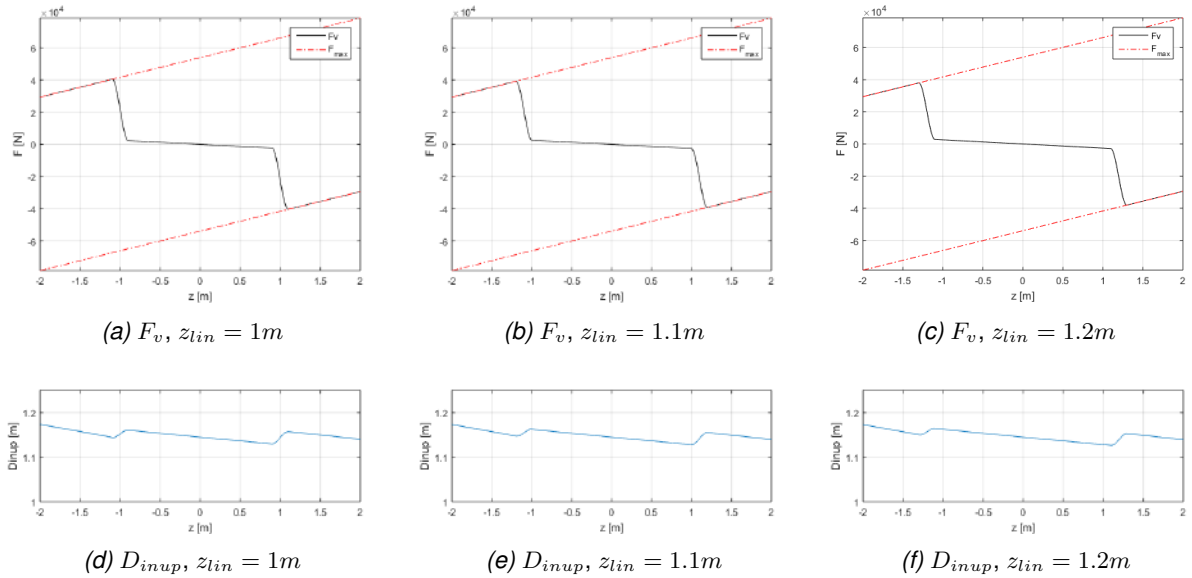

(a) F_v, $z_{lin} = 1m$ *(b)* F_v, $z_{lin} = 1.1m$ *(c)* F_v, $z_{lin} = 1.2m$

(d) D_{inup}, $z_{lin} = 1m$ *(e)* D_{inup}, $z_{lin} = 1.1m$ *(f)* D_{inup}, $z_{lin} = 1.2m$

Figure 4.5: Spring force profile and corresponding length of the full linear spring

H_s	η_k	$z_{lin} = 1m$	1.1m	1.2m
<0.5m				
0.5 - 1.0m	5,0 %	17W	16W	17W
1.0 - 1.5m	23.0 %	196W	206W	218W
1.5 - 2.0m	24.1 %	342W	371W	395W
2.0 - 2.5m	16.9 %	325W	354W	379W
2.5 - 3.0m	10.7 %	255W	283W	304W
3.0 - 3.5m	6.7 %	192W	209W	225W
3.5 - 4.0m	4.7 %	155W	171W	187W
4.0 - 4.5m	2.9 %	110W	97W	110W
4.5 - 5.0m	2.4 %	76W	36W	37W
5.0 - 6.0m	2.2 %	20W	3W	20W
>6m	1.4 %			
Total	100 %	1689W	1747W	1892W
Gain		-	+3.4%	+12.0%
ω_{turb} at $T_e = 10s$		288.9	316.7	350.5

Table 4.3: P_k, Power times probability per length of the S-curve

By increasing the velocity of the floater also the rotation speed of the turbine increases. The turbine is designed for 350 rpm a higher rotational speed would cause the efficiency to decrease. It is given from the design that a rotational speed of 350 rpm is the maximum rotation speed allowed in the system during a sea state with a period time of 10s. From this can be concluded that the most optimal design of the spring force has a linear stroke of 1.2m from the equilibrium position.

4.6 Final Design

In this section the final design, that was shown in Fig.4.5(c) and 4.5(f), will be discussed and more detailed performance parameters will be given. Three sections are visible in geometry. First of all on both ends the add spring force for controlling high sea waves. Moreover, in the mid section a tuned linear spring is present, which is ideal for low sea waves that have the highest probability. Finally, in between a S-curve is applied to make the geometry more smooth.
With the Time Domain model several simulation have been done on the final design. Over the full spectrum of sea waves the power output, $P_{i,k}$, is given in Fig.4.6(a). A graphical interpretation of the probability of each sea state can be seen in Fig.4.6(b). The average power output $< P >$ can be calculate by:

$$< P > \approx \sum_{i=1}^{I} \sum_{i=k}^{K} P_{i,k} \cdot \eta_{i,k}. \tag{4.14}$$

These figures show that the power output is positive correlated to the wave height. On one hand the probability for high sea waves is low but wide spread, while on the other hand for low sea waves the probability is high and concentrated in a small area. This indicates the challenge from extracting energy from the sea. Other interesting parameters are listed in table C.1 in the appendix.

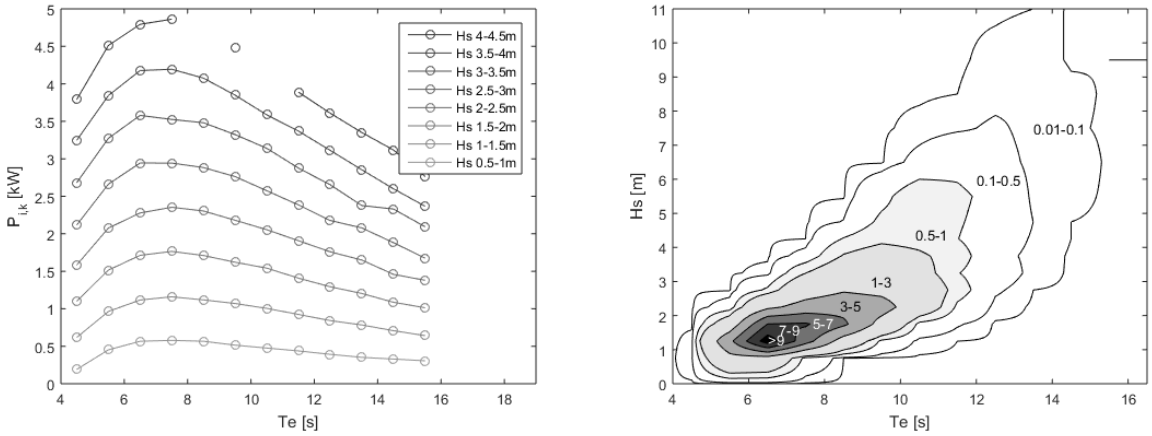

(a) Power output $P_{i,k}$ in kW as function of H_s and T_e

(b) $\eta_{i,k}$ in $\%$

Figure 4.6: Performance and probability of the final spring design

Chapter 5

Conclusions and Recommendations

5.1 Conclusions

Three major conclusions can be drawn from this research.

First of all, a simplified model shows that a point absorber system benefits from making use of a negative spring, since it gives the system a low natural frequency without the need of adding extra mass.

Secondly, simplifying the non-linear model to a linear model by the use of a describing function method or least square method is possible. However, the results only give a rough solution when the calculations are done at a harmonic wave. In case the wave height was close to the maximum allowed wave height the linear model shows deviation.

At last it can be concluded that it is possible to design a mechanical buffer that keeps the movement of the floater within its maximum stroke when exposed to a time dependent waves. This research has shown that the optimal design of the Symphony is one that has a larger spring force on both ends for controlling high sea waves, while in the mid section a tuned linear spring is present, which is ideal for low sea waves that have the highest probability. And in between a S-curve that makes the geometry more smooth. The mechanical buffer in the Symphony leads to an operation rate of 94.6% (time in operation divided by total time). It is taken into account that the system is not allowed to pull up the anchor from the ground or make the chain go slack. Also the geometry of the buffer system had to be continuous without sharp corners. During the design process it became clear that two design parameters are conflicting: the maximum allowed force and control without electrical demand. At acceptable wave heights $H_s > 2m$, it is impossible to keep the system within its boundaries while it is operational without resistance from the PTO and at the same time the anchor is not pulled up or the chain goes slack.

5.2 Discussion and Recommendations

5.2.1 Controlling without electrical demand

It is shortly investigated during this research why the floater cannot be controlled within its boundaries when there is no damping from the PTO. This could be solved by using an electric resistance, which can be activated when the electrical demand drops to zero. From preliminary calculations can be seen that in the current design a 30kW constant power take off works however a more detailed research is needed.

5.2.2 Time domain model

Most calculations have been done with the use of a combined Matlab and Simulink model. This model provides the movement of the floater over time when the system is exposed to a time dependent wave. In this model some simplifications and assumptions have been made: only the forces in z direction are modelled and the damping is simplified to quadratic function. The current model focuses on short calculation times. For future research, test results can contribute to a more accurate model.

5.2.3 Added buffer

It is recommended to add an additional buffer at the end of the stroke. This gives the system a higher spring force when in rough conditions, which results in pulling up the anchor or the chain going slack. The reason is that, without this extra buffer, when an unexpected, non-modelled wave comes in, the systems membranes will be pulled apart. An example of an added buffer to the spring force can be seen in Fig.5.1(a) with corresponding diameter of the inner membrane containment in Fig.5.1(b).

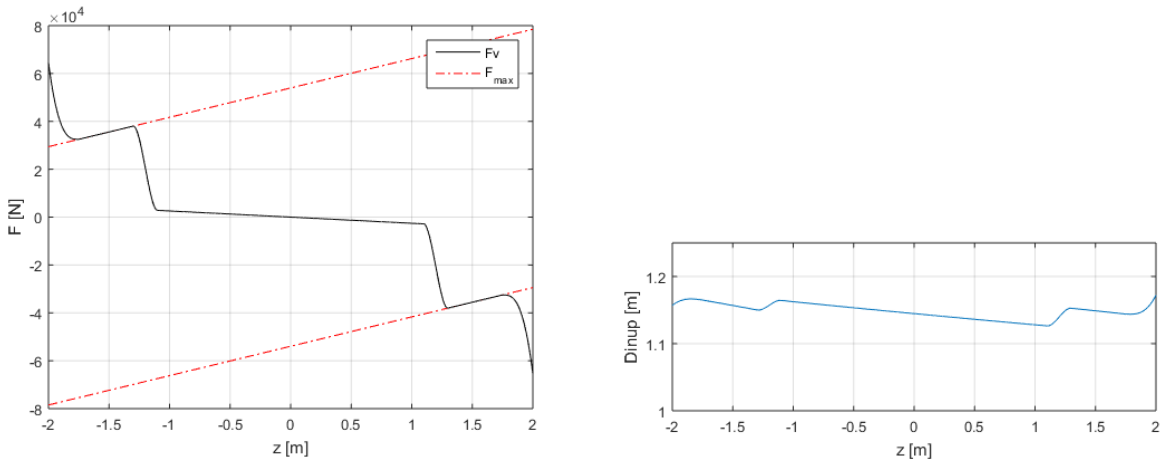

(a) Example of spring force

(b) Example of D_{inup}

Figure 5.1: Example of the final design with an added buffer at the end of the stroke

5.2.4 Controlling a tuned system

The current control system applied in the Symphony is a P-controller, which calculates the maximum energy in the system and extracts this from the current potential and kinetic energy. For further research, a change to a PI(D)-controller should be considered to control the system more efficiently [10]. Adding a feed-forward could even benefit the energy extraction more. The disadvantage of the current controller is that it not only limits the extraction but also the maximum speed.
At last, real time tuning of the pressure in the air chamber of the Symphony could be implemented. This is only possible when the system can detect what is the current sea state, but for this real time weather measurements are needed. These challenges still need to be tackled.

Bibliography

[1] K. Gunn and C. Stock-Williams, "Quantifying the global wave power resource," *Renewable Energy*, vol. 44, pp. 296–304, 2012.

[2] A. F. O. Facao, "Modelling of wave energy conversion," Instituto Superior Tcnico, Universidade Tcnica de Lisboa, 2014.

[3] Teamwork Technology, "Presentation: Ocean energy, how to design a wave energy converter."

[4] J.C.C.Henriques, A. Falcao, R. Gomes, and L.M.C.Gato, "Latching control of an oscillating water column spar-buoy wave energy converter in regular waves," *J. Offshore Mech. Arct. Eng*, vol. 135, Feb. 2013.

[5] J. Engstrm, *Hydrodynamic Mocelling for a Point Absorbing Wave Energy Converter*. ACTAuniversitatis upsaliensis Uppsala, 2011.

[6] P. Signell, "Damped driven oscillations; mechanical resonances," Physnet, 2001.

[7] "Fourier transforms and differential equations," University of Western Australia, Methods of Experimental Physics Lecture 5, 2005.

[8] A. Kooiman, "Adjustments of the gas spring in the symphony wave power device," 2016.

[9] "Resonant wave energy converters, background, technology and test results," CorPower Ocean, sep 2015.

[10] J. Falness, *Ocean waves and oscillating systems*. Cambridge University Press, 2002.

[11] A. Gelb and W. E. V. Velde, *Multiple-Input Describing Functions and Nonlinear System Design*. McGraw Hill, 1968.

[12] T. Lyche and K. Morken, *Spline Methods Draft*. University of Oslo, 2008.

Appendix A

Symphony Time Domain Model

For validating the design of the Symphony it is important to simulate the behaviour of the Symphony. To do this a time domain model is used, calculating all the relevant forces over time, which results in the position of the Symphony.

$$m\ddot{z} = F_{Wave}(t) + F_G + F_{HS}(z) + F_{Gas}(z) + F_{AirTop}(z) + F_{PTO}(\dot{z}, z) + F_D(\dot{z}) + F_{Rad}(\dot{z}) \quad \text{(A.1)}$$

With:

$$\ddot{z} = \ddot{z}(t) = \frac{d\dot{z}(t)}{dt} = \frac{d^2 z(t)}{dt^2}$$

For which:

m: Total mass of the Symphony; this includes total weight and added mass by the surrounding water

- $z(t)$: Vertical position of the floater
- t: Time past in the simulation
- F_{Wave}: Vertical forces due to waves above the floater
- F_G: Gravitational force on the Symphony
- F_{HS}: Hydrostatic force on the top of the floater due to changing position and tide
- F_{Gas}: Gas force due to compression of the air spring in the floater
- F_{AirTop}: Air force top created by air pressure in the top of the floater
- F_{PTO}: PTO force due to pressure difference created by the PTO
- F_D: Drag force due to movement of the Symphony through the water
- F_{Rad}: Radiation force due to moving the floater in an inviscid fluid. This force is too small for this model of the Symphony and is by this reason left out of this report.

All different forces are described in a more detailed description in the following sections.

A.1 Gravitational Force

Due to the Earths gravitational field acting on the Symphony, it experiences a force in the negative vertical direction. The weight can be split in weight of the floater from all components and water added in the membranes. The weight of the water works on the floater and on the cocoon. This force is described in the following equation:

$$F_G = -g \cdot (m_{fl} + \frac{m_w}{2}) \tag{A.2}$$

For which:

- g: Gravitational acceleration $[m/s^2]$.
- m_{fl}: Total weight of the floater $[kg]$.
- m_w: Weight added to the Symphony due to the water inside the membranes $[kg]$.

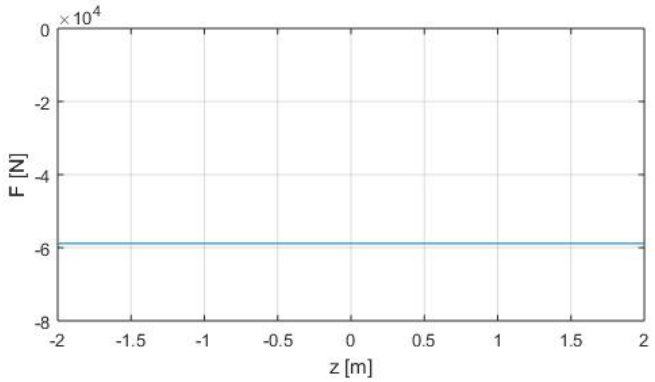

Figure A.1: Example of F_g with final design parameter

A.2 Hydrostatic Force

The hydrostatic force is the force created by the hydrostatic pressure of a fluid on a submerged object. For the floater this force is the difference between the pressure on top times the top area and the bottom pressure times the bottom area. The bottom side of the floater has only two areas that result in an upwards force on the floater. These areas are from the middle of the lower membrane to the inside of the floater and from the inside to the outside of the floater. All other area's react on the cocoon and are not taken into account in this model. The resulting formula is:

$$F_{HS} = \underbrace{-A_{pp}\Big(P_{amb} + \rho g(H_{pp} - z(t))\Big)}_{\text{Top of the floater}} + \underbrace{A_{m_b}\Big(P_{amb} + \rho g(H_{mb} - z(t)/2)\Big)}_{\text{Bottom membrane}} \\ ... + \underbrace{A_b\Big(P_{amb} + \rho g(H_b - z(t)\Big)}_{\text{Bottom of the floater}} \quad \text{(A.3)}$$

With the height from the water surface to the pressure point H_{pp}, bottom H_b and bottom membrane H_{mb} and areas of at that certain height, A_{pp}, A_b and A_{mb}. These parameters can all be described as:

$$H_{pp} = H_{tide} + H_{dclr} + \frac{1}{2}H_{smax} + H_{Lstpp} - H_{off} \qquad A_{pp} = \frac{\pi}{4}D_{out}^2$$
$$H_b = H_{tide} + H_{dclr} + \frac{1}{2}H_{smax} + H_{floater} - H_{off} \qquad A_b = \frac{\pi}{4}(D_{out}^2 - d_{out}^2)$$
$$H_{mb} = H_{tide} + H_{dclr} + \frac{1}{2}H_{smax} + H_{Ltfbm} - H_{off}$$

$$A_{m_b} = \frac{\pi}{4}\big(D_{in_d}^2 - (d_{out} + \frac{D_{in_d} - d_{out}}{2})^2\big) = \frac{\pi}{16}(d_{out} - D_{in_d})(3d_{out} + D_{in_d})$$

For which:

- P_{amb}: Ambient air pressure at sea level $[Pa]$.
- ρ: Density of sea water $[kg/m^3]$.
- H_{tide}: Height of tide $[m]$.
- H_{dclr}: Height of water on top of the floater in top position with no tide $[m]$.
- H_{smax}: Maximum allowed stroke of the floater $[m]$.
- H_{Lstpp}: Height from top of the floater to pressure point of top force $[m]$.
- H_{off}: Offset height from equilibrium position.
- $H_{floater}$: Height from top of the floater to bottom $[m]$.
- H_{Ltfbm}: Height from top of the floater to lower membrane in equilibrium position $[m]$.
- D_{out}: Outer diameter of the floater $[m]$.

- d_{out}: Outer diameter of the membrane containment $[m]$.
- D_{in_d}: Inner diameter of the lower membrane containment $[m]$.
- $z(t)$ and g: are described in earlier sections.

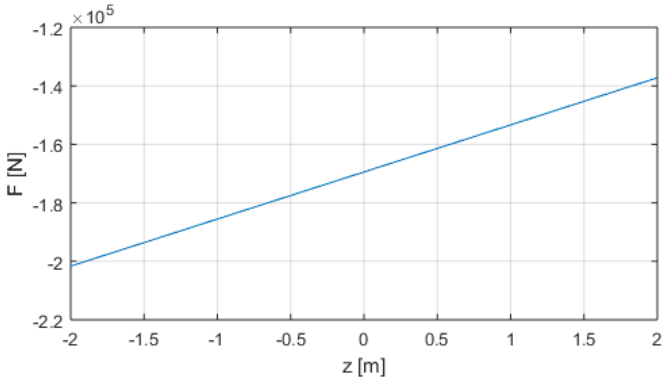

Figure A.2: Example of F_{hs} with final design parameter

A.3 Gas Force

The gas force is the force caused by the pressure in the air spring in the cocoon and water in the membranes. The pressure works due to the water on the membranes. The volume of the gas can be calculated by the volume of gas in equilibrium position minus the difference in volume between top and bottom membranes by the movement. The pressure can be calculated by the ideal gas law. Which can be seen in the following equation:

$$F_{Gas}(z) = (A_{m_b} - A_{m_u}(z)) \cdot \underbrace{V_{gas}(z) \cdot \left(\frac{V_{gaseq}}{P_{gaseq}}\right)^{\gamma}}_{\text{Ideal gas law}} \tag{A.4}$$

With:

$$A_{m_u}(z) = \frac{\pi}{16}(d_{out} - D_{inup}(z))(3d_{out} + D_{inup}(z))$$
$$V_{gas}(z) = V_{gaseq} + \frac{\pi}{4}\int_0^{z(t)} d_{out}^2 - D_{inup}^2(z)\, dz$$

Where:

- $A_{m_u}(z)$: Area from the middle of the membrane to outside of the floater $[m^2]$.
- V_{gas}: Volume of gas in the air spring $[m^3]$.
- V_{gaseq}: Volume of gas in equilibrium position $[m^3]$.
- P_{gaseq}: Pressure of gas in equilibrium position $[Pa]$.
- γ: Adiabatic constant of gas $[-]$.
- $D_{inup}(z)$: Diameter of the inner side of the top membrane $[m]$.
- A_{m_b}, d_{out}, $z(t)$, D_{out}: are described in section A.2.

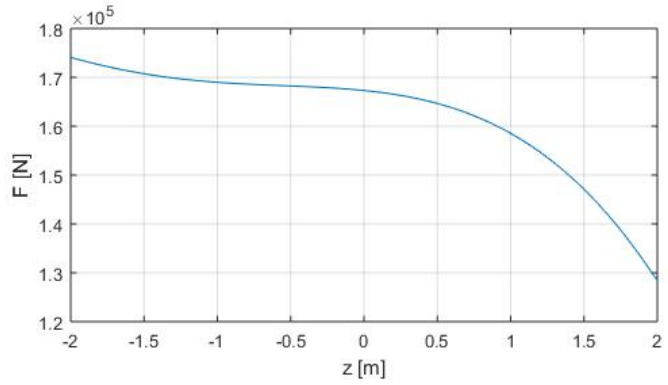

Figure A.3: Example of F_{gas} with final design parameter

A.4 Air Force Top

In the top compartment of the Symphony air is trapped. The pressure of the trapped air creates a downward force on the membrane. But the volume of the compartment changes when the membranes are moving up and down. The pressure multiplied by the area gives the force on the floater. This can be calculated by the following formula:

$$F_{AirTop} = V_{ac} P_{amb} \left(\frac{V_{top}}{V_{top} + \frac{\pi}{4}\, d_{out}^2\, (z - z_{0vac}) - \Delta V_{gas}(z)} \right)^{\gamma} \cdot \left(\frac{\pi}{4} d_{out}^2 - A_{m_u}(z) \right) \tag{A.5}$$

With:

$$\Delta V_{gas}(z) = \frac{\pi}{4} \int_0^z d_{out}^2 - D_{inup}^2(z)\; dz$$

Where:

- V_{ac}: Factor of initial pressure precision $[-]$.
- V_{top}: Volume of gas on top of the membrane in equilibrium position $[m^3]$.
- z_{0vac}: z value at which the initial pressure is reached, in this case P_{atm} $[m]$.
- $\Delta V_{gas}(z)$: Volume of membranes that are coming up $[m^3]$.
- P_{amb}, d_{out}, $z(t)$, γ, A_{m_u} and D_{inup}: are described in earlier sections A.2 and A.3.

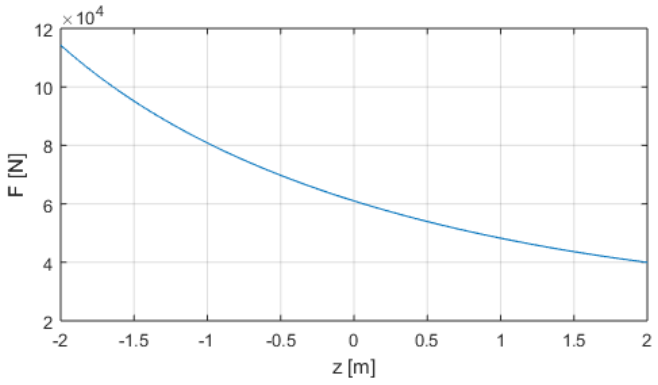

Figure A.4: Example of F_{AirTop} with final design parameter

A.5 PTO Force

By moving the floater up and down water is flowing by the membranes through the turbine. By adding resistance at the turbine rotation, the PTO force is created. This resistance is directly coupled to the power output of the Symphony and is used to control the motion of the Symphony. The added pressure is calculated by multiplying the output of the control system times the velocity. The input of the control system is calculated by the total kinetic and potential energy minus the maximum potential energy in the system. The velocity is used because the direction of the velocity is the desired path the Symphony has to follow. The resulting force can be calculated by:

$$F_{PTO} = (A_{m_b} - A_{m_u}(z)) \cdot \Delta P_{con} \tag{A.6}$$

With:

$$\Delta P_{con} = K_{con} \cdot \underbrace{\left(\frac{1}{2} m \dot{z}^2 + \int_0^z k_s(z) z \, dz - \int_0^{z_{max}} k_s(z) z \, dz\right)}_{\text{Energy error}} \qquad \text{for } |\Delta P_{con}| \leq \Delta P_{max}$$

*NOTE: If the control pressure is larger than the possible output of the turbine the output pressure ΔP_{con} is kept at the its maximum value ΔP_{max} in the corresponding sign.
For which:

- ΔP_{con}: Output pressure difference from the generator $[Pa]$.
- ΔP_{max}: Maximum output pressure difference created by the generator $[Pa]$.
- K_{con}: Control system (will be specified in the next section) $[-]$.
- $k_s(z)$: Stiffness of the Symphony $[N/m]$.
- z_{max}: Desired stroke length for the control system $[m]$.
- A_{m_b}, A_{m_u}, $z(t)$ and m: are described in earlier sections A.2 and A.3.

Control system

For this research a simple P-controller has been used. This means the energy error is only multiplied by a single factor. It can be assumed that PI-controller, PID-controller or even a feed forward PID-controller could beneficed the system. Later research should give the best solution. These control parameters are given by:

- K_p: Proportional gain of the control system $[-]$.
- K_i: Integrational gain of the control system $[-]$.
- K_d: Differential gain of the control system $[-]$.

Power output

From the pressure difference created by the PTO, energy is extracted from the system. This energy gives a power output from the turbine, which results in a torque and angular velocity. Which is on its side coupled to the torque on the generator which results in actual power output from the Symphony. The following equations have been used to calculate the parameters:

$$P = \Delta P_{con} \dot{V} \tag{A.7a}$$

$$\omega_t = 2\pi \frac{\dot{V}}{V_t} \tag{A.7b}$$

$$T_t = \frac{P_t}{\omega_t} \tag{A.7c}$$

$$T_g = T_t - \dot{\omega_t} I_t \tag{A.7d}$$

For which:

- P: Power output of the turbine $[W]$.
- $\dot{V}$: Volume speed of water from the membranes trough the turbine $[m^3/s]$.
- ω_t: Angular speed of the turbine $[rad/s]$.
- V_t: Volume of the turbine per cycle $[m^3]$.
- T_t: Torque on the turbine $[Nm]$.
- T_g: Torque on the generator $[Nm]$.
- I_t: Inertia of the turbine $[kgm^2]$.

A.6 Drag Force

The drag force due to movement of a submersed system through water can be calculated by the formula $F_D = 1/2\rho A\dot{z}^2 C_D$ [5]. This force is always opposite to the movement and since the top and bottom surface of the Symphony differ a lot both drag coefficients are different. These are defined as: C_{Dup} and C_{Ddw}. Which were found in earlier researches. The formula for the drag force on the Symphony is given by:

$$F_D = \begin{cases} -\frac{1}{2}\rho\ A_{pp}\ \dot{z}(t)|\dot{z}(t)|\ C_{Ddw} & \text{if } \dot{z}(t) < 0, \\ -\frac{1}{2}\rho\ A_{pp}\ \dot{z}(t)|\dot{z}(t)|\ C_{Dup} & \text{if } \dot{z}(t) > 0. \end{cases}$$

For which:

- C_{Ddw}: Downwards drag coefficient $[-]$.
- C_{Ddup}: Upwards drag coefficient $[-]$.
- ρ, A_{pp}, $z(t)$: are described in earlier sections A.2 and A.3.

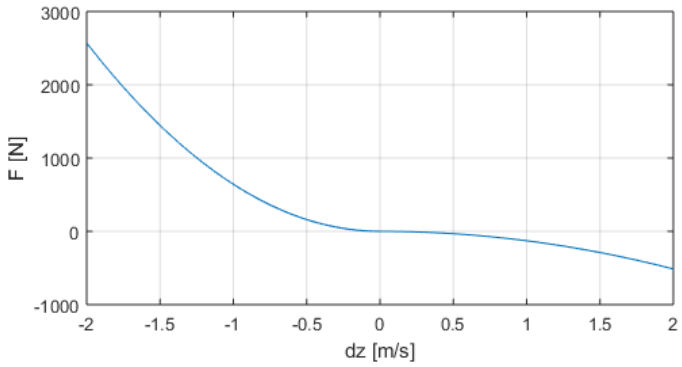

Figure A.5: Example of F_{drag} with final design parameter

A.7 Wave Force

The time domain model can be reviewed by two different sea states: the Monochromatic sea state in which the sea is a single sinusoid wave and the a Bretschneider sea state. Both sea states can be used for different purposes. While the monochromatic sea state gives the best information on the behaviour of the Symphony, the Bretschneider gives a more realistic view on the behaviour in the sea [5].

$$
\begin{aligned}
F_{wave} &= \sum_{i=1}^{N}(F_{w1} + F_{w2} + F_{w3})sin(\frac{2\pi}{T_e}t) \\
F_{w1} &= -\rho g A_i K_{p1} \cdot A_{pp} \cdot \frac{sin(k_i D_{out}/2)}{k_i D_{out}/2} \\
F_{w2} &= \quad \rho g A_i K_{p2} \cdot A_{pp} \cdot \frac{sin(k_i D_{out}/2)}{k_i D_{out}/2} \\
F_{w3} &= -\rho g A_i K_{p2} \cdot \frac{\pi}{4} D_{in_d}^2 \cdot \frac{sin(k_i D_{in_d}/2)}{k_i D_{in_d}/2} \\
K_{p1} &= \frac{cosh(k_i \cdot (h_{sea} - H_{pp}))}{cosh(k_i \cdot h_{sea})} \\
K_{p2} &= \frac{cosh(k_i \cdot (h_{sea} - H_{mb}))}{cosh(k_i \cdot h_{sea})}
\end{aligned}
$$

For which:

- N: Last wave component used for the simulation $[-]$.
- $F_{w1,2,3}$: Wave force working on top and bottom of the Symphony $[N]$.
- T_e: Energy period of the wave $[s^{-1}]$.
- A_i: The (complex) amplitude of the wave $[m]$.
- $K_{p1,p2}$: The pressure factors that accounts for how much the wave dynamic pressure decreases with depth $[-]$.
- k_i: Wave number of the wave component i $[rad/m]$.
- h_{sea}: Total water depth $[m]$.
- ρ, g, A_{pp}, D_{out}, D_{in_d} and H_{pp}: are described in section A.2.

A.7.1 Monochromatic

The monochromatic wave mode is made so the Symphony can be simulated in a specific type of wave. The only two parameters needed for a continues sinusoid are the amplitude A_i and period time T_e. By giving this the a monochromatic sea state can be simulated in the time domain.

A.7.2 Bretschneider

This spectrum is used to analyse the Symphony in a more realistic sea state. The calculation of a force in the Bretschneider spectrum is a bit more complex. It gives the variance spectral density per frequency. The Bretschneider spectrum can be given by the significant wave length H_s and the peak frequency T_p. From these two values the complex amplitude A_i and energy period T_e can be calculated. When using a random factor times the probability of a wave, a random sea state can be simulated that is realistic for the sea at a certain position. The Bretschneider spectrum is a single peak spectrum given by [5]:

$$S(\omega) = 5\frac{\omega_p^4}{\omega^5}\frac{H_s^2}{16}e^{-\frac{5}{4}(\frac{\omega_p}{\omega})^4} \tag{A.8}$$

With the spectral moment of order i is given by [5]:

$$m_i = \int_0^\infty \omega^i S(\omega) d\omega \tag{A.9}$$

For which:

- $S(\omega)$: Variance spectral density $[\frac{m^2 s}{rad}]$.
- $\omega_p = \frac{2\pi}{T_p}$: Peak frequency of the spectrum $[s^{-1}]$.
- ω: Frequency spectrum $[s^{-1}]$.
- H_s: Significant wave height given by $H_s = 4\sqrt{m_0}$ and is representing the mean of the highest third of the possible waves $[m]$ [5].
- T_c: Crest period given by $T_c = 2\pi\sqrt{\frac{m_2}{m_4}}$. This period gives the average time between successive crests $[s]$.
- T_z: Zero crossing period by $T_z = 2\pi\sqrt{\frac{m_0}{m_2}}$. This period gives the average time between zero up-crossings $[s]$.
- T_e: Energy period by $T_E = 2\pi\frac{m_{-1}}{m_0}$. This period determines the power level of the spectrum $[s]$ [5].
- $Bandwidth$: Broadness factor by $Bandwidth = \sqrt{1 - \frac{m_2^2}{m_0 m_4}} = \sqrt{1 - \left(\frac{T_c}{T_z}\right)^2}$. This period gives the average time between zero up-crossings $[-]$.

Appendix B

Geometry calculation

B.1 Calculation of the inner wall

The floater of the Symphony spring forces concern four major forces: gravity force F_g, hydrostatic force F_{HS}, pressure force created by air on top of the membrane F_{AirTop} and at last the force from the gas spring F_{Gas}. The total of these spring forces is called F_{res} and can be calculated in:

$$F_{res}(z) = F_G + F_{HS}(z) + F_{AirTop}(z) + F_{Gas}(z) \tag{B.1}$$

All forces are individual described in Appendix A and are for readability not repeated. In chapter4 the most ideal profile of F_{res} is designed. It can be seen that all parameters are known except D_{inup}, which is the inner diameter of the membrane containment. By the following procedure the diameter of the inner wall of the membrane containment can be calculated. The start position is at the equilibrium position at which the diameter of the wall is calculated. From this position the diameter is upwards and downwards calculated step by step. The height of each step Δz gives accuracy of the design. It is important to keep this as low as possible but not lower than the accuracy of production. By the following procedure in top and bottom direction the full geometry can be estimated.

B.2 Procedure

Step 1: Use equilibrium conditions P_{gaseq} and V_{gaseq} at $z = 0$

Step 2: Calculate $F_{AirTop}(z) + F_{Gas}(z) = F_{res}(z) - F_G - F_{HS}(z)$

Step 3: Solve D_{inup} with $F_{AirTop}(z) + F_{Gas}(z)$

Step 4: Take D_{inup} over a length Δz

Step 5: Calculate conditions $V_{gas}(z + \Delta z)$ and $P_{gas}(z + \Delta z)$

Step 6: Return to step 2 and use $z = z + \Delta z$, continue until $z = z_{stroke}$

Step 7: Follow same procedure with in step 6 $z = z - \Delta z$ until $z = -z_{stroke}$

B.3 Geometry of the final design

To give a physical explanation of the procedure in Fig. the final design of the spring forces can be seen and its corresponding diameter.

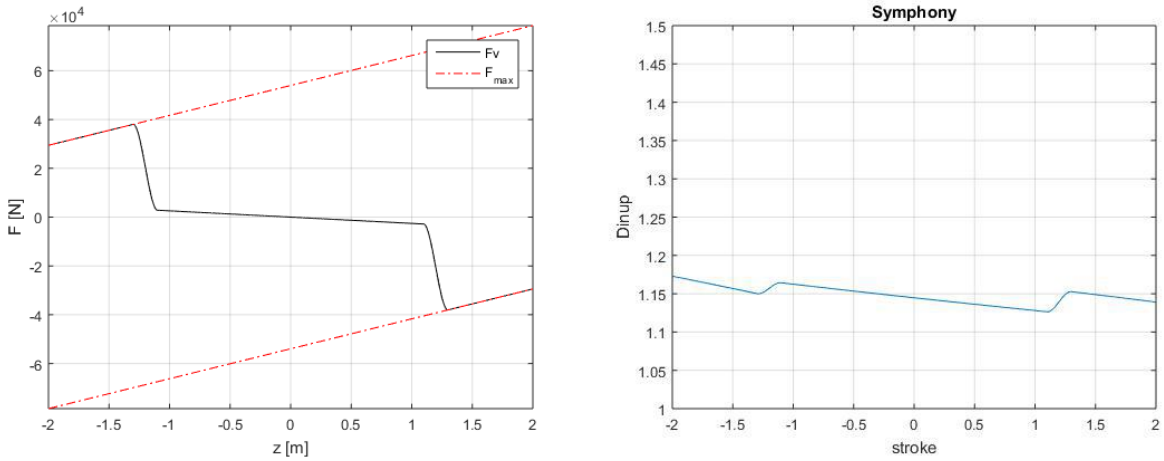

(a) Spring force F_{res} during stroke

(b) Wall diameter D_{inup} during stroke

Figure B.1: Wall diameter D_{inup} with corresponding resulting spring forces F_{res}

Appendix C

Final Design

Geometrical parameters			
k	2574	$[N/m]$	Linear spring stiffness
z_{lin}	1.2	$[m]$	Length of linear spring without S-curve
z_{max}	2.0	$[m]$	Maximum stroke
S-curve	0.2	$[m]$	Length of S-curve
$F_b(-z_{max})$	3.0	$[kN]$	Buoyancy with floater in bottom position
$F_b(z_{max})$	8.0	$[kN]$	Buoyancy with floater in top position
F_{cmax}	3.0	$[kN]$	Gravity for of the anchor
Operational parameters			
P	1830	$[W]$	Average power
E	16.0	$[Mwh]$	Average annual energy
H_s at $max(P_k)$	4.5-5	$[m]$	Significant wave height for maximum power production
T_e at $max(P_k)$	7-8	$[s]$	Energy period time for maximum power production
$max(P_k)$	5465	$[W]$	Max. power output
$\frac{t_{down}}{t_{total}}$	5.4	$[\%]$	Downtime
$P_{gas}(z_{max})$	10.8	$[bar]$	Pressure in gas spring with floater in top position
$P_{gas}(-z_{max})$	21.4	$[bar]$	Pressure in gas spring with floater in bottom position
$max(\omega)$	350.5	$[RPM]$	Maximum rotational speed normal operation conditions

Table C.1: Performance of the final spring design

Appendix D

Weather conditions Leixous

The design of the spring force profile of the symphony is optimized for the sea states in Leixous, Portugal. These sea states are given in a scatter diagram, see table D.1. This diagram gives information about the probability of appearance of a certain significant wave height H_s with a certain energy period T_e.

P[Hs vs Te](%)	=< 0.5m	0.5-1m	1-1.5m	1.5-2m	2-2.5m	2.5-3m	3-3.5m	3.5-4m	4-4.5m	4.5-5m	5-6m	6-7m	7-8m	8-9m	9-10m	10-12m	P[Te]
=< 4 s																	0,0
4 - 5 s		0,07	0,03														0,1
5 - 6 s		2,41	4,53	1,73	0,23												8,9
6 - 7 s		2,21	10,14	7,04	2,57	0,59	0,03										22,6
7 - 8 s		0,33	5,8	7,22	3,77	2,01	0,99	0,18	0,01								20,3
8 - 9 s		0,01	2,03	5,39	4,28	2,82	1,74	1,05	0,53	0,11							18,0
9 - 10 s			0,38	2,29	3,78	2,52	1,77	1,43	0,83	0,6	0,36						14,0
10 - 11 s			0,05	0,34	1,77	1,88	1,35	1,12	0,75	0,7	0,83	0,17	0,03				9,0
11 - 12 s			0,01	0,12	0,41	0,71	0,52	0,7	0,51	0,55	0,61	0,34	0,07	0,01			4,6
12 - 13 s					0,05	0,13	0,23	0,16	0,22	0,29	0,33	0,18	0,13	0,05	0,03		1,8
13 - 14 s						0,01	0,05	0,06	0,08	0,1	0,07	0,06	0,05	0,09	0,05	0,01	0,6
14 - 15 s									0,01	0,01	0,03	0,05	0,02	0,03		0,01	0,2
15 - 16 s															0,01		0,0
16 - 17 s															0,01		0,0
17 - 18 s																	0,0
18 - 19 s																	0,0
19 - 20 s																	0,0
20 - 21 s																	0,0
21 - 22 s																	0,0
> 22 s																	0,0
P[Hs] (%)	0,0	5,0	23,0	24,1	16,9	10,7	6,7	4,7	2,9	2,4	2,2	0,8	0,3	0,2	0,1	0,0	100

Table D.1: Scatter diagram of Leixous used for this project

F. Extracts of the preliminary turbine design exercise for the Symphony:

Jarno de Jong:
"Design of Power Take Off Turbine for the Symphony Wave Energy Converter"

Alkmaar, Netherlands: MSc thesis Aeronautical Engineering, Hogeschool INHOLLAND Delft HBO., 2015

3 TURBINES

Chapter two introduced the reader into the field of wave energy conversion and explained the working of the Symphony. It was shown how the Symphony uses the pressure differential under a wave to generate an oscillating water flow. A turbine is a device designed to extract energy from a fluid flow. The fluid flowing through a turbine can be any liquid or a gas, but for now the working medium is assumed to be water. Water enters the turbine through the inlet and interacts with the vanes of the runner. This interaction transfers energy from the fluid to the runner which makes the runner spin. The fluid leaves the turbine through the outlet. The runner is attached on an axis where the work, generated by a turbine, can be transferred to another device. This device can be used e.g. for generating electricity or powering other rotating equipment (e.g. a pump or an industrial process). The first turbine-like constructions were waterwheels, built by the Romans around 70 B.C.

This chapter introduces the reader to the basics of turbine design and serves as a guidebook for future reference. This means that not all information is directly related to the main research question or one of the sub questions. When designing a turbine, the pressure difference over the turbine and the volume flow are the most important design input characteristics. Because the flow over the turbine is oscillating, the pressure drop and volume flow are also oscillating. For the design of the turbine, the maximum volume flow and pressure difference are assumed to be constant for this phase of selecting the most suitable turbine for our type of flow. More information of selection criteria and decisions in the selection process can be found in chapter four.

This chapter starts with the introduction of velocity diagrams (3.1). These diagrams show how a fluid flow is altered during the interaction with the components of a turbine. Knowing how to read velocity diagrams is necessary before being able to comprehend several sections of this chapter. The momentum theory (section 3.2) uses Newton's second law of motion to estimate the power produced in a turbine. During the transfer of power from the fluid to the output shaft of the runner, some losses occur (i.e. the efficiency is lower than 100%). The total efficiency is divided into several sub-efficiencies, which is further discussed in section 3.3. The working medium is, as stated in chapter 2, assumed to be water. Water can be assumed to be incompressible. A small statement about the subject of fluid compressibility can be found in section 3.4. If during the design process of a turbine tests are going to be performed using scale models, scaling rules must be followed. If the fluid properties would not be adjusted to the scaled situation, tests results would be useless. Dimensionless numbers can be used to find the right flow for test operations (section 3.5). A very common problem in operating turbines is cavitation. Cavitation is the imploding of small vapour bubbles in a flow that form when the pressure in a flow reaches lower values than the vapour pressure of a liquid. More information about cavitation can be found in section 3.6. Up to this point in the chapter, no distinction is made between several types of turbines. Section 3.7 changes this by introducing the reader to impulse and reaction turbines. These turbines are elaborated in section 3.8 (impulse turbines) and section 3.9 (reaction turbines). Section 3.10 discusses the possibility to use turbine designs which are usually only used for pumps. In the end, turbines and pumps are the same devices with the only difference that turbines extract energy from fluid flows and pumps add energy to fluid flows. Section 3.11 concludes this chapter by making a more in depth comparison between pumps and turbines.

3.1 VELOCITY DIAGRAM

Velocity diagrams are a common way to illustrate the angles and velocities of a fluid passing a compressor or turbine stage. It is possible to estimate the required or generated power by using basic goniometric calculations. Each turbine stage consists of a nozzle, or a row of nozzle blades, and rotor blades.

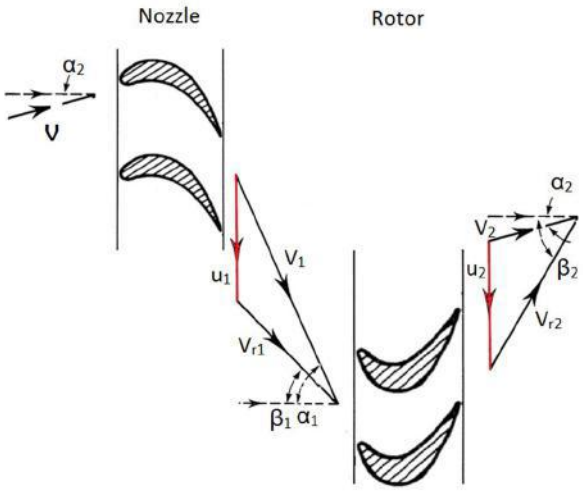

Figure 13: Velocity diagram for a turbine (40)

Figure 13 shows the velocity diagram for a turbine. The flow enters the turbine at the nozzle. The nozzle is fixed to the casing of the turbine and changes the direction and velocity of the flow so the rotor is able to extract more energy from the flow. The nozzle increases the efficiency of the turbine. The rotor is fixed on the axis of the turbine and is therefore able to rotate. The rotor rotates with velocity U. The rotor changes the magnitude and direction of the velocity of the flow. The way energy is extracted from the flow depends on whether the turbine is an impulse or reaction turbine. The difference between these turbines will be discussed in paragraph 3.7.

Two velocities are distinguished in the diagram: The absolute velocity (V) and the relative velocity (V_r). The absolute velocity is the velocity of a fluid particle in respect to the open world. The relative velocity is the velocity someone would observe when looking from the point of view of a rotor blade. The angle α is the angle between the shaft axis of the turbine and the absolute velocity of the fluid. The angle between the shaft axis and the relative velocity of the fluid is denoted by β. These triangles give the relationships between the airflow before and after the turbine. The momentum theory uses Newton's second law of motion to determine the force which the fluid exerts on the blade.

$$F = ma$$

In other words: The acceleration in a specific direction times the mass of the fluid, is equal to the force exerted on a blade.

3.2 MOMENTUM THEORY

A motion of a fluid can be decomposed to three velocity components: Tangential, axial and radial (Figure 14). The change in each of these directions relates to the force delivered to the runner. A change in tangential velocity (V_u) influences the rotational velocity of the turbine. The tangential velocity of a flow is often referred to as swirl. Thrust is delivered by change in axial velocity and a change in radial velocity causes bending of the shaft. The radial turbine, which will be discussed later, generates power by decreasing the radial velocity through the runner.

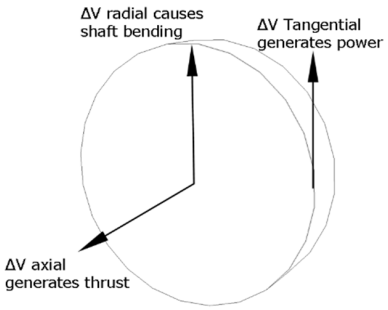

Figure 14: Turbine velocities

As stated in the previous section, Newton's second law of motion can be used to estimate the generated power by a turbine. The mass flow is assumed to be constant, because otherwise there would be a mass accumulation somewhere in the turbine. This means that the force exerted by a fluid in any direction is related linear the change in velocity. The change in momentum in the tangential direction is:

$$F = \dot{m}(V_{u1} - V_{u2})$$

The torque applied by the fluid to the runner of a turbine is the change in angular momentum which is the result of multiplying the change in momentum by the radius of the runner:

$$\tau = \dot{m}(V_{u1}r_1 - V_{u2}r_2)$$

Power is defined as:

$$P = \tau\,\omega$$

Where $\omega = \frac{2\pi N}{60}$ is the angular velocity of the runner in rad/s and N is the rotational velocity of the runner in rotations per minute. By substituting the formula for torque, power can be calculated as:

$$P = \dot{m}\frac{2\pi N}{60}(V_{u1}r_1 - V_{u2}r_2)$$

The terms $\frac{2\pi N}{60}r_1$ and $\frac{2\pi N}{60}r_2$ are the rotational velocities at inlet (U_1) and exit (U_2). The final formula obtained is:

$$P = \dot{m}(V_{u1}U_1 - V_{u2}U_2)$$

This formula is derived by Leonhard Euler and is known as the Euler turbine equation. The formula shows that the generated power is equal to change in tangential momentum of the fluid.

Power generated in three components

Note that the Euler turbine equation only accounts for the change in velocity for the tangential direction. As stated earlier in this section, the velocity is divided into three directions. This also means that the fluid is able to exert a force on the runner in three directions. Any change in the axial velocity of the fluid results in a force parallel to the runners' axis. Therefore, any change in axial velocity does not contribute to the angular momentum on the blades. The change in relative velocity can be expressed in terms of tangential and radial velocity.

Review the velocity triangles in Figure 13. The cosine rule gives:

$$V_{r1}^2 = V_1^2 + V_{U1}^2 - 2V_{u1}V_1 \cos\gamma_1$$

And:

$$V_{r2}^2 = V_2^2 + V_{u2}^2 - 2V_{u2}V_2 \cos\gamma_2$$

Where $\gamma = 90 - \alpha$. The tangential velocity of the fluid for inlet and outlet is: $V_u = V\cos\gamma$. This can be substituted into the formula above when both sides are multiplied by U.

For inlet and outlet:

$$UV\ \cos\alpha = V_u U = \frac{V^2 + V_u^2 - V_r^2}{2}$$

If this formula is filled into the Euler equation for power, the following formula is found:

$$P = \dot{m}\frac{(V_1^2 + U_1^2 - V_{r1}^2) - (V_2^2 + U_2^2 - V_{r2}^2)}{2}$$

Rearranging the terms gives:

$$P = \dot{m}\frac{(V_1^2 - V_2^2) + (U_1^2 - U_2^2) + (V_{r2}^2 - V_{r1}^2)}{2}$$

The formula above shows the contribution to power generation of each term. Three terms can be distinguished contributing to the total work done. The difference between an impulse turbine and reaction turbine is explained later, but a small distinction can already be made:

$(V_1^2 - V_2^2)$ is the change in absolute velocity. The impulse turbine is totally dependent on this term as the other terms are zero.

$(u_1^2 - u_2^2)$ is the change in tangential velocity and will be present in radial flow turbines only.

$(V_{r2}^2 - V_{r1}^2)$ is the relative acceleration in the turbine. This term indicates that the fluid is accelerated in the rotor, which is a characteristic for a reaction turbine.

The only turbine where all three terms are present is the Francis turbine, which is a radial flow, impulse-reaction turbine. These types of turbines will be discussed later in this report.

3.3 TURBINE EFFICIENCY

In reality, not all available energy in the fluid can be converted to useful work at the output shaft. Several losses must be accounted for. Losses can be grouped into several groups. This gives a clear overview where a turbine loses any energy. The efficiency of the total system is the product of these efficiency groups.

Hydraulic efficiency

A turbine extracts power from a water flow. This means that the water flow enters the turbine with a certain amount of energy and leaves the turbine with a lower amount of energy (i.e. lower velocity or pressure).

$$\eta_H = \frac{P_{turbine}}{\rho QgH}$$

Volumetric efficiency

Not all water flowing through a turbine delivers work to the runner. Some water is wasted due to (blade tip) leakages. The volumetric efficiency is the ratio between the water that actually delivers work to the runner and the total volume flow that flows through the turbine.

$$\eta_V = \frac{Volumeflowdeliveringenergyto the turbine}{Total volumeflowfromsource} = \frac{Q - \Delta Q}{Q}$$

Volumetric efficiency is usually between 0.96 and 1, but in many cases neglected.

Mechanical efficiency

In a turbine, a lot of parts are rotating, often at high velocities. Some energy is lost in parts like a gearbox or bearings. The mechanical energy is defined as the ratio between the power produced by the turbine blades and the power available at the turbine shaft.

$$\eta_m = \frac{P_{shaft}}{P_{blades}}$$

The overall efficiency can now be calculated as:

$$\eta_{o=}\eta_H\ \eta_V\ \eta_m$$

3.4 INCOMPRESSIBLE FLOW

The main difference between a gas turbine and water turbine is that for a water turbine the flow can be considered incompressible. This section proves that compressibility effects can be neglected for the power take-off turbine of the Symphony. This assumption can be justified by using the bulk modulus E.

$$E = \rho\frac{\delta P}{\delta \rho}$$

Where δP denotes the change is pressure and δρ the change is density. Hence:

$$\delta\rho = \rho\frac{\delta P}{E}$$

The bulk modulus for water is 2.2 x 10^9 Pa and for air 1.42 x 10^5 Pa. The maximum operating pressure in the Symphony is 25 bar. For air, a pressure change of 25 bar (25 x 10^5 Pa) means a density change of a factor $\frac{25}{E} = \frac{25\times10^5}{1.42\times10^5} = 17.60 \approx 1760\%$. The same pressure change for water means: $\frac{25}{E} = \frac{25\times10^5}{2.2\times10^9} = 0.0011 \approx 0.11\%$ The pressure drop over the turbine is at maximum only 2.5 bar. So the influence of compressibility will be only 1/10^{th} of 0.11% for water. The density change for water is small enough to be neglected. The change in density for air is of great influence on the performance of, for example, a gas turbine.

3.5 TESTING AND MODELLING

Testing and modelling of turbines is a very complex task. One problem which rises during testing a turbine is that the results depend on the size and rotational velocity of the turbine. To be able to compare different turbines, dimensionless variables are introduced which give results independent to size and velocity. The first step in defining these dimensionless variables is to check which variables influence flow, pressure and power. The formulas to calculate flow is the runners' area, multiplied by the axial velocity. The axial velocity is expressed as the tangential velocity times factor a.

$$Q = \frac{\pi}{4} D^2 \cdot V_u \cdot a$$

The formula for pressure difference is (section 3.10):

$$h = \frac{V_{u2} u_2 - V_{u1} u_1}{g}$$

And for power:

$$P = \rho Q (V_{u1} U_1 - V_{u2} U_2)$$

Where V_u and U are for now assumed to be equal (runner velocity = fluid velocity) and can be calculated as: $\frac{\pi ND}{60}$. The three variables are depending on diameter D and rotational velocity N as follow:

$$Q: f(N, D^3)$$

$$P: f(N^3, D^5, \rho)$$

$$h: f(N^2, D^2, \rho)$$

Power and pressure difference are also dependent on density, which may be variable for non-water turbines. By dividing each variable by its depending factors, a non-dimensional coefficient is acquired. In other words: The dimensionless coefficient is the amount of flow, power or pressure change per length unit diameter per rotation.

Flow coefficient

$$C_f = \frac{Q}{ND^3}$$

Power coefficient

$$C_p = \frac{P}{\rho N^3 D^5}$$

Head coefficient

The head coefficient uses the amount of input energy per unit mass instead of the pressure difference only.

$$C_h = \frac{gh}{N^2 D^2}$$

Using the dimensionless variables above, two other variables can be derived. These variables are used to compare testing results independent to rotational velocity (specific speed) or diameter (specific diameter). The flow and head coefficient are used for this purpose

Specific speed

The specific speed for turbines is the rotational speed where 1 kW power is generated per meter head input pressure. To find the specific head for turbines, the power coefficient and head coefficient are divided by each other so that the diameter is cancelled out of the equation:

$$C_p^2 = \frac{P^2}{\rho^2 N^6 D^{10}}$$

$$C_h^5 = \frac{(gh)^5}{N^{10} D^{10}}$$

$$\frac{C_p^2}{C_h^5} = \frac{P^2}{\rho^2 N^6 D^{10}} * \frac{N^{10} D^{10}}{(gh)^5} = \frac{P^2 N^4}{\rho^2 (gh)^5}$$

$$N_s = \frac{N\sqrt{P}}{\rho^{\frac{1}{2}} (gh)^{\frac{5}{4}}}$$

Because the density of water does not change with pressure and the gravitational velocity is constant around the world, the specific diameter is also given as $N_s = \frac{N\sqrt{P}}{h^{\frac{5}{4}}}$. Power is often given is kW. However, this is not a global standard and the units are often given at figures dealing with specific speed. The specific speed for pumps is not based on power, but on flow. The specific speed for turbines indicate the rotational speed where 1 m^3/s flow is pumped with a head rise of 1 meter water column. For pumps, the flow coefficient is divided by the head coefficient so that the diameter is cancelled out of the equation:

$$C_f^2 = \frac{Q^2}{N^2 D^6}$$

$$C_h^3 = \frac{(gh)^3}{N^6 D^6}$$

$$\frac{C_f^2}{C_h^3} = \frac{Q^2}{N^2 D^6} \frac{N^6 D^6}{(gh)^3} = \frac{Q^2 N^4}{(gh)^3}$$

$$N_s = \frac{N\sqrt{Q}}{(gh)^{\frac{3}{4}}}$$

Specific diameter

For pumps, the specific diameter is sometimes used during testing. The specific diameter indicates the diameter required to deliver one meter head rise for one m^3 flow rate. The specific diameter is found the same way as the specific speed for pumps, but now the rotational velocity is cancelled out of the equation.

$$C_f^2 = \frac{Q^2}{N^2 D^6}$$

$$C_h = \frac{gh}{N^2 D^2}$$

$$\frac{C_h}{C_f^2} = \frac{N^2 D^6}{Q^2} \frac{gh}{N^2 D^2} = \frac{D^4 gh}{Q^2}$$

$$D_s = \frac{D(gh)^{\frac{1}{4}}}{\sqrt{Q}}$$

When testing a smaller model of a design, all dimensionless variables must be equal to the original situation which is simulated. The specific speed is especially interesting when selecting the type of turbine for a given input flow and output flow. If the power output is kept as a constant, the specific speed will increase if head decreases. This relationship is very useful for the selection of the most efficient type of turbine for the specific situation. It must be emphasised that this is only a theoretical approach and results must be tested and verified. However, this approach is accurate enough for the conceptual design phase.

3.6 CAVITATION

Cavitation is a problem when designing hydro turbines. Cavitation is a phenomenon that occurs when the pressure in a liquid drops below the vapour pressure. Small vapour bubbles start to appear. These vapour bubbles implode when transferred to a higher pressure region. A turbine runner experiences very high dynamic pressures on its surface at very high frequencies. Cavitation can cause severe damage to the surface of the turbine blades or casing (Figure 15). Cavitation usually occurs at reaction turbines only because impulse turbines function mainly with open water jets where a pressure build up is not possible. The most likely location for cavitation to occur is at runner exit or draft tube inlet where a water pressures beneath atmospheric pressures may occur. The most important cavitation characteristic is the Thoma cavitation coefficient σ (2).

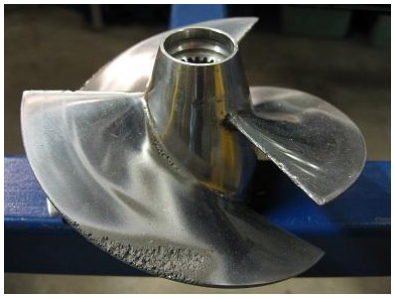

Figure 15: Damage on a watercraft propeller due to cavitation (41)

$$\sigma = \frac{H_a - H_r - z}{h}$$

Where H_a is the atmospheric pressure in meter head, H_r is the vapour pressure in meter head, z is the vertical distance between the turbine runner exit and water surface and h is the total change in pressure over the turbine. The operational limits for cavitation can be found by reducing the suction head under constant operating conditions. By measuring the cavitation up to an acceptable amount, operational limits can be found. The critical Thoma number is identical for turbines which are geometrical similar at maximum efficiency. The fact that the specific speed is related to the shape of the turbine indicates that there is a correlation between the Thoma number and the specific speed. Experiments performed by Moody and Zowski lead to the following empirical correlations between the specific speed and critical Thoma number for the Francis and Kaplan turbine:

Francis turbine:

$$\sigma_c = 0.006 + 0.55\left(\frac{N_s}{444.6}\right)^{1.8}$$

Kaplan turbine:

$$\sigma_c = 0.1 + 0.3\left(\frac{N_s}{444.6}\right)^{2.5}$$

For cavitation to occur, the water pressure has to drop below the vapour pressure. The operating pressure of the Symphony oscillates between around 15 bar. This makes it very unlikely that cavitation will occur as the vapour pressure of water at temperatures of 20-40 degrees Celsius is well under 1 bar.

3.7 REACTION AND IMPULSE TURBINE

Up to this point, no distinction was made between any type of turbine. However, turbines can be subdivided into two classes, based on the working of the runner. An impulse turbine uses the kinetic energy in the flow to produce power. A reaction turbine accelerates the fluid in the rotor by converting potential energy to kinetic energy. This are the two main turbine types. More types of turbines can be distinguished, but the fundamental principle the turbine is based on is always the impulse turbine, reaction turbine or a combination between these turbines. A small note must be made on the classification of impulse and reaction turbines. A turbine can be 100% impulse. A 100% reaction turbine does not exist. In every reaction turbine, a certain amount of potential energy is converted to kinetic energy in the nozzle before the rotor. The ratio between the energy converted in the nozzle and the energy converted in the total turbine is called the degree of reaction.

In general, the impulse turbine is a turbine where the flow has a high inlet velocity. Impulse turbines operate therefore with high rotational speeds. Energy sources for the impulse turbine have high heads which is necessary to reach these high inlet velocities. Reaction turbines are able to extract the same amount of energy from sources with smaller heads, but require a larger volume flow. If the power output is kept as a constant, the specific speed will increase with decreasing head. Hence, the specific speed tells something about the best type of turbine (impulse or reaction) for a given situation. Figure 16 shows which turbine is the most efficient based on specific speed. The impulse (Pelton turbine 3.8.1) turbine is the most efficient between specific speeds of 0-12. The radial flow turbine (Francis turbine 3.9.1) is the best choice in the specific speed range of 20-100. The axial flow turbine (Kaplan turbine 3.9.2) is the most efficient at higher specific speeds (3). The following section will discuss the specific characteristics of the impulse and reaction turbine in a further extent.

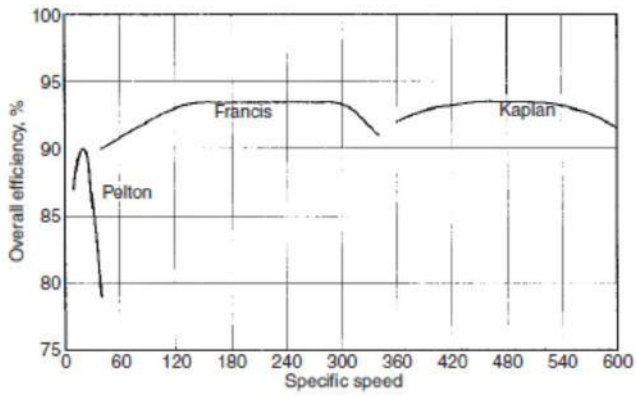

Figure 16: Efficiency for the Pelton, Francis and Kaplan turbine

3.8 IMPULSE TURBINE

As stated earlier, chapter 3 serves as A simplified model of the impulse turbine is shown in Figure 17 (4). Fixed nozzles just ahead of the runner convert as much potential energy as possible to kinetic energy by decreasing the pressure and increasing the velocity of the flow. The rotor changes the direction and velocity of the fluid flow. The pressure does not change over the rotor. If a lot of potential energy (high head) is available in an energy source, a nozzle will be able to convert this energy to a high velocity. The required flow area to convert the kinetic energy to work in the rotor will be just the exit area of the nozzle and not the entire runner circumference. Multiple jets can be used in a situation when the flow is too high for just one nozzle. The most simple impulse turbine is a cup with the shape of a half-moon where water follows the surface of the cup. However, already for a long time engineers tried to increase the turbine efficiency. The Pelton turbine was the first innovation and is described in paragraph (3.8.1). The Turgo (3.8.2) and crossflow turbine (3.8.3) are slightly different designs, but the fundamentals are identical to the Pelton turbine. The estimated power output can be estimated by the same set of formulas.

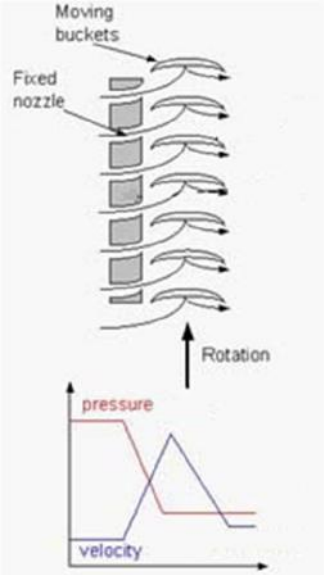

Figure 17: Flow through an impulse turbine (4)

3.8.1 PELTON TURBINE

The Pelton turbine is named after its inventor: Lester A. Pelton (1829-1908). Pelton worked in the gold mines of California and Nevada. Gold mines required power to crush ore, pump air into the mines and later for generating electricity. Mines often used steam engines to generate this power, which required a significant amount of firewood, or inefficient waterwheels in mountain creeks. To improve the power output of water wheels, mine owners built the first water turbines which consisted of simple hemispherical cups where a jet of water was directed on. The water was supplied from a reservoir higher up the mountain. The story goes that Pelton was watching such a water turbine when one of the pins holding a cup broke which misaligned the cup. Instead of hitting the cup in the middle, the water jet now hit the cup on the side which caused half-circle shaped water flow. Pelton saw how the direction of the water flow was inversed and instead of slowing down, the turbine accelerated. This gave Pelton the inspiration for the design of the Pelton Turbine (5).

Figure 18 shows the assembly of the Pelton turbine. The main components are a horizontal axis, a disk with buckets or vanes and a nozzle with flow control spear. Accessory components are a jet deflector, brake nozzle and a casing. A spear is used to control the flow through the nozzle. The water before the nozzle has a large amount of potential energy (pressure). The nozzle converts this to kinetic energy (velocity). The runner is a heavy construction which contains a lot of energy when rotating at high speed. If the water supply would be shut off, the runner could continue to spin for a while. To gain control over the rotational speed of the runner, a break nozzle is installed to the assembly. Water on this nozzle hits the backside of the buckets and slows the turbine down. The casing has no functionality for the turbine itself, but is necessary for safe operation.

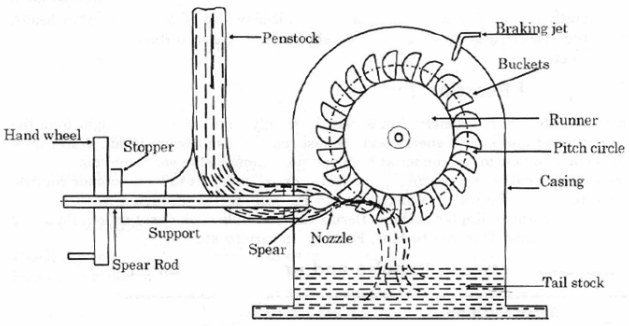

Figure 18: Pelton turbine (2)

The flow over a Pelton bucket is shown in figure 19. The absolute inlet velocity is denoted as V_1 which is the sum of the blade speed (U) and the relative velocity (V_{r1}) (6). In the following calculations, subscript 1 refers to the situation at the inlet and subscript 2 refers to the situation at the outlet

$$V_1 = V_{r1} + U$$

And:

$$V_2 = V_{r2}\cos\beta + U$$

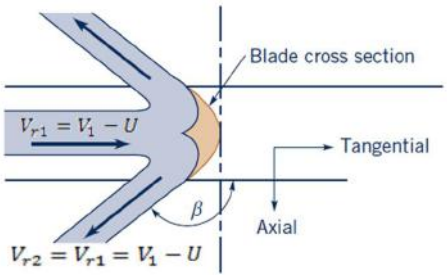

Figure 19: Flow over a Pelton bucket (6)

If the viscous effects are neglected, the relative velocity of the water stays constant:

$$V_{r1} = V_{r2}$$

The change in absolute velocity will be (by combining the equations above):

$$V_2 - V_1 = (U - V_1)(1 - \cos\beta)$$

If the torque (T) is expressed as velocity times mass times the distance to the shaft, the total torque generated by the water flow on the shaft is:

$$T_{shaft} = -T_{in} + T_{out}$$

$$T_{shaft} = -\dot{m}_1(r_1V_1) + \dot{m}_2(r_2V_2)$$

Mass flow and mean radius are constant:

$$T_{shaft} = \dot{m}r_m(U - V_1)(1 - \cos\beta)$$

The power output is the torque times the angular velocity in rad/s (ω) and U=rω.

$$P_{shaft} = T_{shaft}\omega = \dot{m}U(U - V_1)(1 - \cos\beta)$$

By reviewing the two derived formulas for torque and power, an optimum rotational speed can be found for a given energy source (V_1 is constant). The formula for torque shows that torque is max when U is zero. But because $\omega = \frac{U}{r}$, the available shaft power also becomes zero. The maximum value for U is when U=V_1 (The fluid can't accelerate the blade more than the velocity of the fluid itself). In this situation, U-V_1=0 and again, no power will be generated.

The ratio between U and V_1 is defined as the speed factor ϕ:

$$\phi = \frac{U}{V_1}$$

If U is expressed as ϕV_1 and power output is plotted for 0<ϕ<1, a maximum power output is found at ϕ=0.5 in an ideal situation (Figure 20). In reality, due to several losses in the turbine, the ideal speed factor is found between 0.46-0.47.

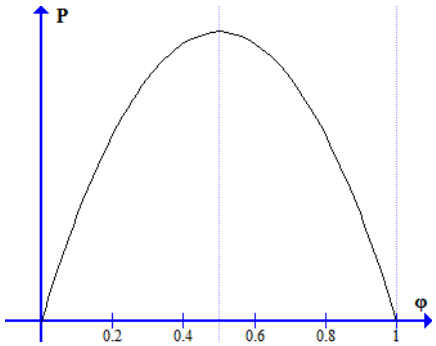

Figure 20: Power versus speed factor

Losses in nozzle

The available head from the energy source is transferred to useful kinetic energy. Some losses occur during the conversion from one energy source to another. The three dissipation methods are:

Head loss in the nozzle:

$$h_{nozzle} = \left(\frac{1}{C_v^2} - 1\right)\left(\frac{V_1^2}{2g}\right)$$

C_v is the velocity coefficient and indicates the efficiency of the nozzle.

Head loss due to fluid friction on the bucket surface:

$$h_f = \frac{V_{r1}^2}{2g}$$

The loss of kinetic energy in the exit flow:

$$h_{KE} = \frac{V_2^2}{2g}$$

The theoretical head which is delivered to the runner is:

$$H = H - h_{nozzle} - h_f - h_{KE}$$

The actual design of a Pelton Turbine is not as simple as stated above. The nozzle and bucket shape are two components where complex fluid mechanical calculations are required to obtain the optimal design. These calculations include flow path design and the structural design of the turbine. However, the moment-of-momentum principle gives a good estimation of the expected performance of the turbine and can also be used for the Turgo and crossflow turbine.

3.8.2 TURGO TURBINE

The Turgo turbine is a more advanced impulse turbine designed by Eric Crewdson in 1919. The design objective for Crewdson was to design an impulse turbine, cheaper than the Pelton turbine and able to operate at higher rotational speeds. Higher speeds enabled the turbine to operate on less expensive high speed generators and also removed the need for a gearbox. The application for a patent on this design took place in May, 1920 (7).

During operation, the water jet enters the Turgo turbine at acute angle, follows the contour of the blade and leaves the turbine on the other side (Figure 21). This differs from the Pelton turbine where the jet is aimed at the centre of a blade and splits into two. This design adds some advantages. The first advantage is that the water jet from the nozzle is not affected by the discharged water from the turbine. This increases the maximum operational possible angle β from Figure 19. Another advantage is that if a water particle "misses' the bucket, it hits the next bucket in the row and is still able to transfer its energy to the runner. The higher rotational speeds mean a smaller runner diameter for the same V_1. Therefore, more energy

Figure 21: Water jet through a Turgo turbine (29)

can be absorbed by a small diameter turbine. The advantage of a Turgo turbine is that it performs better in part load operation than the Francis turbine (8). The smaller runner diameter requires a smaller inlet velocity for a higher rotational speed. The Turgo turbine therefore operates on the higher specific speed range of the Pelton turbine and closes the gap between the Pelton turbine and Francis turbine (Figure 16).

3.8.3 CROSS-FLOW TURBINE

The cross-flow turbine is developed by Anthony Michell, Donát Bánki and Fritz Ossberger. The cross-flow turbine is also called the Bánki-Michell turbine or the Ossberger turbine. The turbine consists of two disks which are connected by curved blades often fixed on a horizontal axis. The water flow enters the turbine radially. The vanes redirect the water flow inwards where the water will interact with the runner a second time before leaving the turbine (Figure 22). The second interaction between the water and the blades generates about 33% of the power.

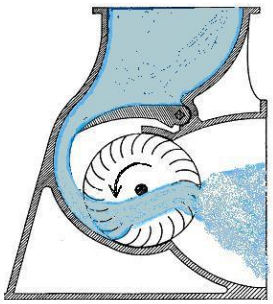

Figure 22: Cross-flow turbine (13)

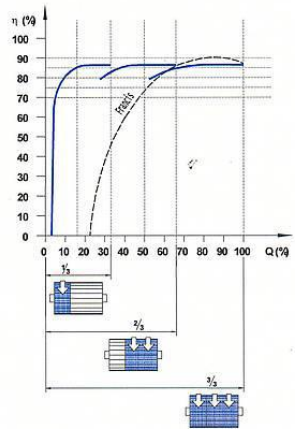

Figure 23: Part load cross-flow turbine (9)

An advantage of the cross-flow turbine is that a very simple arrangement can be made for part load operation. The drum-like construction makes it possible to divide the turbine into multiple sections. A subsection of the turbine will be able to operate under ideal conditions while the other sections are out of operation. An efficiency curve of a cross-flow turbine with two sections is shown in figure 23. In this case, the drum is divided into two sections where one section accounts for 2/3 of the turbine and the other section for 1/3. If only 1/3 of the water flow is available, a single section of the turbine will operate. Because this section operates under full load condition, the efficiency will be maximum. At full load conditions, a Pelton or Turgo turbine will be more efficient, but the benefit of the cross-flow turbine is the wide range of high efficiency part load operation (9).

3.8.4 TURBINE EFFICIENCY

The hydraulic efficiency of an impulse turbine can be calculated using the formulas given in paragraph 3.3: Turbine efficiencies. The hydraulic efficiency is the ratio between the generated power and the power available in the water source. Assumed is that the water is supplied from a large water basin where the velocity, and thus the kinetic energy, is zero.

$$\eta_H = \frac{P}{\rho Q g H} = \frac{P}{\dot{m} g H} = \frac{\dot{m} U (U - V_1)(1 - \cos\beta)}{\dot{m} g H}$$

If all of potential energy from the water head is converted to kinetic energy in the nozzle then:

$$V_1^2 = 2gH$$

Combining the formulas above and substituting the optimum value of U = 0.5V_1 gives:

$$\eta_H = \frac{-0.25 V_1^2 (1 - \cos\beta)}{\frac{V_1^2}{2}}$$

$$\eta_H = \frac{1 + \cos\beta}{2}$$

This means that if β = 180°, the hydraulic efficiency will be 100%. Due to practical limitations, it is not possible to design a hydraulic turbine with an efficiency of 100% (the waterjet must enter and leave the runner and therefore requires an axial flow component).

3.9 REACTION TURBINES

An impulse turbine transfers all of the potential energy in the nozzle and extracts this energy in the rotor. A reaction turbine diverges from this concept by converting a part of the potential energy in the rotor. The stator increases the absolute velocity and gives the fluid the right angle to interact with the rotor. In the rotor, the fluid is accelerated in the opposite direction as the rotational direction of the rotor. The relative velocity increases over the rotor, but the absolute velocity decreases. The process means that the pressure drops over both the stator and rotor. This process is visualized in figure 24. The turbine operates in a fully submerged environment where pressure differences are of vital importance for the functioning of the turbine. Hence, a pressurized casing is necessary for reaction turbines. All the blades interact with the water during the full circumference of the turbine. This is another important difference with the impulse turbine where only a few blades are affected by the water jet simultaneously.

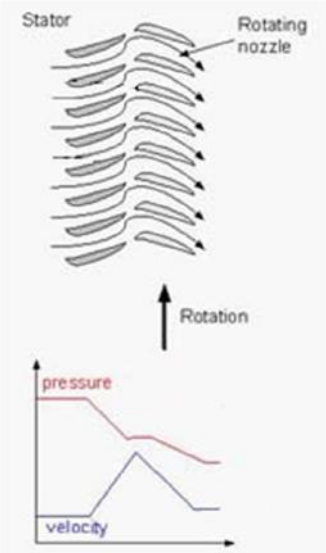

Figure 24: Flow through a reaction turbine (4)

Reaction turbines can be separated in categories based on the direction of the fluid flow through the turbine. A radial turbine has a radial fluid inlet. This kind of turbine is usually called the Francis turbine. A Kaplan turbine is fully axial. Francis turbines are often used in situations where the available head and volume flow are moderate. Kaplan turbines are used when only a small amount of potential energy is available, but the energy source is able to deliver a moderate to high volume flow. A mixed-flow turbine compromises the Francis and Kaplan turbine.

3.9.1 FRANCIS TURBINE

The first turbine comparable to the current Francis turbine is developed by the French engineer Bonoît Fourneyron in 1826 (10). This turbine achieved an efficiency of about 80%. Water entered the Fourneyron turbine in the inner core and was directed outwards. The vanes of the turbine swirled the flow and distributed the water around the inner periphery. Uriah A. Boyden developed an improved version of the Fourneyron turbine. The main design change was that the direction of the water flow was reversed (outwards in). Boyden also developed a conical inlet for the turbine which reduced the losses of potential energy due to abrupt area changes in the fluid flow. Another innovation was the submerged diffuser and diverging exit passage which converted residual kinetic energy to pressure. This increased the effective head across the turbine.

It was James B. Francis who developed standard methods for performance evaluation of hydro turbines. Francis also developed a scientific design method for turbines based on the path of water particles through the turbine and their different relative velocities under a given head. Francis bought the patent rights for the inward-flow turbine in 1847. The first model of the Francis type turbine reached a maximum efficiency of 71%. This model was an inward flow turbine with simple inlet guide vanes with increasing area to accelerate the fluid. The turbine blades had no curvature. Despite of the lower performance of the turbine, the simple design allowed Francis to test the calculations for his turbine performance theory. In the following years Francis improved his design by adding pre-swirl to the water before interacting with the turbine, adding curvature to the turbine and inlet guide vanes and improving the water discharge at the turbine exit. Francis calculated the efficiency of his turbine to be 79.31%. Testing proved that the efficiency was actually 79.37%.

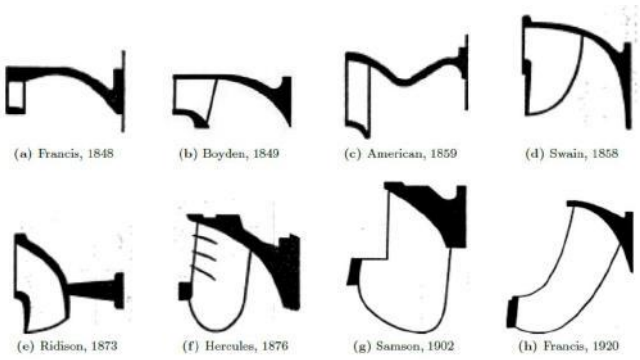

Figure 25: Timeline development Francis Turbine runner (10)

Many other engineers improved the Francis turbine. An overview of the most important design improvements is shown in figure 25 finishing with the last design in 1920, which is named after James B. Francis. The main components of this design are the spiral casing, inlet guide vanes, turbine blades and diffuser (Figure 26). The fluid is delivered to the turbine at the inlet with a certain velocity. The spiral casing distributes the fluid equally over the runners' circumference. To keep the velocity of the fluid constant, the area of the spiral casing gradually decreases. This prevents an uneven load distribution over the runner. The inlet guide vanes redirect the water in the proper direction and while doing so, convert potential energy to kinetic energy to accelerate the fluid before interacting with the runner blades. So the guide vanes double function as a nozzle. The diffuser decreases the velocity of the water leaving the runner.

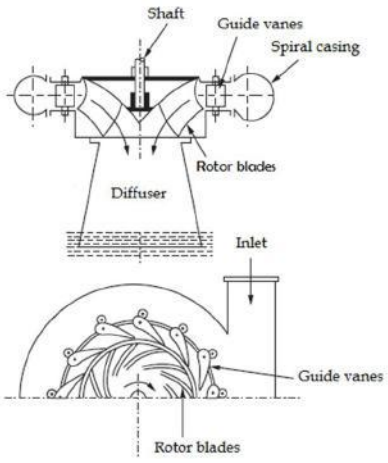

Figure 26: Francis turbine (2)

The diffuser

The diffuser of the turbine converts kinetic energy to potential energy (pressure). This increase in pressure enables the runner to expand the water to a pressure below atmospheric without inducing back flow through the turbine exit. In other words: the effective head of the turbine is increased. The head gain H_d can be calculated:

$$H_d = H + \frac{V_1^2 - V_2^2}{2g} - h_f$$

Where H is the height of the turbine above the tail water level, V_1 and V_2 represent the velocity at the inlet and outlet of the diffuser and h_f are the friction losses expressed in head.

In general, three types of diffusers can be distinguished: Straight diverging tube, bell mouthed tube and elbow shaped tube (Figure 27).

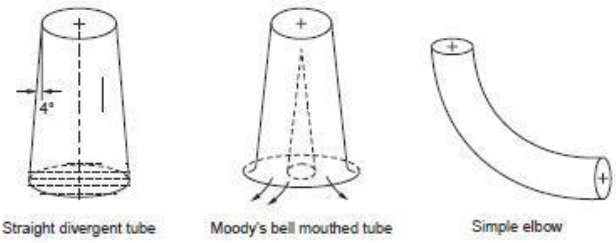

Figure 27: Most common diffuser models

The rotational velocity of the turbine must be as high as possible for a more efficient runner. Often, other equipment coupled to the turbine, like a generator, determines the most practical speed of the runner. This value gives the real specific speed, but only if the required power output is already determined.

The flow rate determines the length of the runner blade in axial direction. Both the specific speed and flow rate depend on available head and required power. The runner accelerates and redirects the fluid and is therefore a combined impulse reaction turbine.

Power generation estimation

A good estimation of the power generated by the Francis turbine is based on the Euler equation:

$$P = \dot{m}(V_{u1}u_1 - V_{u2}u_2)$$

To minimize the energy loss at the exit of the runner, the absolute velocity of the fluid must be minimal. If the swirl in the flow is minimal then the total velocity will equal the axial flow velocity. Consequential, V_{u2}=0. Hence:

$$P = \dot{m}V_{u1}u_1$$

The energy per kg flow rate transferred from fluid to runner is:

$$E_1 = V_{u1}u_1$$

The available energy per kg flow is:

$$E_a = gH$$

The work per unit flow generated is the difference between the available energy minus the energy in the exit flow:

$$W = gH - \frac{V_2^2}{2g}$$

The hydraulic efficiency is the ratio between the generated energy and the amount of energy available in the inlet fluid flow:

$$\eta_H = \frac{E_1}{E_a} = \frac{V_{u1}u_1}{gH} \quad OR \quad \eta_H = \frac{gH - \frac{V_2^2}{2g}}{gH} = 1 - \frac{V_2^2}{2gH}$$

3.9.2 PROPELLER TURBINE

A propeller turbine is very similar to the propeller on an airplane or a ship, but the goal of the turbine is the opposite: The turbine wants to extract power from the fluid flow where a propeller on an airplane or ship wants to deliver power to the fluid flow in order to generate thrust. The fluid enters and leaves the runner of a propeller turbine in axial direction. The best well-known propeller turbine design is the Kaplan turbine. Other propeller turbines are the Bulb, Straflo and S-type turbine, which are derived from the Kaplan turbine, only designed for specific situations.

Kaplan turbine

The Kaplan turbine is the result of the same series of developments as where the Francis turbine originates from. Viktor Kaplan published his first paper on turbines in 1908. The Kaplan turbine was introduced in 1913. The major improvement of the Kaplan turbine in respect to the Francis turbine is that variable blades and guide vanes increased the efficiency in part load operation. Another major difference with the Francis turbine is that the flow is redirected before entering the turbine which makes the Kaplan turbine an axial flow turbine (Figure 28). The Kaplan turbine is especially suitable for applications where the inlet flow fluctuates very much. The number of blades a Kaplan turbine requires varies from 3 at a head of 3 meter to 10 at a head of 70 meter. Due to the axial design the local tangential velocity on a blade differs with the radius of the turbine. The volume flow into the turbine is constant across the radius of the turbine. Therefore, the blade angle should differ with the radius of the blade. The combination of variable guide vanes and variable rotor blades enables the operator to find a combination for maximum efficiency for a wide varying range of flow conditions. For every situation, an optimal guide vane and rotor blade setting can be found. Experimental data provides a relationship between the size of the runner and the flow conditions. This relationship is based on the ratio between the runner diameter and the required power output but will not be discussed further at this moment.

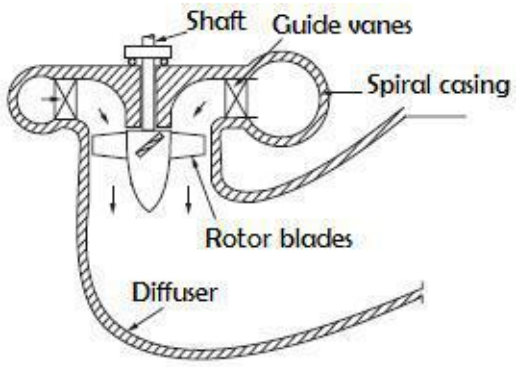

Figure 28: Kaplan turbine (2)

Variations on the Kaplan turbine

The Bulb turbine figure 29 is a turbine where the runner and generator are placed within a “bulb” in the fluid flow. The flow enters the turbine axial, converges around the bulb and passes the runner fully axial. The Bulb turbine design doesn’t require a spiral casing. The advantage of a Bulb turbine is the very compact arrangement of components which increases the flexibility for a hydroelectric power plant design. The disadvantage is that the bulb needs an additional ventilation arrangement for cooling air for the generator.

Figure 29: Bulb turbine (18)

Straflo stands for STRAight FLOw turbines. These turbines are very compact because the generator which is attached to the periphery of the runner (Figure 30). S-type turbines (Figure 31) are turbines where the flow is redirected just after the runner. The generator can now be situated after the runner. The Deriaz turbine is a mixed flow turbine, which means that the inlet flow direction is a mix between radial flow and axial flow.

Many more turbines are designed over the years. Each turbine solves a problem for a very specific situation. It is unfeasible to describe all these systems in this report. For this phase of the project it is enough to know that all these turbines are a variation on the Kaplan or Francis turbine.

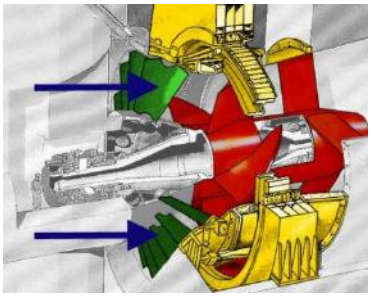

Figure 30: Straflo turbine (30)

Figure 31: S-type turbine (31)

3.10 POSITIVE DISPLACEMENT TURBINE

Designing a turbine can be a very time and money consuming task. Another option is to use a reversed pump as a turbine. This opens up the possibility to use the turbine as a pump in situations where it is necessary to force the Archimedes to a desired position. This is very useful when the movement of the Archimedes must be reinitiated after a period with no waves or when the device must be secured into a position if the waves are too high (see chapter 2).

Two types of pumps can be distinguished on the basic principles of the pump: displacement pumps and rotodynamic pumps. Rotodynamic pumps work on the sample principle as the Francis and Kaplan turbine, only reversed. For the centrifugal pump, the flow enters the runner near the axis and is compressed outwards to the volute. The design makes this type of pump (like the Francis turbine) irreversible. The axial flow pump works on the same principle as the Kaplan turbine. Due to their similar nature, the pump and turbine designs will be joined into one concept later in this report. Section 3.11 will give more clarification about this subject.

Positive displacement pumps are not comparable to any type of turbine. This is why the term positive displacement turbine is introduced. A positive displacement turbine is a hydro device which operates the same way a positive displacement pump does. However, the turbine extracts energy from a flow while the pump adds energy to a flow. This sections starts with a review on pump theories and uses the information in the previous sections about turbines. If the reader is new to this subject, it is advised to read the previous section of chapter 3 before continuing.

3.10.1 ROTODYNAMIC AXIAL PUMPS

Most of the formula's used for turbine design, are also usable for pump design. The purpose of the pump is exactly the opposite than the purpose of a turbine. Therefore, some of the formulas are redefined to fit the inversed design philosophy. The axial velocity is constant over the runner of the pump. The rotational velocity varies with the radius and so will the angles of the velocity triangle of the rotor. Assuming that the whirl at inlet is zero, the theoretical gain in head over the runner is:

$$H_{th} = \frac{u_2 V_{u2}}{g}$$

Where u_2 is the rotor speed in rpm and V_{u2} the rotational velocity in m/s.

The dimensionless head, flow and power coefficient are similar for pumps and turbines. Only the specific speeds differs. The specific speed for pumps is based on volume flow instead of power output.

Dimensionless specific speed: $N_s = \frac{N\sqrt{Q}}{(gh)^{\frac{3}{4}}}$

Dimensional specific speed: $N_s = \frac{N\sqrt{Q}}{h^{\frac{3}{4}}}$

Ideal head rise by impeller

Review the velocity triangles in figure 1. The energy added to the fluid can be calculated using the Euler equation:

$$P = \dot{m}(V_{u1}u_1 - V_{u2}u_2)$$

The absorbed energy from the fluid flow per unit mass is:

$$W = -(V_{u1}u_1 - V_{u2}u_2) = (V_{u2}u_2 - V_{u1}u_1)$$

The gain in head for an ideal situation is:

$$h_{ideal} = \frac{V_{u2}u_2 - V_{u1}u_1}{g}$$

3.10.2 SLIP AND MANOMETRIC HEAD

If the assumption is made that there is no inlet whirl, the term $V_{u1}u_1$ becomes zero. For this ideal head, the assumption is made that the fluid passes the runner at an equal velocity over the full blade length. In reality, the pressure at the leading edge is higher than the pressure at the trailing edge. Subsequently, the velocity is higher at the trailing edge. This induces a circular flow over the blade tips (i.e. the fluid leaks around the blade tips). In reality, the fluid leaves the blade with an average lower angle than the blade angle. A lower angle means a lower exit whirl velocity V_{u2}. This phenomenon is called slip. Losses due to slip are discussed after the trade-off in chapter 6. The slip factor σ_s corrects the theoretical head gain:

$$H_{th} = \sigma_s \frac{V_{u2}u_2}{g}$$

A pump is designed to increase the pressure of the fluid flowing through the runner. The pump must, besides increasing the pressure, compensate the pressure losses in piping and valves in the system. The total required pressure change is called the manometric head.

$$Total\ energy\ suction\ side = Total\ energy\ delivery\ side$$

$$\frac{P_s}{\gamma} + \frac{V_s^2}{2g} + Z_s = \frac{P_d}{\gamma} + \frac{V_d^2}{2g} + Z_d$$

Where Z is the height of the suction or delivery gauge. γ is the specific weight defined as $\gamma = \frac{g}{g_0}\rho$. The term g_0 is a dimensional constant which value depends on the units selected for the equation. In this case, $g_0 = 1\ \frac{kg\ m}{N\ s^2}$ which gives γ the units $\frac{N}{m^3}$. Pressure is now expressed as meter head. Subscript s indicates the value at the suction side and the d stands for delivery side. The manometric head is:

$$h_m = \left(\frac{H_d}{\gamma} - \frac{H_s}{\gamma}\right) + \frac{V_d^2 - V_s^2}{2g} + (Z_d - Z_s)$$

The change in pressure between the suction and delivery side can be expressed as the sum of change is potential energy (effective head h_c) and kinetic energy where assumed is that all velocity is transferred to static pressure (i.e. V_d=0). The statement above results in the following formulas:

$$\frac{H_d}{\gamma} - \frac{H_s}{\gamma} = h_c + \frac{V_s^2}{2g}$$

Substituted into the formula for the manometric head:

$$h_m = h_c + \frac{V_d^2}{2g} + (Z_d - Z_s)$$

As stated before, the velocity at the delivery side is assumed to be zero. The difference between Z_d and Z_s is also very small and can be neglected. This means that the manometric head is equal to the change in static head + all losses.

Efficiencies

The overall efficiency of a pump is divided over three terms:

The manometric efficiency is the ratio between the manometric head and the ideal head.

$$\eta_m = \frac{H_m\, g}{V_{u2}u_2 - V_{u1}u_1}$$

The mechanical efficiency is the ratio between rise in total energy in the fluid and the power input

$$\eta_{mech} = \frac{Energy\,delivered\,to\,the\,fluid}{Work\,input} = \frac{(u_2V_2)Q\rho}{power\,input}$$

The volumetric efficiency is equal to the volumetric efficiency of a turbine:

$$\eta_{vol} = \frac{Volume\,delivered\,to\,the\,pump}{Volume\,passing\,the\,impeller}$$

The overall efficiency is:

$$\eta_o = \eta_m\, \eta_{mech}\, \eta_{vol}$$

3.10.3 POSITIVE DISPLACEMENT PUMPS

A displacement pump traps a volume and forces it down the runner. A displacement pump is a constant flow pump which means that the volume flow is not dependable on the discharge pressure. In practice, this is not entirely true because leakages and other losses often increase with pressure. Displacement pump can be divided into two other categories: Rotary and reciprocating type pumps.

Reciprocating pumps

A reciprocating pump consists of a cylinder which is connected by a crank to a rotating engine (Figure 32). If the piston moves downwards (increasing the volume of the cylinder), the pressure in the cylinder drops and water is sucked in from the low pressure side. If the piston moves upwards, the volume of the cylinder is reduced and the water pressure rises. The high pressure water is discharged to the other side of the engine. Valves regulate the in- and outflow of the water to the right pressure side. The discharge only takes place half a revolution of the drive shaft, the other half is for suction of the fluid into the cylinder. This creates a fluctuating volume flow. It is possible to reduce this fluctuating by using a double action cylinder or a multi cylinder pump. The volume flow Q in m^3/s is calculated by:

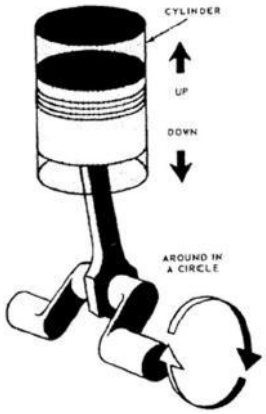

Figure 32: Reciprocating pump (19)

$$Q = \frac{LAN}{60}$$

Where L is the stroke length of the piston, A is the piston area and N are the revolutions per minute of the engine. If the rotational speed of the engine is expressed in ω and r is half a stroke length, then:

$$Q = \frac{A\omega r}{\pi}$$

Slip in a reciprocating pump are leakages along the valves, pistons, packing, etc. The percentage slip can be calculated as:

$$percentage\,slip = \frac{Q_{th} - Q_{ac}}{Q_{th}} \times 100\%$$

Where Q_{th} is the theoretical volume flow as calculated earlier and Q_{ac} is the actual measured volume flow. The coefficient of discharge C_d is:

$$C_d = \frac{Q_{ac}}{Q_{th}}$$

Rotary positive displacement pumps

A more simple construction than the reciprocating pimp is the rotary displacement pump. The theory is the same for both concepts. However, the way suction and the displacement of the fluid are achieved diverges. A rotating mechanism sucks fluid into a trapped volume created by the dimensions of the pump. A rotating movement forces the trapped volume forwards and delivers the fluid to the high pressure side. An example of a rotary displacement pump is the screw pump. This pump is used to explain the principle. More types of pumps are mentioned later.

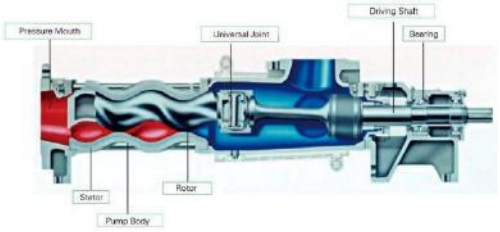

Figure 33: Single screw configuration (20)

Screw pumps originate from the Archimedes screw pump which was designed to transfer large water volumes over small vertical distances. The Archimedes screw pump is still used for this purpose today. Modern screw pumps are able to pump liquids up to pressures of 310 bar. Twin screw pumps are relative expensive to produce due to their complex geometry. A single screw pump is shown in Figure 33. Single screw pump can be very effective for high pressure applications if enough space is available for multiple stages. The twin screw pump has shafts with a screw rotor each (Figure 34). The two screws do not touch each other but are synchronized by an external gear. No blade contact also means that there is some leakage of fluid at the blade tips. The usage of screw pumps are especially beneficial for high viscosity fluids such as oils and asphalt. Also for low viscosity flows at high pressure and low flow rates, screw pumps are able to deliver a non-pulsating flow which is necessary in, for example, a fuel combustors. A typical performance curve of a multiple screw pump is shown in figure 35. Notice how efficiency levels are maintained high for higher viscosity levels (water has a viscosity of 1 cSt or mPa·s).

Figure 34: Twin screw rotor (33)

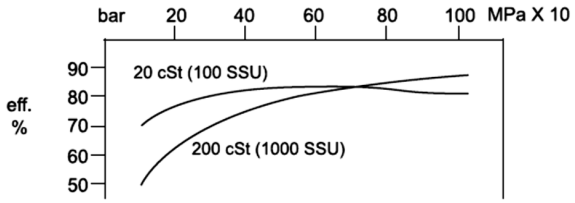

Figure 35: Screw pump efficiency curve (34)

Pump types

Table 1 gives an overview of pump types which can be used as a turbine. A small description is given for each pump. The exact working of each pump is not described because this is not necessary to perform a solid trade-off.

Type	Name	Working	Description
Rotating positive displacement pumps	Lobe pump	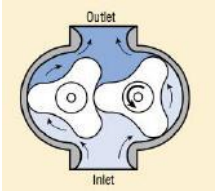 (11)	The two runners increase the area at the inlet of the pump which creates suction. The fluid is now forced along the circumference of the pump towards the high pressure outlet. The two runners are not in contact with each other but are synchronized by an external gear
	Circumferential piston pump	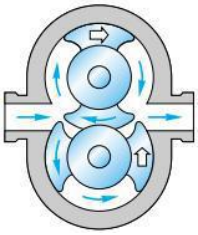 (12)	This pump is a variant on the lobe pump. The rotor design reduces slip and handles high viscosity fluids better.
	Gear pump	 (11)	Works on the same principle as the lobe pump. For the gear pump, one gear is driven which turns the other gear.
	Screw pump	 (13)	The design of the runner creates a closed volume which is forced down the axis.
	Variable vane pump	 (14)	The vanes are pushed outwards by either centrifugal force, springs or pressurized slots. The area between the vanes increase near the inlet, creating suction. The area near the outlet decreases which forces the fluid out.

	Flexible impeller pump		Based on the same working principle as the vane pump. Instead of variable vanes, the vanes are made flexible which bend to the variable outer surface.
	Peristaltic pump	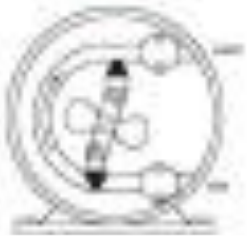 (3)	A volume is trapped within a flexible tube between two rollers. The fluid is forced towards the high pressure outlet.
Reciprocating positive displacement pump	Plunger/piston pump		A piston is connected by a crank to a rotating shaft. The crank provides one upwards and one downwards movement per rotation. The fluid is sucked into the cylinder in one direction and pushed out under pressure on the other direction.
Rotodynamic pumps (15)	Radial flow	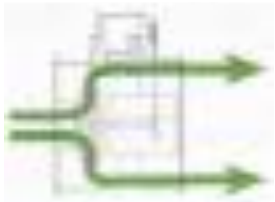	An impeller adds kinetic energy to the fluid by creating a whirl in the flow. This kinetic energy is transferred to potential energy before leaving the impeller. Radial flow pumps are often used for high pressure, low flow rate applications. Axial flow pumps are more often used in low pressure, high flow rate situations. A mixed flow pump compromises both pumps.
	Mixed flow	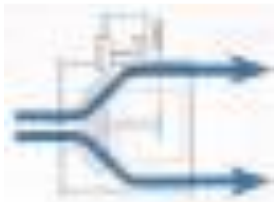	
	Axial flow		

Table 2: Working of the most common pump types

3.11 SIMILARITIES BETWEEN PUMPS AND TURBINES

A lot of turbines and pumps are discussed in this chapter. To bring some order, many turbines and pumps are already divided into groups. A small review for the turbines and their pump counterpart follows.

Rotodynamic pumps can be compared to the reaction turbines. The radial flow pump can be seen as a reversed Francis turbine. Both are not bidirectional. The application of this kind of impeller would be possible but complicates the design of the power take off. The axial flow pump is a reversed Kaplan turbine. This results in two concepts for the trade-off: The Francis concept and the Kaplan concept.

An impulse turbine rotates because a fluid pushes against the turbine blades. This corresponds with the positive displacement pump where the runner pushes the fluid towards a high pressure area. However, the runner design of conventional impulse turbines diverse very much from runners of positive displacement pumps. Every type of runner has its own strengths and weaknesses. Therefore, the impulse type hydro devices also have two concepts in the trade-off: The impulse concept and the positive displacement turbine concept.

The joining of the turbine and pump designs into one concepts reduced the many possibilities into four concepts. The four concepts are explained further in chapter four. Refer to this chapter for more information about how this report handles the differences between the derived concepts.

7 CONCLUSION AND RECOMMENDATIONS

7.1 CONCLUSION

Impulse turbines and reaction turbines are the two main groups of hydro turbines used for energy extraction from water flows. The impulse turbine extracts energy by reducing the absolute tangential velocity of the flow. The reaction turbine extracts energy by using pressure to accelerate water in the runner which exerts a force on the blades (2nd law of Newton). Four concepts are suitable as power take-off device for the Symphony wave energy converter: Positive displacement turbine, Impulse turbine, Francis turbine and Kaplan turbine. All four concepts meet the requirements following from operational limitations. The most important requirements for the prototype are that the device must be able to handle 130 litres per second at 350 rotations per minute. The turbine must extract 32.5 kW of power from the flow without adding excessive heat to the flow. The concepts are compared using six criteria. The efficiency indicates how much the turbine influences the flow and whether any heat is generated by interacting with the turbine. Due to the extraordinary nature of the Symphony, water flows through the turbine in two directions. This means that the turbine assembly must be designed to operate bidirectionally. The pumping functionality indicates how well the turbine works as a pump, which would ease the forced positioning of the outer cylinder. Manufacturing and maintenance are both cost driven. The fact that the device operates submerged fixed to an ocean floor is of great influence for the maintenance criterion. The reliability indicates how well a device operates outside its design conditions and how likely a concept is to fail.

The positive displacement turbine concept is the suitable concept for the prototype of the Symphony. The trade-off had an inconclusive result for the full scale model. More research is required to be able to give a clear answer. Lessons learned from the prototype will be used during this research. The positive displacement turbine concept is the most suitable concept for the prototype of the Symphony. This concept scored high on the most important criteria bidirectional, pump functionality and reliability. From all pumps which were considered possible positive displacement turbine, the lobe pump and external circumferential piston pump (ECP) were considered most suitable. The lobe pump was preferred due to earlier experiences of Teamwork Technology and its partners. However, during the further development of the lobe turbine, new insights were gained which led to a reconsideration of the pump selection.

The final result of this project, and answer to the main research question, is that the ECP turbine is considered the best power take-off device for the Symphony wave energy converter. The advantage of the ECP pump in respect to the lobe turbine is that the ECP turbine has less slip, a non-pulsating flow and less critical synchronization requirements. The slip reduction is the result of a longer seal between runner and casing. The pulsation is gone due to the constant position of the sealing point between a runner and the axis of the other runner. This sealing method between runners makes the synchronization system for the two runners less critical. The project will continue with working towards a manufacturing design for the ECP turbine.

7.2 RECOMMENDATIONS

The following recommendations are made to optimize the current design and elaborate this conceptual design into a product.

Modelling and testing
The lower slip and reduced pulsation properties of the ECP turbine are very promising as optimal power take-off turbine solution. The design of this turbine must be developed further to be able to predict its performance more accurate. The crossing rotating regions of the lobe and ECP turbine make it impossible to simulate the performance of these turbines with (free) low level modelling software. Advanced modelling software is able to perform these simulations and can be used to investigate the difference in performance between the lobe and EPC turbine. The runners of the ECP turbine have to be designed to reduces losses and optimize efficiency. Results from computational fluid simulations must be validated during (scale) model testing.

Flow path design
The design in this report is limited to the runners only. The complete flow path, including inlet and outlet, must be optimized to reduce losses. Also the possibility to use flow guides to reduce vortices or highly turbulent flow must be investigated.

Labyrinth sealing
The use of labyrinth sealing to reduce slip was investigated in section 5.5. It was found that improper labyrinth design can increase slip instead of reducing slip. A more extensive study to labyrinth sealing must establish if labyrinth sealing is a useful addition to the turbine design. This study can include a literature study as well as simulations or testing.

Accessory components
Other mechanical components of the turbine assembly still have to be designed. The most important components are the synchronization mechanism and the interface where the turbine is connected to the generator. Gears are usually used as synchronization mechanism for lobe and ECP pumps. The turbine will change its rotating direction every five seconds which will induce high fatigue loads and wear on the mechanism. It is advised to investigate if gears are also suitable for this situation and if there are any acceptable alternatives.

8 REFERENCES

1. **Drew, B, Plummer, A R en Sahinkaya, M N.** *A review of wave energy converter technology.* Bath, UK : Department of Mechanical Engineering, University of Bath, 2009.
2. **Kothandaraman, C.P. en R, Rudramoorthy.** *Fluid Mechanics and Machinery.* New Delhi : New Age International, 2007. 978-81-224-2558-1.
3. **Round, G.F.** *Incompressible Flow Turbomachines: Design, selection, applications, and theory.* Oxford : Gulf Professional, 2004. 0750676035.
4. **Turbines info.** What is a turbine? *What is a turbine?* [Online] Turbines info. [Citaat van: 13 05 2015.] http://www.turbinesinfo.com/what-is-a-turbine/.
5. **Stern, Dr. David P.** Planetary Swing-by and the Pelton Turbine. *Planetary Gravity-Assist and the Pelton Turbine.* [Online] 01 05 2015. http://www-istp.gsfc.nasa.gov/stargaze/Spelton.htm.
6. **Munson, Bruce R, Young, Donald F en Okiishi, Theodore H.** *Fundamentals of Fluid Mechanics.* Hoboken : John Wiley & Sons, 1998. 9780471170242.
7. **Gilbert Gilkes & Gordon Ltd.** A Brief History of a Good Company. *About Gilkes - Water Turbine Company in Kendal.* [Online] [Citaat van: 07 05 2015.] http://www.gilkes.com/user_uploads/gilkes%20history.pdf.
8. **Gilbert Gilkes & Gordon Ltd .** Gilkes Turgo Impulse Hydro Turbine. *Turgo Turbine Manufacturers - Gilkes Product Range.* [Online] [Citaat van: 07 05 2015.] http://www.gilkes.com/user_uploads/turgo%20paper2.pdf.
9. **Water21.** Ossberger Crossflow Turbine. *Issberger Crossflow Turbine.* [Online] Water21. [Citaat van: 07 05 2015.] http://www.water21.org.uk/hydropower/ossberger-hydroturbines/the-ossberger-turbine/.
10. **Lewis, B.J., Cimbala, J.M. en Wouden, A.M.** *Major historical developments in the design of water wheels and Francis hydroturbines.* State College : Department of Mechanical and Nuclear Engineering, The Pennsylvania State University, 2014.
11. **Hydraulics and Pneumatics.** Hydraulics and Pneumatics. *Hydraulics and Pneumatics | Fluid power basic content from Hydraulics and Dynamics.* [Online] Hydraulics and Dynamics magazine, 1 1 2012. [Citaat van: 10 06 2015.] http://hydraulicspneumatics.com/200/TechZone/HydraulicPumpsM/Article/False/6401/TechZone-HydraulicPumpsM.
12. **Mechanical Prasad.** Pumps | Mechanical Prasad. *Mechanical Prasad | Home of engineering data.* [Online] Mechanical Prasad, 15 02 2011. [Citaat van: 15 06 2015.] https://mechanicaldatahelp.wordpress.com/2011/02/15/pumps/.
13. **Microhydro.** Types of Turbines. *Microhydro Ireland domestic and commercial hydroelectric schemes.* [Online] [Citaat van: 07 05 2015.] http://www.microhydro.ie/section/TypesofTurbines.
14. **Encyclopædia Britannica Online.** Vane Pump | Britannica.com. *Britannica.com.* [Online] Encyclopædia Britannica Online. [Citaat van: 10 06 2015.] http://www.britannica.com/technology/vane-pump.
15. **IHS Engineering360.** Impellers Information on GlobalSpec. *IHS Engineering360 - Engineering Search & Industrial Supplier Catalogs.* [Online] IHS Engineering360. [Citaat van: 10 06 2015.] http://www.globalspec.com/learnmore/flow_control_flow_transfer/pumps/impellers.
16. **Volk, Michael.** *Pump Characteristics and Applications.* Boca Raton : Taylor & Francis Group, 2005. 9780824727550.
17. **Karassik, Igor J, et al.** *Pump Handbook Third Edition.* New York : McGraw-Hill, 2001. 0070340323.

18. **Hitachi.** 2001 Special Issues. *Hitachi review.* [Online] 08 2001. [Citaat van: 12 05 2015.] http://www.hitachi.com/rev/pdf/2001/r2001_technology_ps.pdf.
19. **Integrated Publishing.** Chapter 12 - Internal Combustion engine. *Integrated Publishing - Your source for military specifications and educational publications.* [Online] Integrated Publishing. [Citaat van: 08 06 2015.] http://www.tpub.com/machines/12.htm.
20. **Direct Industry.** Screw pump/ for viscid fluids. *Direct Industry: The online Industrial Exhibition.* [Online] Direct Industry. [Citaat van: 22 05 2015.] http://www.directindustry.com/prod/zhejiang-xingsheng-machinery-co-ltd/screw-pumps-viscous-fluids-61717-1289283.html.
21. **Wallace, James S.** *Wind, Waves and Tides: Alternative Energy Systems.* University of Toronto, 2014.
22. **Stewart, Robert H.** *Introduction to Physical Oceanography.* sl : University Press of Florida, 2008. 1616100451.
23. **Robert G. Dean, Robert A. Dalrymple.** *Water Wave Mechanics for Engineers and Scientists.* Singapore : World Scientific, 1991. 9789810204211.
24. **KVDP.** *Map prevailing winds on earth.* Own work, sl : 2009.
25. **Anthoni, Dr J Floor.** Oceanography: waves. *theory and principles of waves, how they work and what causes them.* [Online] Seafriends, 2000. [Citaat van: 24 04 2015.] http://www.seafriends.org.nz/oceano/waves.htm.
26. **NASA.** NASA - Ocean Surface Topography Mission/Jason 2 Begins Mapping Oceans. *NASA - Ocean Surface Topography Mission/Jason 2 Begins Mapping Oceans.* [Online] NASA, 30 07 2008. [Citaat van: 28 04 2015.] http://www.nasa.gov/mission_pages/ostm/news/ostm-20080730.html#.VUOODfntmko.
27. **World Meteorological Organization.** *Manual on Codes: International Codes Volume I.1.* Geneva : World Meteorological Organization, 2014. 978-92-63-10306-2.
28. **World Meteorological Organization .** *Guide to Meteorological Instruments and Methods of Observation.* Geneva : World Meteorological Organization, 2008. 978-92-63-10008-5.
29. **Renewables First.** Pelton & Turgo Turbines. *Hydropower Turbines & Windpower Turbines fir Farms.* [Online] Renewables First. [Citaat van: 07 05 2015.] http://www.renewablesfirst.co.uk/hydro-learning-centre/pelton-turgo-turbines/.
30. **VPE.** STRAFLO-Turbine. *VPE.* [Online] [Citaat van: 29 07 2015.] http://www.vpe.ch/html/straflo.php.
31. **Addnew.** Water Turbines, Hydro Turbines, hydropower stations, ADDNEW. *Hydro Turbines, Generators, Water Turbines, Electrical Equiment, etc.* [Online] [Citaat van: 29 07 2015.] http://www.addnew.com.hk/hydropower%20turbines/.
32. **PetroWiki.** Positive displacement pumps. *PetroWiki.* [Online] [Citaat van: 03 06 2015.] http://petrowiki.org/Positive_displacement_pumps.
33. **Motorhead at English Wikipedia (Own work).** *Lysholm screw rotors.* 17 06 2006.
34. **James R. Brennan.** *High Efficiency Multipe Screw Pumps.* sl : Colfax Corporation, 2007.
35. **PureServe Systems.** Sanitary PD pumps, Rotary Lobe & Gear Pumps & Parts. *PureServe Systems - Sanitary and High Purity Fluid Handling Equipment.* [Online] [Citaat van: 19 08 2015.] http://www.pureservesystems.com/rotary_lobe_gear_pump.aspx#fl-3.
36. ***SmugMug.* [Online] [Citaat van: 15 08 2015.] http://need-media.smugmug.com/keyword/Wave;energy/i-L3vwCzL/A.**
37. Alternative Energy Tutorials. Wave Energy Devices that Harness Wave Energy. *Alternative Energy Tutorials - Green Energy for the Home.* [Online] [Citaat van: 21 08 2015.] http://www.alternative-energy-tutorials.com/wave-energy/wave-energy-devices.html.
38. Subsea World News Staff. UK: Aquamarine Power Unveils Proposals for Lewis Wave Energy Project. [Online] Subsea Word News, 05 03 2012. [Citaat van: 21 08 2015.] http://subseaworldnews.com/2012/03/05/uk-aquamarine-power-unveils-proposals-for-lewis-wave-energy-project/.

39. Fristam Pumpen. *Manufacturer of high quality hygienic pumps.* [Online] [Citaat van: 28 08 2015.] http://www.fristam.de/.
40. Bremer, Marc. Powerpoint slides Matching and Control, minor Gas Turbines. Amsterdam : Hogeschool van Amsterdam, 2015.
41. Axda0002 at English Wikipedia. Wikimedia commons. [Online] 20 05 2006. [Citaat van: 31 08 2015.] https://commons.wikimedia.org/wiki/File:Cavitation_Propeller_Damage.JPG.
42. Wave Dragon. Wave Dragon - Principles. *Wave Dragon.* [Online] [Citaat van: 21 08 2015.] http://www.wavedragon.net/index.php?option=com_content&task=view&id=6&Itemid=5 21-08-2015.
43. Brighthub. Find science and technology articles. *Archemides Wave Swing Mechanism.* [Online] Brighthub, 29 06 2009. [Citaat van: 30 10 2015.] http://www.brighthub.com/environment/renewable-energy/articles/40548.aspx.